





## ABSTRACT

Post-combustion CO<sub>2</sub> capture by means of temperature swing adsorption using amine-functionalized sorbents has the potential of overcoming many deficiencies of the current state-of-the-art in this field, i.e. aqueous amine scrubbing. In the past decade, an effort has been made in developing CO<sub>2</sub> sorbents suitable for post-combustion CO<sub>2</sub> capture, whereas the development of processes that implement these newly developed sorbents has gained comparably little attention.

At the Institute for Chemical, Environmental and Biological Engineering at TU Wien, a temperature swing adsorption process based on an interconnected multi-stage fluidized bed design has been developed and extensively investigated at bench scale. The bench scale unit features two reactor columns, the adsorber and the desorber, which each consisting of five vertically stacked fluidized bed stages. This design enables a counter-current contacting regime of gas and solids, which is necessary for efficient CO<sub>2</sub> capture operation. The sorbent materials utilized in the bench scale unit feature amine groups on the surface, which allow for selective and reversible CO<sub>2</sub> adsorption.

For further upscaling of the temperature swing adsorption process, it must be ensured that CO<sub>2</sub> can be captured in an efficient and cost-effective manner, especially in comparison to the current state-of-the-art. Subject matters with high practical relevance were investigated in the course of numerous experimental studies in the temperature swing adsorption bench scale unit. The obtained results were used to derive recommendations for the post-combustion CO<sub>2</sub> capture process based on temperature swing adsorption using amine-functionalized sorbents.

Results obtained from parameter variations showed that high CO<sub>2</sub> capture efficiencies can be achieved in a wide range of operating conditions within the proposed temperature swing adsorption system.

It was shown that sufficient heat transfer in the fluidized bed columns becomes critical at high CO<sub>2</sub> feeding rates, whereas at high flue gas feeding velocities in the adsorber, fast reaction kinetics and efficient gas-solids contact are required to ensure efficient CO<sub>2</sub> capture operation. Reactive gas constituents, such as SO<sub>2</sub> and NO<sub>x</sub>, are typically present in flue gases at ppm-levels. Even at these low concentrations, degradation of amine-functionalized sorbents has been documented by other workers. An experimental campaign at the site of a combined heat and power plant revealed the detrimental impact of these gas constituents on the CO<sub>2</sub> capture performance of the temperature swing adsorption bench scale unit. The removal of process emissions can increase construction cost, as well as the operational cost associated with CO<sub>2</sub> capture units. Therefore, potential environmental emissions need to be identified and quantified. Two 120-hour experiments were conducted in the bench scale unit, each with a different amine-functionalized sorbent to allow for assessment in this regard. It was shown that nitrogenous emissions from the temperature swing adsorption process are significantly lower than comparable emissions from an amine scrubbing process using the benchmark solvent i.e. aqueous monoethanolamine. A major constituent of flue gas is water. Since amine-functionalized sorbents are able to co-adsorb considerable amounts of water, it is important to understand the role of water in the temperature swing adsorption process. In a dedicated experiment, the impact of water co-adsorption on the process heat demand was identified and possible strategies for controlling water co-adsorption are discussed. Heat integration within a process can contribute in a reduction of the process heat demand. In amine scrubbing, a heat exchanger is used to transfer heat

from the hot lean solvent to the cooler rich solvent. A similar strategy was investigated in the temperature swing adsorption bench scale unit. Here, a heated moving bed heat exchanger was used to pre-heat rich sorbent before it enters the desorber, and a cooled moving bed heat exchanger was used to simulate the recovery of sensible heat from the lean sorbent exiting the desorber. In an initial experiment with these heat exchangers, a considerable reduction in the desorber heat demand could be observed.

From the conducted work, a number of recommendations are drawn regarding the design of the next-scale temperature swing adsorption unit for post-combustion CO<sub>2</sub> capture. These design recommendations are aimed at intensifying gas-solids contact in the adsorber as well as improving heat transfer within the fluidized bed columns and facilitating heat integration within the process. A sorbent recommendation is given that allows for operation with low environmental emissions and low sorbent degradation. Furthermore, critical flue gas constituents that have shown to cause sorbent degradation are identified and corresponding flue gas specifications are given. Additionally, co-adsorption and subsequent transport of water between the columns has been identified to allow for higher flexibility in a techno-economic evaluation.

## KURZFASSUNG

Temperaturwechseladsorption mittels Amin-funktionalisierten Adsorbens hat das Potential zahlreiche Defizite des gegenwärtigen Standes der Technik auf dem Gebiet der CO<sub>2</sub>-Abscheidung aus Verbrennungsabgasen zu überwinden. In den letzten zehn Jahren wurden große Anstrengungen im Bereich der CO<sub>2</sub>-Adsorbens-Forschung unternommen, während die Entwicklung von Prozessen, die diese neuartige Adsorbentien implementiert, vergleichsweise wenig Beachtung gefunden hat.

Am Institut für Verfahrenstechnik, Umwelttechnik und technische Biowissenschaften an der TU Wien wurde ein Temperaturwechseladsorptionsverfahren auf Basis eines mehrstufigen Wirbelschichtdesigns entwickelt und im Labormaßstab umfassend untersucht. Die dafür verwendete Versuchsanlage verfügt über zwei Reaktorkolonnen, den Adsorber und den Desorber. Diese Kolonnen bestehen jeweils aus fünf Wirbelschichtstufen die senkrecht übereinander angeordnet sind. Das mehrstufige Reaktordesign ermöglicht den, für einen effizienten CO<sub>2</sub>-Abscheidebetrieb, notwendigen Gegenstromkontakt von Gas und Feststoff. Die untersuchten Adsorbensmaterialien verfügen über Amingruppen auf ihrer Oberfläche die es ihnen erlaubt CO<sub>2</sub> reversibel und selektiv zu adsorbieren. Im nächstgrößeren Prozessmaßstab muss sichergestellt werden, dass CO<sub>2</sub> effektiv und kosteneffizient abgeschieden werden kann, ins besondere in Hinblick auf den gegenwärtigen Stand der Technik, der Rauchgaswäsche mittels wässrigen Amin-Lösungen. Im Laufe von zahlreichen experimentellen Studien wurden Themengebiete mit besonders hoher praktischer Relevanz behandelt. Die Ergebnisse aus diesen Untersuchungen wurden in weiterer Folge dazu genutzt Designempfehlungen für den nächsten Skalierungsschritt abzuleiten.

Ergebnisse aus einigen Parametervariationen haben gezeigt, dass es mit dem vorgeschlagenen Temperaturwechseladsorptionssystem möglich ist unter einer Vielzahl verschiedener Betriebsbedingungen CO<sub>2</sub> effizient abzuscheiden. Es hat sich gezeigt, dass bei hohen CO<sub>2</sub>-Einspeiseraten die Wärmeübertragung zwischen Wärmetauschern und der Wirbelschicht besonders wichtig wird. Des Weiteren wurde gezeigt das bei hohen Rauchgasgeschwindigkeiten im Adsorber, eine schnelle Reaktionskinetik und ein effizienter Gas-Feststoff-Kontakt erforderlich sind, um einen effizienten CO<sub>2</sub>-Abscheidebetrieb sicherzustellen. Reaktive Gasbestandteile wie SO<sub>2</sub> und NO<sub>x</sub> liegen in Rauchgasen typischerweise im ppm-Bereich vor. Selbst bei diesen niedrigen Konzentrationen wurde eine Vergiftung des Amin-funktionalisierten Adsorbens dokumentiert. Eine experimentelle Kampagne am Standort eines Blockheizkraftwerks hat den nachteiligen Einfluss dieser Gasbestandteile auf die CO<sub>2</sub>-Abscheideleistung des Prozesses bestätigt. Maßnahmen zur Beseitigung von Prozessemissionen kann Bau- und Betriebskosten von CO<sub>2</sub>-Abscheideanlagen beträchtlich erhöhen. Daher müssen potenzielle Umweltemissionen identifiziert und quantifiziert werden. Um Prozessemissionen in dieser Hinsicht zu beurteilen, wurden zwei 120-Stunden Experimente mit jeweils einem anderen Amin-funktionalisierten Adsorbens durchgeführt. Es wurde gezeigt, dass stickstoffhaltige Prozessemissionen signifikant niedriger sind als vergleichbare Emissionen aus der Aminwäsche mit einer Monoethanolamin-Lösung. Ein Hauptbestandteil von Rauchgasen ist Wasserdampf. Da Amin-funktionalisierte Adsorbentien in der Lage sind erhebliche Mengen an Wasser zu adsorbieren, ist es wichtig, die Rolle von Wasser im Temperaturwechseladsorptionsprozess zu verstehen. In einem gesonderten Experiment wurde der Einfluss der Wasser-Ko-Adsorption auf den Prozesswärmebedarf ermittelt und mögliche Strategien zur Steuerung der Wasser-Ko-Adsorption diskutiert. Die Wärmeintegration innerhalb eines Prozesses kann zur Reduzierung des Prozesswärmebedarfs

beitragen. Bei der Rauchgaswäsche mit wässrigen Amin-Lösungen wird ein Wärmetauscher verwendet, um Wärme von der heißen CO<sub>2</sub>-armen Lösung auf die kühlere, CO<sub>2</sub>-reiche Lösung zu übertragen. Eine ähnliche Strategie wurde in der Laboranlage untersucht. Hier wurde ein beheizter Fließbettwärmetauscher verwendet, um CO<sub>2</sub>-reiches Adsorbens vor dem Eintritt in den Desorber vorzuwärmen, während in einem gekühlten Fließbettwärmetauscher die Rückgewinnung von sensibler Wärme simuliert wurde. In einem ersten Versuch mit diesen Wärmetauschern konnte der Wärmebedarf im Desorber erheblich reduziert werden.

# ACKNOWLEDGEMENTS

This thesis is the product of almost five years of research. On this journey, I have received much support, which I would like to acknowledge in the following.

I would like to thank my doctoral supervisor **Hermann Hofbauer** for giving me the opportunity to work in a research group dedicated to a subject that is now more relevant than ever: zero emissions technologies. I also very much appreciate the possibility to write this thesis and his input throughout the years.

Thank you **Gerhard Schöny** for the numerous motivational speeches and insightful discussions in the past years. The suggestions and the feedback you gave on this work were priceless, thank you.

I would also like to express a great thank you to **Johannes Fuchs**. Thank you for always sharing your technical expertise and thank you for the pleasant times at the workshop. I also thank you for contributing to this work by producing the technical drawings shown herein.

Special thanks to **Julius Pirklbauer**, **Elisabeth Zerobin** and **Egon Zehetner** who have contributed greatly in creating a pleasant working environment within our group. I would also like to thank you for your friendship and for all the inspiring discussions we had in the years.

I would also like to extend my gratitude towards the remaining members of the Zero Emissions Technology group, i.e. **Karl Mayer**, **Stefan Penthor**, **Michael Stollhof**, **Stephan Piesenberger** and **Robert Pachler** as well as towards my colleagues from BOKU i.e. **Florian Zerobin** and **Gerhard Hofer**. You have all contributed to this thesis either by sharing your perspectives and expertise in discussions and/or by helping out during the 120-hour tests. I also thank **Tobias Geißbüchler** for his hard work during the experiments dedicated to evaluating water transport.

Furthermore, I would like to express my deepest gratitude to **my family** Special thanks to my parents **Barbara** and **Johann** for their long lasting support and their encouragement throughout my studies. I also owe a debt in gratitude to **Heinz** for sparking my interest in industrial processes and engineering.

Finally, I would like to thank the person who is dearest to me and who knows me best, **Julia**. Imagining a life together with you and **Oskar** has always kept me going; you have been a source of endless inspiration and motivation, knowing that I can count on your support means everything to me.

# TABLE OF CONTENTS

ABSTRACT .....	I
KURZFASSUNG .....	III
ACKNOWLEDGEMENTS.....	V
TABLE OF CONTENTS .....	VI
<b>1. INTRODUCTION .....</b>	<b>1</b>
<b>1.1 ANTHROPOGENIC CO<sub>2</sub> EMISSIONS &amp; CLIMATE CHANGE .....</b>	<b>1</b>
<b>1.2 CARBON CAPTURE &amp; SEQUESTRATION .....</b>	<b>4</b>
<b>1.3 AQUEOUS AMINE SCRUBBING .....</b>	<b>6</b>
1.3.1 <i>General process description .....</i>	6
1.3.2 <i>Main cost drivers .....</i>	8
<b>1.4 PROBLEM DEFINITION .....</b>	<b>9</b>
<b>1.5 KEY OBJECTIVES .....</b>	<b>10</b>
<b>1.6 ORGANIZATION OF THIS WORK .....</b>	<b>11</b>
<b>2. LITERATURE REVIEW .....</b>	<b>12</b>
<b>2.1 FUNDAMENTALS OF ADSORPTION .....</b>	<b>12</b>
2.1.1 <i>Definition and history of adsorption.....</i>	12
2.1.2 <i>Adsorption of gases on solid surfaces .....</i>	14
2.1.3 <i>The Langmuir adsorption model .....</i>	16
2.1.4 <i>Process cycles for gas separation by adsorption .....</i>	17
<b>2.2 FUNDAMENTALS OF FLUIDIZED BED TECHNOLOGY.....</b>	<b>20</b>
2.2.1 <i>Definition and history of fluidization engineering.....</i>	20
2.2.2 <i>Particle characterization .....</i>	21
2.2.3 <i>General aspects of fluidization .....</i>	22
2.2.4 <i>Geldart classification .....</i>	24
2.2.5 <i>Fluidization regimes.....</i>	25
2.2.6 <i>Gas bubbles in fluidized beds.....</i>	26
2.2.7 <i>Particle entrainment and pneumatic transport.....</i>	28
2.2.8 <i>Bubbling fluidized bed-to-surface heat transfer.....</i>	30
<b>2.3 ENVIRONMENTAL EMISSIONS FROM THE MEA SCRUBBING PROCESS.....</b>	<b>34</b>
<b>2.4 POST-COMBUSTION CO<sub>2</sub> CAPTURE BY TEMPERATURE SWING ADSORPTION USING AMINE FUNCTIONALIZED SORBENTS .....</b>	<b>36</b>
2.4.1 <i>Amine functionalized sorbents .....</i>	36
2.4.2 <i>Requirements for efficient TSA and proposed process configurations.....</i>	43
<b>3. EXPERIMENTAL SETUP &amp; METHODS .....</b>	<b>48</b>
<b>3.1 BENCH SCALE UNIT.....</b>	<b>48</b>
3.1.1 <i>Downcomer design.....</i>	50
3.1.2 <i>Gas distribution .....</i>	51



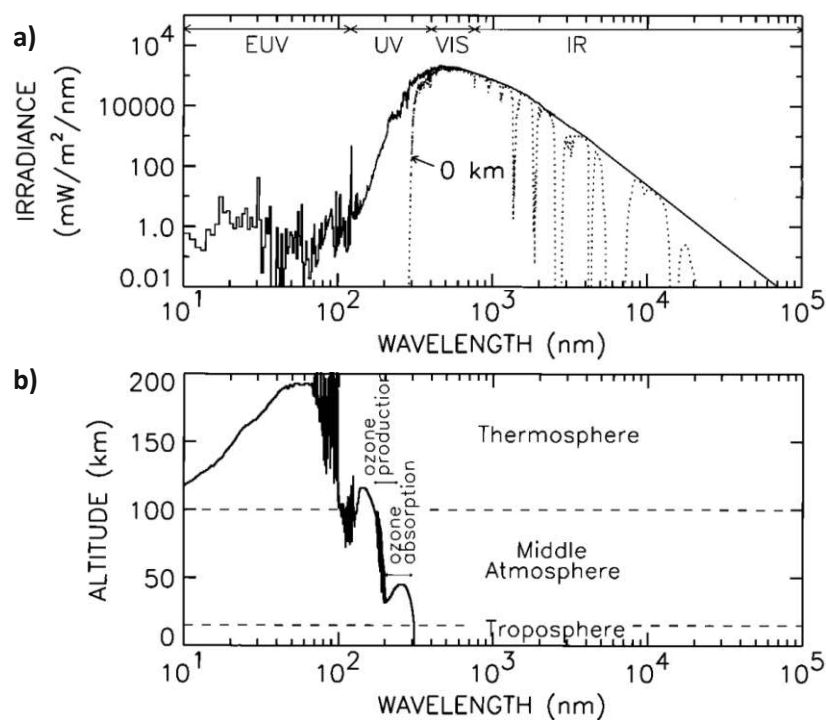
3.1.3	<i>Heat exchange</i> .....	51
3.1.4	<i>Freeboards</i> .....	53
3.1.5	<i>Solids transport section</i> .....	54
3.1.6	<i>Sampling</i> .....	55
<b>3.2</b>	<b>INSTRUMENTATION</b> .....	<b>56</b>
3.2.1	<i>Pressure measurement</i> .....	56
3.2.2	<i>Temperature measurement of fluidized beds</i> .....	58
3.2.3	<i>Gas analysis</i> .....	58
3.2.4	<i>Flow rate measurements of gases</i> .....	58
3.2.5	<i>Instrumentation of the cooling and heating system</i> .....	60
<b>3.3</b>	<b>METHODS</b> .....	<b>61</b>
3.3.1	<i>Startup</i> .....	61
3.3.2	<i>Control and determination of the solids circulation rate</i> .....	61
3.3.3	<i>Shutdown</i> .....	62
3.3.4	<i>Key process performance parameters</i> .....	63
<b>3.4</b>	<b>UTILIZED SORBENT MATERIAL</b> .....	<b>65</b>
3.4.1	<i>Sorbent A</i> .....	65
3.4.2	<i>Sorbent B</i> .....	65
<b>4.</b>	<b>EXPERIMENTAL</b> .....	<b>67</b>
<b>4.1</b>	<b>ADSORBER FEED GAS VELOCITY VARIATIONS</b> .....	<b>67</b>
4.1.1	<i>Operating conditions</i> .....	67
4.1.2	<i>Results &amp; Discussion</i> .....	68
4.1.3	<i>Conclusion</i> .....	71
<b>4.2</b>	<b>VARIATION OF ADSORBER TEMPERATURE AND FLUE GAS CO<sub>2</sub> CONCENTRATION</b> .....	<b>72</b>
4.2.1	<i>Operating conditions</i> .....	72
4.2.2	<i>Results &amp; Discussion</i> .....	73
4.2.3	<i>Conclusion</i> .....	76
<b>4.3</b>	<b>DEGRADATION IN PRESENCE OF NO<sub>x</sub> &amp; SO<sub>2</sub></b> .....	<b>78</b>
4.3.1	<i>Experimental setup</i> .....	78
4.3.2	<i>Operating conditions</i> .....	81
4.3.3	<i>Results &amp; Discussion</i> .....	82
4.3.4	<i>Conclusion</i> .....	84
<b>4.4</b>	<b>EMISSIONS FROM AMINE FUNCTIONALIZED SOLID SORBENT</b> .....	<b>86</b>
4.4.1	<i>Experimental Setup</i> .....	86
4.4.2	<i>Analytical methods</i> .....	88
4.4.3	<i>Operating conditions</i> .....	89
4.4.4	<i>Results &amp; Discussion</i> .....	91
4.4.5	<i>Comparison with emissions from the MEA scrubbing process</i> .....	98
4.4.6	<i>Conclusion</i> .....	99
<b>4.5</b>	<b>WATER TRANSPORT</b> .....	<b>100</b>
4.5.1	<i>Experimental setup</i> .....	100
4.5.2	<i>Methods</i> .....	101

4.5.3	<i>Operating conditions</i> .....	104
4.5.4	<i>Results &amp; Discussion</i> .....	105
4.5.5	<i>Conclusion</i> .....	109
<b>4.6</b>	<b>LEAN/RICH HEAT EXCHANGE</b> .....	<b>111</b>
4.6.1	<i>Experimental setup</i> .....	111
4.6.2	<i>Data analysis</i> .....	115
4.6.3	<i>Operating Conditions</i> .....	116
4.6.4	<i>Results &amp; Discussion</i> .....	117
4.6.5	<i>Conclusion</i> .....	122
<b>5.</b>	<b>CONCLUSIONS AND RECOMMENDATIONS FOR NEXT SCALE</b> .....	<b>124</b>
<b>6.</b>	<b>OUTLOOK AND PROPOSALS FOR FUTURE RESEARCH</b> .....	<b>128</b>
<b>7.</b>	<b>NOTATION</b> .....	<b>130</b>
	<b>REFERENCES</b> .....	<b>134</b>
<b>8.</b>	<b>APPENDIX</b> .....	<b>143</b>
<b>8.1</b>	<b>GAS DISTRIBUTOR PRESSURE DROP AS A FUNCTION OF THE SUPERFICIAL GAS VELOCITY IN THE COLUMNS</b> <b>143</b>	
<b>8.2</b>	<b>CALCULATION OF THE MEASURING ERROR OF RTDs ACCORDING TO DIN EN 60751</b> .....	<b>144</b>
<b>8.3</b>	<b>CALCULATION OF THE MEASURING ERROR OF VARIABLE AREA FLOW METERS ACCORDING TO VDI/VDE</b> <b>351</b>	<b>144</b>
<b>8.4</b>	<b>LEGEND OF SYMBOLS USED IN P&amp;IDS</b> .....	<b>144</b>
<b>8.5</b>	<b>DESORBER HEAT LOSS AS A FUNCTION OF THE FORWARD FLOW TEMPERATURE OF THERMAL OIL</b> .....	<b>145</b>
<b>8.6</b>	<b>PERFORMANCE INDICATORS IN THE COURSE OF 24-HOUR DEGRADATION TESTS</b> .....	<b>145</b>
<b>8.7</b>	<b>SUPPLEMENTARY INFORMATION TO 120-HOUR EXPERIMENTS</b> .....	<b>146</b>
<b>8.8</b>	<b>MOVING-BED HEAT EXCHANGER DESIGN</b> .....	<b>148</b>
<b>8.9</b>	<b>HEAT TRANSFER COEFFICIENT BETWEEN A MOVING BED OF SOLIDS AND A FINNED TUBE</b> .....	<b>150</b>

# 1. INTRODUCTION

## 1.1 ANTHROPOGENIC CO<sub>2</sub> EMISSIONS & CLIMATE CHANGE

The global climate is fundamentally driven by solar radiation hitting the Earth. Therefore, changes in the Earth's climate are a result of changes in the radiative energy budget of the Earth, which in turn is influenced by a large number of factors. Notwithstanding effects such as changes in solar irradiance hitting the Earth or shifts in the Earth's orbit, the Earth's atmosphere as well as its surface play a central role in the balance of the Earth's radiation budget. As seen in Figure 1, the majority of incident radiation at wavelengths below 300 nm is absorbed above the troposphere by atmospheric gases such as ozone, whereas bulk radiation between 400 nm and 800 nm (i.e. visible light) reaches the Earth's surface [1]. Within the infrared spectrum (i.e. between 700 nm and 10<sup>6</sup> nm), it can be seen that radiation in several distinct bands do not reach the surface as they are already absorbed by gaseous species in the atmosphere e.g. water vapor or carbon dioxide [2]. The portion of the spectrum that reaches the Earth's surface is subsequently absorbed by the surface or reflected by albedo.



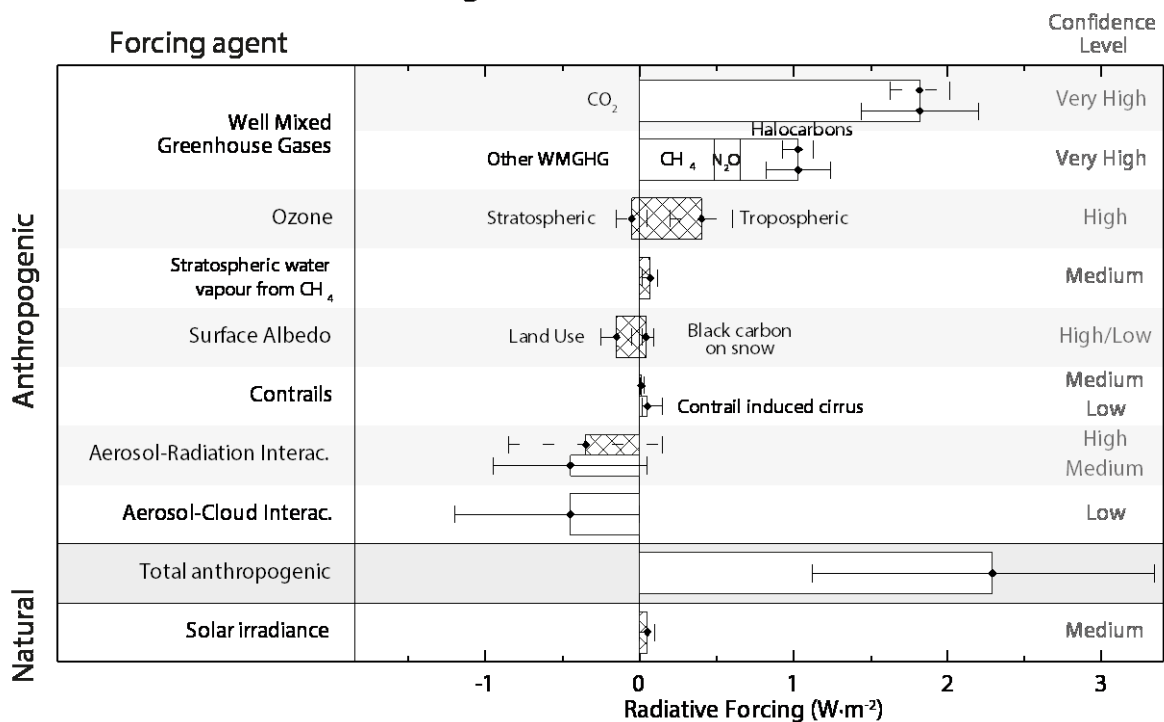
**Figure 1: a) The Sun's radiation incident at the top of the Earth's atmosphere (solid line) and at the Earth's surface (0 km, dotted line), b) Deposition of the Sun's radiative energy in the Earth's atmosphere as a function of altitude [1].**

The absorbed incident radiation results in a mean global surface air temperature of approximately 14°C [3]. According to Wien's law, this temperature will result in the emission of thermal radiation in the infrared spectrum with a peak at a wavelength of 10<sup>4</sup> nm. To contribute as a sink in the global radiative budget, this thermal radiation must be emitted back into space. As shown in Figure 1 a), the

atmosphere contains constituents that absorb radiation in the infrared band. Therefore, a portion of this outbound radiation is absorbed by the atmosphere and subsequently emitted in all directions as thermal radiation. This effect is known as the greenhouse effect, whereas atmospheric gases that contribute to this effect by absorbing infrared radiation are known as greenhouse gases (GHGs). The change in the radiative flux (downward flux minus upward flux, given in  $\text{W}\cdot\text{m}^{-2}$ ) due to an imposed change is known as radiative forcing (RF) [4]. An increase of RF can therefore lead to an increase of the global temperature whereas a decrease can entail global cooling. Radiative forcing agents include GHGs in the Earth's atmosphere, solar activity or the Earth's surface albedo [5].

As seen in Figure 2, climate model results published by the Intergovernmental Panel on Climate Change (IPCC) [4] show that since the industrial era, so-called long-lived GHGs or well-mixed GHG (WMGHG) have contributed most to an increase in RF between 1750 and 2011. It must be noted that differently to RF, effective radiative forcing (ERF) (as shown in Figure 2) takes into account the effect of the forcing agent as well as rapid adjustment, i.e. short-term responses brought about by the forcing agent (e.g. a temperature change).

### Radiative forcing of climate between 1750 and 2011

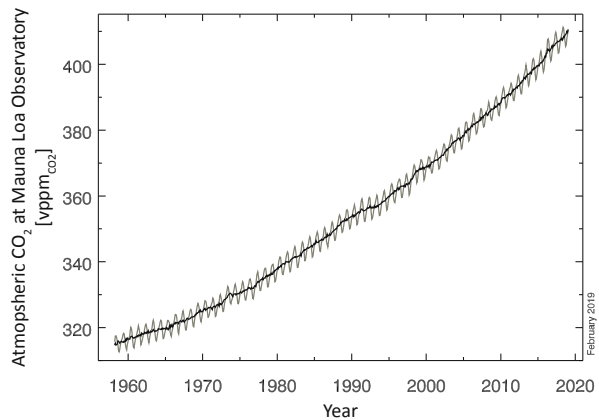


**Figure 2: Bar chart showing radiative forcing (hatched) and effective radiative forcing (solid) for the period 1750-2011. Uncertainties (90% confidence range) are given for RF (dotted lines) and ERF (solid lines) (adapted from Stocker et al. [4])**

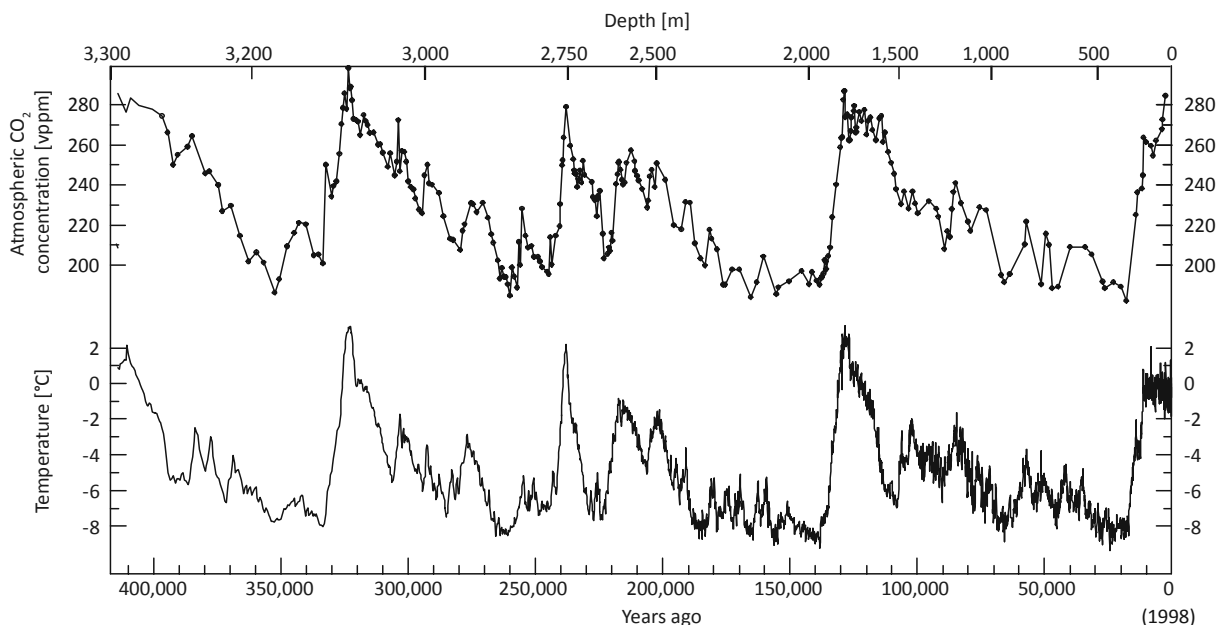
In 2011 the most important anthropogenic WMGHGs were carbon dioxide (CO<sub>2</sub>) followed by methane (CH<sub>4</sub>), nitrous oxide (N<sub>2</sub>O) and dichlorodifluoromethane (CFC-12) [4]. Despite the fact that water vapor is the single most important GHG, tropospheric water vapor is not listed in Figure 2. This is because the emission of water vapor by human activity (i.e. through power plant cooling, fossil fuel combustion, land-use etc.) has a negligible impact on the overall water content of the troposphere compared to "natural" evaporation, which is controlled by temperature. Therefore, the concentration of

tropospheric water vapor is typically considered as positive feedback in climate models, rather than a forcing in itself [4].

CO<sub>2</sub> is the single greatest contributor to radiative forcing and its concentration in the atmosphere has risen drastically since the industrial era. In 1750, the estimated atmospheric CO<sub>2</sub> concentration was between 276 vppmCO<sub>2</sub> and 280 vppmCO<sub>2</sub>, whereas at present this value has reached approx. 410 vppmCO<sub>2</sub> [6] (as seen in Figure 3). Although the global temperature and atmospheric CO<sub>2</sub> concentration have been subject to constant change in the past 420,000 years (see Figure 4), a CO<sub>2</sub> concentration of 300 vppmCO<sub>2</sub> has never been exceeded in last 800,000 years [7].



**Figure 3: Atmospheric CO<sub>2</sub> concentration measured at Mauna Loa Observatory, Hawaii from 1958-2019 (adapted from Earth System Research Laboratory: Global Monitoring Division [6])**



**Figure 4: Temperature and CO<sub>2</sub> profile over the past 420,000 years, gained from the Vostok ice core (adapted from Petit et al. [8])**

This drastic change in the composition of the Earth's atmosphere is caused by human activity and has led to an increase of the global mean surface temperature of 0.86 °C in the observation period of 1850-1900 to 2006-2015 [9]. 20 %-40 % of the population has experienced significantly higher warmings, in the order of 1.5 °C in the course of at least one season [10]. Notwithstanding the numerous negative impacts of global warming on human and natural systems, strategies have been developed by which global warming can be limited to 1.5 °C compared to pre-industrial levels. According to the IPCC [11], there is a two-out-of-three chance that global warming can be limited to 1.5 °C (without overshoot) if CO<sub>2</sub> emissions from 2018 onwards do not exceed 420 Gt<sub>CO2</sub>. Furthermore, a fifty-fifty chance has been predicted for meeting the 1.5 °C goal if cumulated CO<sub>2</sub> emissions from 2018 onward do not exceed 580 Gt<sub>CO2</sub>. For the more lenient of the two scenarios, a drastic cut in CO<sub>2</sub>

emissions must occur in the coming decades (i.e. a reduction of 45 % compared to 2010 levels by 2030) and a reduction to net zero CO<sub>2</sub> emissions needs to take place by 2050 [12]. For reference, in 2017 alone, CO<sub>2</sub> emissions were estimated to 41.4 ± 4.4 Gt<sub>CO2</sub>, whereas 36.3 ± 1.8 Gt<sub>CO2</sub> was attributed to fossil fuel use and industry [13]. This underlines the urgency to implement extensive measures that significantly reduce CO<sub>2</sub> emissions from fossil sources.

## 1.2 CARBON CAPTURE & SEQUESTRATION

As can be seen in Figure 5, the power generation sector and the industrial sector are the most CO<sub>2</sub>-intensive energy-related sectors and together made up approx. 45 % of CO<sub>2</sub> emissions in 2017 [13,14].

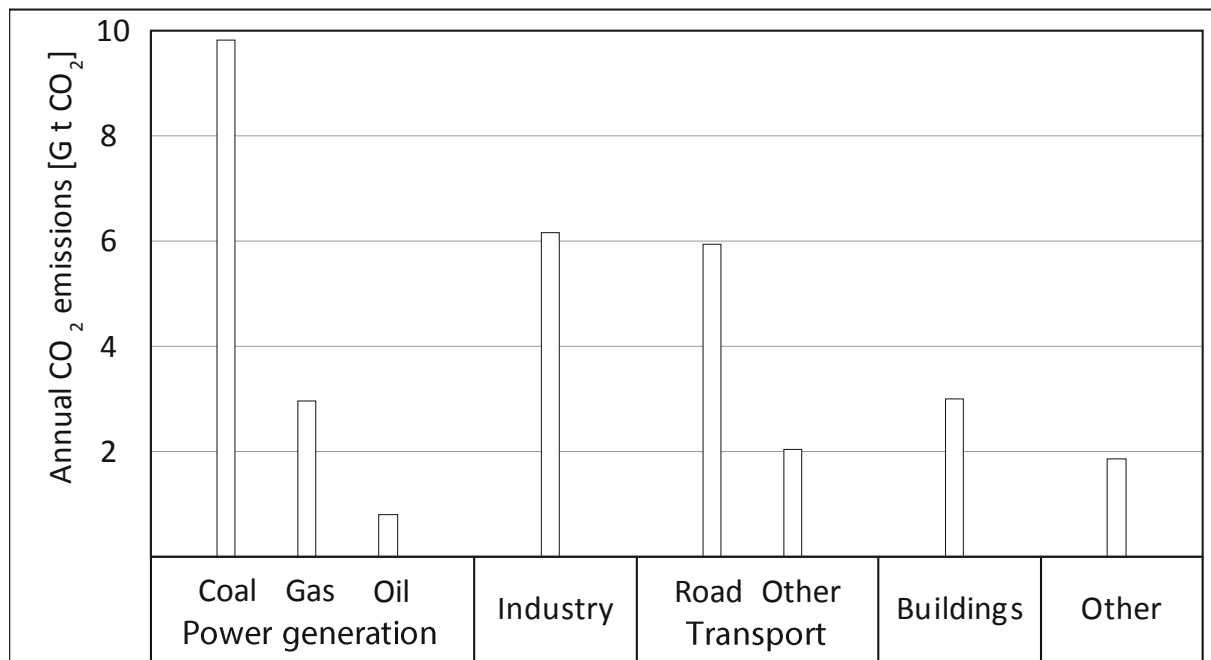
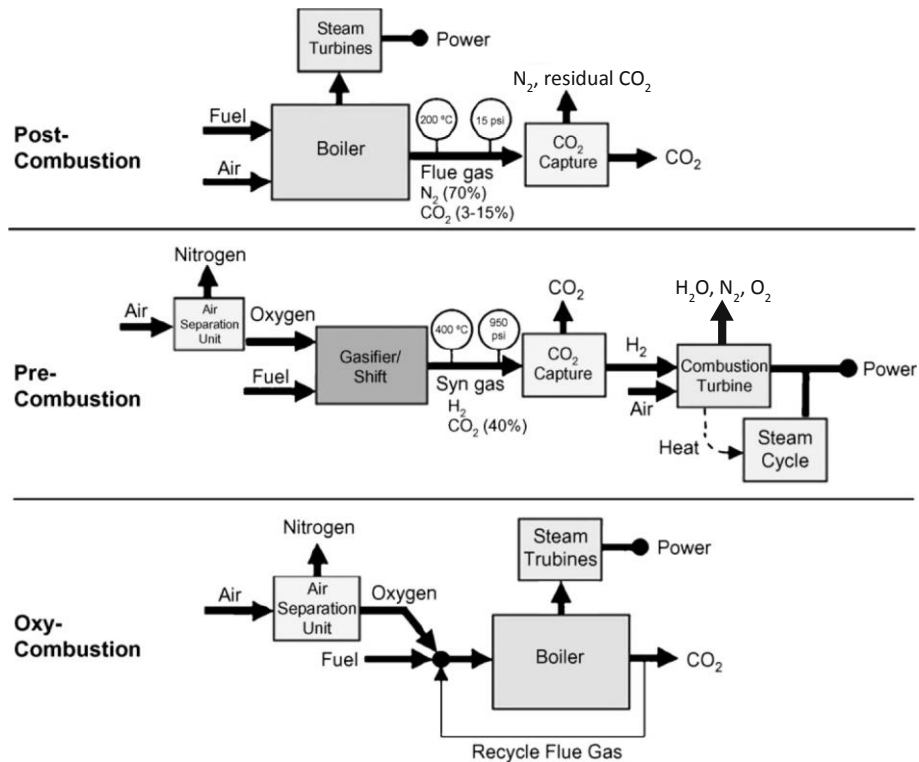


Figure 5: Energy-related CO<sub>2</sub> emissions by sector in 2017 (adapted from IEA [14])

A number of scenarios have been developed by the IPCC and the IEA that limit global warming to 1.5 °C and 2 °C respectively. Both organizations have concluded that Carbon Capture and Sequestration (CCS) will play an important role in mitigating CO<sub>2</sub> emissions in the developed scenarios. CCS is generally aimed at capturing CO<sub>2</sub> from large point sources and sequestration of the captured CO<sub>2</sub> so that it cannot be an active GHG in the Earth's atmosphere. In the first step, a method is applied by which CO<sub>2</sub> is extracted from the CO<sub>2</sub>-emitting process. Subsequently the captured CO<sub>2</sub> is transported to a suitable storage site where it is stored for an indefinite period. To make transport and storage efficient CO<sub>2</sub> is compressed. Thus CCS has the potential to reduce CO<sub>2</sub> emission from various carbon intensive processes and act as a carbon sink when paired with fuel production and power generation from renewable sources i.e. biomass [12,15]. The necessity of CCS is further emphasized by an increase of the modelled CO<sub>2</sub> emission mitigation cost if removed from the portfolio of technologies required to limit global warming [16]. In the 1.5 °C-scenarios described by the IPCC [17], a maximum of 300 Gt<sub>CO2</sub> will be captured by 2050. To counter-balance a potential overshoot in CO<sub>2</sub> emissions in these scenarios

up to 140 Gt<sub>CO<sub>2</sub></sub> must be captured and stored from biomass-based sources [17]. If the global temperature is allowed to rise by 2 °C, as described in an IEA scenario, up to 142 Gt<sub>CO<sub>2</sub></sub> must be capture and stored by 2060, whereas 37 Gt<sub>CO<sub>2</sub></sub> must be capture and stored from bio-energy sources [15].

As can be seen in Figure 6, three CO<sub>2</sub> capture methods can be applied in the energy sector. These methods can be divided into post-combustion CO<sub>2</sub> capture, pre-combustion CO<sub>2</sub> capture and oxy-combustion (also known as oxyfuel combustion).



**Figure 6: Block-diagrams illustrating implemented CCS systems in the power sector (adapted from Figueroa et al. [18])**

As implied by the naming, post-combustion CO<sub>2</sub> capture (PCCC) is applied after a combustion process. Since most flue gases contain CO<sub>2</sub> in a diluted form (i.e. 3 vol%CO<sub>2</sub>- 15 vol%CO<sub>2</sub> [19]), the development of a suitable and cost-effective CO<sub>2</sub> capture process presents a technical challenge [18,20]. At present, the most mature PCCC technology is the amine-scrubbing process. Here an aqueous amine solution is used to separate CO<sub>2</sub> from a flue gas in the absorber. The CO<sub>2</sub> loaded amine solution is subsequently pumped to a second vessel where it is regenerated and a highly pure CO<sub>2</sub> product is obtained [21].

A typical process that employs pre-combustion CO<sub>2</sub> capture is the integrated gasification combined cycle (IGCC). In a gasifier a fuel, such as coal or biomass, is treated with a gasification agent (e.g. steam or oxygen) to yield a gas mixture rich in hydrogen and carbon monoxide, the so-called “synthesis gas” [19]. In a shift reactor, located downstream of the gasifier, a catalytic reaction between the synthesis gas and steam takes place, which converts carbon monoxide and steam into additional hydrogen and CO<sub>2</sub>. The CO<sub>2</sub> content of the resulting gas can lie between 15 vol%CO<sub>2</sub> and 60 vol%CO<sub>2</sub>. In pre-combustion CO<sub>2</sub> capture, CO<sub>2</sub> is removed from the H<sub>2</sub>-rich product gas before H<sub>2</sub> is combusted in a turbine.

The third common CCS technology is oxy-fuel combustion. Here the combustion of a fuel takes place in the absence of atmospheric nitrogen. However, for the production of oxygen, a rather costly cryogenic air separation process must be applied [20]. The resulting flue gas is ideally only composed of CO<sub>2</sub> and water vapor. A similar approach is taken in chemical looping combustion. Here, a metal/metal-oxide is circulated between an air reactor and a fuel reactor. In the air reactor, the metal is oxidized to a metal oxide. Subsequently, the metal-oxide is transported to the fuel reactor and reduced by a fuel. In this way, oxygen is selectively transported from the air reactor to the fuel reactor and used to combust fuels in the absence of atmospheric N<sub>2</sub> [22].

In the 1.5 °C and 2 °C scenarios, CCS must not only play a significant role in the energy sector but also contribute in decarbonizing the industrial sector [12,15]. Some processes in industry inherently produce highly pure CO<sub>2</sub> streams (e.g. hydrogen production or methanol production). Since the CO<sub>2</sub> capture and compression steps are considered the costliest part of the CCS-chain [15,19,23], storing CO<sub>2</sub> from these sources may not pose a particular economic challenge. However, in industries such as the cement, steel and iron industry, where process emissions are high and CO<sub>2</sub> is not emitted at high purity, CO<sub>2</sub> capture plants may be implemented as a retrofit to preserve the value of existing assets. However, scenarios developed by the IEA show that retrofitting of existing CO<sub>2</sub> emitters with CCS technology will not only have to play a role in the industrial sector but will occur in the energy sector as well. In the 2 °C scenario, over 200 GW of installed coal- and gas-fired capacity will be retrofitted with CCS by 2060, whilst approx. 1500 GW will be retired. [15]

Since PCCC technologies are generally implemented as an end-of-pipe technology, they can be used to retrofit any CO<sub>2</sub> emitting process in both the energy and industrial sector. However, the current state-of-the-art technology in the field of PCCC i.e. aqueous amine scrubbing, suffers from a high CO<sub>2</sub> capture cost, which is a result of deficiencies that are intrinsic to the process. To understand the intrinsic shortcomings of the aqueous amine scrubbing process, fundamentals on the process as well as the main cost drivers will be detailed in the following.

## 1.3 AQUEOUS AMINE SCRUBBING

### 1.3.1 General process description

Since its patenting in 1930 by Bottoms [24], scrubbing using aqueous amine solution has been a popular process for bulk acid gas removal, i.e. the removal of H<sub>2</sub>S and CO<sub>2</sub> from various gas streams. The widespread implementation and the associated maturity of the amine scrubbing technology made the process a suitable candidate for application in post-combustion CO<sub>2</sub> capture (PCCC). The success of amine scrubbing systems in this field is marked with the construction and operation of large scale CCS projects such as Boundary Dam and Petra Nova, which have a CO<sub>2</sub> capture capacity of 1 Mt<sub>CO<sub>2</sub></sub>·year<sup>-1</sup> [25] and 1.6 Mt<sub>CO<sub>2</sub></sub>·year<sup>-1</sup> [26] respectively. Therefore, amine scrubbing can be considered the state-of-the-art PCCC technology.

The principle of amine scrubbing for CO<sub>2</sub> capture is the selective separation of CO<sub>2</sub> by dissolution in an aqueous amine solution (henceforth called solvent) and subsequent chemical reaction with the amine present in the solvent. Contacting of the CO<sub>2</sub> containing gas and the solvent takes place in a vessel called the absorber. Here, the CO<sub>2</sub>-lean solvent is introduced at the top, and subsequently flows from top to bottom by gravity. The CO<sub>2</sub> containing gas is introduced at the bottom, thereby realizing counter-current contact of the gas and liquid. To increase the gas-liquid contacting area, the absorber



is typically filled with a packing, e.g. stainless steel rings of a few centimeters [21], on which the solvent forms a thin film. On its journey through the absorber, the solvent is increasingly loaded with CO<sub>2</sub>. After exiting the absorber, the CO<sub>2</sub> loaded (or rich) solvent is pumped through a heat exchanger where it is preheated by indirect contact with the hot CO<sub>2</sub>-lean solvent exiting the stripper (as seen in Figure 7). The rich solvent enters the stripper in which the regeneration step takes place at an elevated temperature. The so-called “reboiler” is located at the base of the stripper. This device heats the solvent to form steam, which then flows upward through the stripper and provides heat to the downward flowing solvent by condensation. The introduction of heat together with the dilution of the gas phase by steam, both contribute to the reversal of the CO<sub>2</sub> absorption step and thus to a reduction of the CO<sub>2</sub> loading of the solvent. It should be noted that the stripper is also filled with a packing so that an increased gas-liquid contacting surface can be provided. The gas mixture exiting the stripper consists primarily of CO<sub>2</sub> and steam. In order to yield a pure CO<sub>2</sub> product, a condenser and a gas-liquid separator are typically installed downstream of the stripper. The lean solvent is subsequently pumped from the stripper to the absorber, via the lean/rich heat exchanger and a lean solvent cooler, where the solvent temperature is gradually reduced to the absorber operating temperature. The solvent is introduced at the top section of the absorber, below the water wash section. Typical amine scrubbing units feature a so-called water wash section at the top of the absorber in which the CO<sub>2</sub> depleted flue-gas is scrubbed with water before it is vented to ambient. By continuously scrubbing the gas with recycled water, at 5-10 °C below the gas temperature, volatile species are condensed and/or absorbed thus reducing the concentration of vapor-based emissions. [21,27]

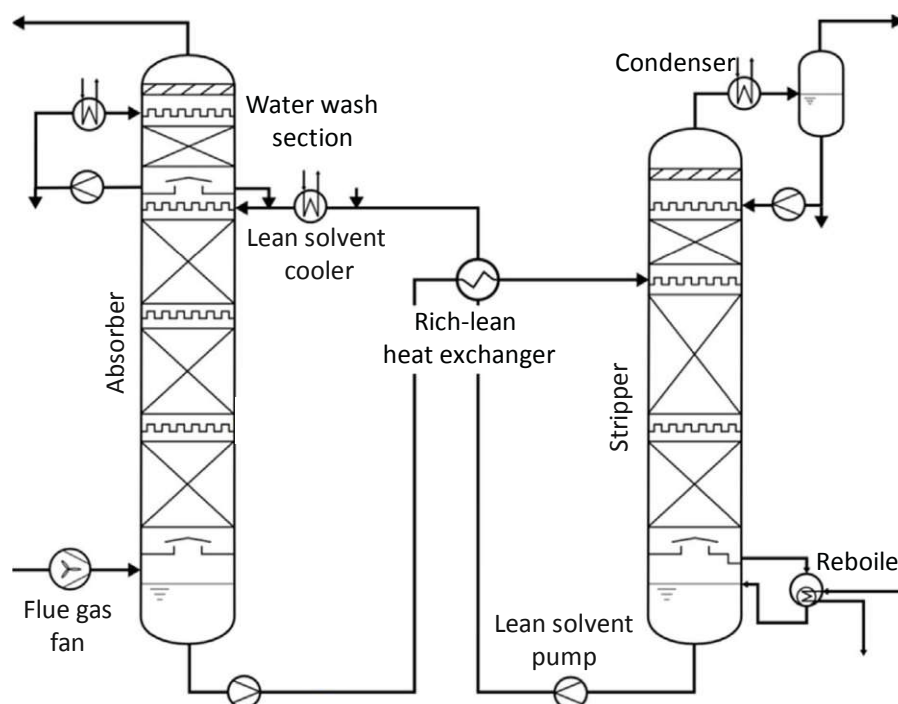


Figure 7: Illustration showing typical setups of amine scrubbing units (adapted from Le Moulec and Neveux [28])

### 1.3.2 Main cost drivers

A vast number of aqueous solvents containing either pure amines or blends of amines have been proposed as working media for the amine scrubbing process. However, the utilized amine has substantial implications on the design and operation of an amine-scrubbing system (e.g. dimensions, operating temperature). For this reason, PCCC technologies are commonly compared to amine scrubbing processes that utilize an aqueous solution containing 30 wt% monoethanolamine (MEA). This benchmark solvent features a high CO<sub>2</sub> absorption capacity, fast reaction kinetics, a high water solubility and a low price. Because processes that use aqueous MEA-solvents have constituted the state-of-the-art in PCCC for decades [29], they are well studied and will therefore also be used as a benchmark in this work.

Construction cost estimations for MEA-based scrubbing units show that there is consensus concerning the main cost driver [30–33]. When regarding only the CO<sub>2</sub> capture process i.e. without CO<sub>2</sub> compression, the costliest equipment is the absorber (i.e. up to 42.6 % of the construction cost [32], see Table 1). In part, this significant contribution to the total capital cost is a result of the required size of the absorber as well as the packing that must be implemented.

Equipment type	Contribution of equipment types to purchase equipment cost	
Absorber	42.6	[%]
Heat exchangers	32.7	[%]
Compressors	14.0	[%]
Pumps	8.6	[%]
Stripper	1.8	[%]
Static vessels	0.3	[%]

**Table 1: Contribution of equipment types to the bare erected cost of aqueous MEA scrubbing unit designed for treating flue gas from a natural gas combine cycle (adapted from Abu-Zahra et al. [32])**

Mass transfer in the absorber is a crucial part of the absorption step. The transport of CO<sub>2</sub> to the amine occurs through diffusion from the bulk gas phase to the gas-liquid interface and subsequent dissolution of CO<sub>2</sub> into the liquid phase [34]. In the absorber, slow diffusional transport governs the mass transfer rate, especially in the bottom section [28,34]. Packings are therefore required so that a large mass transfer area, i.e. a large gas-liquid contacting area, can be provided in a low volume. Furthermore, packings contribute to the intensification of mass transfer by facilitating fast convective mass transfer by randomly directed gas through the interstitial volume of the packing [28]. By implementing packings, the height of the absorber can be decreased, whereas the column footprint can be decreased by increasing the superficial gas velocity. However, to allow sufficient gas/liquid contact time, a trade-off must be made between the column footprint and the column height. Nevertheless, due to the high volumetric flows of flue gas that must be treated in PCCC, high superficial gas velocities in the range of 1-3 m·s<sup>-1</sup> are typically applied in the absorber [31,35].

The second greatest contributor to capital cost is associated with heat integration within the amine scrubbing process. Aqueous solvents consist mostly of water, thus their high heat capacity has a notable impact on the process heat demand. The reboiler, which is the primary heat source for the amine scrubbing process, is typically heated by low-pressure steam extracted from the CO<sub>2</sub> emitting

process. Thus, the heat demand of the amine scrubbing process results in a parasitic load on the CO<sub>2</sub> emitting process. However lean/rich heat exchange allows for reducing the reboiler duty by 30-40 % [36] (see Table 1). In the lean/rich heat exchanger, heat is transferred from the hot lean solvent exiting the stripper to the colder rich solvent. The importance of this equipment is emphasized by the fact that it was part of the original amine scrubber design depicted in the patent of 1930 [24]. The rather high overall heat transfer coefficients that can be achieved in liquid-liquid heat exchangers (e.g. 425-625 W·m<sup>-2</sup>·K<sup>-1</sup> for shell-and-tube using 30 wt% MEA [31]) make high heat recovery rates economically feasible. Typically, a rather low approach of 10 K on the hot side of the heat exchanger is targeted [31,37]. In a MEA scrubbing process with operating temperatures of the absorber and the stripper of 40 °C and 120°C respectively, this approach translates into a heat recovery of 87.5 %. Nonetheless, the high amounts of heat that must be transferred require heat exchangers with a correspondingly large heat transfer surface area, therefore the lean/rich heat exchanger installed in MEA scrubbing units can account for up to 32.7 % of total construction costs [32].

Additionally to the abovementioned cost-drivers, the following factors contribute to the overall cost of amine scrubbing systems. The cost for solvent make-up is one of the greatest contributors to the operational and maintenance cost of MEA scrubbing systems [31,33]. Active amine in the solvent is not only lost through thermal and oxidative degradation, but MEA can be degraded by gas constituents present in the flue gas such as SO<sub>x</sub> and NO<sub>x</sub> [38]. Furthermore, due to the aqueous nature of the solvents, corrosion is an issue in amine scrubbing units. Therefore, corrosion inhibitors are typically added to the solvent to enable the use of carbon steel as a vessel material [39].

## 1.4 PROBLEM DEFINITION

Due to the abovementioned shortcomings of the state-of-the-art post-combustion CO<sub>2</sub> capture technology and the urgency of widespread implementation of CCS, a worldwide effort is made in developing cost effective and energy efficient alternatives to the aqueous amine scrubbing process. In the past decade, temperature swing adsorption (TSA) using amine-functionalized solid sorbent has gained much attention in the field of post-combustion CO<sub>2</sub> capture. Amine-functionalized solid sorbents feature a high selectivity towards CO<sub>2</sub> [40] as well as high adsorption capacities even at low CO<sub>2</sub> partial pressures [41] and are expected to have higher cyclic CO<sub>2</sub> capacities and cause less corrosion in contacting vessels compared to typical solvents used in aqueous amine scrubbing [42–44]. Furthermore, due to the lower heat capacity of solid sorbents compared to aqueous solvents, the regeneration heat demand of TSA processes is expected to be significantly lower [45]. Consequently, TSA has the potential of reducing the cost of CO<sub>2</sub> capture compared to the current state-of-the-art. Intense research in the field of solid CO<sub>2</sub> sorbents has led to the development of a wide range of amine-functionalized sorbents, some of which are commercially available. However, development of a suitable reactor system that utilizes these sorbents lags behind.

In recent years, a small number of research groups has developed TSA reactor systems suitable for CO<sub>2</sub> capture. However, up to the present the focus of experimental investigations was laid on the proof of concept rather than on subject matters with high practical relevance. For further upscaling of TSA reactor systems, it must be ensured that CO<sub>2</sub> capture by means of TSA can be efficient and cost-effective, especially in comparison to the aqueous MEA scrubbing process. Therefore, the following subject matters need to be investigated:

- **Unit design:** A major cost driver of amine scrubbing units is the large size of the absorption column. For TSA a compact and simple unit design should be targeted to reduce construction cost.
- **Operating window:** The flexibility of TSA systems must be demonstrated. It must be shown that efficient CO<sub>2</sub> capture can be realized from a wide variety of different flue gases using TSA.
- **Durability of the utilized sorbent material:** The influence of sorbent degradation caused by trace components found in many flue gases, such as SO<sub>2</sub> and NO<sub>x</sub>, as well as the influence of thermal, oxidative and mechanical degradation must be investigated under realistic conditions.
- **Potential to reduce process emissions:** Implementation of emission reduction measures adds to the cost of CO<sub>2</sub> capture. Therefore, emissions from TSA units that use amine-functionalized sorbents need to be identified and quantified to establish whether emission reduction measures will be necessary.
- **Impact of water on process operation:** It has been established that many amine-functionalized sorbents have a high capacity for water. Since water is a major constituent of typical flue gases, the adsorption of water alongside CO<sub>2</sub> in the adsorber of a TSA unit is a likely scenario. However, experimental investigations that show the effect of water co-adsorption on the operating conditions of functioning TSA units have not yet been carried out.
- **Heat recovery from lean sorbent:** To minimize the process heat demand in TSA systems, heat recovery measures must be explored.

## 1.5 KEY OBJECTIVES

Based on the above-mentioned problem definition, the key objectives of this work can be formulated as follows:

- Investigate the impact of decreasing adsorber footprints in the existing TSA bench scale unit by maximizing the flue gas velocity in the adsorber column and identify potential limitations.
- Investigate the flexibility of the existing TSA bench scale unit regarding the CO<sub>2</sub> capture performance at varying adsorber operating temperatures and flue gas CO<sub>2</sub> concentrations.
- Conduct an experiment in which flue gas from a combustion process is treated. Investigate the influence of trace-gases typical for combustion processes, i.e. SO<sub>2</sub> and NO<sub>x</sub>, on the CO<sub>2</sub> capture performance of the TSA bench scale unit.
- Evaluate the degradation rate of amine-functionalized sorbents in the course of prolonged CO<sub>2</sub> capture operation in the TSA bench scale unit.
- Quantify process emissions resulting from the use of amine-functionalized solid sorbents in the TSA bench scale unit and compare the results to environmental emissions from an aqueous monoethanolamine (MEA) scrubbing process.
- Assess the effect of water co-adsorption on the TSA bench scale unit and investigate if and how water co-adsorption can be influenced by changes in the operating conditions of the TSA process.
- Integrate a setup in the TSA bench scale unit that can be used for heat recovery and investigate the performance of this subsystem.
- Make recommendations on general process design and further up-scaling of the TSA process for CO<sub>2</sub> capture using amine-functionalized solid sorbents.

## 1.6 ORGANIZATION OF THIS WORK

Section 2 is the theoretical backbone of this thesis. Here, fundamentals of adsorption technology will be treated as well as an introduction into amine-functionalized sorbents and fluidized bed technology will be given.

The conducted experimental investigations were carried out in a bench scale unit for temperature swing adsorption, which implements a multi-stage fluidized bed design. A detailed description of the general experimental setup including details concerning the utilized instrumentation as well as information on the applied methods and the utilized sorbent materials can be found in Section 3.

Section 4 is divided into subsections, each will treat an experimental campaign in the TSA bench scale unit, which was carried out to address the key objectives given in Section 1.5. The general approach for the experimental campaign will be described in a preface, which will also detail any deviations to the experimental setup or instrumentation given in Section 3. Furthermore, any additional analytical methods or calculated values that are particular to the experimental campaign will also be described. Subsequently, the gained results will be presented and discussed, whereas each subsection will feature conclusion that can be drawn from the respective experimental campaign.

This thesis will be concluded by Section **Fehler! Verweisquelle konnte nicht gefunden werden.** and 6, in which recommendations for further up-scaling of the TSA process and suggestions for future research will be given respectively.

## 2. LITERATURE REVIEW

### 2.1 FUNDAMENTALS OF ADSORPTION

#### 2.1.1 Definition and history of adsorption

According to the IUPAC Compendium of Chemical Terminology, adsorption is defined as “an increase in the concentration of a dissolved substance at the interface of a condensed and a liquid phase due to the operation of surface forces. Adsorption can also occur at the interface of a condensed and a gaseous phase” [46]. Due to the broad definition of the term, it is unsurprising that adsorption is widespread in nature and that humans have applied the principle of adsorption for thousands of years in separation processes. In ancient Egypt, for example, “healing powder and Earths” were used to treat wounds and Phoenicians had documented the use of “sand and coal” for water purification purposes [47,48]. Despite the fact that adsorption had been put to practical use in various applications, it was in the late 18<sup>th</sup> century that adsorption of gas on a solid surface was first documented in the course of scientific investigations. In 1773, Carl Wilhelm Scheele, a Swedish pharmaceutical chemist, conducted numerous experiments with the aim of investigating fire and its interaction with air. During these experiments, Scheele observed that “air” could be adsorbed and desorbed from “coal” by extracting and introducing heat [49]. In the years that followed, Priestley (1775) and Fontana (1777) observed adsorption in the course of similar studies [48,50]. Almost a decade after these discoveries, Lowitz found a new application for the adsorption process in the growing textile industry. It was found that charcoal could adsorb impurities in liquids and could thus be used in the production of tartaric acid to yield a colourless product [47,51]. This application of adsorption technology triggered intense research. Two notable discoveries, made by von Saussure in 1814 and Mitscherlich in 1843, laid the foundation for a deeper understanding of adsorption. From experiments with a variety of different porous sorbents, von Saussure established that the adsorption process was exothermal and noted that the uptake capacity of the tested porous solids, was especially high for gases with low boiling points (i.e. ammonia, steam, diethylether) [52]. Mitscherlich found that the high gas-uptake of porous carbon, make it plausible that the adsorbed gas may well be in the liquid state once adsorbed [50]. In 1881, both Chappius [53] and Kayser [54,55] correlated the adsorbed amount of gas on a sorbent to the pressure and temperature. By doing so, these researchers paved the way for the definition of adsorption isotherms that are widely used to describe the uptake characteristics of sorbents at constant temperature. It must also be noted that it was Kayser, who introduced and coined the term “adsorption” [54]. Although Kayser began developing a theoretical concept on the adsorption phenomenon, mathematical equations that described adsorption behavior at various conditions were introduced at the turn of the century. The earliest of its kind was introduced by Freundlich in 1907 [56], who was the equations eponym. However, the Freundlich equation is entirely empirical and thus theoretically unjustified for estimating adsorption behavior. Between 1914 and 1918, understanding of adsorption theory was vastly expanded by contributions from Polanyi and Langmuir. In Polanyi’s “potential theory”, adsorption of a gas on a surface is brought about by attractive forces governed by adsorption potential [48,57]. According to this theory, the adsorbed gas is present as a compressed layer on the sorbent’s surface, which decreases in density with increasing distance from the surface. Between 1916 and 1918, Langmuir published a series of articles [58–60], which had a sustained impact on surface science. In his 1918 publication [60], Langmuir criticized investigations, which attempted to

characterize and quantify the adsorption phenomenon using porous bodies with unknown surface structures and the use of vapors that were nearly saturated. In these investigations, it is likely that the investigated vapors condense due to capillary forces, thus the gathered data does not reflect “true adsorption”. Langmuir’s previous work [58,59], showed that “true adsorbed films” consist of a single layer of the adsorbed molecule i.e. a mono-molecular layer or monolayer. Furthermore, it was determined that the monolayer is held to the surface by the same forces that hold solid bodies together i.e. primary and secondary valence forces. As a result, a novel model for adsorption was developed. The most prominent equation described so-called simple adsorption. Here it is assumed that all adsorption sites are energetically equal (i.e. no preferred adsorption sites) and thus adsorption is complete when a monomolecular layer is formed on the surface. The resulting adsorption isotherms are described by Langmuir’s model for simple adsorption. It should be noted that Langmuir’s monolayer adsorption model is most-commonly used to describe chemisorption, i.e. the adsorption of substances that form chemical bonds (e.g. covalent bonds) with a surface.

A significant contribution to a deeper understanding of adsorption by means of van-der-Waals forces, so-called physical adsorption (or physisorption), was made by Brunauer, Emmett and Teller. In a 1937 publication by Emmett and Brunauer [61], adsorption data for several gas/catalysts systems was obtained experimentally. A distinct S-shape of the adsorption isotherm could be identified at temperatures near the boiling points of the utilized gas. The isotherms exhibit a concave section at low pressures, whilst at high pressures the isotherm becomes convex. At the beginning of a linear section of the isotherm, a point “B” was defined and considered the point of monolayer completion. In 1938, Brunauer, Emmett and Teller [62] expanded on this topic and derived an isotherm equation for multilayer adsorption (i.e. the BET-equation) based on an equation given by Langmuir (“Case VI” in Langmuir’s 1918 article [60]). It was determined that the volume of gas required to form the first layer  $v_m$  in the BET-equation, is in good agreement with so-called point “B” of the corresponding adsorption isotherm. If  $v_m$  and the average area covered by a single molecule are known, the surface area of the sorbent can be calculated. This method, the so-called BET-method, has since been the standard for determining the specific surface area of porous solids and has been adopted in the corresponding ISO standard (ISO 9277:2010).

The work carried out by Langmuir, Brunauer, Emmett and Teller made invaluable contributions to adsorption theory by enabling the quantitative characterization of various adsorption systems and thus allowing predictive and efficient implementation of adsorption technology in a wide range of applications. Industrial applications of adsorption processes include catalysis, gas purification and separation processes, membrane processes, chromatographic techniques and ion exchange methods [48,63].

### 2.1.2 Adsorption of gases on solid surfaces

As mentioned in the previous section, adsorption is a phenomenon that can take place at an interface between a condensed phase and a liquid phase or a condensed phase and a gaseous phase. In this section, the focus will be on adsorption of gases on solids, i.e. on adsorption at the interface between a condensed and gaseous phase. For the sake of simplicity, a number of terms associated with adsorption are defined beforehand:

<b>Adsorptive</b>	The substance that is capable of being adsorbed [46]
<b>Adsorbent</b>	Material on the surface of which adsorption takes place [50]
<b>Adsorbate</b>	Substance in the adsorbed state [50]

Since adsorption is a surface phenomenon, solid sorbents used in adsorption processes are typically highly porous. By providing a high specific surface area (given in  $\text{m}^2\cdot\text{g}^{-1}$ ), the number of sites at which adsorption can take place can be increased, thus also increasing the adsorption capacity. A porous sorbent can feature an internal and an external surface area. Whilst the internal surface area considers the surface area of pore walls only, the external surface area does not consider pores. As seen in Figure 8, the form and accessibility of pores can vary, therefore the term pore is clearly defined as surface irregularities that are deeper than they are wide [64]. Therefore, the indentation “R” in Figure 8 contributes to the external surface area rather than to the internal surface area. Nevertheless, the cavity indicated by a “C” in Figure 8 is regarded a closed pore. Whether such closed pores are considered in the specific surface area depends on the method used for determining the surface area [50]. The BET-method for example measures the surface area within accessible pores only. Porous sorbents are also characterized in term of their pore volume and their mean pore size. The pore volume refers to the volume of all accessible pores per mass of sorbent and is typically given in  $\text{cm}^3\cdot\text{g}^{-1}$ . Since the geometry of the pores is seldom well-defined, the pores size is given as the minimal distance between two opposing pore walls, thus also giving the maximum size of the molecules that can access the pore [50]. IUPAC has established a classification system for the pores of solid sorbent, whereby micropores are pores with a size smaller than 2 nm, mesoporous have a pore size between 2 nm and 100 nm and macropores are defined as pores with a size over 100 nm.

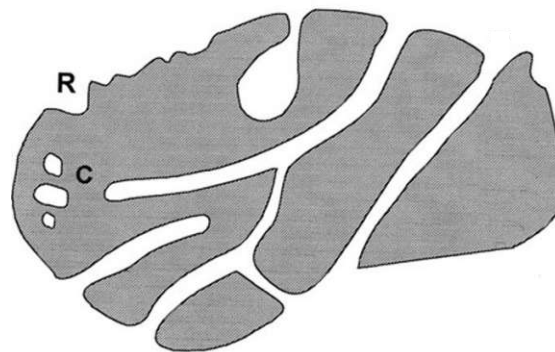


Figure 8: Schematic cross-section of a porous sorbent (adapted from Rouquerol et al. [64])



As an example, Table 1 shows surface data of three mesoporous sorbents that have recently been suggested for CO<sub>2</sub> adsorption. It can be seen that the sorbents feature a BET surface area between 753 m<sup>2</sup>·g<sup>-1</sup> and 1229 m<sup>2</sup>·g<sup>-1</sup> and a pore volume between 1.5 cm<sup>3</sup>·g<sup>-1</sup> and 6.6 cm<sup>3</sup>·g<sup>-1</sup>. It can also be seen that the BET method was used for determination of the specific surface area, thus only accessible pores are considered in the given surface areas.

	<b>MCM-41 [65]</b>	<b>SBA-15 [66]</b>	<b>Mesoporous carbon [67]</b>	
BET surface area	1229	753	798	[m <sup>2</sup> ·g <sup>-1</sup> ]
Pore size	2.7	5.5	6.3	[nm]
Pore volume	2.7	6.6	1.5	[cm <sup>3</sup> ·g <sup>-1</sup> ]

**Table 2: BET surface area, pore size and pore volume of three mesoporous sorbents suggested for CO<sub>2</sub> adsorption**

The solid sorbents shown in Table 1 do not feature functional groups that can form chemical bonds with CO<sub>2</sub>, but rather bind CO<sub>2</sub> to the surface by van-der-Waals forces. For the characterization of sorbents, a distinction is generally made between the forces responsible for binding the adsorbate to the surface.

Chemisorption involves the formation of chemical bonds, e.g. covalent bonds, between the adsorbate and the sorbent surface. For this reason the chemical specificity of the adsorption process is high and the adsorbate is only formed at specific adsorption sites on the sorbent surface [68]. Once the adsorbate reacts with the sorbent surface, the depth of the formed adsorbate is limited to a single molecular layer (i.e. a monolayer). However, at high pressures physisorption may also occur and lead to the formation of a multi-layer [50,69]. The chemical reaction itself may require an activation energy, whereas the overall heat of adsorption will lie in the range of the heat of reaction [50,68]. Furthermore, depending on the nature of the chemical reaction that occurs, chemisorption may not be reversible [48,69].

In physisorption on the other hand, the adsorbate is only weakly bound to the sorbent by van-der-Waals attraction [50,68]. Since a polarization of the adsorbate occurs, rather than a transfer of electrons between the adsorbate and the sorbent, physisorption is always a reversible process [48,68,69]. Opposed to chemisorption, where adsorption sites determine the location at which adsorption may take place, attractive forces that act between the physisorbent and the adsorbate are evenly distributed across the entire surface [68]. Furthermore, the heat of adsorption is in a similar range as the heat of liquefaction for the corresponding gas [69,70]. Since physisorption is a spontaneous process, the Gibbs free energy decreases. Additionally, the adsorbate loses at least one degree of freedom, which reduces its entropy. According to the definition of the Gibbs free energy, these changes entail a release of heat, thus physisorption is always an exothermal process [48,70]. It should also be mentioned that physisorption is only relevant for gases below their critical temperature whereas the adsorption process itself occurs rapidly [69].

### 2.1.3 The Langmuir adsorption model

Adsorption behavior is typically described by adsorption isotherms. These isotherms give the amount adsorbed (or sorbent loading) as a function of the partial pressure of the adsorptive at constant temperature. The model for simple adsorption described in Langmuir's 1918 article [60] describes monolayer adsorption and is a widely accepted model to describe chemisorption and adsorption behavior of various other systems at moderately low coverage [70]. In the Langmuir adsorption model, the following assumptions are made [47]:

- All adsorption sites are energetically equal
- All adsorption sites are accessible
- No interaction between adsorbed molecules
- Each adsorption site can hold one molecule i.e. adsorption is complete when a monolayer is formed
- The number of adsorption sites is finite

If the assumptions listed above are made, the sorbent loading ( $q$ , given in  $\text{mol}\cdot\text{kg}^{-1}$ ) can be defined as shown in Eq. 1:

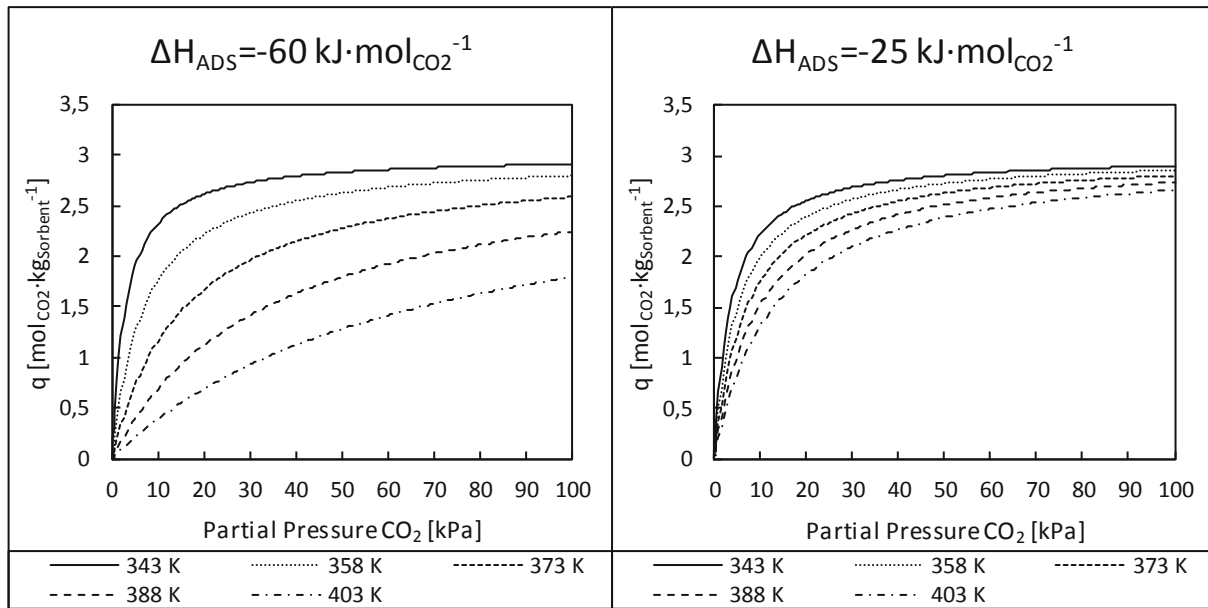
$$q = q_m \cdot \frac{b(T) \cdot p_A}{1 + b(T) \cdot p_A} \quad \text{Eq. 1}$$

Here  $q_m$  is the sorbent loading required to attain monolayer completion,  $p_A$  is the partial pressure of the adsorptive and  $b(T)$  the adsorption constant. For the sake of simplicity Eq. 1 will be referred to simply as the "Langmuir equation". The temperature dependency of the adsorption constant follows the van't Hoff equation as shown in Eq. 2 [63].

$$b(T) = \frac{k_{ADS}}{k_{DES}} \cdot \exp\left(\frac{-\Delta H_{ADS}}{R \cdot T}\right) = K \cdot \exp\left(\frac{-\Delta H_{ADS}}{R \cdot T}\right) \quad \text{Eq. 2}$$

Eq. 2 shows that the adsorption constant depends on the pre-exponential factor ( $K$ ), the enthalpy of adsorption ( $\Delta H_{ADS}$ ), the ideal gas constant ( $R$ ) and the temperature ( $T$ ). It should be noted that the pre-exponential factor is the ratio of the rate constant for the adsorption step ( $k_{ADS}$ ) to the rate constant for the desorption step ( $k_{DES}$ ). In practice  $K$ ,  $\Delta H_{ADS}$  and  $q_m$  can be determined by fitting Eq. 1 to adsorption data obtained through adsorption experiments.

Figure 9 shows adsorption isotherms of two different hypothetical  $\text{CO}_2$  sorbents in a temperature range between 70 °C (i.e. 343 K) and 130 °C (i.e. 403 K).



**Figure 9: Exemplary adsorption isotherms showcasing the effect of adsorption temperature and different adsorption enthalpies on the equilibrium sorbent loading of two sorbents (adapted from Berger and Bhowm [45])**

The adsorption parameters of the sorbents have been chosen in a way that both sorbents exhibit identical adsorption behavior at 343 K, whilst featuring two different adsorption enthalpies. The sorbent shown on the left of Figure 9 shall represent a chemisorbent, with a high affinity towards  $\text{CO}_2$  and a correspondingly high heat of adsorption, whilst the sorbent on the right shall represent a physisorbent with a heat of adsorption of  $-25 \text{ kJ}\cdot\text{mol}_{\text{CO}_2}^{-1}$ . As can be seen, the chemisorbent shows a higher dependence of the  $\text{CO}_2$  loading from temperature. As a result, a higher change in the  $\text{CO}_2$  loading is achieved at a given temperature change with a chemisorbent compared to a physisorbent.

### 2.1.4 Process cycles for gas separation by adsorption

In gas separation processes that employ adsorption, the gas is initially brought into contact with the sorbent so that the adsorption process can take place. During the adsorption step, the rate of adsorption is greater than the rate of desorption until thermodynamic equilibrium is reached [70]. Once this state has been reached, the sorbent loading cannot be increased any further because the adsorption rate and desorption rate are equal. In typical industrial applications, the loaded sorbent is regenerated in a desorption step and reused, thus the process is typically operated in a cyclic manner. During the adsorption step the operating conditions are chosen in a way that allow a high sorbent loading ( $q_{\text{ADS}}$ ), whereas during desorption, low sorbent loadings ( $q_{\text{DES}}$ ) are targeted. The difference in sorbent capacity between the adsorption and the desorption step ( $q_{\text{ADS}} - q_{\text{DES}}$ ) is known as the working capacity and represents an important parameter for adsorption processes. The achievable working capacity depends highly on the adsorption characteristics of the utilized sorbent as well as the conditions during the adsorption step and the desorption step, which in turn depend on the applied process cycle. It is worth noting that the extracted product after desorption is typically referred to as the desorbate. [63,71,72]

The most common process cycles for adsorption processes are listed in the following [63,71,72]:

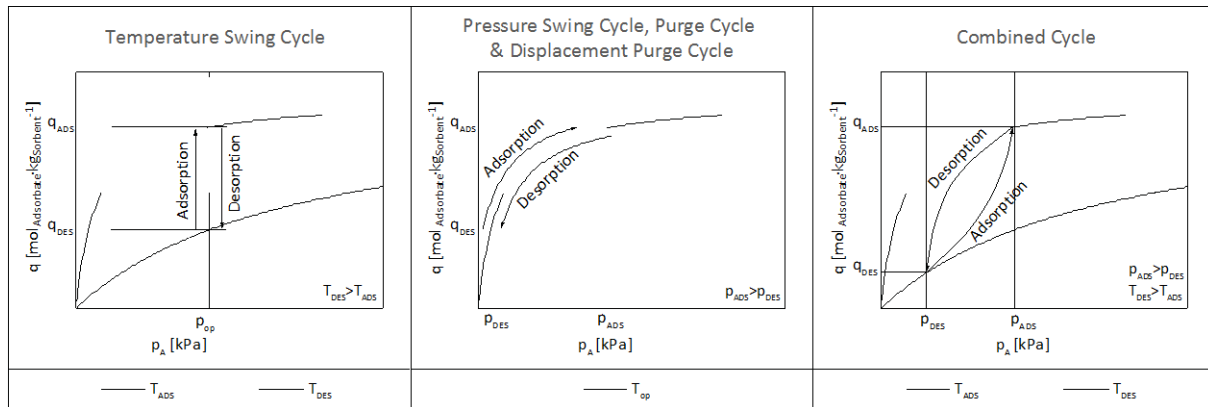


Figure 10: Schematic illustrations of the temperature swing cycle (left), pressure swing cycle, purge cycle and displacement cycle (middle) and combined cycle (right).

- Temperature swing:** Adsorption is carried out at a low temperature, where a high equilibrium loading of the sorbent can be achieved. The sorbent is subsequently regenerated at an increased temperature, which reduces the equilibrium loading of the sorbent and leads to the release of the adsorbate. As shown in Figure 10 (left), the temperature swing cycle may be operated at a constant partial pressure of the adsorptive ( $p_A = p_{op}$ ) in the bulk phase.
- Pressure swing:** The partial pressure of the adsorptive can be influenced by changing the total pressure of the gas phase. During the pressure swing cycle, adsorption is carried out at an elevated gas pressure, so that an increased partial pressure of the adsorptive can be achieved and thus high sorbent loadings. The total pressure of the gas is reduced so that the adsorbate can be desorbed. As shown in Figure 10 (middle), the pressure swing cycle may be carried out at constant temperature ( $T_{op}$ ).
- Purge cycle:** Similar to the pressure swing cycle, the partial pressure dependency of the sorbent loading is exploited in the purge cycle. However, contrary to the pressure swing cycle, the total pressure of the gas is kept constant. During desorption, the sorbent is contact with an inert purge gas (often also referred to as “sweep gas” or “stripping gas”), which reduces the partial pressure of the adsorptive in the gas phase and thus leads to the release of the adsorbate. If enough purge gas is used in the desorption step, it is possible to completely remove the adsorbate. In this case, the maximum working capacity is equal to the achieved sorbent loading at adsorption conditions ( $q_{ADS}$ ). Furthermore, the purge gas cycle may be carried out in an isothermal manner, as indicated in Figure 10 (middle).
- Displacement purge cycle:** This cycle is carried out analogously to the purge cycle, only that a purge gas is used that is competitively adsorbed. Desorption is thus brought about by both a reduction in the adsorptive partial pressure in the gas phase and the higher affinity of the purge gas to the adsorption sites. In the subsequent adsorption step, the purge gas is released from the sorbent due to a reduction of its partial pressure in the gas phase. Therefore, the utilized purge gas will be present in both product gas streams and must either be removed in an auxiliary process or be tolerable within the product gas streams. Differently to the aforementioned cycles, a particularly low heating and cooling demand is required for the desorption step and adsorption step respectively. This is because the purge gas inherently features a higher heat of adsorption than the adsorptive, due to its higher affinity to the

adsorption sites. Therefore, only the difference in the heats of adsorption between the purge gas and the adsorbate needs to be extracted during the desorption step and introduced during the adsorption step. This cycle, similarly to the pressure swing cycle and the purge cycle, may typically be carried out at constant temperature, as shown in Figure 10 (middle).

- **Combined Cycle:** To further promote desorption of the adsorbate, the abovementioned cycles are often combined. As an example, a combination of a temperature swing with a purge cycle at constant absolute pressure is shown in Figure 10 (right). In this cycle, adsorption is carried out at a particular temperature and partial pressure of the adsorbate in the gas phase. Subsequently, the sorbent is brought to an elevated temperature whilst a purge gas is used to reduce the partial pressure of the adsorbate in the gas phase. The advantage of this combination is the particular low adsorbate loadings that can be achieved during the desorption step.

A low loading of the sorbent after the desorption step is critical for high separation efficiencies since this determines the lowest achievable partial pressure of the adsorbate in the treated gas. However, both technical and economic factors need to be considered in the selection of a suitable process cycle for adsorbate gas separation. A general guideline in the form of advantages and disadvantages of each desorption method is given by Ruthven [63] and shown in Table 3.

Method	Advantages	Disadvantages
<i>Thermal Swing</i>	<ul style="list-style-type: none"> <li>• Good for strongly adsorbed species; small change in temperature gives large change in sorbent loading (see Figure 9)</li> <li>• Desorbate may be recovered at high concentration</li> </ul>	<ul style="list-style-type: none"> <li>• Unsuitable for rapid cycling so adsorbent cannot be used with maximum efficiency</li> <li>• Heat loss means inefficiency in energy usage</li> <li>• Thermal aging of adsorbent</li> </ul>
<i>Pressure swing</i>	<ul style="list-style-type: none"> <li>• Good where weakly adsorbed species is required in high purity</li> <li>• Rapid cycling – efficient use of adsorbent</li> </ul>	<ul style="list-style-type: none"> <li>• Very low pressure may be required</li> <li>• Mechanical energy more expensive than heat</li> <li>• Desorbate recovery at low purity</li> </ul>
<i>Displacement purge swing</i>	<ul style="list-style-type: none"> <li>• Good for strongly held species</li> <li>• Avoids risk of cracking reaction during regeneration</li> <li>• Avoids thermal aging of adsorbent</li> </ul>	<ul style="list-style-type: none"> <li>• Product separation and recovery needed (choice of purge gas is crucial)</li> </ul>

**Table 3: Summary of factors governing choice of desorption method (adapted from Ruthven [63])**

## 2.2 FUNDAMENTALS OF FLUIDIZED BED TECHNOLOGY

### 2.2.1 Definition and history of fluidization engineering

Fluid-particle contacting plays an essential role in many industrial applications. In its simplest form, a fluid-solids contactor may be a vessel containing a bed of particles through which a fluid is passed in an upward direction. Whilst, the buoyancy and the gravitational force of each particle is fixed and depends on both the gas and the bed particle, the drag force imposed by an upward flowing gas increases with gas velocity. At low fluid velocities, the drag force imposed on the particles will not be able to overcome the gravitational force, thus the bed of particles will remain fixed. In this state, the contacting mode is referred to as a “fixed bed”. As soon as the fluid velocity is increased to the point that the fluid-induced drag force together with the buoyancy exceeds the gravitational force, particles begin to move. This fluid velocity marks the beginning of the fluidized bed regime and is thus referred to as the minimum fluidization velocity ( $U_{mf}$ ). In this contacting mode, the bed of particles has many characteristics of a fluid, thus coining the term fluidization. Depending on the gas-particulate system, the bed particles may move apart and cause bed expansion or gas bubbles may form and contribute to solids mixing as they move upward through the bed. Vigorous solids movement in the fluidized bed regime brings about many beneficial properties of these reactor systems. For this reason, fluidized beds have become the preferred contacting method for numerous industrial processes. [73]

The first large scale fluidized bed reactor was put into operation in Germany in 1926 and was used for coal gasification. Although this reactor design was used in Germany and Japan, to supply the industrial sector with synthesis gas, development of fluidized bed reactor systems gained momentum in the 1940s [73]. Due to the looming involvement of the U.S. in the Second World War and the associated demand for fuels, new methods were required for transforming heavy fractions of oil (i.e. kerosene and gas oil) into lighter ones (i.e. naphtha). At the time, the Houdry cracking process was available as well as a suitable alumina-type catalyst. However, in the course of the cracking process, the catalyst becomes increasingly coated with coke, which ultimately leads to its deactivation. The Houdry process applied fixed beds, which were alternately contacted with gas oil and air. Due to poor heat transfer within the reactors, the temperature could not be well controlled, thus the process was considered unsuitable for large-scale application. An alternative process design emerged in a cooperation between engineers of the Standard Oil Company of New Jersey and Professors Lewis and Gilliland of the Massachusetts Institute of Technology. The proposed process design incorporated two fluidized beds and pneumatic transport lines, thus laying the foundation for the fluid catalytic cracking (FCC) process. The first commercial-scale FCC unit based on this design was constructed and put into operation in 1942 at the Baton Rouge refinery [73,74]. This success, together with the benefits fluidized bed reactor systems offered over fixed bed contactors, led to rapid development and implementation of fluidized bed reactor systems in numerous industrial applications.

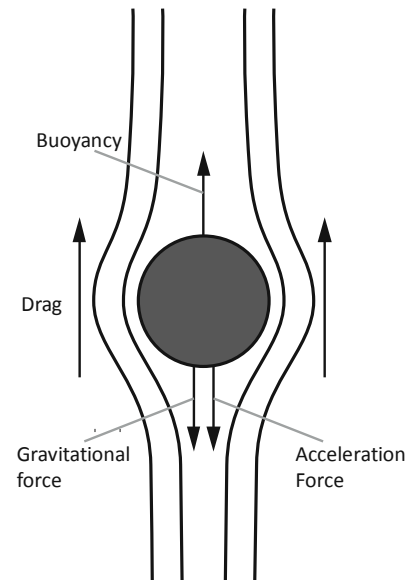


Figure 11: Forces that act on a single particle (adapted from Hofbauer [76])

Since gas-particle fluidized beds are of particular significance in this work, liquid-particle systems will not be discussed herein.

### 2.2.2 Particle characterization

The physical properties of the particles that make up a bed play a central role in its behavior once fluidized. One of the most important properties is the particle size, which is often given in terms of a particle diameter. However, particles in a bed rarely feature a uniform size and are seldom spherical in shape. For this reason, a number of key figures have been introduced to aid in particle characterization.

The size of particles is often related to the diameter of a sphere with mutual geometric properties. Typically, parameters such as the sieve diameter ( $d_p$ ), volume diameter ( $d_v$ ), surface diameter ( $d_s$ ) and the Sauter mean diameter ( $d_{sv}$ ), as defined in Eq. 3-Eq. 5 [75], are used to describe the particle size.

$$d_s = \sqrt{\frac{A_p}{\pi}} \quad \text{Eq. 3}$$

$$d_v = \sqrt[3]{\frac{6 \cdot V_p}{\pi}} \quad \text{Eq. 4}$$

$$d_{sv} = \frac{d_v}{d_s} = 6 \cdot \frac{V_p}{A_p} \quad \text{Eq. 5}$$

In fluidization engineering, the  $d_{sv}$  is of particular relevance. This is because the pressure drop of a bed is proportional to the surface area of the contained particles and the bed porosity. Therefore, similar bed pressure drops can be achieved with a bed of spherical particles with identical  $d_{sv}$  [76]. The so-called sphericity ( $\Phi_s$ ) is used to describe a particles deviation from the spherical shape. As can be seen in Eq. 6 [73], the sphericity is given as the ratio between the surface area of a sphere with the same volume as the particle and the external surface area of the particle itself, thus unity is reached when the particle has a spherical shape.

$$\Phi_s = \left( \frac{\text{Surface of sphere}}{\text{Surface of particle}} \right)_{\text{of same volume}} \quad \text{Eq. 6}$$

To determine the gravitational force that act on a particle, knowledge of its density is required. Whilst the density is always defined as the quotient of mass and volume, in fluidized bed engineering three different densities are commonly used. The material density describes the density of the particle without considering pores. Contrary to the material density, the particle density ( $\rho_p$ ) also considers pores. Thus the material density is equal to the particle density if the particle lacks pores. The bulk density ( $\rho_b$ ) is the density of bulk particles in a certain packing condition and includes the void space between particles. Therefore, the material density is usually greater than the particle density, whereas both these values are always greater than the bulk density [75]. It should be noted that bed voidage

( $\varepsilon$ ), i.e. the fraction of void space within a bed of particles, describes the relationship between the particle density ( $\rho_p$ ) and the bulk density ( $\rho_b$ ) according to Eq. 7:

$$\varepsilon = 1 - \frac{\rho_b}{\rho_p} \quad \text{Eq. 7}$$

### 2.2.3 General aspects of fluidization

When considering a vessel containing bulk particles and a pressure measurement over a defined segment of the vessel (as shown in Figure 12), the pressure drop between the measuring points is equal to zero if there is no gas flow through the bed. If an evenly distributed flow of gas is introduced from the bottom of the vessel, the measured pressure drop ( $dp$ ) will increase due to the flow resistance brought about by the bed.

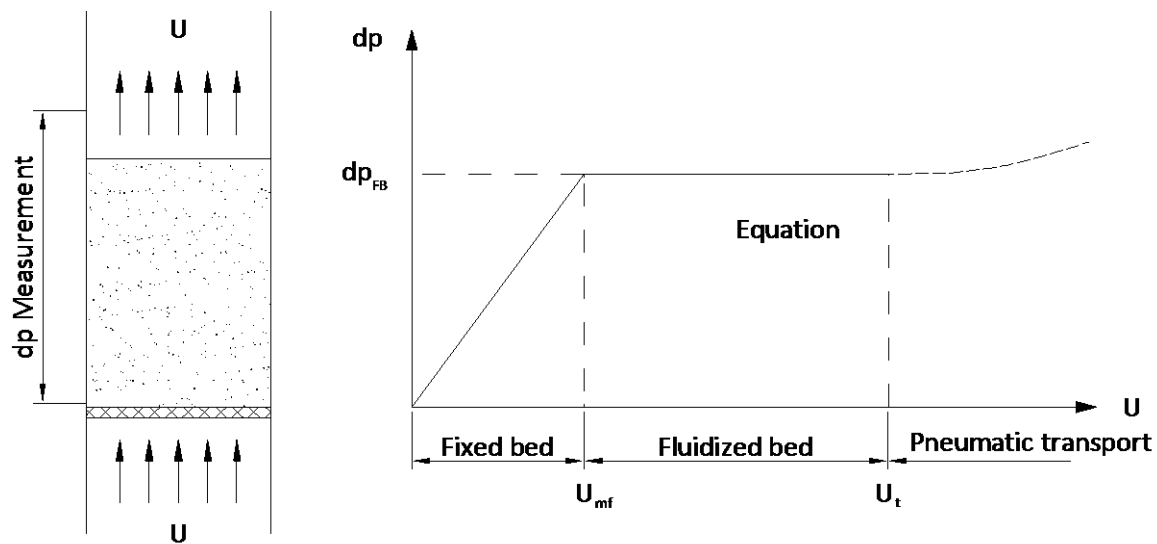


Figure 12: Schematic illustration showing the characteristic pressure drop across a bed of particles as a function of the superficial fluid velocity (adapted from Zehetner [77])

As seen in Figure 12, the pressure drop will increase with increasing superficial gas velocity  $U$ . The superficial gas velocity is typically given in  $\text{m}\cdot\text{s}^{-1}$  and is calculated by dividing the actual gas flow rate by the vessel cross-section as shown in Eq. 8.

$$U = \frac{\dot{V}_{Gas}}{A_{Vessel}} \quad \text{Eq. 8}$$

At gas velocities below the minimum fluidization velocity  $U_{mf}$ , the pressure drop of the bed  $dp$  increases linearly with the superficial gas velocity for laminar flow. Since the pressure drop in this region depends on the flow regime of the gas, the Reynolds number must be calculated before the packed bed pressure drop can be calculated. The Reynolds number ( $Re_p$ ) is a dimensionless number used to characterize the flow regime of fluids and is calculated according to Eq. 9.



$$Re_p = \frac{U \cdot \rho_g \cdot d_{sv}}{\mu} \quad \text{Eq. 9}$$

If the fluid flow is laminar, i.e.  $Re < 1$ , the Carman-Kozeny (as shown in Eq. 10) has shown to be in good alignment with measured values.

$$\frac{dp}{L} = 180 \cdot \frac{(1 - \varepsilon)^2}{\varepsilon^3} \cdot \frac{\mu \cdot U}{d_{sv}^2} \quad \text{Eq. 10}$$

If the gas flow is turbulent and  $Re > 1$ , a modified version of the Carman-Kozeny equation, the so-called Ergun equation (as shown in Eq. 11) is to be used [78]. In this scenario, a quadratic component is added to the existing linear relationship between pressure drop and superficial gas velocity.

$$\frac{dp}{L} = 150 \cdot \frac{(1 - \varepsilon)^2}{\varepsilon^3} \cdot \frac{\mu \cdot U}{d_{sv}^2} + 1.75 \cdot \frac{1 - \varepsilon}{\varepsilon^3} \cdot \frac{\rho_g \cdot U^2}{d_{sv}} \quad \text{Eq. 11}$$

Once the minimum fluidization velocity ( $U_{mf}$ ) is surpassed, a fluidized bed is formed above the gas distributor. As long as the bed particles stay in the vessel, i.e. no particles are entrained, the pressure drop will stay constant. Since the weight of the bed particles (minus particle buoyancy) is fully supported by the drag forces of the gas, the fundamental fluidization equation can be used to describe the pressure drop in a fluidized bed, according to Eq. 12

$$\frac{dp}{L} = (1 - \varepsilon) \cdot (\rho_p - \rho_g) \cdot g \quad \text{Eq. 12}$$

A generalized method for predicting the minimal fluidization velocity was given by Wen and Yu [79], which involves the Archimedes number (see Eq. 13 & Eq. 14). Eq. 14 has shown to be in good agreement with experimental data gained for various gas-particulate systems and a Reynolds number range of 0.001-4000.

$$Ar = \frac{\rho_g \cdot d_{sv}^3 (\rho_p - \rho_g) \cdot g}{\mu^2} \quad \text{Eq. 13}$$

$$U_{mf} = \frac{\mu}{\rho_g \cdot d_{sv}} \cdot \left[ \sqrt{33.7^2 + 0,0408 \cdot Ar} - 33.7 \right] \quad \text{Eq. 14}$$

When the superficial gas velocity is increased above the terminal velocity  $U_t$  (or free-fall velocity) of the particles, bed particles are lifted upwards and are thus entrained from the vessel. If the entrained particles are returned to the bed, the force required to reaccelerate these bed particles manifests in an increase of the measured bed pressure drop. The terminal velocity of a single particle can be derived by means of a force balance of a particle as shown in Eq. 15. It should be noted that the particle acceleration is zero in this case, since particle forces at the terminal velocity are considered. For information regarding the drag coefficient ( $C_w$ ) that must be used in this equation, the reader is referred to Wang and Fan [75].

$$U_t = \sqrt{\frac{4}{3} \cdot \frac{d_p \cdot (\rho_p - \rho_g) \cdot g}{\rho_g \cdot C_W}} \quad \text{Eq. 15}$$

### 2.2.4 Geldart classification

In 1973, Geldart [80] showed that fluid-particle systems can be divided into four distinct groups based on the Sauter mean diameter of the bed particles and the difference between particle density and fluid density. Each Geldart group will be briefly described in the following [73,76,80].

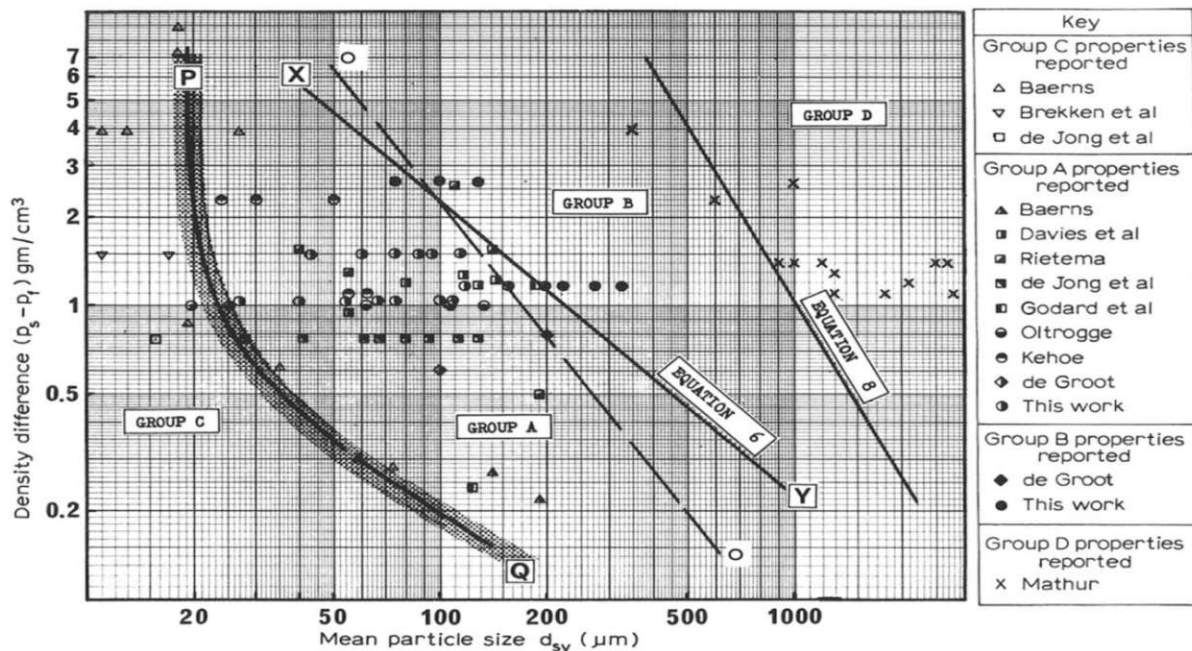


Figure 13: Powder classification diagram for fluidization by air at ambient temperatures [80]

#### Group C

As can be seen in Figure 13, this group represents powders of the smallest size. Due to the small particle size, cohesive forces between the particles are particularly strong relative to forces that can be applied by a flowing fluid. Fluidization of a bed of Group C powders is challenging since the bed is prone to the formation of channels. This behavior leads to gas bypassing and thus poor mass transfer, whereas the limited solids movement entails poor heat transfer. To break-up inter-particle forces, it is recommended to use devices such as mechanical stirrers immersed in the bed.

#### Group A

A bed of Group A particles shows uniform bed expansion upon fluidization, whereas gas bubbles are formed well beyond  $U_{mf}$ , at a distinct superficial fluid velocity known as the minimum bubble velocity ( $U_{mb}$ ). The formed gas bubbles split and coalesce frequently as they rise through the bed. Furthermore, once the flow of fluidizing agent is stopped, a bed of Group A particles collapses slowly.

**Group B**

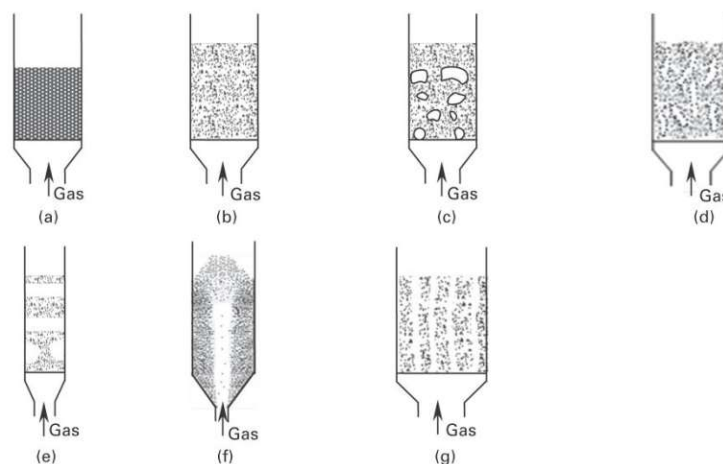
Group B particles readily form bubbles as soon as  $U_{mf}$  is surpassed, therefore  $U_{mf}$  can be considered similar to  $U_{mb}$ . Contrary to the bubble behavior observed in Group A fluidized beds, bubbles coalesce frequently, whereas their size is independent from the particle size. Furthermore, bubble size can be correlated to the distance from the gas distributor as well as the superficial gas velocity. It should be noted that the rising bubbles encourage vigorous mixing of solids in the fluidized bed. Furthermore, the fluid can rapidly exit the bed of particles, thus leading to a collapse of the fluidized bed once fluid flow is stopped.

**Group D**

Group D represents large particles. Similar to Group B solids, bubbles are formed as soon as the  $U_{mf}$  is surpassed, whereas these bubbles grow rapidly to large sizes. Fluidized beds containing Group D solids spout readily, which is characteristic for this particle class.

**2.2.5 Fluidization regimes**

Within the existence range of fluidized beds, i.e. within a fluid velocity range between  $U_{mf}$  and  $U_t$ , a number of different flow regimes can be observed in fluid-particulate systems. Figure 14 gives a schematic illustration of seven different dense-phase flow regimes.



**Figure 14: Dense phase fluidization regimes: (a) fixed bed; (b) particulate fluidization; (c) bubbling fluidization; (d) turbulent fluidization; (e) slugging; (f) spouting; (g) channeling (taken from Wang and Fan [75])**

The occurring flow regime will depend both on the superficial velocity of the fluid and the Geldart classification of the bed particles. At gas velocities below  $U_{mf}$ , the fluid passes through the interstitial volume of the bed without causing any disturbance of the particles. This flow regime as seen as a) in Figure 14 is known as the fixed bed flow regime. When the fluid velocity is increased beyond  $U_{mf}$  one of two phenomena occur. If the bed comprises Group A particles, the bed will expand uniformly as the gas velocity increases, without forming observable gas bubbles; this regime is known as the particulate regime or smooth fluidization regime and is shown in Figure 14 b). For Group B and Group D (and for Group A gas-particulate systems beyond  $U_{mb}$ ), two distinct phases, an emulsion phase and a bubble

phase, become observable. These gas bubbles travel upward through the bed and may coalesce with other bubbles and grow, or break up and form smaller bubbles. Regardless, these bubbles lead to intense particle motion and support solids mixing within the bed. This regime is known as the bubbling fluidization regime and is seen in Figure 14 c). At even higher gas velocities, an increasing amount of particles are ejected into the section above the dense bed, known as the freeboard. At gas velocities in the range of  $U > 10 \cdot U_{mf}$ , the freeboard becomes increasingly hazy, the bed surface becomes rough and a clear distinction between the emulsion phase and the bubble phase can no longer be made. Gas bubbles coalesce and strands of solids within the gas phase are observable. Due to the absence of rising bubbles, the amplitude of pressure drop fluctuations decreases, thus coining the term “turbulent fluidization”. A schematic illustration of the turbulent fluidized bed regime is seen in Figure 14 d). Slugging, as seen by Figure 14 e), is a special mode of bubbling fluidization. Slugs are bubbles that coalesce to the size of the fluidized bed cross-section. They are typically formed in tall, narrow fluidized beds. The spouting fluidized beds as shown in Figure 14 f) are typically realized for Group D solids. As shown in Figure 14 f) a gas jet is introduced at the bottom of a conical vessel, which leads to the ejection of solids into the freeboard. Solids land near the wall region and are again transported toward the gas jet. Thus, a circular flow of solids is realized within the bed. Channeling, as seen in Figure 14 g), is an unwanted behavior brought about by cohesive forces between particles and leads to significant bypassing of the fluidizing agent. [73,75,76]

## 2.2.6 Gas bubbles in fluidized beds

Gas bubbles that rise through a fluidized bed can significantly enhance particle mixing. This brings about a homogenous temperature distribution throughout the entire fluidized bed and high wall-to-bed heat transfer rates [76]. Furthermore, gas bubbles in low-viscose liquids share numerous mutual properties with gas bubbles in bubbling fluidized beds, as summarized by Kunii and Levenspiel [73]:

- **Shape:** Gas bubbles are close to spherical in shape when small and become flatter and more distorted as they grow. When large, gas bubbles resemble spherical caps.
- **Rise velocity depends on size:** The rise velocity of spherical cap bubbles can be described by similar equations in both systems. The bubble rise velocity  $U_{br}$  through a low-viscose liquid was described by Davies and Taylor [81] as shown in Eq. 16. Eq. 17 shows the bubble rise velocity in a fluidized bed as summarized from experimental data by Clift and Grace [82]. It should be mentioned that  $R_n$  and  $d_b$  are the radius of curvature at the nose of the gas bubble and the diameter of a sphere with the same volume as the spherical cap bubble respectively. As can be seen from the equations, large bubbles rise faster than small bubbles.

$$U_{br} = \frac{2}{3} \cdot (g \cdot R_n)^{0.5} \quad \text{Eq. 16}$$

$$U_{br} = 0.711 \cdot (g \cdot d_b)^{0.5} \quad \text{Eq. 17}$$

- **Bubble Coalescence:** A train of bubbles can coalesce to form larger bubbles.
- **Wall effect:** Wall effects reduce the bubble rise velocity in both systems. In fluidized beds a considerable influence is seen by walls when the quotient of  $d_b$  and the tube diameter  $d_t$  exceeds 0.125. As shown in Eq. 18, Wallis [83] suggested an equation for bubbles where  $0.125 < \frac{d_b}{d_t} < 0.6$ .

$$U_{br} = (0.711 \cdot (g \cdot d_b)^{0.5}) \cdot 1.2 \cdot e^{-1.49 \frac{d_b}{d_t}} \quad \text{Eq. 18}$$

Fluidized bed systems are considered to feature slugs rather than bubbles when  $\frac{d_b}{d_t} > 0.6$ .

- **Two-phase theory:** Experiments in bubbling fluidized beds have shown that gas in excess of the minimum fluidization rate, passes through the bed in the bubble phase, whilst the emulsion phase remains at approximately minimum fluidization conditions. In liquids, any gas that is in excess of saturation will rise in the form of bubbles whilst the density of the liquid phase remains constant.

Opposed to gas bubbles in liquids, the gas contained in bubbles that rise through fluidized beds can freely move between the bubble and the emulsion phase. A widely accepted model that describes the flow behavior of gas between a bubble and the emulsion phase was proposed by Davidson [84]. Here, the following assumptions are made [73,85]:

- The bubble is free of solids and features a circular shape
- Particles in the emulsion phase flow like an inviscid fluid with the density of the bed at minimum fluidization conditions i.e.  $\rho_s \cdot (1 - \varepsilon_{mf})$
- In the emulsion phase, the gas flows like an incompressible viscous fluid
- The pressure in the bubble is constant
- Far from the bubble, an undisturbed pressure gradient exists

As can be seen in Figure 15, these assumption entail that the flow pattern of gas surrounding a bubble is solely dependent on the quotient of the bubble rise velocity  $U_{br}$  and the velocity of the emulsion gas  $U_f$ .

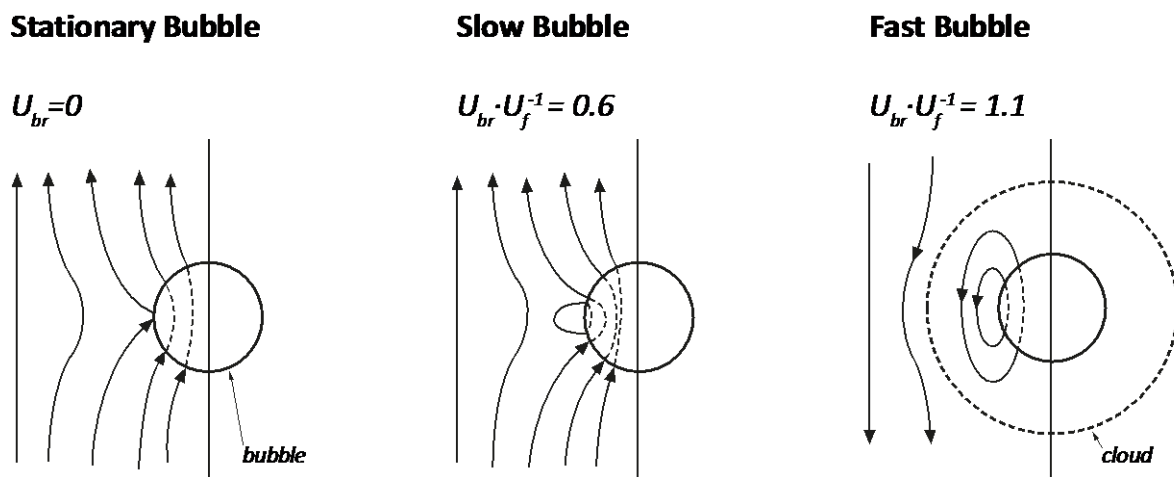


Figure 15: Gas streamlines near gas bubbles from the Davidson model. From left to right, a stationary and slow cloudless bubble and a fast clouded bubble (adapted from Kunii and Levenspiel [73] and Dennis [85]).

In a stationary bubble, the emulsion gas can partially bypass the bed through the bubble. The gas enters the bubble at the bottom, and leaves at the top. As the bubble rise velocity increases, an increasing amount of gas begins to circulate between the bubble and the emulsion phase. This annular ring-type flow pattern rises with the bubble through the bed. When the bubble rise velocity exceeds the emulsion gas velocity i.e.  $U_{br} > U_f$ , the gas that flows through the bubble exits at the top similarly

to the aforementioned cases. However, due to the higher velocity of the bubble relative to the gas in the emulsion phase, the gas re-enters the bubble at the bottom. This recirculating gas does not mix with the gas in the emulsion phase, thus coining the term “cloud” for the region around the bubble that is penetrated by the recirculating gas. The higher  $U_{br}$ , the smaller the cloud radius becomes and the more the flow of recirculating gas moves towards the center of the gas bubble. Due to this effect, gas-solids contacting deteriorates as the bubble rise velocity increases. It should be noted that  $U_{br}$  is slow relative to  $U_f$  for fluidized beds containing Geldart D-type solids, whereas the opposite is typically observed for Geldart A and Geldart B gas-particulate systems. [73,85]

### 2.2.7 Particle entrainment and pneumatic transport

In bubbling and turbulent fluidized beds, bed particles are continuously catapulted into the freeboard, therefore the gas leaving the fluidized bed will contain solids. In bubbling fluidized beds, this occurs due to bursting bubbles. In turbulent beds on the other hand, particle clusters are lifted into the freeboard, which subsequently disperse into individual particles. As shown in Figure 16, the vessel containing a fluidized bed can be divided into two sections: a dense phase and a lean phase, whereas the upper surface of the dense phase represents the border between the two phases. It is worth mentioning that the particles present in the freeboards contain the entire size spectrum of particles within the dense bed. As can be seen, the density of solids present in the lean phase decreases with increasing height of the vessel and becomes constant at a certain height. This height is known as the transport disengaging height, or TDH, and marks the point where coarse particles, i.e. particles for which  $U_t$  is not exceeded, are no longer present. It should be noted that particles for which  $U_t$  is exceeded always exit the vessel regardless of the vessel height. The process of removing this particle fraction is referred to as elutriation. [73]

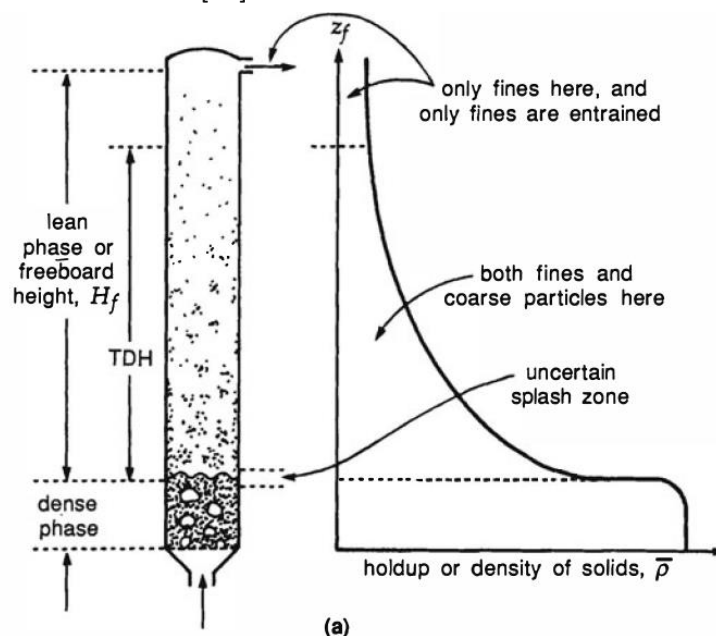


Figure 16: Schematic illustration of the development of the holdup as a function of the vessel height [73]

If the elutriated solids are not returned to the vessel by means of a suitable fluid-solids separation device and a solids transport circuit, the share of this particle fraction within the bed will ultimately decrease to zero. Beyond  $U_t$ , a distinction is generally made between the fast fluidization regime, dense suspension upflow (for Geldart A particles only) and dilute phase flow (i.e. pneumatic conveying) [86]. As the fluid velocity is increased beyond  $U_t$ , the fast fluidization regime is encountered first, followed by pneumatic conveying. Since dense suspension flow is a special case for Group A particles, it will not be discussed herein, for more information the reader is referred to Grace et al. [87]. In the fast fluidized bed regime, the bed can again be divided into two phases. A dilute suspension traveling upward within the axial core of the vessel, whilst clusters comprising a dense phase of solids travel downward near the vessel walls. If the gas velocity is increased or the solids feeding rate is decreased, a transition from the fast fluidization regime to the pneumatic conveying regime takes place. Here solids are widely dispersed in the upward flow of gas. [73]

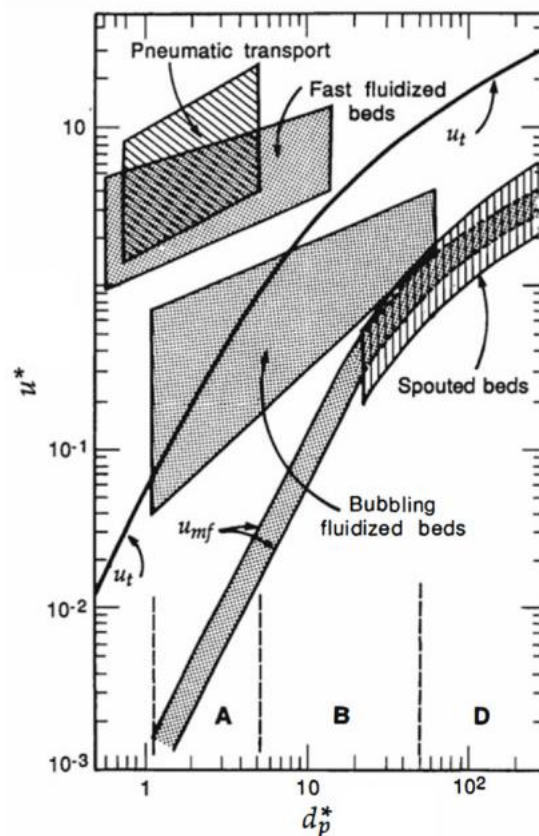


Figure 17: Flow regime diagram (adapted from Grace [88])

A regime map showing the boundaries of various fluidized bed regimes can be seen in Figure 17. Here,  $U^*$  and  $d_p^*$  are the dimensionless superficial gas velocity and the dimensionless particle diameter respectively. These figures are defined as shown in Eq. 21 and Eq. 22.

$$U^* = \frac{Re_p}{Ar^{\frac{1}{3}}} = U \cdot \left( \frac{\rho_g^2}{\mu \cdot g \cdot (\rho_p - \rho_g)} \right)^{\frac{1}{3}} \quad \text{Eq. 19}$$

$$d_p^* = Ar^{\frac{1}{3}} = d_p \cdot \left( \frac{\rho_g \cdot g \cdot (\rho_p - \rho_g)}{\mu^2} \right)^{\frac{1}{3}} \quad \text{Eq. 20}$$

It should be noted that vessels containing a gas-particulate system in the fast fluidization regime or the pneumatic transport regime are typically referred to as “risers”. Under certain conditions, the solids flux through a riser can be simply estimated according to Eq. 21 [77] using the superficial gas velocity ( $U$ ), the terminal velocity of the solids ( $U_t$ ) and the pressure drop ( $dp$ ) over a defined height ( $H$ ). However, a number of requirements must be met so that this estimation yields acceptable results [77,89,90].

- The pressure measurement needs to be taken in a section of the riser in which the axial solids holdup can be assumed constant
- There is no downward flow of solids (due to e.g. reflections at the solids outlet of the riser)
- Solids flow is heavily dilute (i.e. the bed voidage approaches unity).
- No solids acceleration in the respective riser section over which the differential pressure measurement  $dp$  is made.

$$G_s = \frac{(U - U_t)}{g} \cdot \frac{dp}{H} \quad \text{Eq. 21}$$

For more information on the estimation of the solids flux in risers, the reader is referred to Stollhof et al. [89].

### 2.2.8 Bubbling fluidized bed-to-surface heat transfer

Amongst the many benefits of fluidized beds, excellent heat and mass transfer may be one of the most remarkable properties. Due to the high surface area encountered by the gas once in contact with the fluidized bed i.e. approximately the surface area of all particles present in the bed, gas-solids heat transfer is rarely a limiting factor [91]. Furthermore, contact amongst bed particles of different temperature, or contact between bed particles and surfaces at different temperatures, i.e. immersed surfaces and vessel walls, is frequent and irregular. Therefore, temperature gradients are equalized rapidly and a uniform fluidized bed temperature is developed. Heat transfer brought about by particle motion is called particle convection, and is responsible for the differences in heat transfer between fluidized beds and fixed beds. [92]

As shown in Eq. 22, the rate of heat flow between a fluidized bed and a surface (shown as  $\dot{Q}$  and given in W) depends on the contact surface area ( $A$  in  $\text{m}^2$ ), the average heat transfer coefficient ( $h$  in  $\text{W}\cdot\text{m}^{-2}\cdot\text{K}^{-1}$ ) and the temperature difference between the surface and the fluidized bed ( $\Delta T$  in K).



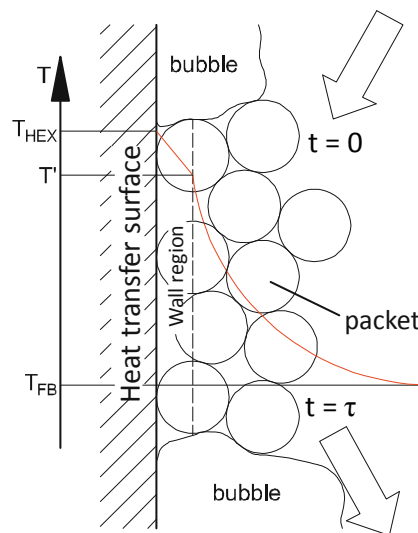
$$\dot{Q} = A \cdot h \cdot \Delta T \quad \text{Eq. 22}$$

Whereas the overall heat transfer coefficient (HTC) can be described as the sum of contributions made by particle convective heat transfer ( $h_{pc}$ ), gas convective heat transfer ( $h_{gc}$ ) and radiative heat transfer ( $h_r$ ), as shown in Eq. 23.

$$h = h_{pc} + h_{gc} + h_r \quad \text{Eq. 23}$$

It should be noted however, that for fluidized beds consisting of small Group B or Group A powders, the gas convective term is small compared to the particle convective term. Additionally, contributions by radiant heat transfer can be neglected at temperatures below 600 °C. [91]

The packet renewal model, proposed by Mickley and Fairbanks [93] and later adapted by Baskakov [94], is a widely accepted model for describing the mechanism of particle convective heat transfer [73]. As shown in Figure 18, a “packet” in the emulsion phase is transported from the bulk bed to the heat transfer surface and stays in contact with the surface for the time ( $\tau$ ). In the moment of contact, the heat transfer rate is at its maximum and decreases over time, as the temperature difference between packet and surface decreases. After the time,  $\tau$ , the packet is swept away from the surface by a gas bubble and is returned to the bulk bed. Whilst the heat transfer surface is in contact with the gas bubble, the heat transfer rate drops considerably. After the bubble passes, a fresh packet takes its place at the heat transfer surface and the cycle begins anew.[76,91]



**Figure 18: Schematic illustration of the packet renewal model proposed by Mickley and Fairbanks (adapted from Schöny [95])**

The rate at which packets are exchanged at the heat transfer surface depends on the bubble frequency and the volumetric fraction of the bubble phase in the fluidized bed. As bubble flow increases, packets are exchanged more frequently, until the gas phase becomes dominant at the heat transfer surface. Therefore, an increase of the heat transfer rate is expected before a reduction occurs due to the

comparably low heat transfer of gas convection. Nevertheless, the instantaneous HTC between an isothermal wall and a packet at the time  $t$  can be defined as shown in Eq. 24. [73,76,91]

$$h_{pt,i} = \left( \frac{k_e \cdot \rho_{mf} \cdot c_{mf}}{\pi \cdot t} \right)^{\frac{1}{2}} = \left( \frac{k_e \cdot \rho_p \cdot c_{p,s} \cdot (1 - \varepsilon_{mf})}{\pi \cdot t} \right)^{\frac{1}{2}} \quad \text{Eq. 24}$$

In Eq. 24,  $k_e$  is the effective thermal conductivity of the emulsion phase,  $\rho_{mf}$  and  $\rho_p$  are the densities of the bed at minimum fluidization condition and of the solids respectively, whereas  $c_{mf}$  and  $c_{p,s}$  are the heat capacity of the bed at minimum fluidization conditions and of the solids respectively. As can be seen in Eq. 24, the solids packet is assumed to have the same packing of the bed at minimum fluidization conditions. Additionally, a contribution of the gas to the packet heat capacity is neglected. Assuming the packet resides at the wall for the period  $\tau$ , the time-averaged HTC can be calculated according to Eq. 25.

$$h_{pt} = \frac{1}{\tau} \int_0^{\tau} h_{pt,i} dt = \left( \frac{k_e \cdot \rho_p \cdot c_{p,s} \cdot (1 - \varepsilon_{mf})}{2 \cdot \pi \cdot \tau} \right)^{\frac{1}{2}} \quad \text{Eq. 25}$$

Assuming that over a prolonged period the volumetric fraction of the emulsion phase ( $1 - \delta_b$ ) and the bubble frequency ( $n_b$ ) remain constant near the heat transfer surface, the residence time of the emulsion phase can be given with Eq. 26.

$$\tau = \frac{1 - \delta_b}{n_b} \quad \text{Eq. 26}$$

Implementing Eq. 26 in Eq. 25 yields Eq. 27.

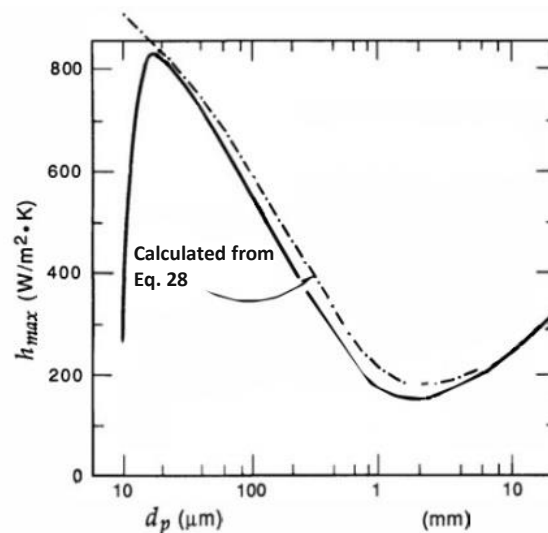
$$h_{pt} = \left( \frac{k_e \cdot \rho_p \cdot c_{p,s} \cdot (1 - \varepsilon_{mf}) \cdot n_b}{2 \cdot \pi \cdot (1 - \delta_b)} \right)^{\frac{1}{2}} \quad \text{Eq. 27}$$

However, in the boundary layer between the heat transfer surface and the main body of the bed, a resistance to heat transfer is encountered, thus the  $h_{pt}$  overestimates the heat transfer brought about by particle convection. As shown in Figure 18, the wall region extends outward from the wall and is half a particle diameter in thickness. With radiative heat transfer ( $h_r$ ), gas convective heat transfer ( $\alpha_w \cdot c_{p,g} \cdot \rho_g \cdot u_0$ ) and heat conduction ( $\frac{2 \cdot k_{e,w}}{d_p}$ ) in the wall region an expression for the heat transfer in the emulsion phase can be given. Together with gas convective and radiative heat transfer in the bubble phase, heat transfer in fluidized beds can be written as shown in Eq. 28.

$$h = \frac{\delta_b}{(h_r + h_g)} + \frac{1 - \delta_b}{\frac{1}{h_r + \frac{2 \cdot k_{e,w}}{d_p} + \alpha_w \cdot c_{p,g} \cdot \rho_g \cdot u_0} + \frac{1}{h_{pt}}} \quad \text{Eq. 28}$$

Here,  $d_p$  represents the particle diameter,  $\alpha_w$  a constant for which a value of 0.05 has shown to yield realistic results and  $u_0$  the gas velocity in the wall region. [73]

As can be seen in Figure 19, Eq. 28 was used to determine the maximum HTC ( $h_{max}$ ) between fluidized beds and surfaces for various particle sizes. A local minimum can be seen at a particle diameter of approx. 2 mm. For larger particles, the gas convective term becomes dominant due to the high gas velocities required for fluidization. The HTC increases when the particle size decreases below 2 mm, since the bubble size decreases and the particle convective term becomes dominant. It can also be seen that Eq. 28 is not suited for determining the HTC between a surface and a fluidized bed consisting of particles smaller than 20  $\mu\text{m}$  (i.e. Geldart Group C powders) due to the cohesive nature of these powders.



**Figure 19: Effect of particle size on the maximum achievable heat transfer coefficient between a fluidized bed and an immersed surface (adapted from Kunii and Levenspiel [73])**

It should be noted that for each gas-particulate system, a specific superficial gas velocity  $U_{opt}$  exists at which  $h_{max}$  can be achieved. At superficial gas velocities above  $U_{opt}$ , particle convection decreases due to an increase of the volumetric fraction of the gas phase in the fluidized bed. For superficial gas velocities below  $U_{opt}$  the residence time of packets at the heat transfer surface increases due to insufficient particle motion. Molerus [96] documented this behavior for three different flow regimes; heat transfer between an immersed surface and a bubbling fluidized bed is represented by curve 2 in Figure 20.

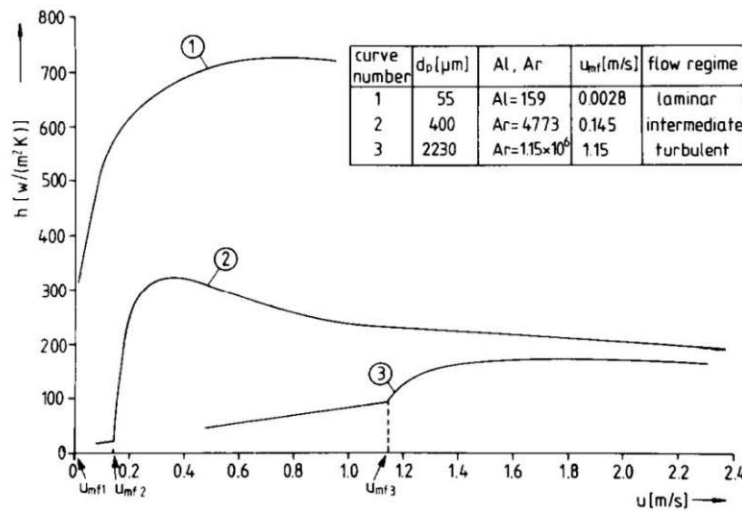


Figure 20: Experimentally determined heat transfer coefficients between fluidized beds of glass beads (behavior bubbling fluidized bed shown curve 2) and an immersed heat transfer surface at varying superficial gas velocities (U) (adapted from Molerus [96])

### 2.3 ENVIRONMENTAL EMISSIONS FROM THE MEA SCRUBBING PROCESS

A wide range of substances with varying toxicity and varying impact on the environment can be emitted from MEA scrubbers. These environmental emissions are typically caused by either degradation of the amine or loss of the utilized amine through the formation of aerosols or evaporation. As the solvent is circulated between the absorber and the stripper, it is subject to different degradation mechanisms. In the low-temperature absorber, reactive gas constituent present in the flue gas, such as  $\text{NO}_x$  or oxygen, are responsible for the formation of degradation products that can be emitted with the  $\text{CO}_2$  depleted flue-gas. Ammonia ( $\text{NH}_3$ ) as well as nitrosamine and nitramines (see general structure in Figure 21) are substances that are formed in such reactions and are of utmost relevance in respect to environmental emissions.

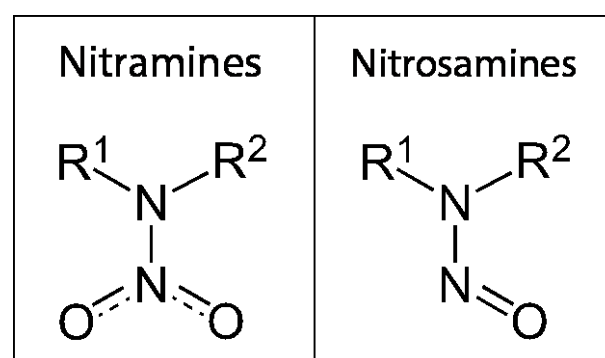


Figure 21: General structure of Nitramines (left) and Nitrosamines (right). R

Although the mechanisms responsible for oxidative degradation of MEA are not well understood, it is known that oxidative degradation often involves the formation of ammonia, organic acids and aldehydes [29,97–100]. The concentration of the formed organic acids and aldehydes in the  $\text{CO}_2$ -depleted flue gas can typically be kept in the ppb-range [101]. Organic acids feature low volatility, thus they accumulate in the liquid phase. The aldehyde concentration in the gas phase is reduced partly

due to oxidation to organic acids and because they can be efficiently removed in the water wash section [101,102]. However,  $\text{NH}_3$  cannot be efficiently removed in the water wash section due to its high volatility and low solubility in the alkaline milieu of the water wash section [103]. Thus, ammonia concentrations of 5-10  $\text{mg}_{\text{NH}_3}\cdot\text{Nm}^{-3}$  (i.e. 7-13  $\text{ppmv}_{\text{NH}_3}$ ) in the  $\text{CO}_2$ -depleted flue gas are considered low for MEA scrubbing units [101,104]. In an effort to reduce these emissions, a number of researchers have proposed additional acid wash scrubbers downstream of the absorber [103,104]. It should be mentioned that cost estimations carried out by Khakharia et al [104] show that such an acid-wash scrubber would increase CAPEX of an aqueous MEA scrubber by approx. 5%.

Currently there is no evidence for the direct emission of nitrosamines or nitramines to the environment via the absorber off-gas. However, due to the highly toxic and possibly carcinogenic nature of these substances, the formation of these substances in amine scrubbing units will be briefly treated herein. In the amine scrubbing process, stable nitrosamines and nitramines are formed in the reaction of  $\text{NO}_x$  (i.e.  $\text{NO}$ ,  $\text{NO}_2$ ,  $\text{N}_2\text{O}_3$ ,  $\text{N}_2\text{O}_4$  or  $\text{HNO}_2$ ) present in the flue gas with a secondary or tertiary amine [99,105]. Although MEA is a primary amine, it was shown by Fostås et al [105] that a mixture of  $\text{NO}$  and  $\text{NO}_2$  can degrade MEA to the secondary amine Dimethanolamine (DEA). In the course of these investigations, it was shown that DEA subsequently nitrosated to the nitrosamine N-nitrosodiethanolamine (NDELA). Nitrosamine formation has also been ascertained in the course of emission tests carried out with a MEA scrubber at pilot scale [101]. Here, nitrosamines with low volatility were found in the solvent and the water used in the water-wash section.

However, nitrosamines can also be formed through photo-oxidation of amines that are emitted from the absorber off-gas [101]. For this reason, it is critical to prevent the emission of amines. Most volatile amines that are formed during the degradation processes (e.g. Methylamine), are mostly absorbed in the water-wash section [101]. However, amines can also be emitted from amine scrubbing processes in the liquid phase in the form of aerosols. It has been shown that both condensed substances present in the flue gas (e.g.  $\text{SO}_3$  [106]) as well as fine sub-micron dust particles can act as condensation nuclei [107]. These nuclei take up the solvent as they travel through the absorber and are emitted in the form of aerosols in large quantities (up to 256  $\text{mg}\cdot\text{Nm}^{-3}$ ) if no suitable counter-measures are in place [108]. The formed aerosols are typically in a size range of 0.04-4  $\mu\text{m}$  and are thus removed neither in standard demisters, which consist of a fine mesh, nor in conventional water-wash sections. Counter-measures such as Brownian Demister Units (BDUs) have shown to reduce aerosol-based MEA emission by 97 %. However, BDUs add a considerable pressure drop (of around 50 mbar) to the flue gas path and thus lead to a considerable increase of the electrical power requirement of the flue-gas fan and consequently to an increase of the operating cost. [27]

## 2.4 POST-COMBUSTION CO<sub>2</sub> CAPTURE BY TEMPERATURE SWING ADSORPTION USING AMINE FUNCTIONALIZED SORBENTS

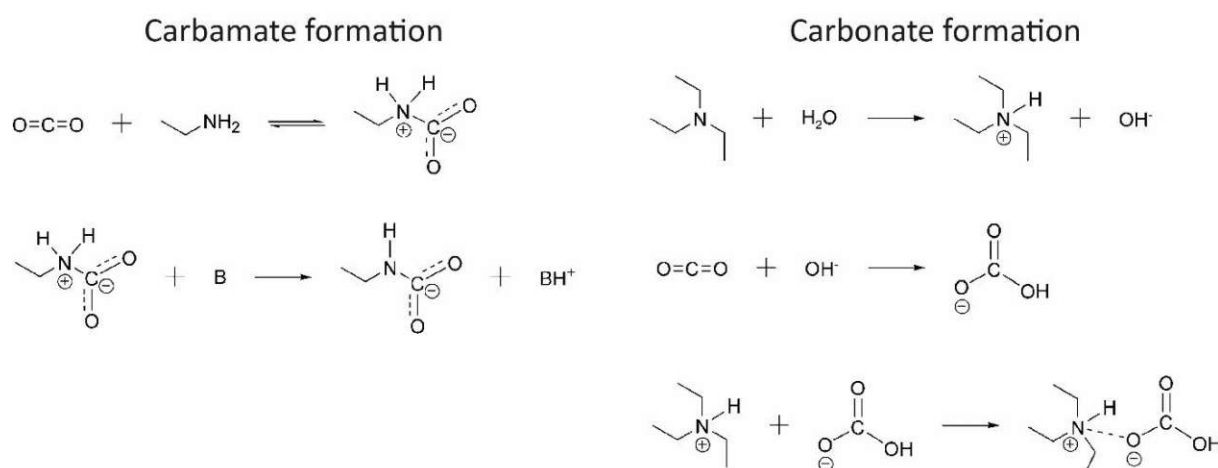
### 2.4.1 Amine functionalized sorbents

The gas separation task for post-combustion CO<sub>2</sub> capture is defined by the separation of CO<sub>2</sub> from a highly diluted gas stream (i.e. a flue gas with a CO<sub>2</sub> concentrations below 15 vol%CO<sub>2</sub>) and the production of a CO<sub>2</sub> stream void of “incondensable” gases (e.g. O<sub>2</sub>, N<sub>2</sub> etc.). Additionally to fulfilling the separation task, the CO<sub>2</sub> capture process must be as energy efficient as possible so that the parasitic load on the CO<sub>2</sub> emitting process is minimalized. For adsorption processes to become competitive compared to the current state-of-the-art, the utilized sorbent must fulfill a number of requirements.

- **High CO<sub>2</sub> selectivity:** Co-adsorption and subsequent desorption of flue-gas constituents such as O<sub>2</sub> and N<sub>2</sub> must be avoided so that the desorbate is not contaminated with these substances. Therefore, the selectivity of the sorbent towards CO<sub>2</sub>, i.e. its CO<sub>2</sub> adsorption capacity compared to the adsorption capacity of other components such as N<sub>2</sub>, must be as high as possible.
- **High CO<sub>2</sub> loadings at low CO<sub>2</sub> partial pressures:** High cycle rates between adsorption and desorption is associated with a high process energy requirement (e.g. a high heat demand in a temperature swing cycle or a high electrical energy demand in a pressure swing cycle). To make low cycle rates possible, high CO<sub>2</sub> loadings of the sorbent must be achieved under adsorption conditions (i.e. at a low CO<sub>2</sub> partial pressure).
- **High adsorption rate:** The adsorption and desorption step must be as fast as possible to reduce the required gas-solids contact time and thus the required adsorber and desorber dimensions.
- **Stability:** To allow prolonged use of the sorbent in the adsorption process, the sorbent must withstand repeated exposure to both adsorption and desorption conditions without degrading. Furthermore, degradation can lead to the formation of emissions, which in turn can make emission reduction measures necessary. In order to minimize sorbent degradation the sorbent must be chemically resistant towards reactive gas components present in the flue gas (i.e. O<sub>2</sub>, and trace components such as SO<sub>2</sub> and NO<sub>x</sub>). Depending on the applied process cycle, additional properties such as the sorbent’s mechanical and thermal stability or the sorbent’s moisture resistance must be assessed.

Chemisorbents have superior selectivity towards CO<sub>2</sub> compared to physisorbents and thus allow the production of a highly pure desorbate. The higher heat of CO<sub>2</sub> adsorption of these sorbents allows for obtaining higher CO<sub>2</sub> loadings at low CO<sub>2</sub> partial pressures compared to physisorbents. Considering these properties, it can be concluded that chemisorbents are in principle well suited for the task of post combustion CO<sub>2</sub> capture. [109–111]

A class of chemisorbents that has been under intense development in the past decades are amine-functionalized sorbents. These sorbents feature amines on their surface, which enable the selective adsorption of CO<sub>2</sub> by the formation of chemical bonds. An amine is a functional group with the general structure R-NH<sub>2</sub> (primary amines), R<sub>2</sub>-NH (secondary amines) or R<sub>3</sub>-N (tertiary amines) [46]. The reactions that takes place between CO<sub>2</sub> and the amine on the surface of the sorbent can be similar to those that occur during CO<sub>2</sub> absorption in amine scrubbing processes. As can be seen in Figure 22, two general reaction mechanism have been proposed for the reaction between CO<sub>2</sub> and amines.



**Figure 22: Carbamate formation (left) and carbonate formation (right) by reaction of CO<sub>2</sub> with amines (adapted from Choi et al. [111])**

In the so-called zwitterion mechanism that is involved in the formation of carbamates. Here, primary and secondary amines react directly with CO<sub>2</sub> to form the zwitterion. The zwitterion undergoes base-catalyzed deprotonation, whereas the base can be represented by H<sub>2</sub>O, OH<sup>-</sup> or other amines. Thus under dry conditions, where H<sub>2</sub>O and OH<sup>-</sup> cannot partake in the deprotonation reaction, the amine efficiency, or stoichiometric N:CO<sub>2</sub> ratio, is 0.5 mol<sub>CO<sub>2</sub></sub>·mol<sub>N</sub><sup>-1</sup>. This is because a second amine is required for the formation of carbamate. It should be noted that the stoichiometric N:CO<sub>2</sub> ratio. Nevertheless, under wet conditions the maximum amine efficiency can double to 1 mol<sub>CO<sub>2</sub></sub>·mol<sub>N</sub><sup>-1</sup>. Tertiary amines cannot form carbamates, but can only form carbonates. It must be mentioned that primary and secondary amines can undergo this reaction as well. Unlike the formation of carbamates, the amine does not react directly with CO<sub>2</sub>, but relies on the presence of water. Water is dissociated, which leads to the protonation of the amine under the formation of an OH<sup>-</sup> ion. Subsequently, OH<sup>-</sup> hydrates CO<sub>2</sub>, which leads to the formation of bicarbonate. In the last step, ionic association of the protonated amine and the carbonate ion takes place. As can be seen, the maximum amine efficiency of the carbonate formation reaction is 1 mol<sub>CO<sub>2</sub></sub>·mol<sub>N</sub><sup>-1</sup>. Whilst the carbamate formation reaction requires a higher activation energy than the carbonate formation reaction, the reaction kinetics of carbamate formation are faster. [109–111]

Although experimental investigations [112–116] have confirmed that moisture present has a beneficial effect on the CO<sub>2</sub> adsorption capacity of amine-functionalized sorbents, the anticipated doubling of the CO<sub>2</sub> adsorption capacity has not been observed.

In order to present a large reaction surface area, highly porous materials act as a support for the amine functional groups. These supports are often mesoporous silica or porous polymers. A distinction is generally made in terms of the bond between the functional group and the supporting material. Amines can either be physically adsorbed on a porous support e.g. by a wet impregnation method, or covalently bound to the surface of a support e.g. by in-situ polymerization or grafting [111].

### **Amine impregnated sorbents**

Amine impregnated sorbents have been extensively investigated by a number of researchers [66,117–123]. Within this sorbent class, sorbents impregnated with aminopolymers, such as polyethyleneimine (PEI), are better suited for practical application compared to sorbents impregnated with alkanolamines

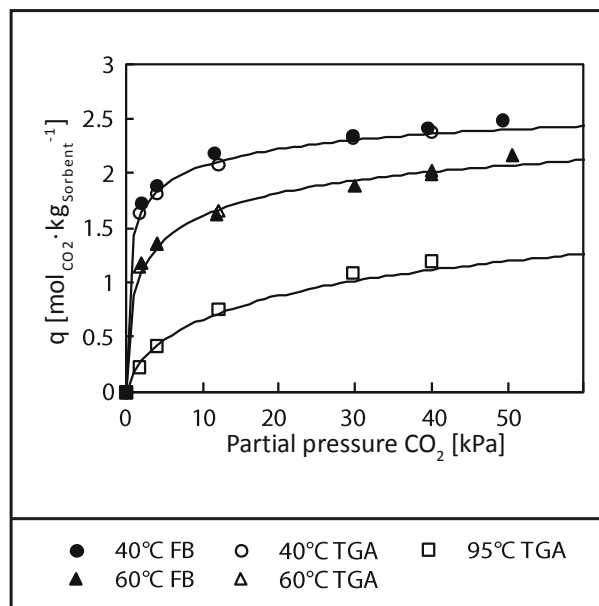
such as diethanolamine or MEA because they are less prone to amine loss through amine evaporation [120]. PEI is available in a linear and a branched form and generally features a high nitrogen content of approx. 33 wt%. Furthermore, the ratio of primary to secondary to tertiary amines is typically assumed equal [111]. Due to the high selectivity towards CO<sub>2</sub> (i.e. >1000 for CO<sub>2</sub>/N<sub>2</sub> and ~180 for CO<sub>2</sub>/O<sub>2</sub> [124]), high CO<sub>2</sub> adsorption capacities, a high tolerance towards water vapor present in the flue gas, and the simple manufacturing method, PEI impregnated silicas are promising candidates for CO<sub>2</sub> capture applications [121,122]. A method for impregnating mesoporous silica with PEI through a wet impregnation process was first introduced by Xu et al. [125] in 2002. Here, PEI is dissolved in methanol and mixed with a porous support. Subsequently, methanol is removed under low pressure and elevated temperature, thus leading to the deposition of PEI in the pore space of the support. Son et al. [66] and Xu et al. [125] both observed higher CO<sub>2</sub> adsorption capacities for PEI impregnated silicas, than for PEI alone, thus indicating a synergetic enhancement of the CO<sub>2</sub> adsorption capacity. Son et al. [66] tested the textural parameters and CO<sub>2</sub> adsorption capacity of PEI impregnated KIT-6 and MCM-41 at various PEI loadings. For both sorbents it was found that the CO<sub>2</sub> adsorption capacity increased with PEI loading and reached its maximum at 50 wt% [66]. This was also the highest amine loading for which the pore volume was still measurable (i.e. above zero), thus indicating that efficient contact of CO<sub>2</sub> and PEI is established when space for gas is left within the pore. At low temperatures, i.e. below 75 °C, the adsorption rate of CO<sub>2</sub> on PEI impregnated sorbents is kinetically limited. This limitation was first observed by Xu et al. [125] for PEI impregnated MCM-41 and later also confirmed for PEI impregnated KIT-6 by Son et al. [66]. Xu et al. [125] hypothesized that at low temperatures, PEI exists in the form of nano-sized particles within the pores of the sorbent. Therefore, CO<sub>2</sub> can only react readily with the amines located on the outer surface of these particles. To react with the majority of amine sites, CO<sub>2</sub> needs to diffuse into the PEI particles, hence limiting the adsorption rate. At higher temperatures, these PEI particles lose structural integrity, thus making all amine sites readily accessible for CO<sub>2</sub> and removing the diffusion-controlled step.

### ***Amine tethered sorbents***

Sorbents with amines covalently bound to the surface of a supporting material are commonly referred to as amine-tethered sorbents. This group can be divided into two classes, whereas one class features an aminosilane group on an oxide support (i.e. Si-O-C bond), whilst the second class features an amine group covalently bound to an organic backbone (i.e. via C-C or C-N bonds) [109,111]. The C-C bond between organic supports and amines possess a higher hydrothermal stability than the Si-O-C bond [126]. Due to this stability, sorbents with a C-C bond to the amine functional group, such as polymeric ion exchange resins with amine functionality, have been investigated for CO<sub>2</sub> capture application by a number of groups [43,44,126,127]. These CO<sub>2</sub> sorbents generally features a lower amine loading than impregnated sorbents, and therefore also a lower CO<sub>2</sub> adsorption capacity [111]. However, Lewatit VP OC 1065, a commercially available resin produced by Lanxess, has shown promising CO<sub>2</sub> adsorption characteristics. Contrary to PEI impregnated sorbents, the macroporous supporting material is cross-linked with divinylbenzene and is functionalized with a benzylamine group (a primary amine) in a Phthalimide addition process [128,129]. Parvazinia et al. [127] compared the CO<sub>2</sub> uptake capacity, as well as adsorption/desorption kinetics of five different ion exchange resins capable of CO<sub>2</sub> adsorption. Amongst the investigated sorbents, Lewatit VP OC 1065 featured the highest CO<sub>2</sub> adsorption capacity as well as fast adsorption and desorption kinetics even at temperatures as low as



25 °C [127]. Sonnleitner et al. [130] measured adsorption isotherms of Lewatit VP OC 1065 at three different temperatures using two different measuring methods. The gained results can be seen Figure 23.



**Figure 23: CO<sub>2</sub> adsorption on Lewatit VP OC 1065 as measured by a fixed bed (FB) method and in TGA at 40 °C, 60 °C and 95 °C at various CO<sub>2</sub> partial pressures (adapted from Sonnleitner et al. [130]).**

### Water co-adsorption

The CO<sub>2</sub> adsorption capacity of amine-functionalized sorbents can be increased significantly when water is present in the gas. As shown in Figure 22, water is involved in base-catalyzed deprotonation of the zwitterion during carbamate formation and enables the formation of carbonates thus increasing the amine efficiency of the CO<sub>2</sub>-amine reaction.

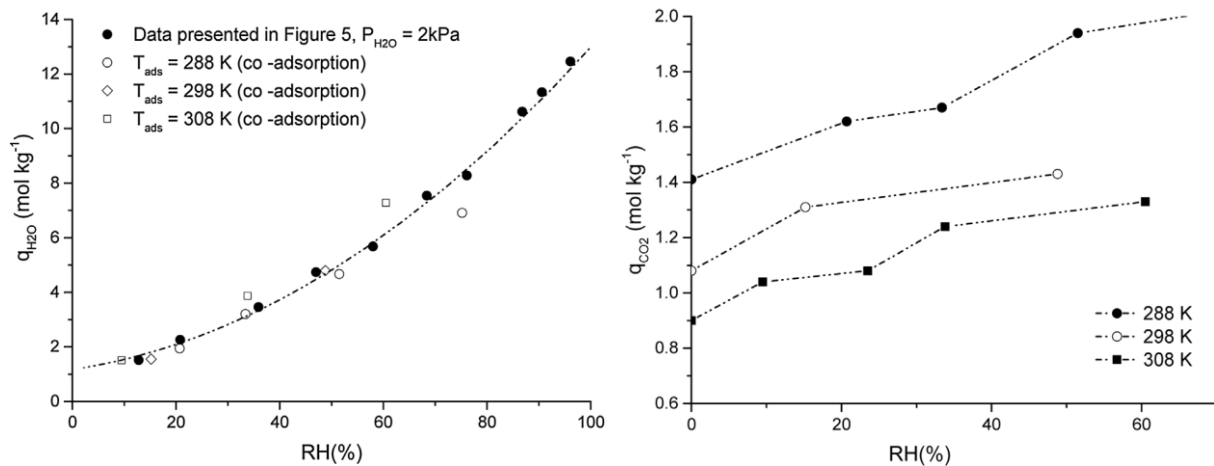
A number of researchers have investigated the impact of water on the CO<sub>2</sub> adsorption capacity of amine-functionalized sorbents. Xu et al. [113] carried out fixed-bed adsorption experiments using a PEI-impregnated MCM-41-type sorbent in which humidified gas mixtures were tested. It was shown that the CO<sub>2</sub> adsorption capacity could be increased by 43.6 % (i.e. from 2.02 mol<sub>CO<sub>2</sub></sub> · kg<sub>sorbent</sub><sup>-1</sup> to 2.90 mol<sub>CO<sub>2</sub></sub> · kg<sub>sorbent</sub><sup>-1</sup>), when the relative humidity of the treated gas increased from zero to 41.5 % albeit a slight decrease of the CO<sub>2</sub> concentration from 14.9 vol%CO<sub>2</sub> to 12.6 vol%CO<sub>2</sub>. By analyzing the amount of adsorbed CO<sub>2</sub> and H<sub>2</sub>O in the course of an adsorption experiment, it could be shown that the beginning of the adsorption process is dominated by the formation of carbamate, despite the presence of water. In the initial 30 minutes, CO<sub>2</sub> was predominantly adsorbed and only little H<sub>2</sub>O. After 30 minutes of adsorption, carbamate began to react with CO<sub>2</sub> and H<sub>2</sub>O to form bicarbonate. Furthermore, after 75 minutes more water was adsorbed than CO<sub>2</sub> from a gas mixture containing 13.6 vol%CO<sub>2</sub> with a relative humidity of 25.7 %. The high water adsorption capacity of impregnated sorbents was also confirmed by Franchi et al. [41] who investigated a diethanolamine (DEA) impregnated pore-expanded MCM-41-type sorbent. Here, a gas mixture containing 5 vol%CO<sub>2</sub> at a relative humidity of 2.3 % was treated. Compared to dry conditions, an enhancement of the CO<sub>2</sub>

adsorption capacity could not be determined. However, the sorbent adsorbed 1.9 times the amount of H<sub>2</sub>O compared to CO<sub>2</sub> i.e.  $5.37 \text{ mol}_{\text{H}_2\text{O}} \cdot \text{kg}_{\text{sorbent}}^{-1}$  compared to  $2.85 \text{ mol}_{\text{CO}_2} \cdot \text{kg}_{\text{sorbent}}^{-1}$ .

Water uptake of Lewatit VP OC 1065, has been extensively investigated by Veneman et al. [114,131]. By means of pore volume distribution measurements it could be determined that the prevailing adsorption mechanism for H<sub>2</sub>O is pore filling at a high relative humidity of 95 %. However, within a relative humidity range of 10 % to 60 %, this adsorption mechanism could not be established. In this humidity range, the amine groups are believed to increase the affinity of the sorbent towards H<sub>2</sub>O because the support material of Lewatit VP OC 1065 alone is hydrophobic and possess a minimal capacity for H<sub>2</sub>O [131].

Similarly to the PEI impregnated sorbents investigated by Xu et al. [113] and Franchi et al. [41], the H<sub>2</sub>O uptake capacity of Lewatit VP OC 1065 was significantly higher than its capacity for CO<sub>2</sub>. Furthermore, a considerable difference between the adsorption enthalpy for CO<sub>2</sub> adsorption (i.e.  $-87 \text{ kJ} \cdot \text{mol}_{\text{CO}_2}^{-1}$ ) and that for H<sub>2</sub>O adsorption (i.e.  $-43 \text{ kJ} \cdot \text{mol}_{\text{H}_2\text{O}}^{-1}$  [131]) was determined. These findings led Veneman et al. to the conclusion that CO<sub>2</sub> and H<sub>2</sub>O do not bind to the sorbent in the same way. Based on the dependency of the water adsorption capacity from the relative humidity, and because the heat of water condensation (i.e.  $-41 \text{ kJ} \cdot \text{mol}_{\text{H}_2\text{O}}^{-1}$  at 100 °C and 1 bar) is similar to the isosteric heat of water adsorption, Veneman et al. [131] suggested that multi-layer adsorption according to the BET-model may be the underlying mechanism for water adsorption. In multi-layer adsorption, the second layer and above, are in the condensed state, thus the heat of adsorption for these layers corresponds to the heat of condensation, whereas the adsorption capacity depends on the relative pressure (i.e. the relative humidity if H<sub>2</sub>O is adsorbed) as shown in Figure 24, left. Veneman et al. [114] also showed that, whilst CO<sub>2</sub> did not interfere with the H<sub>2</sub>O adsorption capacity of Lewatit VP OC 1065, H<sub>2</sub>O present in the treated gas increased the sorbent's CO<sub>2</sub> adsorption capacity in a relative humidity range between 10 % and 60 % (as seen in Figure 24, right). Alesi and Kitchin [126] showed that Lewatit VP OC 1065 readily forms bicarbonate even when CO<sub>2</sub> is adsorbed from a dry gas and water is only available within the sorbent itself. Thus, the observed increase in the CO<sub>2</sub> adsorption capacity, shown in Figure 24 (right), can be attributed to the formation of bicarbonate.

It should be mentioned that the adsorption rate for H<sub>2</sub>O was found to be similarly fast as CO<sub>2</sub> adsorption [114].



**Figure 24: H<sub>2</sub>O adsorption capacity of Lewatit VP OC 1065 at varying relative humidity with and without CO<sub>2</sub> co-adsorption (left), and CO<sub>2</sub> adsorption capacity of Lewatit VP OC 1065 at varying temperatures and relative humidity at p<sub>CO<sub>2</sub></sub>=40 Pa (right)**

### **Degradation of amine functionalized sorbents**

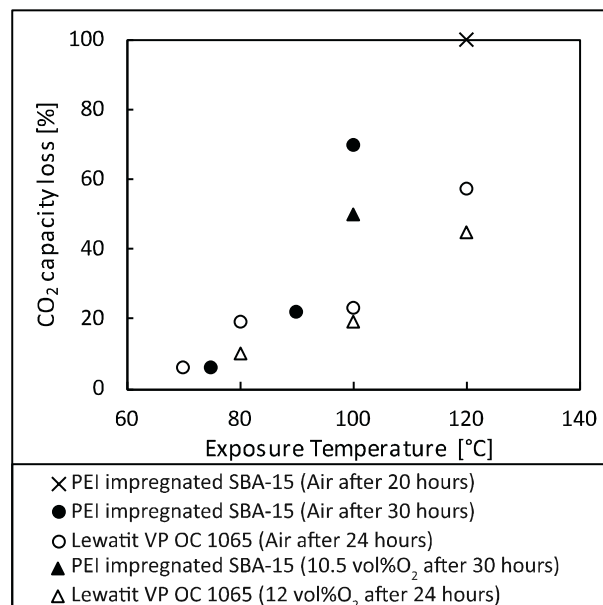
Despite the high CO<sub>2</sub> adsorption capacities that can be achieved by amine-impregnated sorbents, a major drawback is brought about by the rather weak bond between amine and the support compared to amine tethered sorbents. Amine leaching, i.e. a reduction in the amine loading of the sorbent caused by amine evaporation, has been observed in a number of cases [120,122,123]. For PEI impregnated silicas, this effect is particularly pronounced at elevated temperatures (as low as 100 °C [117,122]) and leads to an observable reduction of the CO<sub>2</sub> adsorption capacity after multiple temperatures swing cycles. In amine-tethered sorbents, amine leaching can be widely avoided [126]. Yu et al. [43] tested the thermal stability of Lewatit VP OC 1065 by exposing sorbent samples to N<sub>2</sub> for a prolonged period at various temperatures. It was reported that Lewatit could withstand temperatures of 150 °C, whereas 200 °C lead to an observable loss in CO<sub>2</sub> adsorption capacity after 10 hours.

However, additionally to high temperatures, chemical reactions with gas constituents can also lead to a reduction of the CO<sub>2</sub> adsorption capacity of amine functionalized sorbents.

Sayari and Belmabkhout [132] was the first to link a reduction of the CO<sub>2</sub> adsorption capacity of both polyamine grafted sorbents and PEI impregnated sorbents to the formation of urea. In the course of repeated adsorption-desorption cycles under dry conditions, a severe reduction of the CO<sub>2</sub> adsorption capacity was observed. A Diffuse Reflectance Infrared Fourier Transform Spectroscopy (DRIFTS) analysis revealed that amine sites were converted to urea. Urea is formed either by reaction of CO<sub>2</sub> with the amine under dry conditions or by dehydration of carbamate. In the course of cyclic CO<sub>2</sub> adsorption/desorption cycles under dry conditions, Parvazinia et al. [127] and Yu et al. [43] both reported that Lewatit VP OC 1065 can also degrade via the urea formation mechanism. It should be noted that urea formation is completely inhibited if moisture is present in the gas phase. Furthermore, it has been stated [117,132] that the CO<sub>2</sub> adsorption capacity of sorbents degraded by the urea formation mechanism can be completely regained by prolonged exposure to steam, thus indicating that urea groups can be converted back to amines if the sorbent is treated with steam.

Heydari-Gorji and Sayari [117] and Yu et al. [43] both exposed amine functionalized sorbents to various gas mixtures containing O<sub>2</sub> to investigate the oxidative degradation behavior of PEI impregnated SBA-15 and Lewatit VP OC 1065 respectively. A summary of results gained during these investigations

can be seen in Figure 25. In order to display the harshest realistic case of oxidative degradation, both sorbents were exposed to air for a prolonged period. A CO<sub>2</sub> adsorption capacity loss of approx. 20 % occurred when PEI impregnated SBA-15 was exposed to air for 30 hours at a temperature of 90 °C, whereas for Lewatit VP OC 1065 this capacity loss was seen upon exposure to air for 24 hours at 100 °C. Furthermore, it should be mentioned that PEI impregnated SBA-15 lost its CO<sub>2</sub> adsorbing properties after being exposed to air at a temperature of 120 °C for 20 hours. Lewatit VP OC 1065 only lost approx. 60 % of its CO<sub>2</sub> adsorption capacity after being exposed to the same temperature for 24 hours. At oxygen level typical for flue gases i.e. 10.5 vol%O<sub>2</sub> to 12 vol%O<sub>2</sub>, and a temperature of 100 °C Lewatit VP OC 1065 also showed a higher oxidative stability than PEI impregnated SBA-15. It should be mentioned that Heydari-Gorji and Sayari [117] observed a reduced degradation by oxygen, when CO<sub>2</sub> was present in the atmosphere. This was because CO<sub>2</sub> reacts with the amines at a faster rate than oxygen. Additionally, carbonates and carbamates are also more resistant toward oxidation, thus the underlying amine is protected from oxidation if CO<sub>2</sub> is also present in the gas phase.



**Figure 25: Graph showing CO<sub>2</sub> capacity loss of PEI impregnated SBA-15 (data from Heydari-Gorji and Sayari [117]) and Lewatit VP OC 1065 (data from Yu et al. [43]) after exposure to an atmosphere containing oxygen as a function of the temperature.**

In addition to oxygen and high temperatures, trace impurities present in the flue gas have also shown to cause degradation of amine-functionalized sorbents. Since sulphur dioxide (SO<sub>2</sub>) and nitrogen oxides (NO<sub>x</sub>) are commonly found in flue gases, the effect of these substances on amine functionalized sorbent has been studied by some groups [40,133–135]. Xu et al. [40] investigated the effect of NO<sub>x</sub> (i.e. NO and NO<sub>2</sub>) on MCM-41 impregnated with PEI. After two adsorption/desorption cycles with 60–70 vppmNO<sub>x</sub> in the flue gas, a considerable reduction in the CO<sub>2</sub> adsorption capacity was observed. It was also shown that the affinity of the amine towards NO<sub>x</sub> is significantly higher than towards CO<sub>2</sub> (i.e. a selectivity of NO<sub>x</sub>:CO<sub>2</sub> of 3000 was measured). Additionally, the adsorbed NO<sub>x</sub> was not desorbed in the course of the sorbent regeneration step. Rezaei and Jones [133] investigated the effect of SO<sub>2</sub>, nitrogen monoxide (NO) and nitrogen dioxide (NO<sub>2</sub>) on the CO<sub>2</sub> adsorption capacity of PEI-impregnated silica and three aminosilane-based sorbents in the course of cyclic breakthrough experiments. It was

shown that 200 ppmSO<sub>2</sub> and 10 ppmNO<sub>2</sub> had a negative effect on the CO<sub>2</sub> adsorption capacity after the first adsorption cycle, whilst 200 ppmNO did not affect the investigated sorbents. It should be mentioned that all investigated sorbents showed similar behavior when exposed to these flue gas contaminants. The degrading effect of SO<sub>2</sub> on PEI impregnated silica was recently confirmed by Nelson et al. [134]. Here a reduction of the CO<sub>2</sub> adsorption capacity by 30 % was observed after 100 adsorption/desorption cycles with 100 ppmSO<sub>2</sub> in the treated flue gas. Hallenbeck and Kitchin [135] carried out cyclic adsorption/desorption tests with Lewatit VP OC 1065. Adsorption was carried out at 50 °C with a flue gas comprising 12.5 vol%CO<sub>2</sub>, 4 vol%O<sub>2</sub> and 431 vppmSO<sub>2</sub> in N<sub>2</sub>. Desorption was carried out at 127 °C under nitrogen. A significant reduction of the CO<sub>2</sub> adsorption capacity was observed within the initial six cycles and no SO<sub>2</sub> was detected at the outlet of the reactor. After becoming saturated with SO<sub>2</sub>, the CO<sub>2</sub> adsorption capacity settles at 13% of its original value (i.e. 0.2 mol<sub>CO<sub>2</sub></sub>·g<sub>Sorbent</sub><sup>-1</sup>). It is notable that Hallenbeck and Kitchin [135] attempted to reclaim the degraded amines by treating the sorbent with 1.5 M NaOH solution. One third of the CO<sub>2</sub> adsorption capacity could be recovered by the proposed method.

#### 2.4.2 Requirements for efficient TSA and proposed process configurations

A temperature swing adsorption (TSA) cycle is well suited for CO<sub>2</sub> capture process that implement amine-functionalized sorbents. This is because the CO<sub>2</sub> adsorption capacity of these sorbents is highly dependent on temperature. In order to be energy efficient, temperature swing adsorption units need to be operated in a continuous manner rather than in batch mode. In batch mode, the reactor vessel needs to be cooled and heated between each adsorption and desorption step, which adds a significant parasitic cooling and heating demand to the process respectively. In continuous TSA, two vessels are required; the adsorber is operated at adsorption temperature ( $T_{ADS}$ ) and the desorber is operated at regeneration temperature ( $T_{DES}$ ) whereas the sorbent is circulated between these vessels.

Transfer of heat and mass need to be carried out in an efficient manner so that the unit size can be small and construction cost can be low. Therefore, a reactor system needs to be implemented, which allows both high heat transfer rates and high mass transfer rates. Fluidized beds are known for exhibiting both these features. As shown in Table 4, a number of researchers [35,44,136–139] have proposed fluidized beds as the gas-solids contacting regime in the adsorber and desorber of TSA processes for CO<sub>2</sub> capture.



As can be seen in Table 4, Veneman et al. [136], Zhao et al. [137] and Breault et al. [138] reported performance data of TSA bench scale units, each with a similar design. In these units, the adsorber is designed as a bubbling fluidized bed reactor followed by a pneumatic transport riser. The cross-section of the adsorber decreases in the freeboard of the bubbling fluidized bed, so that particles are continuously entrained into the pneumatic transport riser. Solids are subsequently transported to the desorber via a setup comprising a cyclone and either a loop-seal or a dipleg. The desorber is designed as a bubbling fluidized bed, which is fluidized with  $N_2$ . The authors note that in practical application,  $N_2$  would be replaced by either  $CO_2$  or stripping steam so that a pure  $CO_2$  product can be gained either directly from the desorber or after steam condensation. In Table 4, it can be seen that these groups reported capture efficiencies between 61 % up to 98.5 % and working capacities between 1.8 wt% and 3.5 wt%.

In bubbling fluidized beds the solids can be considered ideally mixed [140]. Although solids mixing is necessary to achieve efficient heat and mass transfer, it brings about a thermodynamic limitation in adsorption processes. Due to ideal mixing, the  $CO_2$  loading of the sorbent within a fluidized bed is at best in equilibrium with the gas exiting the fluidized bed. A similar behavior is also seen in systems where a co-current gas-solids contacting regime is prevalent, e.g. in pneumatic transport risers. Here, the  $CO_2$  loading of the sorbent at the outlet is at best in equilibrium with the gas at the outlet. To illustrate the impact of this effect on the achievable working capacity of the sorbent, exemplary process conditions are schematically plotted on two  $CO_2$  adsorption isotherms in Figure 26. To achieve high capture efficiencies, the  $CO_2$  partial pressure of the  $CO_2$  depleted flue gas ( $p_{ADS,out}$ ) must be low. As shown in Figure 26, the  $CO_2$  loading of the sorbent at the adsorber outlet ( $q_{ADS,out}$ ) is at best in equilibrium with the low  $CO_2$  partial pressure at the adsorber outlet ( $p_{ADS,out}$ ). Furthermore, to achieve the low  $CO_2$  loadings of the sorbent at the inlet of the adsorber ( $q_{ADS,in} = q_{DES,out}$ ), the  $CO_2$  partial pressure at the outlet of the desorber ( $p_{DES,out}$ ) must either be low or the operating temperature of the desorber ( $T_{DES}$ ) must be particularly high. To decrease  $p_{DES,out}$ , the stripping steam flow rate must be high to sufficiently dilute the released  $CO_2$ , whereas an increase in  $T_{DES}$  leads to an increase of the sensible energy demand of the process, and a higher risk of thermal degradation of the utilized sorbent. In such systems, the upper limit of the working capacity ( $\Delta q$ ) is inherently low for high capture efficiencies. It should be noted that  $\Delta q$  is significantly lower than the theoretical maximum ( $\Delta q_\infty$ ) i.e. the working capacity of the sorbent if it were in equilibrium with the adsorber inlet  $CO_2$  partial pressure ( $p_{ADS,in}$ ).

In an ideal adsorber, the sorbent equilibrates with the  $CO_2$  concentration of the flue gas, in which case the ideal working capacity ( $\Delta q_\infty$  as seen in Figure 26 & Figure 27) is reached. However, to allow the sorbent loading to increase above  $q_{ADS,out}$ , as shown in Figure 26, a counter-current contacting regime must be implemented. In a counter-current contactor, the sorbent loading at the outlet of the contactor is no longer in equilibrium with the partial pressure of the gas at the outlet. In this way, the aforementioned thermodynamic limitation can be overcome. As can be seen in the exemplary TSA system shown in Figure 27, the adsorber and desorber are each composed of five interconnected ideally mixed reactors, where solids flows from top-to-bottom whilst the gas flows from bottom-to-top. The adsorption isotherms show that only the top-most adsorber stage (ADS-St5) is in equilibrium with the  $CO_2$  concentration of the  $CO_2$  depleted flue gas, whilst the  $CO_2$  loading of the sorbent contained in the stages below increases successively. It should be mentioned that in such multi-stage

systems, the ideal working capacity ( $\Delta q_{\infty}$ ) can only be reached when an infinite number of stages is implemented.

As can be seen in Figure 27, a counter-current flow regime in the adsorber enables higher CO<sub>2</sub> loadings of the sorbent at the outlet and can thus enable higher working capacities. When a purge gas is used in the desorber, implementing a counter-current gas-solids flow regime can reduce the purge gas demand (i.e. lower OPEX) and thus enable higher partial pressures of the adsorptive at its outlet.

Due to the mentioned advantages of counter-current contacting regimes, a number of researchers [35,44,139,141] have started developing fluidized bed systems that allow counter-current contact of gas and solids in at least one of the two contacting vessels of the TSA process. Krutka et al. [44], Nelson et al. [139] and Pröll et al. [141] have proposed reactor designs in which multiple stationary fluidized beds are stacked vertically. Here downcomers are used to facilitate solids transport from top-to-bottom. The flue gas is fed to the adsorber at the bottom and flows in an upward direction through the adsorber, thus acting as a fluidizing agent for the multi-stage fluidized bed column.

As can be seen in Table 4, Krutka et al. [44] investigated a process design consisting of a 3-stage bubbling fluidized bed column and a single fluidized bed reactor, which were used as an adsorber and a desorber respectively. This design utilizes CO<sub>2</sub> as a fluidizing agent in the desorber, thus the sorbent loading can only be influenced by the desorber operating temperature and the absolute pressure. For this reason, there is no advantage of implementing a counter-current contacting regime in the desorber.

Nelson et al. [139] are developing a TSA system at pilot scale, which consists of a 3-stage fluidized bed adsorber and a 3-stage fluidized bed desorber, which utilizes steam as a stripping agent. At bench scale, this group used a moving bed reactor without a sweep gas as a desorber and reported a capture efficiency of 90 %.

Veneman et al. [35] investigated a TSA system in which a gas-solids trickle flow column is used as an adsorber and a desorber that is designed as a 5-stage fluidized bed column. Here, solids are introduced at the top of the adsorber and trickle through the vessel from top-to-bottom, whilst the flue gas flows from bottom-to-top. Furthermore, the adsorber is filled with a packing to increase the residence time of the sorbent. Once in the desorber column, the CO<sub>2</sub>-loaded sorbent is heated to the desorber operating temperature by immersed bed heat exchangers, whilst stripping steam is used to reduce the CO<sub>2</sub> partial pressure and thus promote CO<sub>2</sub> desorption. Although this unit was able to treat flue gas at a high superficial gas velocity in the adsorber i.e. up to 1 m·s<sup>-1</sup>, the achieved working capacity of 1.1 wt% and 2.3 wt% are rather low for a system that implements a counter-current gas-solids contacting regime in the adsorber.

The TSA process investigated in this work is based on a design introduced by Pröll et al. [141]. Here, the adsorber and the desorber are each designed as a five-stage fluidized bed column and the respective fluidization gases are fed to the columns below the bottom-most stage. As the gas moves upward through the column, it fluidizes each fluidized bed stage. The net solids transport direction in each column is downward, whereas solids transport from stage to stage is facilitated by downcomers. The regenerated (or lean) sorbent material enters the adsorber at the top. Because the partial pressure of CO<sub>2</sub> increases from stage to stage, the sorbent is gradually loaded with CO<sub>2</sub> as it moves downward through the adsorber. The loaded (or rich) sorbent is subsequently transported to the top-most stage



of the desorber. The desorber column is operated at an elevated temperature level, whereas, similarly to the reactor systems proposed by Veneman et al. [35] and Nelson et al. [139], stripping steam is used to promote sorbent regeneration. Since stripping steam is introduced at the bottom of the desorber, the CO<sub>2</sub> partial pressure decreases from top-to-bottom thus the sorbent is gradually regenerated as it moves downward through the desorber. The regenerated sorbent is then returned to the top-most adsorber stage.

A bench scale unit based on this design has shown to enable high CO<sub>2</sub> capture efficiencies of over 95 % whilst allowing working capacities in the range of 8.5 wt% in continuous prolonged operation as shown in Section 4.4 of this work. This unit is used for experimental investigations in this work and will be presented in the next chapter.

## 3. EXPERIMENTAL SETUP & METHODS

### 3.1 BENCH SCALE UNIT

As shown in Figure 28, the TSA bench scale unit (BSU) consists of four major segments, two multi-stage fluidized bed (FB) columns operated in the bubbling fluidized bed regime and two sorbent transport loops. The process setup detailed in the following was used to conduct all experimental investigations presented in this work.

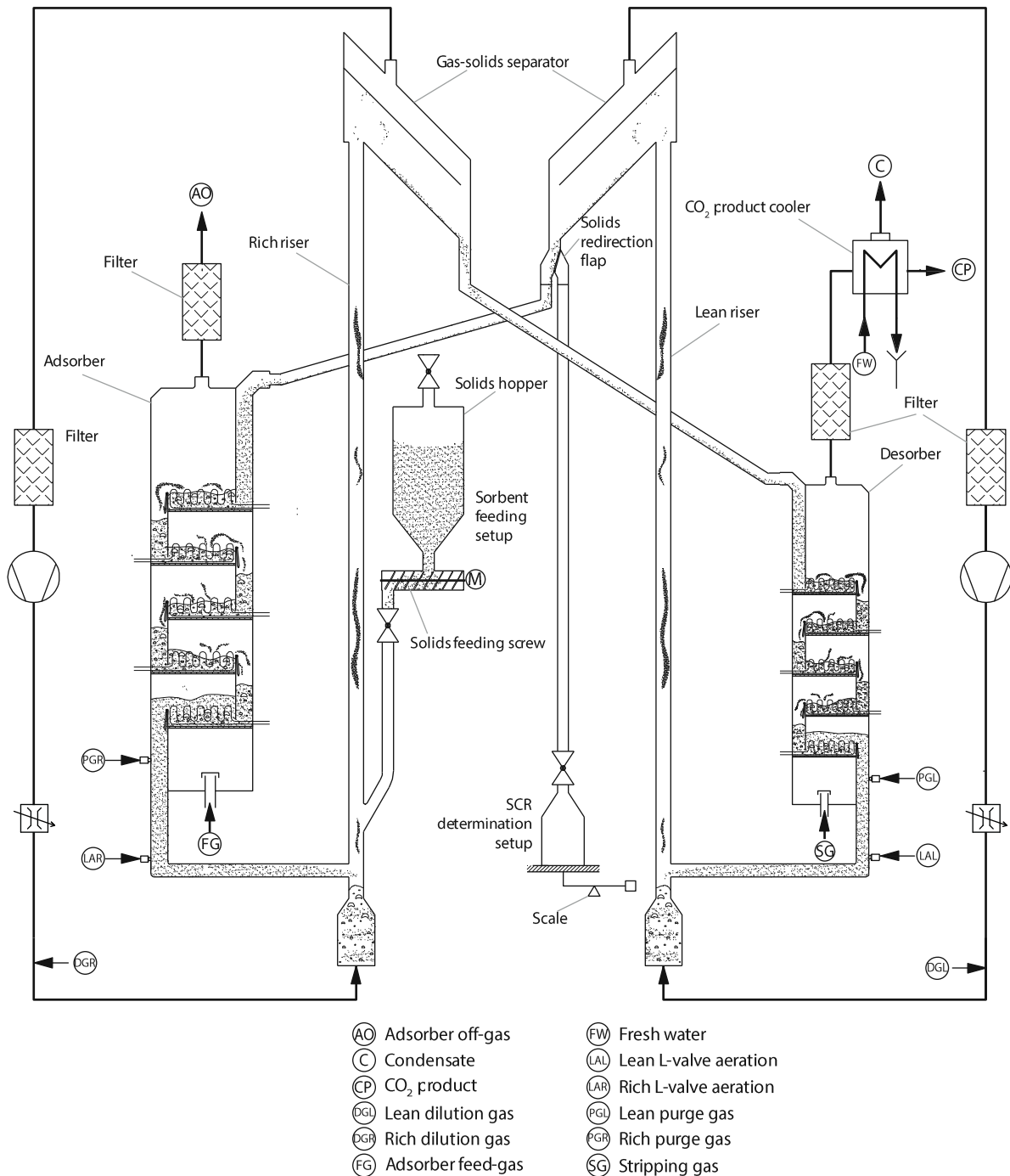


Figure 28: Schematic illustration of the TSA BSU (adapted from Dietrich et al. [142])

As can be seen in Figure 28, flue gas is used as a fluidizing agent in the adsorber. Once it has passed through all five fluidized bed stages, the CO<sub>2</sub> depleted flue gas exits the adsorber and passes through a filter before it is vented. The CO<sub>2</sub>-rich sorbent material exits the adsorber at the bottom through the so-called rich transport loop. This transport loop consists of an L-valve located at the bottom of a standpipe, a pneumatic transport riser, a gravitational gas-solids separator and a recycle gas blower. The L-valve is used to control the flow of sorbent from the standpipe into the pneumatic transport riser. Here, the CO<sub>2</sub> loaded sorbent is lifted into the gravitational gas-solids separator and subsequently enters the top-most desorber stage. Lean sorbent transport from the desorber back to the adsorber is enabled by the second (i.e. the lean) solids transport loop, which is identical to the rich transport loop. The desorber off-gas enters the CO<sub>2</sub> product cooler after passing a heated filter. This is done to reduce the dew point of the CO<sub>2</sub> product. As indicated in Figure 28, each fluidized bed stage is equipped with a gas distributor, a heat exchanger and a weir. These subsystems will be described in detail in the following sections.

The so-called “sorbent feeding setup” (seen in Figure 28) is used to feed fresh sorbent to the system via the rich riser. This setup consists of two ball valves, used to isolate the setup towards ambient and towards the riser, a sorbent hopper, a sorbent feeding screw and an electrical motor to drive the screw. Furthermore, a “SCR determination” setup consisting of a sorbent redirection flap, a ball valve, a container and a balance is used to determine the solids circulation rate (SCR).

All relevant dimensions of the TSA BSU columns together with the total column height of the adsorber and the desorber are shown in Table 5. Figure 29 shows a perspective view of the TSA BSU without the riser gas recycle lines.

It should be mentioned that for the sake of simplicity, the FB stages are henceforth referred to in numerical order from bottom to top. The top-most stage will therefore be referred to as “Stage 5” whereas the bottom-most stage will be referred to as “Stage 1”.

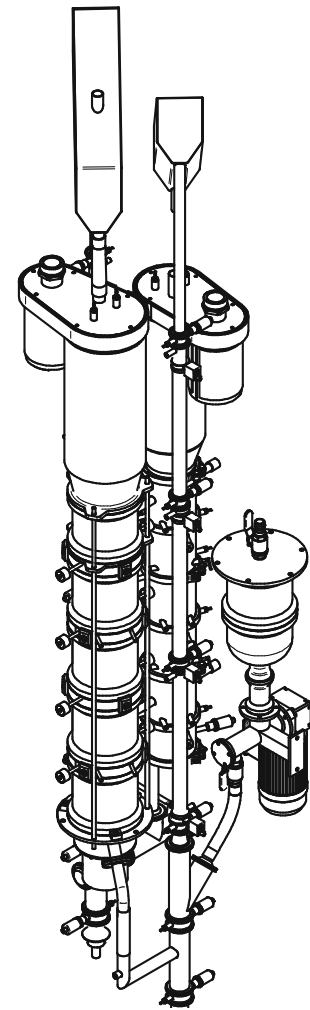


Figure 29: Isometric view of the TSA BSU (riser gas recycle lines not including)

	Adsorber	Desorber	
Stage height ( $H_{Stage}$ )	0.21	0.11	[m]
Weir height ( $H_{Weir}$ )	0.08	0.08	[m]
Column diameter ( $d_{col}$ )	0.15	0.11	[m]
Total column height	1.74	1.44	[m]
Gas distributor area ( $A_{distr}$ )	15727	8458	[mm <sup>2</sup> ]
Relative downcomer area ( $A_{DC}/A_{col}$ )	11	11	[%]

Table 5: Dimensioning of the fluidized bed columns in the TSA BSU

### 3.1.1 Downcomer design

Figure 30 shows two exemplary FB stages within a multi-stage FB column. Whilst the weirs can be exchanged to adapt the fluidized bed height, all experimental investigations in this work were carried out with a weir height of 80 mm in all fluidized bed stages. Nevertheless, weir also serves as a separation between the fluidized bed zone and the downcomer. In operation, the downcomer is continuously fed with sorbent material from the FB by bursting bubbles that catapult solids over the weir. The downcomers are located inside the column rather than located externally. The advantage of this setup is that no additional control measures nor additional aeration gases are required to promote downward-bound solids to enter the FB because the gas distributor can be designed in a way that allows a flow of gas into the downcomer section. However, only a small portion of the heat exchangers extends into the downcomer section thus the material within cannot efficiently partake in the exothermal  $\text{CO}_2$  adsorption or endothermal  $\text{CO}_2$  desorption process. Furthermore, at the small scale of the TSA BSU, a rather large share of the entire column cross-section (i.e. two times 11 %) needed to be attributed to the downcomers to allow high solids throughput. Due to the rather large downcomer cross-section, it is possible that a portion of the fluidization gas bypasses the fluidized bed in which the immersed bed heat exchangers are located. More detail on the design of downcomer in multi-stage fluidized bed columns can be found elsewhere [143].

Not shown in Figure 30 are metal flaps installed in the downcomer section at the height of the gas distributors. These flaps prevent the flow of solids through the downcomer when in a horizontal position and significantly reduce the flow of gas through the downcomer. In the vertical position, solids and gas can flow freely through the downcomer. These flaps are essential for the startup procedure, which is detailed in Section 3.3.1.

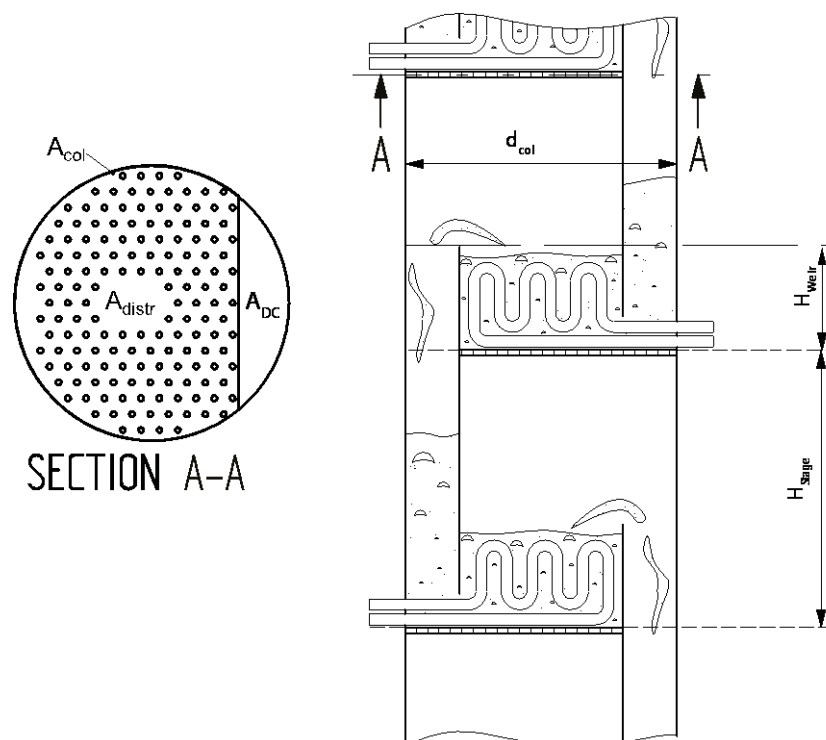


Figure 30: Schematic illustration showing a section of two FB stages in the multi-stage FB column and a cross section of a gas distributor (adapted from Schöny [95])

### 3.1.2 Gas distribution

The perforated-plate-type gas distributors of stages 2-5 are identical within a particular column. As seen in Figure 31, both designs feature a triangular pitch and a perforation diameter of 3 mm in the adsorber and the desorber. It should be mentioned that the perforation diameter is significantly larger than size of particles used in the TSA BSU, thus the sorbent material trickles through the gas distributor and accumulates in the stage 1 of the columns when gas flow to the columns is stopped. Hydrodynamic properties of the utilized sorbent materials are shown in Section 3.4.

In the commissioning phase of the TSA BSU, large bubbles or even slugs in the downcomers of the desorber prevented continuous solids transport at the design operating conditions. To reduce the amount of gas that is allowed to enter the downcomer section, perforation of the gas distributor were closed in the downcomer section (see Figure 31, right), which led to a significant improvement in the solids transport behavior.

Figure 28 also shows the so-called “windboxes” installed below stage 1 of each column. Windboxes were implemented to ensure homogenous distribution of gas across the entire cross-section of the column. In order to prevent sorbent material from entering the windbox, a sintered-filter-type gas distributor was installed in stage 1 of each column.

Graphs showing the measured bed pressure drop of the each fluidized bed stage of the adsorber and the desorber with closed downcomer flaps as a function of the superficial gas velocity are shown in the appendix of this work (see Figure 63 and Figure 64).

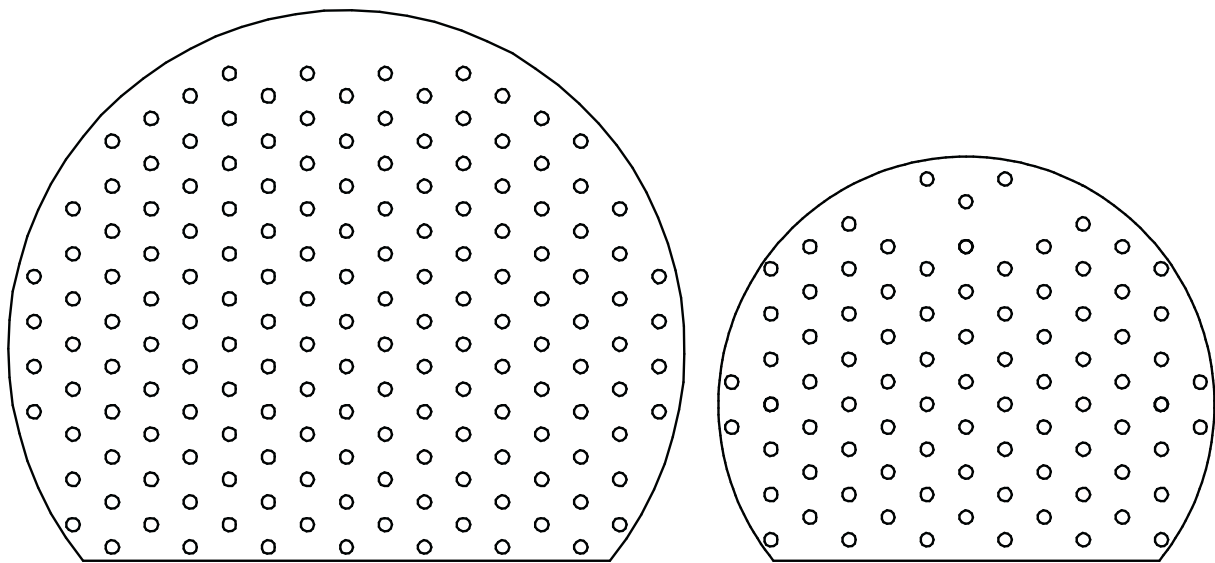
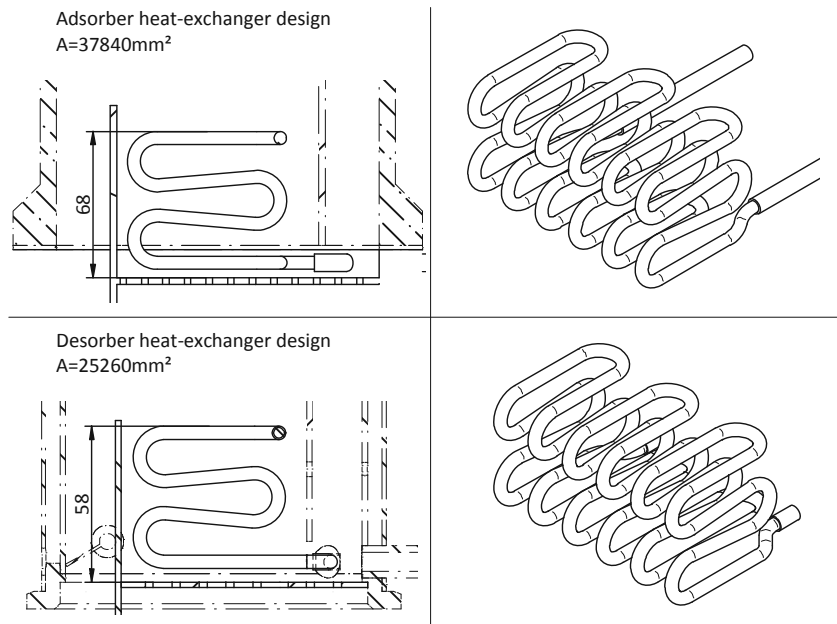


Figure 31: Gas distributor designs of stages 2 to 4 used in the adsorber (left) and the desorber (right) columns.

### 3.1.3 Heat exchange

As indicated in Figure 30, each stage is equipped with an immersed bed heat exchanger, the design of which was improved within the initial months after commissioning of the TSA BSU. The new design of the immersed bed heat exchangers provided as much heat transfer surface as feasible at the given scale. A more detailed view of the immersed bed heat exchangers can be seen in Figure 32.



**Figure 32: Technical drawing showing the design of the immersed bed heat exchangers in a longitudinal section of an adsorber (top left) and desorber (bottom left) stage. On the right perspective views of the respective heat-exchangers are shown (adapted from Schöny [95]).**

The technical drawing shows that the design of the adsorber and desorber heat exchangers is similar. All heat exchangers are made of copper pipes with an outer diameter of 4 mm. Heat transfer fluids flow through the heat exchanger coils to cool and heat the fluidized beds in the adsorber and desorber respectively. In the adsorber, a 30% glycol-water mixture is used as a cooling medium, and will henceforth be referred to simply as cooling water. “Texatherm HT22”, a thermal oil supplied by Texaco, is used to heat the desorber. The most important properties of the utilized heat transfer fluids can be seen in Table 6.

	Cooling water	Thermal oil	
Operating temperature	30	110	[°C]
Density (at operating temperature)	1032	817	[kg·m <sup>-3</sup> ]
Heat capacity (at operating temperature)	3.66	2.29	[kJ·kg <sup>-1</sup> ·K <sup>-1</sup> ]

**Table 6: Density and heat capacity of the utilized heat transfer media used in the TSA BSU at typical operating temperatures.**

Due to the larger dimensions of the adsorber compared to the desorber, the bed volume per stage is significantly larger as well. Therefore, a heat exchanger with a higher surface area could be installed in the fluidized bed stages of the adsorber i.e.  $37840\text{ mm}^2$  per adsorber stage compared to  $25260\text{ mm}^2$  per desorber stage. The section of the desorber stage (seen in the bottom left of Figure 32) shows that the desorber features a double wall, which can also be heated using thermal oil. However, only a small part of the reactor wall, i.e.  $885\text{ mm}^2$  per stage, can participate in particle convective heat transfer and thus exhibits a similarly high HTC as the immersed bed heat exchangers. High heat losses to the environment are an inherent weakness of reactors at this scale due to the high surface-area-to-volume ratio. Therefore, the primary goal of the heated reactor walls is to minimize the risk of condensation when steam is used as a stripping gas. In the adsorber, where the heat of  $\text{CO}_2$  adsorption is released,

heat losses via the uninsulated borosilicate walls reduce the required cooling duty via the heat exchangers.

### **3.1.4 Freeboards**

The technical drawings of the multi-stage FB columns of the TSA BSU in Figure 33 shows that the design of the freeboards of the top-most fluidized bed stages feature a different design than the freeboards of stages 1-4. The chosen design serves the primary purpose of minimizing unwanted entrainment of bed material. This is achieved by two measures. Firstly, the diameter of the freeboard section is increased from 150 mm and 110 mm to 190 mm and 160 mm in top stages of the adsorber and desorber respectively. Secondly, the freeboard of the top stages of each column is 550 mm in height and thus 2.6 and 5 times higher than the height of stages 1-4 in the adsorber and desorber respectively. To allow the evaluation of entrained fines produced by e.g. attrition of the sorbent material, the canister filters installed at the outlet of the columns can be easily removed and weighed.

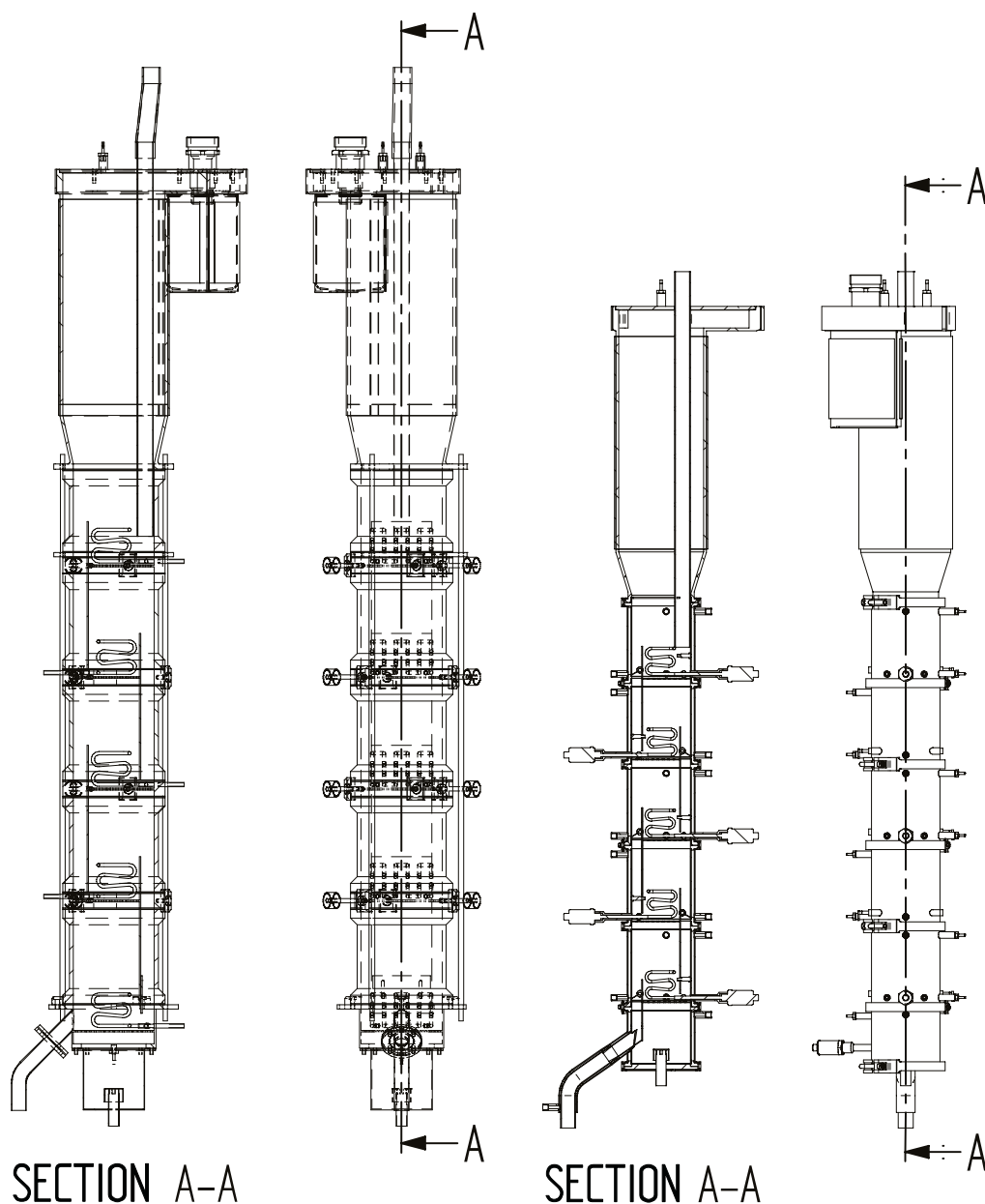


Figure 33: Technical drawings showing the design of the adsorber (left) and desorber (right) column of the TSA BSU

### 3.1.5 Solids transport section

The solids transport sections consist of an L-valve, a pneumatic transport riser as well as a blower and a 10- $\mu\text{m}$  canister filter installed in the gas recycle line. Solids exit the column and enter a standpipe, at the bottom of which a L-valve is located. To enable controlled flow of sorbent material into the bottom section of the riser, nitrogen is injected as an aeration gas (seen as an encircled “LAL” or “LAR” in Figure 28). A recycled gas is used as a fluidizing agent in the risers to lift the sorbent into the gas-solids separator. Whilst the sorbent exits the gas-solids separator through a downcomer, the gas exits the gas-solids separator at the top. Subsequently the gas is passed through a canister filter before it is returned to the blower. It should be noted that the composition of the recycle gas is determined by the slip of gas from the columns and by adsorption or desorption of gas. In order to have the means to control the gas composition in the riser loops, a nozzle was installed through which so called “dilution



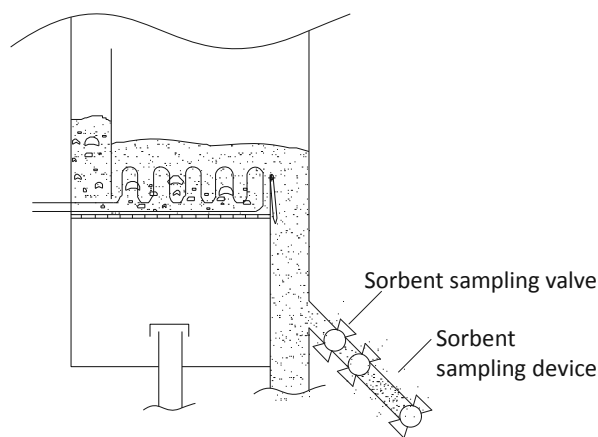
gas” (seen as an encircled “DGL” or “DGR” in Figure 28), i.e. nitrogen, can be injected. Especially for operating conditions where the recycle gas is humid, injection of nitrogen as a dilution gas in the riser loops can prevent condensation on cold spots. It should also be noted that the flow rate of gas that slips from the riser loops into the columns depends on the slip of gas from the L-valves section into the riser, the flow rate of dilution gas into the riser and the amount of gas that is desorbed from the sorbent in the riser. As indicated in Figure 28, the design of both solids transport sections were identical. The most significant dimensions of selected components in the solids transport sections can be seen in Table 7.

Inner diameter riser	25	[mm]
Riser height	2.16	[m]
Inner diameter L-valve	12	[mm]
L-valve horizontal length	190	[mm]
Desorber standpipe height	400	[mm]
Adsorber standpipe height	370	[mm]

**Table 7: Dimensions of main components of the solids transport section**

### 3.1.6 Sampling

For the investigation of sorbent degradation and process emissions, it is essential to be able to sample sorbent material as well as individual gas streams from the BSU that are vented or drained from a TSA unit in real application. To enable sampling of rich and lean sorbent material, sorbent sampling valves are located in the standpipe below the adsorber and desorber respectively. Special sorbent sampling devices, shown in Figure 34, have been designed.



**Figure 34: Schematic illustration of the sorbent sampling device**

These sorbent sampling devices allow for sampling of the sorbent together with the atmosphere present in the standpipe, thereby preserving the CO<sub>2</sub> loading of the sorbent. It should be mentioned that the dead volume in the leg between moving bed and sorbent sampling valve is discarded, so that representative sorbent samples can be obtained. This is part of the sorbent sampling procedure, which will be briefly described in the following. At the beginning of the sorbent sampling procedure, the

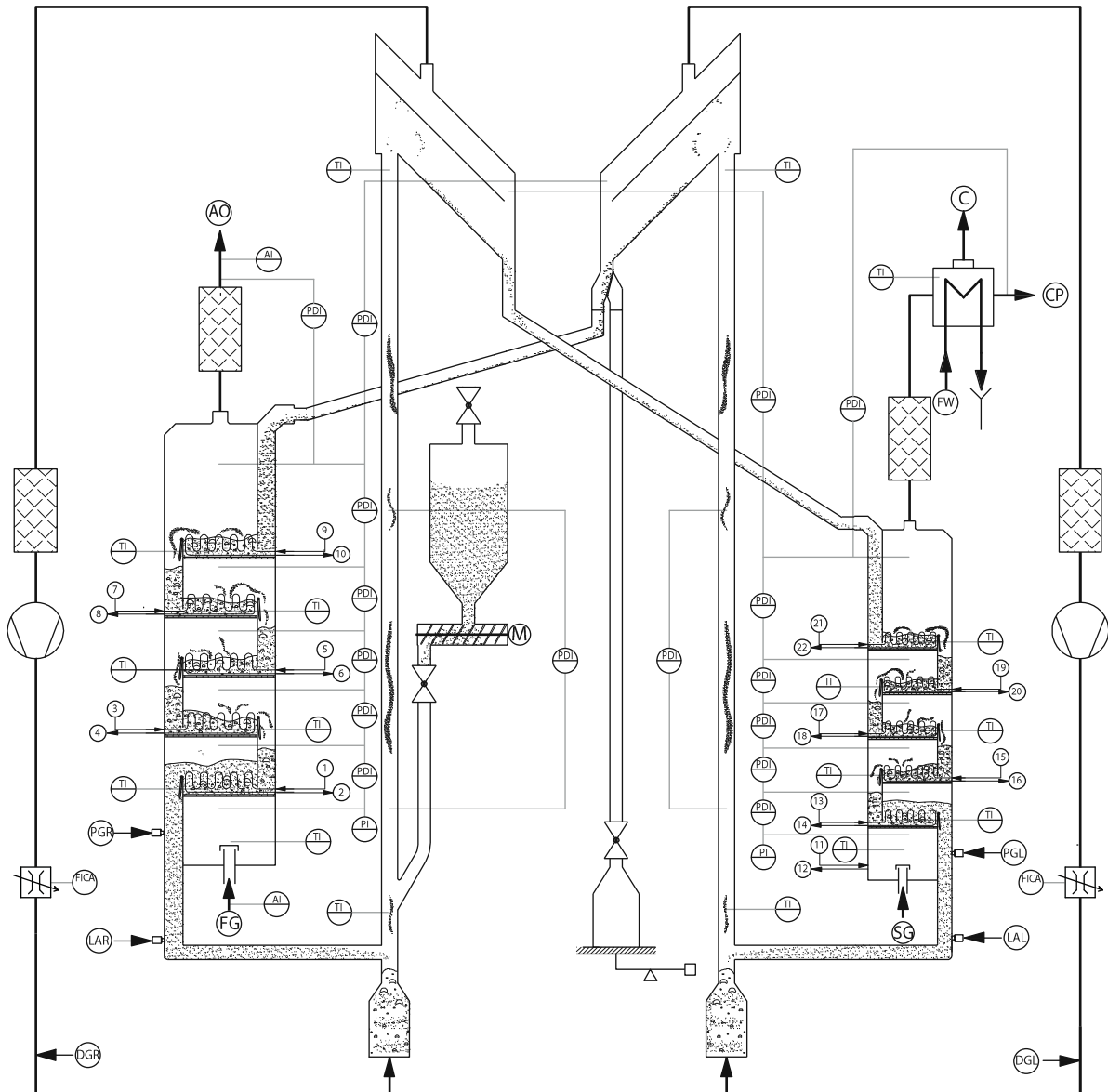
sampling device is installed and a collection cup placed below the sampling device so that discarded sorbent material can be collected. The valves are subsequently opened from top-to-bottom, so that sorbent flows from the moving bed through the sorbent sampling device into the sorbent collection cup. After a few seconds, i.e. the time it takes to flush the dead volume with sorbent material from the process, the valves are closed from bottom to top. The sorbent sampling device can then be disconnected.

Nozzles installed downstream of the adsorber off-gas filter and downstream of the CO<sub>2</sub> product cooler make sampling of adsorber off-gas and CO<sub>2</sub> product possible. It should be noted that the locations of the nozzles were chosen in a way that neither dust nor mist should be expected in the gas sample hence it is not necessary to follow isokinetic sampling methods when extracting the gas sample. Apart from the adsorber off-gas, the condensate formed in the CO<sub>2</sub> cooler is of special interest for emission investigations and can be sampled in via a nozzle located in the condensate drain line.

## 3.2 INSTRUMENTATION

### 3.2.1 Pressure measurement

All pressure measurements throughout the BSU are made using Kalinsky DS2-420-type pressure transducers with a measuring accuracy of 1 % of full scale. Whilst absolute pressure measurements in the desorber windbox and in the adsorber windbox feature a measuring range of 0-250 mbar, all other pressure sensors have a measuring range of 0-10 mbar. It should be noted that silicone hoses are used as measuring lines connecting the pressure sensors to the pressure taps on the unit. These lines are purged with a constant flow of N<sub>2</sub> at a flow rate of 1 l·min<sup>-1</sup> to protect the pressure sensors from moisture. Differential pressure measurements are made in each FB stage within the columns as well as, at a number of other points of interest. As seen in **Figure 35**, the pressure taps in the columns are located in the freeboard section of stages 1-5 and in the wind box.



**Figure 35: Schematic illustration of the instrumentation used in the TSA BSU (adapted from Dietrich et al. [142]) (a legend of symbols used in the above P&ID can be found in the appendix of this work, see Section 8.4)**

The placement of pressure taps in the columns was chosen in a way that blockages of the measuring lines by sorbent material can be prevented. In cases where the pneumatic transport of solids takes place, the pressure drop across a defined segment can be used to calculate the mass flow rate of solids. To evaluate when the canister filters downstream of the columns needed to be replaced, the pressure drop across the canister filter was monitored. A differential pressure measurement is taken between the freeboard of stage 5 of each column and the gas-solids separator to allow for determination of the flow direction of gas between the riser loops and the columns. Furthermore, this measurement can be used as an indicator for blockages of solids in this section.

### 3.2.2 Temperature measurement of fluidized beds

All temperature measurements in the columns and the risers were performed using CANTrans-T temperature probes supplied by Jumo. These PT-1000-type resistance temperature detectors (RTDs) have a measuring range from -50 °C to 150 °C and an accuracy that complies with class B of the DIN EN 60751 standard.

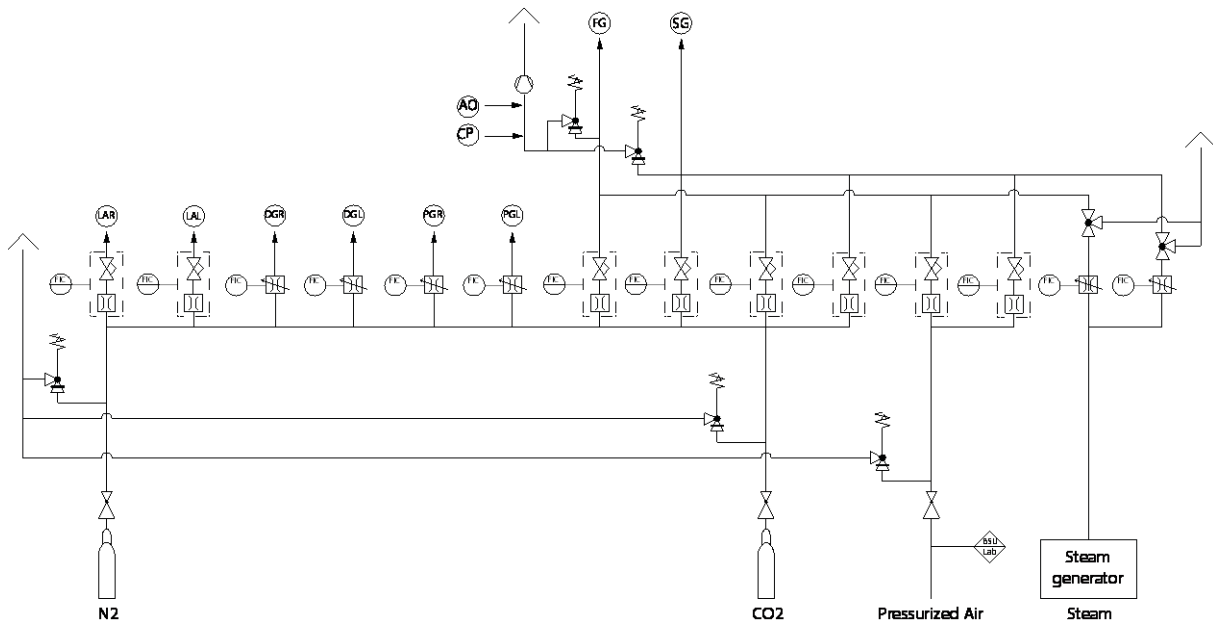
The operating temperature of the CO<sub>2</sub> product cooler was measured using a PT-100-type RTD in the accuracy class B of the DIN EN 60751 standard. Equations used for the calculation of the allowed measuring error according to the DIN EN 60751 standard can be seen in the appendix of this work (see Section 8.1).

### 3.2.3 Gas analysis

An “ULTRAMAT 23”-type multi-component gas analyzer supplied by Siemens is used to measure the inlet and outlet CO<sub>2</sub> concentrations of the adsorber as well as the O<sub>2</sub> concentration at the adsorber inlet. Non-dispersive infrared sensors with a measuring range of 0-25 vol%CO<sub>2</sub> and 0-5vol%CO<sub>2</sub> are used to measure the CO<sub>2</sub> concentration at the inlet and outlet of the adsorber respectively. In an effort to reduce the error of the CO<sub>2</sub> analyzers, three different calibration gases with the concentrations 0 vol%CO<sub>2</sub>, 0.5 vol%CO<sub>2</sub> and 5.1 vol%CO<sub>2</sub> were used before and after an experiment to verify the readings by the sensors. Additionally, the Siemens Ultramat 23 features an electrochemical O<sub>2</sub> analyzer, with a measuring range of 0-25 vol%O<sub>2</sub>. Air and nitrogen were used to calibrate this sensor between experiments.

### 3.2.4 Flow rate measurements of gases

As indicated in **Figure 35**, rotameters with integrated needle valves are used to set the flow rate of recycle gas in the riser loops. The variable area flow meters used here are of the type VA40V/R supplied by Krohne and have a measuring range of 2 Nm<sup>3</sup>·h<sup>-1</sup>-20 Nm<sup>3</sup>·h<sup>-1</sup>. Furthermore, the accuracy of these rotameters conforms to class 1 of the VDI/VDE 351 standard. An equation for the maximum error of the utilized variable area flow rates is given in the appendix (see Section 8.3). Unlike the aforementioned pressure and temperature sensors, the values measured by these rotameters are not automatically recorded by the process control system (PCS). However, they are equipped with a limit switch, which triggers an alarm in the PCS, should the measured flow rate deviate from the flow rate set by the operator.



**Figure 36: Schematic illustration of BSU feed gas paths and associated instrumentation (a legend of symbols used in the above P&ID can be found in the appendix of this work, see Section 8.4)**

As can be seen in Figure 36, the gases that can be used in the BSU are  $N_2$  and  $CO_2$  supplied from gas bottles, pressurized air (PA) supplied by the PA system of a laboratory and steam, which is generated by a steam generator located on-site. Furthermore, mass flow controllers (MFCs) are used to measure and simultaneously control the flow rate of various gases to the BSU. The MFCs used to control and measure the  $N_2$  aeration to both L-valves were supplied by Bürkert and are of the type 8741. They feature a measuring range of  $0.1 \text{ NI}\cdot\text{min}^{-1}$  to  $5 \text{ NI}\cdot\text{min}^{-1}$  whereas the measuring accuracy is given with  $\pm 0.3 \%$  of the full-scale value. The dilution gas that can be added to the riser loops is controlled by DK800-type variable area flow meters supplied by Krohne. These rotameters are in the accuracy class 2.5 of the VDI/VDE 351 standard and exhibit a measuring range of  $0.144 \text{ Nm}^3\cdot\text{h}^{-1}$  to  $0.9 \text{ Nm}^3\cdot\text{h}^{-1}$ . The adsorber feed gas and the stripping gas used in the desorber can be any mixture of  $N_2$ ,  $CO_2$ , PA and steam. The MFCs which control and measure the flow of  $N_2$ ,  $CO_2$  and PA to the adsorber and desorber are Bürkert 8746-type MFCs with an accuracy of  $\pm 0.3 \%$  of the full-scale value whereas the range of each of these MFCs is listed in Table 8. In addition to these MFCs, two setups consisting of a H250/RR/M40-type rotameter by Krohne and a needle valve are used to measure and control the flow rate of steam to the adsorber and desorber. The rotameters used in the adsorber and desorber have a measuring range of  $0.5 \text{ m}^3\cdot\text{h}^{-1}$  to  $5 \text{ m}^3\cdot\text{h}^{-1}$  and  $1.7 \text{ m}^3\cdot\text{h}^{-1}$  to  $17 \text{ m}^3\cdot\text{h}^{-1}$  respectively and are within the accuracy class 1.6 of the VDI/VDE 351 standard.

Medium	Adsorber	Desorber	
$N_2$	0.6-30	0.3-15	$[\text{Nm}^3\cdot\text{h}^{-1}]$
$CO_2$	0.096-4.8	0.3-15	$[\text{Nm}^3\cdot\text{h}^{-1}]$
PA	0.096-4.8	0.3-15	$[\text{Nm}^3\cdot\text{h}^{-1}]$

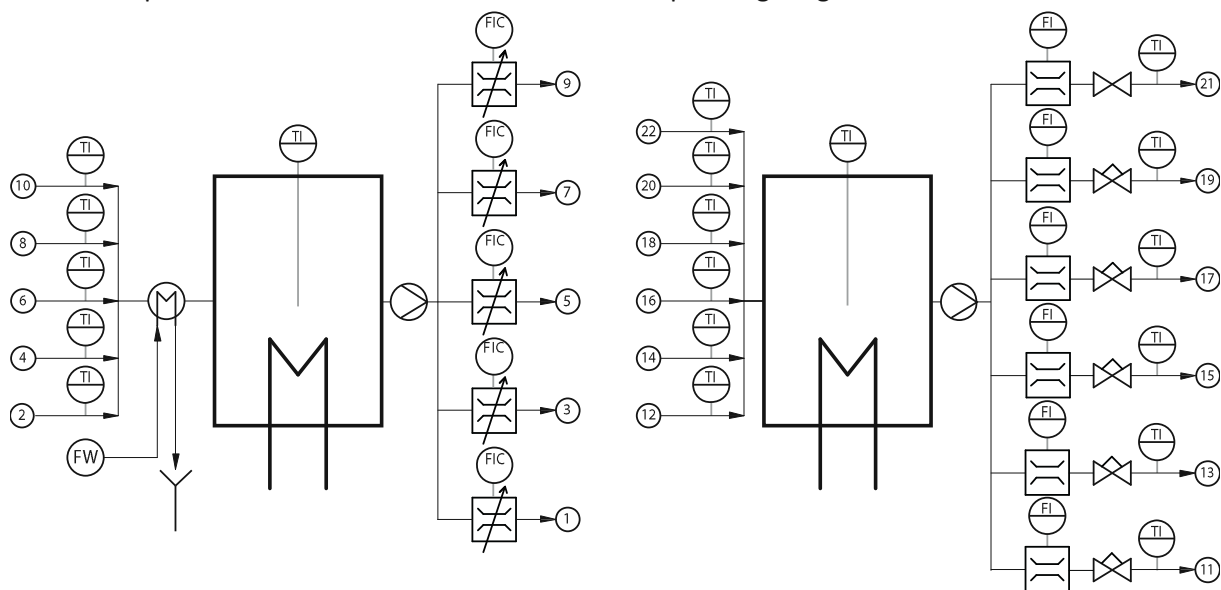
**Table 8: Operating ranges of MFCs used for the generation of the adsorber and desorber feed gases**

### 3.2.5 Instrumentation of the cooling and heating system

As seen in Figure 37, the setups used for thermal oil and cooling water distribution are similar. The bulk of cooling water and thermal oil is stored in storage tanks, each equipped with heating cartridges and a PT-100-type RTD in the accuracy class B of the DIN EN 60751 standard.

The cooling water is pumped into a manifold where it is distributed. Before entering the heat exchanger of a particular stage, the cooling water passes a rotameter with an integrated needle valve. These DK800-type rotameters were supplied by Krohne and feature a measuring range of  $12 \text{ l}\cdot\text{h}^{-1}$ – $120 \text{ l}\cdot\text{h}^{-1}$ , whereas the accuracy is within class 2.5 of the VDI/VDE 351 standard. The return temperature of the cooling water is measured by PT-100-type RTDs at the outlet of the copper heat exchanger. These RTDs have a measuring range from  $0 \text{ }^{\circ}\text{C}$ – $180 \text{ }^{\circ}\text{C}$  and are within the accuracy class B of the DIN EN 60751 standard. Before returning to the cooling water storage tank, the cooling water passes a water-cooled plate heat exchanger.

The thermal oil is pumped into a similar manifold, which distributes the thermal oil into a setup consisting of needle valve and a turbine flow meter, before it can enter the heat exchanger of an individual desorber stages. The turbine flow meters were manually calibrated using thermal oil at temperatures typically set during BSU experiments. Since the difference in forward and return flow temperatures of thermal oil are used for heat input calculations, RTDs with higher precision were installed directly at the thermal oil inlet and outlet of each desorber stage. These PT100-type temperature sensors comply with the 1/3 class B standard of the DIN EN 60751. However, in an effort to increase the accuracy of these temperature sensors beyond the specifications of the standard, a calibration procedure was carried out in the intended operating range.



**Figure 37: Schematic illustration of the cooling water tank, thermal oil tank and associated instrumentation (a legend of symbols used in the above P&ID can be found in the appendix of this work, see Section 8.4)**

### 3.3 METHODS

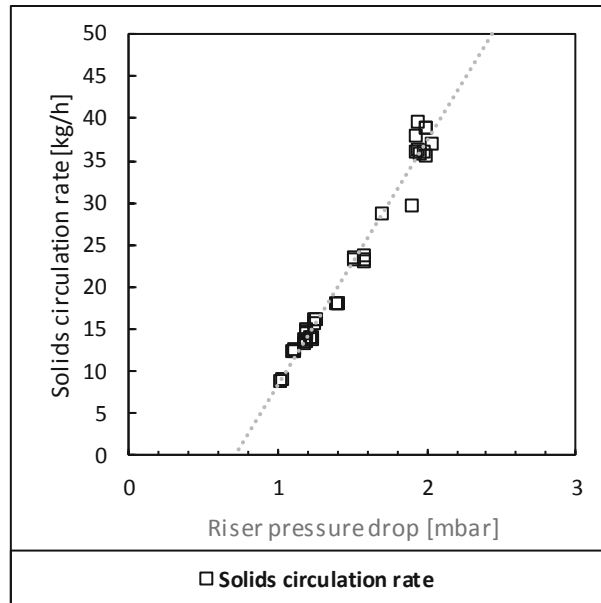
#### 3.3.1 Startup

A specific startup procedure needs to be followed to put the TSA BSU into CO<sub>2</sub> capture operation. For the sake of simplicity, it will be assumed that the unit is empty, i.e. sorbent material from the previous experiment has been removed. The first step of the startup procedure requires all downcomer flaps to be closed to prevent gas bypassing through the downcomer sections of the fluidized bed stages. Afterwards, the recycle blowers in the solids transport loops are put into operation and the needle valves adjusted to achieve a gas velocity that exceeds the terminal gas velocity in the risers ( $U > U_t$ ). In the columns a flow rate of N<sub>2</sub> is set that exceeds the minimum fluidization velocity ( $U > U_{mf}$ ). Flow rates of around 11 Nm<sup>3</sup>·h<sup>-1</sup> in the riser loops and a N<sub>2</sub> flow rate of 16 Nm<sup>3</sup>·h<sup>-1</sup> in the adsorber and 7 Nm<sup>3</sup>·h<sup>-1</sup> in the desorber have shown to be sufficient for the tested sorbent materials. In the next step, the columns need to be filled with sufficient sorbent material to allow for continuous operation. For this purpose, the sorbent feeding screw (shown in Figure 28) needs to be used to transport sorbent material from the sorbent hopper into the rich riser, and into the top stage of the desorber. After sufficient sorbent material has entered the fifth desorber stage, a fluidized bed will begin to form above the gas distributor. The dense phase of the fluidized bed increases in height and bursting bubbles will convey solids into the downcomer section, where a fixed bed will form on top of the closed downcomer flap. Once the pressure drop of the fifth desorber stage reaches a certain threshold (i.e. 3.5 mbar-4 mbar, from experience), the downcomer flap is opened, thus allowing the sorbent to enter the stage below. This procedure is repeated until all desorber stages are filled with sorbent material. A low aeration rate of the lean L-valve (i.e. 0.5 l·min<sup>-1</sup>) is subsequently set, which will transport sorbent material into the lean riser and thus initiate the adsorber filling procedure. The adsorber filling procedure is identical to the filling procedure of the desorber. As soon as the bottom-most stage is filled, the sorbent feeding screw can be deactivated. It is critical to start the automatic control of the L-valve aeration so that sorbent circulation is attained. In the next stage of the startup procedure, the thermal oil pump is activated and all associated needle valves are open so that all desorber heat exchangers are supplied with thermal oil. Furthermore, automatic temperature control of the thermal oil tank is activated and the target temperature successively increased up to 120 °C. Simultaneously to desorber heat-up, trace heating can be activated on the column feed gas lines, the steam generator can be started up and the CO<sub>2</sub> product cooler can be put into operation. Once the FB temperature in the desorber is sufficiently high, solids circulation is temporarily deactivated and nitrogen in the desorber feed gas is successively replaced with steam. By adding steam to the fluidization gas of the desorber, a steep increase of the fluidized bed temperatures is typically observed. When the desorber feed gas consists of steam only, solids circulation can be reactivated and CO<sub>2</sub> can be added to the adsorber feed gas. CO<sub>2</sub> presence in the adsorber will lead to a rapid increase of the FB temperatures. To counter-act this, the cooling water pump and plate heat exchanger in the return line of the cooling water need to be activated so that the adsorber is cooled.

#### 3.3.2 Control and determination of the solids circulation rate

For the evaluation of operating points, steady-state conditions needed to be maintained. This requires the solids circulation rate (SCR) as well as the distribution of the solids inventory between the columns to remain constant for the duration of an operating point. As can be seen in Figure 38, the solids

circulation rate and the pressure drop over the riser can be correlated linearly with a rather low margin of error. This is because the riser in the TSA BSU fulfills the requirements given in Section 2.2.7, thus the solids flux is a linear function of the pressure drop over a riser segment in which the solids holdup can be considered constant according to Eq. 21.



**Figure 38: Correlation of the measured solids circulation rate over the riser pressure drop [142]**

The rich L-valve aeration rate is automatically controlled in a way that the pressure drop over a one-meter segment of the rich riser corresponds to the desired SCR according to the correlation shown in Figure 38. The lean L-valve aeration rate is also controlled automatically. Here, the difference in pressure drops between the adsorber and the desorber is maintained according to the desired inventory distribution between the columns. It should be noted that due to this control scheme, any changes of the column pressure drops brought about by e.g. a change in the feed gas flow rate of one of the columns, requires an adjustment of the set value.

After each operating point, the solids circulation rate is directly measured. This is done by discharging solids via the solids redirecting flaps, shown in Figure 28, into the SCR determination setup. The discharged solids are directed into a container, which is weighed by a scale. The mass of accumulated sorbent material within a timeframe of at least 30 seconds is measured. The position of the solids redirection flap is subsequently returned to its original position so that the rich sorbent can enter the desorber. When changing the position of the flap, it was observed that the absolute pressure change in the riser system was negligible. Hence, a change in the solids circulation rate is not expected during the measurement. The weight of the accumulated solids in the container was then divided by the accumulation time to yield the SCR in  $\text{kg}\cdot\text{h}^{-1}$ . This procedure is repeated three times and the arithmetic average of results is used for further evaluation.

### 3.3.3 Shutdown

In a first step, solids circulation is interrupted and the desorber feed gas is changed to consist entirely of  $\text{N}_2$ . Sorbent circulation is restarted and continued until the entire sorbent inventory has passed the desorber. This is important because any co-adsorbed steam is stripped from the sorbent, thus



condensation of steam in the subsequent cool-down phase can be prevented. Subsequently, the heating cartridges in the cooling water tank and thermal oil tank are deactivated together with the corresponding pumps. Trace heating of the column feed gas lines is also deactivated. The BSU is operated under these conditions until the maximum temperature in the desorber FB stages reaches 70°C. The flow of feed gases to the columns as well as the flow of N<sub>2</sub> to the L-valve is stopped and the blowers in the riser loops are deactivated. In the last step, the flow of cooling water to the CO<sub>2</sub> product cooler and the plate heat exchanger is stopped together with the flow of dilution gases. The columns can be emptied of sorbent material via an opening in the standpipe section below each column.

### 3.3.4 Key process performance parameters

- **Capture efficiency:** The capture efficiency ( $\eta_{capt}$ ) is defined as the amount of captured CO<sub>2</sub> relative to the amount of CO<sub>2</sub> in the treated flue gas and is one of the most important performance parameters in PCCC systems. The capture efficiency can be simply calculated when the inlet and outlet flow rates of CO<sub>2</sub> are known according to Eq. 29.

$$\eta_{capt} = \frac{F_{CO_2,ADS,in} - F_{CO_2,ADS,out}}{F_{CO_2,ADS,in}} \cdot 100\% \quad \text{Eq. 29}$$

However, since the current experimental setup does not allow for directly measuring the flow rate of CO<sub>2</sub> at the outlet of the adsorber, these values must be calculated from the measured flow rates of gases that are not adsorbed and the measured inlet and outlet CO<sub>2</sub> concentrations of the adsorber as shown in Eq. 30-Eq. 33.

$$F_{CO_2,ADS,in} = y_{CO_2,ADS,in} \cdot (F_{N_2,ADS,in} + F_{Air,ADS,in} + F_{CO_2,ADS,in}) \quad \text{Eq. 30}$$

$$F_{CO_2,ADS,in} = \frac{y_{CO_2,ADS,in} \cdot (F_{N_2,ADS,in} + F_{Air,ADS,in})}{1 - y_{CO_2,ADS,in}} \quad \text{Eq. 31}$$

$$F_{CO_2,ADS,out} = y_{CO_2,ADS,out} \cdot (F_{N_2,ADS,in} + F_{Air,ADS,in} + F_{N_2,PGL} + F_{DGL} + F_{CO_2,ADS,out}) \quad \text{Eq. 32}$$

$$F_{CO_2,ADS,out} = \frac{y_{CO_2,ADS,out} \cdot (F_{N_2,ADS,in} + F_{Air,ADS,in} + F_{N_2,PGL} + F_{DGL})}{(1 - y_{CO_2,ADS,out})} \quad \text{Eq. 33}$$

As can be seen the lean purge gas flow and lean dilution flow are assumed to end up in the adsorber off-gas, thus contributing to a dilution of the adsorber off-gas. Furthermore, it is assumed that gas leakages from the adsorber into the rich transport line can be neglected. It should be mentioned that the flow of nitrogen used to purge the pressure taps is not considered in these calculations due to its low flow rate. Putting Eq. 31 and Eq. 33 into Eq. 29 yields Eq. 34.

$$\eta_{capt} = 1 - \frac{y_{CO_2,ADS,out} \cdot (F_{N_2,ADS,in} + F_{Air,ADS,in} + F_{N_2,PGL} + F_{DGL}) \cdot (1 - y_{CO_2,ADS,in})}{y_{CO_2,ADS,in} \cdot (F_{N_2,ADS,in} + F_{Air,ADS,in}) \cdot (1 - y_{CO_2,ADS,out})} \cdot 100\% \quad \text{Eq. 34}$$

- **CO<sub>2</sub> capture rate:** In addition to the capture efficiency, the CO<sub>2</sub> capture rate,  $\dot{m}_{capt}$  (given in kilograms of CO<sub>2</sub> captured per 24 hours), is used as a second process performance indicator. The capture rate was calculated according to Eq. 35.

$$\dot{m}_{capt} = 24 \cdot F_{CO_2,ADS,in} \cdot \eta_{capt} \cdot \rho_{CO_2} \quad \text{Eq. 35}$$

- **Dynamic sorbent loading:** High working capacities are required to achieve a low sensible heating demand of the circulating solids and thus important to allow a low overall process heat demand. Determination of the working capacity would require analytical work. To have an online indicator for the working capacity that can be derived from measured data, the so-called “dynamic sorbent loading” was introduced. The dynamic sorbent loading ( $dSl$ ) is determined by dividing the captured amount of  $CO_2$  ( $\dot{m}_{capt}$ ) by the solids circulation rate ( $SCR$ ), as shown in Eq. 36.

$$dSl = \frac{\dot{m}_{capt}}{24 \cdot SCR} \quad \text{Eq. 36}$$

- **Specific solids circulation rate:** In some cases, it is useful to increase the SCR proportionally to the amount of  $CO_2$  in the adsorber feed gas. For this reason the, the so-called specific solids circulation rate ( $SCR_{spec}$ ) was define as shown in Eq. 37.

$$SCR_{spec} = \frac{SCR}{\dot{m}_{CO_2,ADS,in}} \quad \text{Eq. 37}$$

- **Desorber heat input:** The heat input in the desorber is calculated by measuring the flow rate of thermal oil in the desorber heat exchanger stages and double wall ( $\dot{m}_{TO, Stage}$ ) together with the forward ( $T_{TO FF, Stage}$ ) and return ( $T_{TO RF, Stage}$ ) flow temperatures of thermal oil. By using the heat capacity ( $c_{p, TO}$ ) of the utilized thermal oil and the pre-determined heat losses of the desorber ( $\dot{Q}_{Loss, Stage}(T_{TO FF})$ ), the effective heat input in the desorber ( $\dot{Q}_{DES, sens}$ , given in kW) was determined according to the Equation seen in Eq. 38. It should be mentioned that stage 0 in Eq. 38 symbolizes the heated wind box.

$$\dot{Q}_{DES} = \sum_{Stage=0}^5 \dot{m}_{TO, Stage} \cdot c_{p, TO} \cdot (T_{TO FF, Stage} - T_{TO RF, Stage}) - \dot{Q}_{Loss, DES}(T_{TO FF}) \quad \text{Eq. 38}$$

The heat loss of the desorber column was determined by measuring the steady-state heat input to the empty isolated column at constant ambient temperature and varying forward flow temperature of thermal oil. A graph showing the heat loss of the desorber as a function of the forward flow temperature of thermal oil is shown in the Appendix of this work (see Figure 66).

- **Specific desorber heat input:** The measured desorber heat input is related to the mass flow of  $CO_2$  that is captured, thereby yielding the specific desorber heat input ( $q_{DES}$ ) given in  $MJ \cdot kg_{CO_2}^{-1}$ .

$$q_{DES} = \frac{\frac{\dot{Q}_{DES}}{1000}}{\frac{\dot{m}_{capt}}{24 \cdot 3600}} \quad \text{Eq. 39}$$

- **Temperature swing:** The temperature swing is a key figure in TSA and particularly important for evaluating the sensible heat requirement of the process. Throughout this work, the temperature swing is defined as the difference in the mean operating temperatures of the columns. As shown in Eq. 40, the mean operating temperature of the columns is defined as the arithmetic mean of the stage temperatures. It should be mentioned that stage 0 in Eq. 40 symbolizes the heated wind box.

$$\Delta T_{DES-ADS} = \frac{\sum_{Stage=0}^5 T_{DES,Stage}}{6} - \frac{\sum_{Stage=0}^5 T_{ADS,Stage}}{6} \quad \text{Eq. 40}$$

### 3.4 UTILIZED SORBENT MATERIAL

#### 3.4.1 Sorbent A

Sorbent A is a highly porous silica, which has been impregnated by polyethyleneimine (PEI). PEI generally features a high amine content of approx. 33% nitrogen by weight, whereas the ratio of primary to secondary to tertiary amines is assumed equal [111]. The PEI loading of Sorbent A is 50 % by weight, thus resulting in a total nitrogen content of 16.6 % by weight.

Selected hydrodynamic properties can be seen in Table 9. It should be mentioned that Sorbent A is within Class B of the Geldart classification under the operating condition within the TSA BSU.

	Sorbent A	
Sauter mean particle diameter ( $d_{sv}$ )	175	[ $\mu\text{m}$ ]
Mean particle diameter ( $d_{50}$ )	297	[ $\mu\text{m}$ ]
Bulk density ( $\rho_b$ )	700	[ $\text{kg}\cdot\text{m}^3$ ]
Minimum fluidization velocity ( $U_{mf}$ in air at ambient conditions)	0.05	[ $\text{m}\cdot\text{s}^{-1}$ ]

Table 9: Hydrodynamic properties of Sorbent A

#### 3.4.2 Sorbent B

Unlike Sorbent A, Sorbent B is commercially available and is sold by Lanxess under the trademark Lewatit VP OC 1065. Lewatit VP OC 1065 is polystyrene-based and features only primary amine groups, which are covalently bound to the macroporous support. The supporting material is cross-linked with Divinylbenzene and functionalized with a benzylamine group in a phthalimide addition process [128,129]. Using the data sheet produced by the manufacturer [129], the loading of benzylamine was calculated to 43 % by weight. This loading of benzylamine results in a total nitrogen content of 5.6 % by weight.

Selected hydrodynamic properties of the sorbents investigated in the course of this work are shown in Table 10. Similar to Sorbent A, Sorbent B is within Class B of the Geldart classification under the operating condition in the TSA BSU. It is worth mentioning that due to the high sphericity of the polymer-bead-type support,  $d_{sv}$  is similar to  $d_{50}$ .

	Sorbent B	
Sauter mean particle diameter ( $d_{sv}$ )	494	[ $\mu\text{m}$ ]
Mean particle diameter ( $d_{50}$ )	509	[ $\mu\text{m}$ ]
Bulk density ( $\rho_b$ )	550	[ $\text{kg}\cdot\text{m}^3$ ]
Minimum fluidization velocity ( $U_{mf}$ in air at ambient conditions)	0.11	[ $\text{m}\cdot\text{s}^{-1}$ ]

**Table 10: Hydrodynamic properties of Sorbent B**

During operation of the TSA BSU with Sorbent B, electro-static charging was observed, likely brought about by the polymer nature of the support. Through the borosilicate walls of the adsorber it was observed that the electro-statically charged sorbent shows cohesive behavior, which severely impaired solids mixing in the fluidized beds. This behavior makes continuous operation of the TSA BSU impossible under dry conditions. However, it was found that a low flow rate of steam added to the adsorber feed gas successfully prevents electro-static charging. For this reason, steam is always added to the adsorber feed gas during BSU experiments in which Sorbent B is used as a bed material.

## 4. EXPERIMENTAL

### 4.1 ADSORBER FEED GAS VELOCITY VARIATIONS

PCCC technologies are typically considered for application at large point sources such as NGCC or coal-fired power plants. This implies that the PCCC technology needs to treat large amounts of flue-gas, which in turn means that the operating flue-gas velocity through the CO<sub>2</sub> capture plant needs to be as high as possible in order to minimize the plant footprint. Moreover, a load change of the CO<sub>2</sub> emitting process can manifest in a change of the flue gas flow rate, thus PCCC systems must be able to efficiently capture CO<sub>2</sub> in a wide flow rate range i.e. PCCC systems must feature a high turndown ratio. A variation in terms of the flue gas velocity in the adsorber can reveal the flexibility of the TSA process in this regard.

However, in stationary fluidized beds, high superficial gas velocities in the fluidized beds lead to both the formation of large bubbles and reduce gas solids contact time. Hence, it is important to identify limitations of the TSA process when operated at high flue gas velocities in the adsorber. In the course of the experimental campaign carried out herein, adsorber feed gas velocity variations were conducted. The defined target during these variations was to increase the superficial gas velocity in the adsorber whilst increasing the SCR proportionally so that a constant spec. SCR is achieved. By operating the BSU in this way, limitations regarding mass transfer and reaction kinetics become particularly pronounced and manifest in changes of the CO<sub>2</sub> capture efficiency and the dynamic sorbent loading.

In the course of this campaign, the experimental setup corresponds to the description given in Section 3.1, whereas the sorbent used throughout this campaign was Sorbent B.

#### 4.1.1 Operating conditions

Table 11 shows the target operating conditions of the TSA BSU together with the column feed gas properties.

	Variation A	Variation B	
Adsorber operating temperature	45-50	50-55	[°C]
Adsorber superficial gas velocity	0.32-0.67	0.32-0.87	[m·s <sup>-1</sup> ]
Adsorber feed gas O <sub>2</sub> concentration	9	9	[vol%O <sub>2</sub> ]
Adsorber feed gas CO <sub>2</sub> concentration	4	3	[vol%CO <sub>2</sub> ]
Steam flow to adsorber	0.6-1.3	0.6-1.7	[kg·h <sup>-1</sup> ]
Desorber operating temperature	100-110	100-110	[°C]
Desorber stripping steam flow-rate	8.5	8.5	[kg·h <sup>-1</sup> ]

**Table 11: Operating conditions held constant during the conducted parameter variations**

It can be seen that two different variations of the adsorber feed gas velocity were conducted, each at slightly different operating conditions of the TSA BSU. In Variation A, the adsorber was operated with a feed gas CO<sub>2</sub> concentration of 4 vol%CO<sub>2</sub> and a target operating temperature window between 45 °C

and 50 °C, whilst during Variation B the flue gas CO<sub>2</sub> concentration was decreased to 3 vol%CO<sub>2</sub> and the target operating temperature of the adsorber increased to 50 °C-55 °C. Variation B, was thus carried out with a lower cooling requirement in the adsorber.

In the course of the initial operating point of each variation, the SCR was set so that a capture efficiency of approx. 90% could be achieved. The SCR of all following operating points was adjusted to achieve the same spec. SCR as in the initial operating point, thereby increasing the SCR proportionally to the increase of the CO<sub>2</sub> feeding rate. It should be noted that the target SCR was set according to the pre-determined correlation between riser pressure drop and SCR (see Figure 38), whereas the actual SCR was measured according to the SCR determination procedure after each operating point.

#### 4.1.2 Results & Discussion

##### Variation A

The results presented in Figure 39, show that the adsorber feed gas velocity was increased from 0.32 m·s<sup>-1</sup> up to 0.67 m·s<sup>-1</sup>.

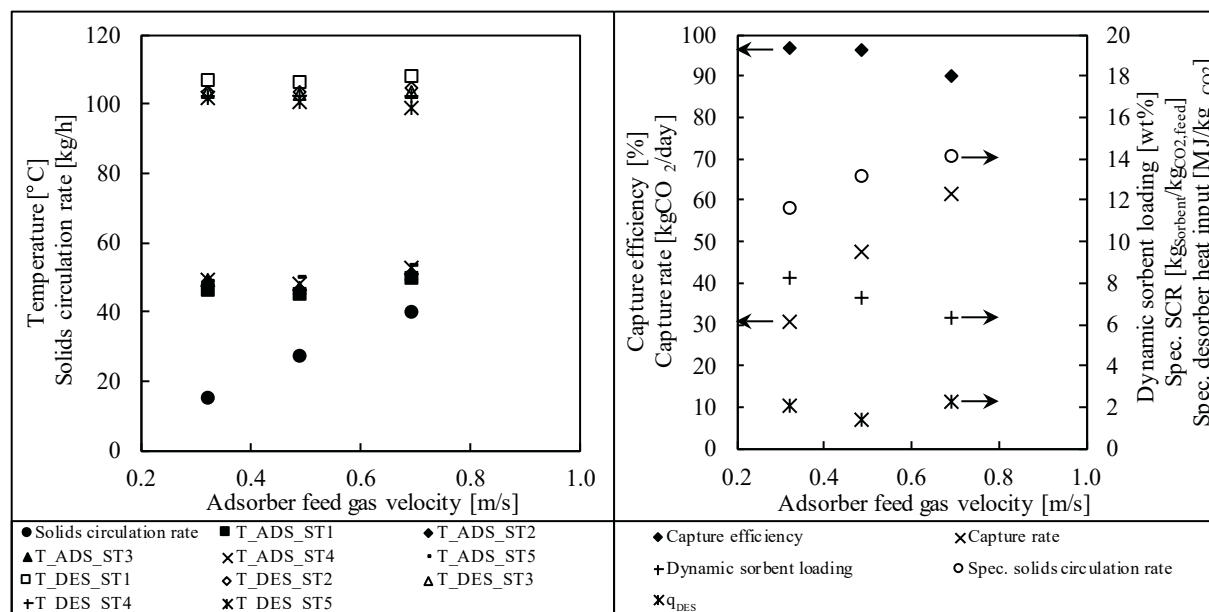


Figure 39: Graphs showing the results from an adsorber feed gas variation at a feed gas CO<sub>2</sub> concentration of 4 vol%CO<sub>2</sub>

In the graph depicting the fluidized bed temperatures and SCR as a function of the adsorber feed gas velocity (Figure 39, left), it can be seen that the SCR was increased almost linearly with the adsorber feed gas velocity. This was done in an effort to achieve the same spec. SCR relative to the initial operating point. When the adsorber feed gas velocity was increased to 0.67 m·s<sup>-1</sup>, the average temperature of the adsorber stages increases from 48 °C to 52 °C. This occurred although the cooling water flow rate to the individual stages was significantly increased whilst the forward flow temperature was decreased from 30 °C to 24 °C. Simultaneously, the average temperature of the desorber stages could be maintained at 103 °C, despite a significant increase of the thermal oil temperature (from 112 °C to 127 °C) in the last operating point. Nevertheless, the insufficient supply of heat resulted in an increase in the axial temperature distribution across the desorber.

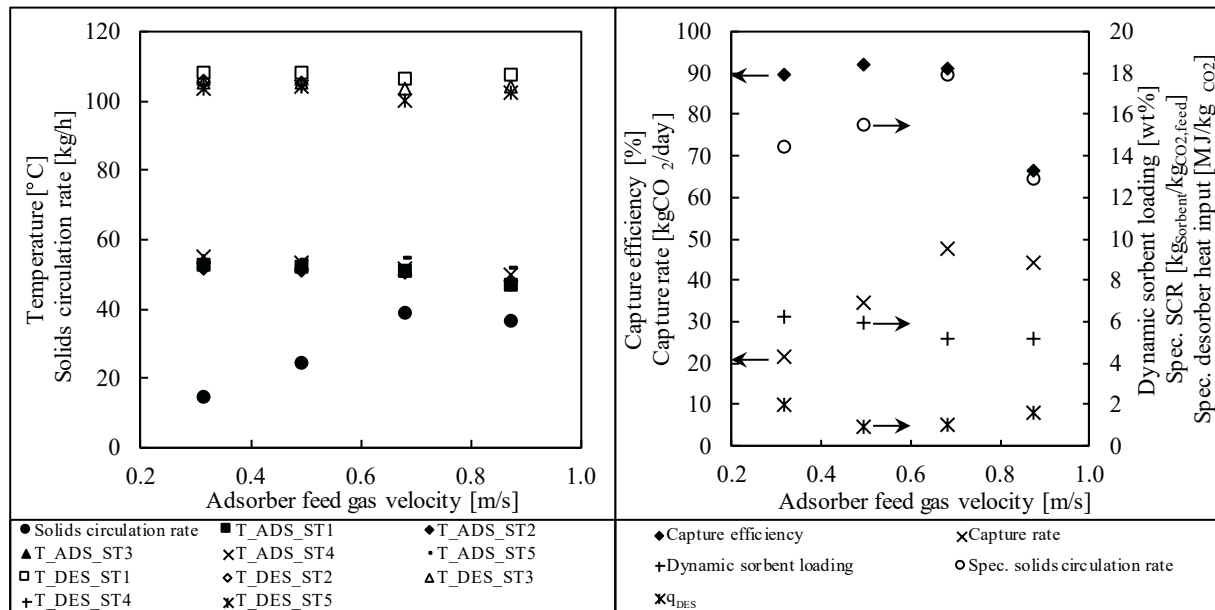
When regarding the process performance indicators (Figure 39, right), it can be seen that the spec. SCR was overshoot in the latter two operating points. This was due to deviations in the correlation between the SCR and the rich riser pressure drop. Furthermore, the capture rate increased throughout the entire variation and peaked at  $61.6 \text{ kg}_{\text{CO}_2}\cdot\text{day}^{-1}$  at  $0.67 \text{ m}\cdot\text{s}^{-1}$ , whilst the achieved capture efficiency could be kept between 90.2 % and 96.7 %.

Although an overshoot of the spec. SCR at constant  $\text{CO}_2$  concentrations in the flue gas should have a positive impact on the  $\text{CO}_2$  capture performance, the  $\text{CO}_2$  capture efficiency decreases in the last operating point. This is due to the observed heat transfer limitation, which led to appreciable decrease of the temperature swing in the last operating point. There are two options for increasing heat transfer that do not involve changes to the sorbent material or changes to the fluidization rate. Either the temperature difference between the heat transfer surface and the FB must be increased or the heat exchanger surface area immersed in the fluidized bed must be increased. A further reduction of the cooling water temperature is not advisable since condensation of steam and consequential sorbent deposition on the heat exchanger surface must be prevented. In the desorber, heat exchanger temperatures that exceed the maximum operating temperature of the sorbent can lead to damage of the sorbent material and subsequently lead to a reduction of the  $\text{CO}_2$  adsorption capacity. Therefore, the only feasible option for improving heat transfer in the columns is to adapt the design of the heat exchangers so an increased ratio between heat transfer surface and bed volume can be achieved. In the BSU this ratio is currently  $34.3 \text{ m}^2\cdot\text{m}^{-3}$ , whereas at a larger scale significantly higher values can be achieved by installing heat exchanger tube bundles. The implementation of such heat exchangers should be considered especially if flue gas with a similar  $\text{CO}_2$  concentration at superficial gas velocities over  $0.68 \text{ m}\cdot\text{s}^{-1}$  is treated.

Because a decrease of the  $\text{CO}_2$  capture performance at high adsorber feed gas velocities may be masked by a reduced temperature swing (i.e. a heat transfer limitation), the results gained from Variation A are unsuited to evaluate the process in terms of a mass transfer limitation or a limitation in terms of the reaction kinetics. Therefore, the variation of the adsorber feed gas velocity was repeated at a lower flue gas  $\text{CO}_2$  concentration.

### **Variation B**

By reducing the  $\text{CO}_2$  concentration of the adsorber feed gas, the absolute  $\text{CO}_2$  feeding rate was decreased by 25% at identical adsorber feed gas velocities. Therefore, the  $\text{CO}_2$  feeding rate at an adsorber feed gas velocity of  $0.68 \text{ m}\cdot\text{s}^{-1}$  and a  $\text{CO}_2$  concentration of 4 vol% $\text{CO}_2$  (i.e.  $2.85 \text{ kg}_{\text{CO}_2}\cdot\text{h}^{-1}$ ) is similar to the  $\text{CO}_2$  feeding rate at  $0.89 \text{ m}\cdot\text{s}^{-1}$  and a  $\text{CO}_2$  concentration of 3 vol% $\text{CO}_2$  (i.e.  $2.81 \text{ kg}_{\text{CO}_2}\cdot\text{h}^{-1}$ ).



**Figure 40: Graphs showing the results from an adsorber feed gas variation at a feed gas CO<sub>2</sub> concentration of 3 vol%CO<sub>2</sub>**

As shown in Figure 40 (left) adsorber cooling was not an issue in the course of the entire variation. Between an adsorber feed gas velocity of  $0.32 \text{ m}\cdot\text{s}^{-1}$  and  $0.49 \text{ m}\cdot\text{s}^{-1}$  the adsorber temperature could be kept in the pre-defined temperature window (i.e.  $50^\circ\text{C}$ - $55^\circ\text{C}$ ). However, in the last operating point, adsorber cooling was overshoot resulting in an adsorber operating temperature window of  $46.6^\circ\text{C}$ - $51.4^\circ\text{C}$ . The desorber stage temperatures were kept constant between  $99.8^\circ\text{C}$  and  $107.9^\circ\text{C}$ , whereas the thermal oil temperature was increased from  $112^\circ\text{C}$  to  $122^\circ\text{C}$  at the highest adsorber feed gas velocity. Throughout the campaign, the SCR was increased significantly to reach the targeted spec. SCR. However, the SCR could not be increased beyond  $36.1 \text{ kg}\cdot\text{h}^{-1}$ . At higher SCRs solids started to accumulate in the 5<sup>th</sup> desorber stage, which is an indication for insufficient solids throughput through the downcomer located between desorber stage 4 and 5. This limitation had reduced the achievable CO<sub>2</sub> capture rate and capture efficiency, and thus considerably reduced the heating and cooling demand at an adsorber feed gas velocity of  $0.89 \text{ m}\cdot\text{s}^{-1}$ . Nevertheless, it can be seen that similarly to Variation A, the spec. SCR was overshoot for all operating points carried out at adsorber feed gas velocities between  $0.49 \text{ m}\cdot\text{s}^{-1}$  and  $0.68 \text{ m}\cdot\text{s}^{-1}$ . During these operating points, the capture efficiency increases from 89.5% to 91.7%. Similarly to Variation A, the capture rate increased almost linearly up to an adsorber feed gas velocity of  $0.68 \text{ m}\cdot\text{s}^{-1}$ , whilst the dynamic sorbent loading decreased slightly in this range. At constant operating temperatures of the columns and a constant flue gas CO<sub>2</sub> concentration, an increase of the spec. SCR results in an increase of the capture efficiency if no limitations are encountered. However, at an adsorber feed-gas velocity of  $0.49 \text{ m}\cdot\text{s}^{-1}$  and  $0.68 \text{ m}\cdot\text{s}^{-1}$  similar capture efficiencies were measured despite a 15.4% increase of the spec. SCR. This is an indication for a limitation in terms of either mass transfer or reaction kinetics. Unfortunately, a distinction between these two mechanisms cannot be made using the current BSU setup. Upon a further increase of the adsorber feed gas velocity to  $0.89 \text{ m}\cdot\text{s}^{-1}$ , large gas bubbles were formed in the downcomer section of the adsorber and the capture efficiency drops considerably. Although the drop in capture efficiency is partly a result of the SCR-limitation, large bubbles were observed in the visible part of the downcomer section. This suggests that large bubbles may also be present in the FB section of the adsorber, which may reduce gas-solids contact due to a slip of gas through the bubbles phase,



thus contributing to a reduction of the CO<sub>2</sub> capture performance. Nevertheless, a turndown ratio of 2.7 was demonstrated and thus a similar turndown ratio can be expected for reactors with a similar multi-stage fluidized bed design.

#### 4.1.3 Conclusion

A variation of the adsorber feed gas velocity was conducted at two different CO<sub>2</sub> concentrations of the treated flue gas to investigate the effect of high gas velocities on the CO<sub>2</sub> capture performance of the TSA. A heat transfer limitation was encountered when a flue gas with 4 vol%CO<sub>2</sub> was treated, which underlined the importance of sufficient heat transfer in the columns. Because this heat transfer limitation could mask limitations in terms of mass transfer or reaction kinetics, the variation was repeated at a lower CO<sub>2</sub> concentration of the adsorber feed gas i.e. 3 vol%CO<sub>2</sub>. Here, a turndown ratio of 2.7 could be demonstrated in the adsorber. However, a decrease of the process performance at superficial gas velocities above 0.68 m·s<sup>-1</sup> indicate a limitation in terms of either mass transfer or reaction kinetics. Furthermore, large bubbles were observed in the downcomer region of the adsorber when the superficial gas velocity was increased to 0.89 m·s<sup>-1</sup>, thus suggesting the presence of large bubbles in the fluidized bed of the adsorber and a subsequent slip of gas from stage to stage.

To reduce gas slip through the fluidized bed section or the downcomer section, appropriate countermeasures must be implemented in larger scale TSA systems. Internals such as baffles, tubes or insert bodies, so-called bubble-breakers, are proven to break large bubbles into smaller ones, thus effectively counteract bubble coalescence [144]. At a larger scale, internals such as heat exchanger tube bundles installed in the fluidized beds and in the downcomer section may thus serve a double purpose.

By closing perforations in the gas distributor below the downcomer section the amount of gas that is allowed to enter the downcomer can be considerably reduced, thus also reducing the risk of gas slip. It should be mentioned that Zehetner et al. [143] showed that this measure had a positive impact on the achievable SCR.

A design of the adsorber with external downcomers, i.e. downcomer pipes located at the exterior of the adsorber, as suggested by Zehetner [77] could be realized in a larger scale TSA unit. The downcomers would be designed as L-valves, whereas the aeration to the respective downcomer L-valves would be used to control the inventory of each stage. The benefit of this setup is that it would decouple the gas-feeding rate to the column from the operating regime in the downcomers whilst solids throughput is managed by an L-valve aeration.

## 4.2 VARIATION OF ADSORBER TEMPERATURE AND FLUE GAS CO<sub>2</sub> CONCENTRATION

In the course of two different parameter variations, the impact of varying operating temperatures in the adsorber and varying CO<sub>2</sub> concentrations in the treated flue gas on the CO<sub>2</sub> capture performance of the TSA BSU were investigated.

By increasing the operating temperature of the adsorber, the cooling duty of the adsorber is reduced at equal SCRs and CO<sub>2</sub> capture rates. At locations where low-temperature cooling water is not available, the trade-off between increased adsorber temperature and decreased CO<sub>2</sub> loading of the rich sorbent may be justifiable. However, an increase of the adsorption temperature does not necessarily entail negative effects. Xu et al. [125] showed that the adsorption rate of CO<sub>2</sub> onto a PEI impregnated sorbent was kinetically controlled at temperatures below 75 °C. To investigate the influence of increasing adsorption temperatures on Sorbent B and to assess whether Sorbent B exhibits a kinetic limitation in the tested temperature range, a variation of the adsorber temperature was conducted. This parameter variation will henceforth be referred to as Variation C.

In the second part of the campaign, the CO<sub>2</sub> concentration of the adsorber feed gas was varied (Variation D). It is important to demonstrate that the TSA process can be implemented as a viable end-of-pipe solution for various combustion processes. Three different CO<sub>2</sub> concentrations were chosen, two of which are typical CO<sub>2</sub> concentration of flue gases found in the energy sector. The flue gas with the lowest CO<sub>2</sub> concentration represents flue gas from a NGCC process, whereas the highest CO<sub>2</sub> concentration is typical for flue gas from a coal combustion process.

In the course of this campaign, the experimental setup corresponds to the description given in Section 3.1, whereas the sorbent used throughout this campaign was Sorbent B.

### 4.2.1 Operating conditions

Table 12 shows a set of parameters that were kept constant in the course of the entire experimental campaign. It can be seen that during this campaign selected gas properties of the column feed gases were kept constant as well as the temperature and flow rate of thermal oil. In keeping these thermal oil properties constant, changes in the desorber heat demand will manifest in changes of the desorber temperature and changes in the axial temperature distribution across the desorber column. Furthermore, it was chosen to adapt the SCR in each operating point so a capture efficiency of 90 %, a benchmark value for PCCC systems, is achieved.

During Variation C, the CO<sub>2</sub> concentration of the adsorber feed gas was kept constant at 3 vol%CO<sub>2</sub> and the adsorber operating temperature varied between 42.4 °C and 58.4 °C. In Variation D, the adsorber temperature was kept between 50 °C and 55 °C, whilst the CO<sub>2</sub> concentration of the adsorber feed gas was varied between 3 vol%CO<sub>2</sub> and 12 vol%CO<sub>2</sub>.

Adsorber superficial gas velocity	0.32	[m·s <sup>-1</sup> ]
Adsorber feed gas O <sub>2</sub> concentration	9	[vol%O <sub>2</sub> ]
Steam flow to adsorber	0.6	[kg·h <sup>-1</sup> ]
Desorber stripping steam flow-rate	8.5	[kg·h <sup>-1</sup> ]
Total thermal oil flow rate	12	[l·min <sup>-1</sup> ]
Thermal oil temperature	112	[°C]

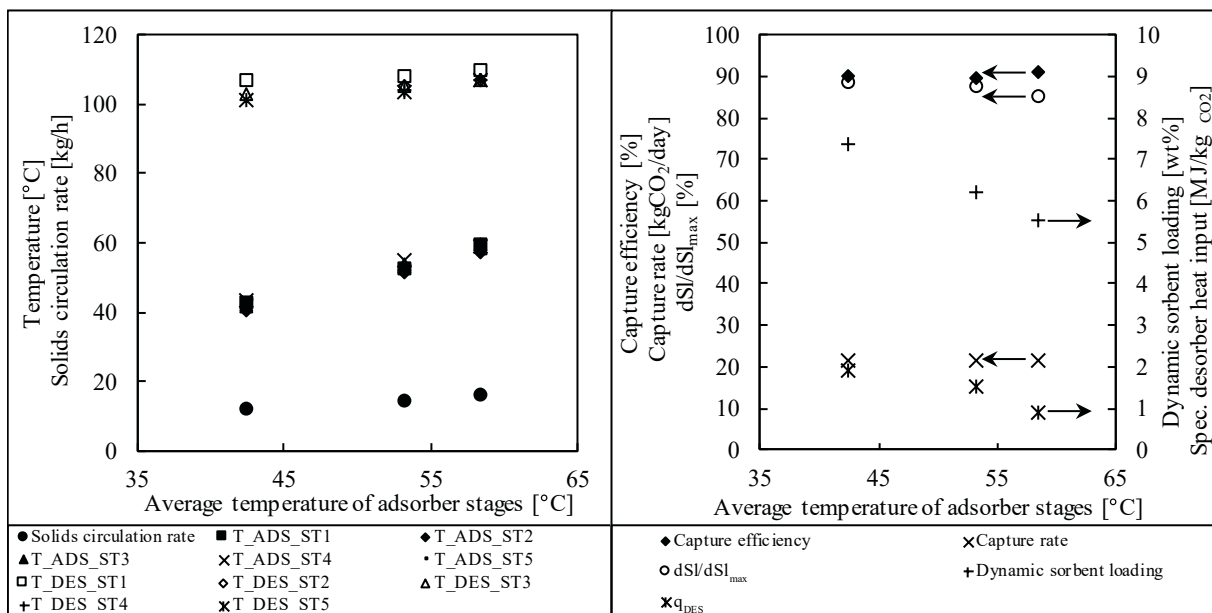
**Table 12: Operating conditions during the conducted variation of adsorber temperature and flue gas CO<sub>2</sub> concentration**

By modelling the operating conditions of the TSA BSU in a thermodynamic process model, the theoretical maximum dynamic sorbent loading was calculated ( $dSl_{max}$ ). These calculations assume that the capture goal is achieved and that the sorbent is completely regenerated in the desorber (i.e. 0 wt%CO<sub>2</sub> on the lean sorbent when it enters the adsorber). The quotient of dynamic sorbent loading and theoretical maximum dynamic sorbent loading is used to assess how close the rich sorbent comes to reaching the equilibrium CO<sub>2</sub> loading at given adsorber operating conditions and is used to evaluate how deep the sorbent can be regenerated.

#### 4.2.2 Results & Discussion

##### Variation C

Figure 41 shows that the average adsorber operating temperature was varied in a rather small range, from 42.4 °C to 58.4 °C.



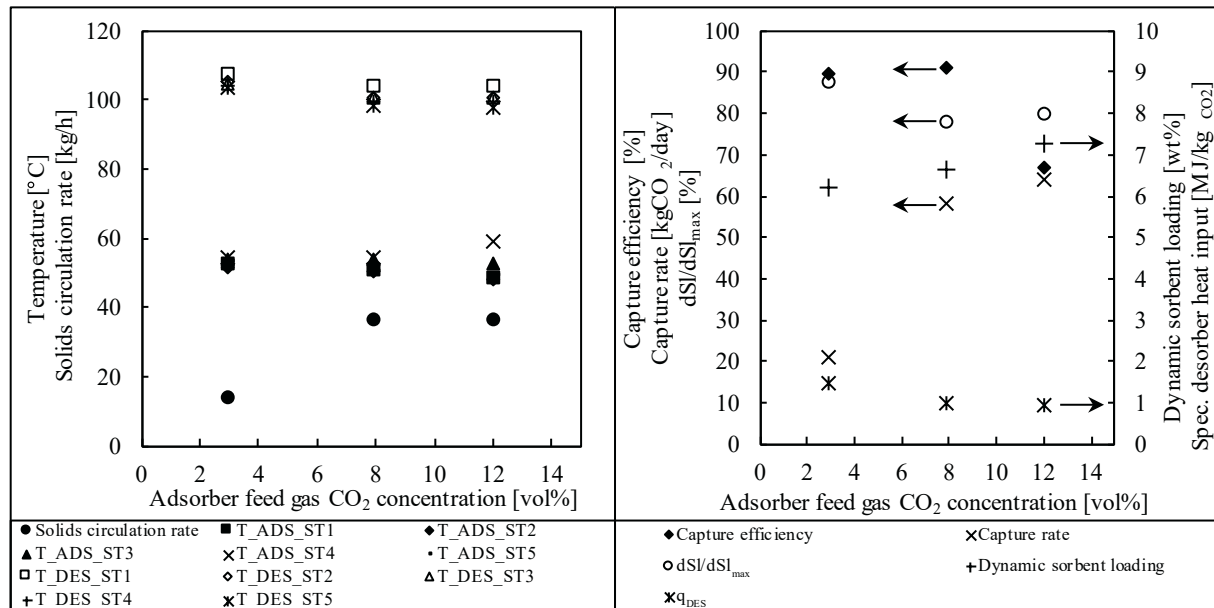
**Figure 41: Graphs showing the results from a variation of the adsorber operating temperature at an adsorber feed gas velocity of 0.32 m·s<sup>-1</sup> and a feed gas CO<sub>2</sub> concentration of 3 vol%CO<sub>2</sub>**

In each operating point, the axial temperature distribution across the adsorber could be kept below 3.1 °C. As can be seen, the temperature increase in the adsorber entailed a reduction of the axial

temperature distribution in the desorber, whereas the average temperature in the desorber increased from 105.2 °C to 107.3 °C. Throughout the entire variation, the CO<sub>2</sub> capture efficiency and the CO<sub>2</sub> capture rate could be kept in a rather small range (i.e. 90.1 % to 90.9 % and 21.2 kg<sub>CO</sub>·day<sup>-1</sup> to 21.6·kg·day<sup>-1</sup> respectively). Due to a decrease of the maximum achievable CO<sub>2</sub> loading of the rich sorbent, brought about by the increasing adsorber operating temperature, an increase of the SCR (i.e. from 12.1 kg·h<sup>-1</sup> to 16.3 kg·h<sup>-1</sup>) was required to keep the CO<sub>2</sub> capture efficiency and the capture rate constant. Because the capture rate is constant, the dynamic sorbent loading can be considered inversely proportional to the SCR. Therefore, the dynamic sorbent loading undergoes a 25 % reduction, from 7.4 wt% to 5.5 wt%, as the adsorber operating temperature is increased. The measured dynamic sorbent loading cannot be used as reference for evaluating the energy efficiency of the operating points carried out in this variation since the column temperatures change considerably. Nevertheless, a significant reduction in the specific desorber heat input was determined as the adsorber operating temperature was increased. When regarding the temperature swing between adsorber and desorber, a decrease of 20 % (from 61.1 °C to 49.0 °C) was observed in the course of the variation, whereas the SCR undergoes an increase of 25 %. Therefore, a change in the sensible heat demand cannot be attributed to the significant reduction of the measured heat input. However, the adsorber feed gas contains considerable amounts of water (i.e. 35.7 g<sub>H<sub>2</sub>O</sub>·Nm<sup>-3</sup>) and an increase in the adsorber operating temperature results in a decrease of the relative humidity in the adsorber feed gas. Since Sorbent B is capable of co-adsorbing water and the adsorption capacity for water can be correlated to the relative humidity [114], more water is transported from the desorber to the adsorber if the relative humidity in the desorber is higher. This entails an increased release of heat through the heat of water-adsorption in the desorber and reduces the amount of heat that must be supplied via the heat exchangers. Nevertheless, it can be seen that  $dSl \cdot dSl_{max}^{-1}$  stays between 85 % and 88 %, whereas no appreciable reduction of this parameter occurs at decreasing adsorber operating temperature. Thus, a dependency of the reaction rate of the sorbent with CO<sub>2</sub> could not be determined for the tested temperature range. Furthermore, the high values of  $dSl \cdot dSl_{max}^{-1}$  that could be achieved suggest that the operating conditions and design of the TSA BSU allow for deep regeneration of the sorbent in the desorber and for the rich sorbent to come close to equilibrium with the adsorber feed gas. High stripping steam flow rates, high desorber operating temperatures, sufficient gas/solids contact, a sufficient solids residence time as well as an adequate number of stages contribute to deep regeneration in the desorber. Similarly, the number of stages contribute to the favorable performance of the adsorber, together with adequate gas/solids contact and a sufficient sorbent residence time.

### Variation D

The results gained from the adsorber feed gas CO<sub>2</sub> concentration variation are shown in Figure 42.



**Figure 42: Graphs showing the results from a variation of the adsorber feed gas CO<sub>2</sub> concentration at an adsorber feed gas velocity of 0.32 m·s<sup>-1</sup>**

As can be seen by the initial decrease of the desorber temperatures (from 105.5 °C to 100.9 °C), the total heat demand in the desorber increases significantly as the CO<sub>2</sub> concentration in the adsorber feed gas increases. Nevertheless, due to disproportionate increase of the capture rate, the specific desorber heat input decreased slightly. Furthermore, the FB temperatures in the adsorber could be kept in a similar range, which suggests that the cooling capacity in the adsorber was sufficient to control the adsorber operating temperature. When regarding the second increase in the CO<sub>2</sub> concentration of the flue gas, from 8 vol%CO<sub>2</sub> to 12 vol%CO<sub>2</sub>, a limitation regarding the achievable SCR was encountered. When attempting to increase the SCR beyond 37 kg·h<sup>-1</sup>, solids started to accumulate in the 5<sup>th</sup> desorber stage, which made continuous operation impossible. This issue has been encountered in the course of Variation B (see Section 4.1.2) and indicates insufficient solids throughput through the downcomer between desorber stages 4 and 5. As can be seen in Figure 42, a noticeable increase in the specific desorber heat demand did not occur. However, in the adsorber the axial temperature distribution increased because adsorber stage 4 could not be sufficiently cooled despite an increase of the cooling water flow rate to this stage. The reason for this temperature increase is not clear, considering that it was possible to cool the sorbent to the adsorber operating temperature in the stage above, i.e. adsorber stage 5, where the cooling demand is typically the highest.

An increase of the CO<sub>2</sub> concentrations in the adsorber feed gas brings about an increase in the driving force of CO<sub>2</sub> adsorption, thus high CO<sub>2</sub> loading of the rich sorbent can be achieved. For the initial two operating points, i.e. the increased from 3 vol%CO<sub>2</sub> to 8 vol%CO<sub>2</sub>, this is reflected by an increase of the dynamic sorbent loading (from 6.2 wt% to 6.5 wt%). However, the significant drop in  $dSI \cdot dSI_{max}^{-1}$  from 87.7 % to 78.2 % indicates that either the sorbent loading distances itself from equilibrium conditions in the adsorber and/or the lean loading of the sorbent at the outlet of the desorber

increased. This is because  $dSl_{max}$  assumes 0 wt%<sub>CO<sub>2</sub></sub> on the lean sorbent, thus an decrease of  $dSl \cdot dSl_{max}^{-1}$  is an indication that equilibrium conditions are not reached in the adsorber and/or the lean loading of the sorbent at the outlet increases.

A similar assumption cannot be made for the second increase of the CO<sub>2</sub> concentration from 8 vol%CO<sub>2</sub> to 12 vol%CO<sub>2</sub> because  $dSl_{max}$  is calculated for a capture efficiency of 90%, which is not achieved in this operating point. It can be assumed that at an adsorber feed gas CO<sub>2</sub> concentration of 12 vol%CO<sub>2</sub> a considerable increase of the SCR would be required to achieve the capture goal of 90%. If the required SCR could be maintained in the BSU, a significant reduction of the desorber temperatures would be likely, which would entail an increase of the CO<sub>2</sub> loading of the lean sorbent. Ultimately this scenario could lead to a decrease of the measured dynamic sorbent loadings and a considerable decrease of  $dSl \cdot dSl_{max}^{-1}$ . It should be mentioned that the dynamic sorbent loading achieved during this operating point was approx. four times higher than the dynamic sorbent loading measured in the TSA system investigated by Veneman et al. [35] when a flue gas with 11vol%CO<sub>2</sub> was treated.

Nevertheless, the performance indicators show an increase of the capture rate throughout the entire variation, whereas the maximum is reached with 64.2 kg<sub>CO<sub>2</sub></sub>·day<sup>-1</sup> at an adsorber feed gas CO<sub>2</sub> concentration of 12 vol%CO<sub>2</sub>. In a previous experiment (see Variation A in Section 4.1.2), a apparent heat transfer limitation was already encountered at a slightly lower capture rate of 61.6 kg<sub>CO<sub>2</sub></sub>·day<sup>-1</sup>. However, because the adsorber feed gas contained a significantly higher CO<sub>2</sub> concentration (12 vol%CO<sub>2</sub> vs 4 vol%CO<sub>2</sub>), higher working capacities could be achieved. Therefore, the contribution of sensible heat to the desorber heat demand is lower here.

### 4.2.3 Conclusion

A variation of the adsorber operating temperature and a variation of the adsorber feed gas CO<sub>2</sub> concentration were conducted in the TSA BSU to investigate the influence of these parameters on the CO<sub>2</sub> capture performance.

During the variation of the adsorber operating temperature, the SCR needed to be increased with increasing temperature so that the desired CO<sub>2</sub> capture goal could be achieved, whilst the specific desorber heat input decreased. The observed reduction in the desorber heat input could not be entirely attributed to a reduction of the sensible heat demand. As the adsorber operating temperature increased, the relative humidity of the adsorber gas decreases and promotes the adsorption of water in the desorber. This entails an increased release of heat through the heat of water-adsorption in the desorber and reduces the amount of heat that must be supplied via the heat exchangers. However, co-adsorbed steam is no longer available in the desorber to act as a fluidization agent. A consequence of this effect was not noticeable in the desorber of the BSU, due to the high stripping steam flow rate. However, in a TSA unit that is optimized for low stripping steam flow rates, more steam may be required to make-up for co-adsorbed steam in order to maintain the operating regime or for sufficient dilution of the desorber gas. Since the heat of water adsorption has been measured to be in the same range as the heat of water evaporation (i.e. 43 kJ·mol<sub>H<sub>2</sub>O</sub><sup>-1</sup> for Sorbent B [114]) the reduction in the measured heat input in the desorber may be added to the heat required to generate additional stripping steam. Due to such implications, it is important to further investigate the impact of water adsorption on the TSA system. Furthermore, increasing dynamic sorbent loadings at decreasing

adsorber operating temperatures are an indication that within the tested range, adsorption of CO<sub>2</sub> on Sorbent B is not limited by reaction kinetics, even at temperatures as low as 42.4 °C.

In the course of the CO<sub>2</sub> concentration variation of the adsorber feed gas, at least 87.7 % of CO<sub>2</sub> could be captured from flue gases containing 3 vol%CO<sub>2</sub> and 8 vol%CO<sub>2</sub>. At the highest CO<sub>2</sub> concentration in the adsorber feed gas, i.e. 12 vol%CO<sub>2</sub>, the capture efficiency was limited by the solids circulation rate. Despite this limitation, a capture rate of 64.2 kg<sub>CO2</sub>·day<sup>-1</sup> could be achieved during this operating point. Nevertheless, it can be assumed that the SCR required to achieve a capture efficiency of 90 % (and thus a capture rate of over 86 kg<sub>CO2</sub>·day<sup>-1</sup>) would exceed the heating and cooling capacity of the TSA BSU. Thus, this operating point underlined the importance of downcomers that allow for achieving high solids throughputs as well as sufficient heating and cooling capacity for achieving the desired capture goal. Downcomer designs that allow for high solids circulation rates, such as those proposed by Zehetner et al. [143] are recommended for larger scale. Regarding heat management, an increased ratio of heat transfer surface to bed volume in the fluidized bed stages or the implementation of heat recovery measures is recommended so that the high sensible and latent heating and cooling demands in the columns can be met even at a high CO<sub>2</sub> concentration in the treated flue gas.

### 4.3 DEGRADATION IN PRESENCE OF NO<sub>x</sub> & SO<sub>2</sub>

Depending on the fuel used in a combustion process, the main constituents of the resulting flue gas are CO<sub>2</sub>, steam, nitrogen, oxygen and trace gases. The general term trace gas refers to gases that are present in very low concentrations, i.e. generally in the ppm range. Trace gases that are specific to combustion processes i.e. SO<sub>2</sub>, NO and NO<sub>2</sub> are of special interest in this campaign since they can induce degradation of amine functionalized sorbents, and thus reduce the CO<sub>2</sub> capture performance of a CO<sub>2</sub> capture process over time. To achieve a constant CO<sub>2</sub> capture performance despite sorbent degradation, degraded sorbent is replaced by fresh sorbent in real application. Thus, sorbent degradation brought about by NO<sub>x</sub> and SO<sub>2</sub> can affect the cost of CO<sub>2</sub> capture. Up to the present, investigations regarding sorbent degradation through SO<sub>2</sub> and NO<sub>x</sub> have only been carried out in thermogravimetric analyzers (TGA) or in fixed-bed setups. In these setups, the contacting regime and the contacting times do not adequately reflect the conditions present in a TSA system that implements FBs. To gain a better understanding of how the CO<sub>2</sub> capture performance of a TSA system, which utilizes an amine-functionalized sorbent, is affected by considerable amounts of SO<sub>2</sub> and NO<sub>x</sub> in the treated flue gas, the BSU was transported to a combined heat and power (CHP) plant in Güssing/Austria, where live flue gas was treated.

It should be noted that the experimental setup during this campaign is not identical to the setup described in Section 3.1. Furthermore, Sorbent A was used throughout the entire campaign.

#### 4.3.1 Experimental setup

##### *Biomass CHP Güssing*

Figure 43 shows the flow diagram of the biomass CHP plant in Güssing/Austria, at which the experimental campaign took place. Biomass chips are fed to a fluidized bed gasifier, where steam is used to produce a high caloric product gas. The product gas is cooled in a heat exchanger, dust is removed in a product gas filter and tar components are separated in a product gas scrubber. The cleaned and cooled product gas is then used for CHP operation. In case the gas engine fails, it is possible to combust the product gas in a hot water boiler for district heating purposes. The off-gas lines of these two components join further downstream. Flue gas was extracted from a nozzle installed in the flue gas duct (see “Tie-in point” in Figure 43).



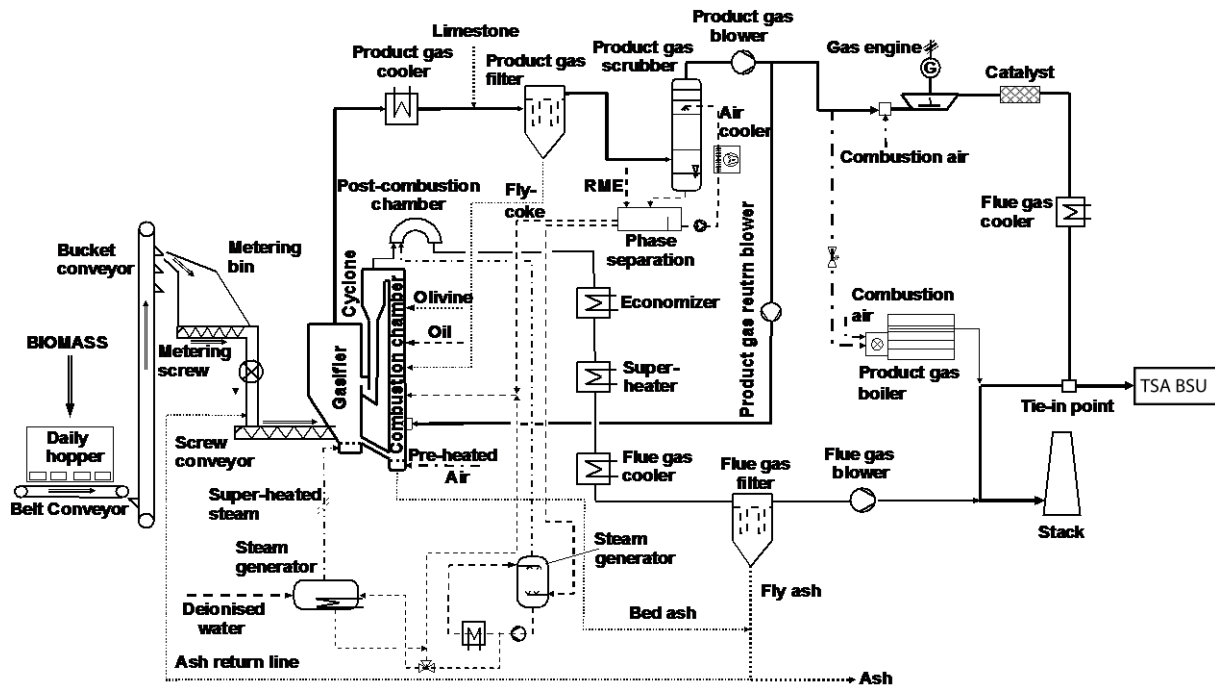


Figure 43: Flow sheet of the CHP-Plant in Güssing, Austria (adapted and translated into English from Güssing Energy Technologies [145])

### BSU setup, instrumentation & methods

This experimental campaign was carried out shortly after the proof of concept for the multi-stage fluidized bed design of the TSA BSU was provided. For this reason, there is slight deviation in the BSU setup compared to the description given in Section 3.1.

The major changes to the experimental setup involve measures implemented to reduce the entrainment rate of coarse solids from the columns, mitigation measures against solids attrition as well as the implementation of additional dust filters and instrumentation to determine the desorber heat demand. In the following, the differences relative to the setup of the TSA BSU as described in Section 3.1 will be detailed.

As can be in Figure 44, two screw conveyors were used in the solids transport section instead of L-valves. It was found that with Sorbent A, these screw conveyors lead to significant attrition. The produced fines pass through the gravitational gas-solids separators and are separated from the recycle gas by the 10- $\mu\text{m}$  canister filters installed upstream of the blowers.

Compared to the configuration shown in Figure 28, the freeboards of the top-most stages were significantly smaller (i.e. 210 mm in the each column compared to 550 mm). This entailed high entrainment rates, not only of fines but also of coarse solids, especially during operational upsets i.e. when solids accumulated in the top-most stages. An exact determination of the solids entrainment rate was not possible since the desorber, where the bulk of solids entrainment occurred, was not equipped with a dust filter between the column exit and the  $\text{CO}_2$  product cooler. For this reason, the entrained solids accumulated in the  $\text{CO}_2$  product cooler and formed a slurry with the formed condensate.

Additionally, a configuration consisting of a fixed bed adsorber (FBA), a three-way valve and a bypass line were installed upstream of the adsorber (not shown in Figure 44). The FBA was filled with “CP

Blend”, an impregnated activated carbon-based pellet-type sorbent supplied by Purafil. This filter material had oxidizing, adsorbing and absorbing properties to separate a broad range of gases including nitrogen oxides ( $\text{NO}_x$ ) and sulphur oxides ( $\text{SO}_x$ ) from the feed gas. With this setup in place, it was possible to pass the flue gas through the FBA to avoid feeding a gas with a high  $\text{NO}_x$  and  $\text{SO}_2$  concentration to the adsorber. Furthermore, the flue gas could be redirected by the three-way valve to bypass the FBA and feed flue gas directly to the adsorber.

It should be noted that a VA40V/R-type rotameter supplied by Krohne followed by a needle valve were used to measure and control the flow rate of extracted flue gas to the adsorber. The utilized rotameter was calibrated for air at  $70^\circ\text{C}$  and a pressure of 1.4 bara, and conformed to the accuracy class 1 according to VDI/VDE 351.

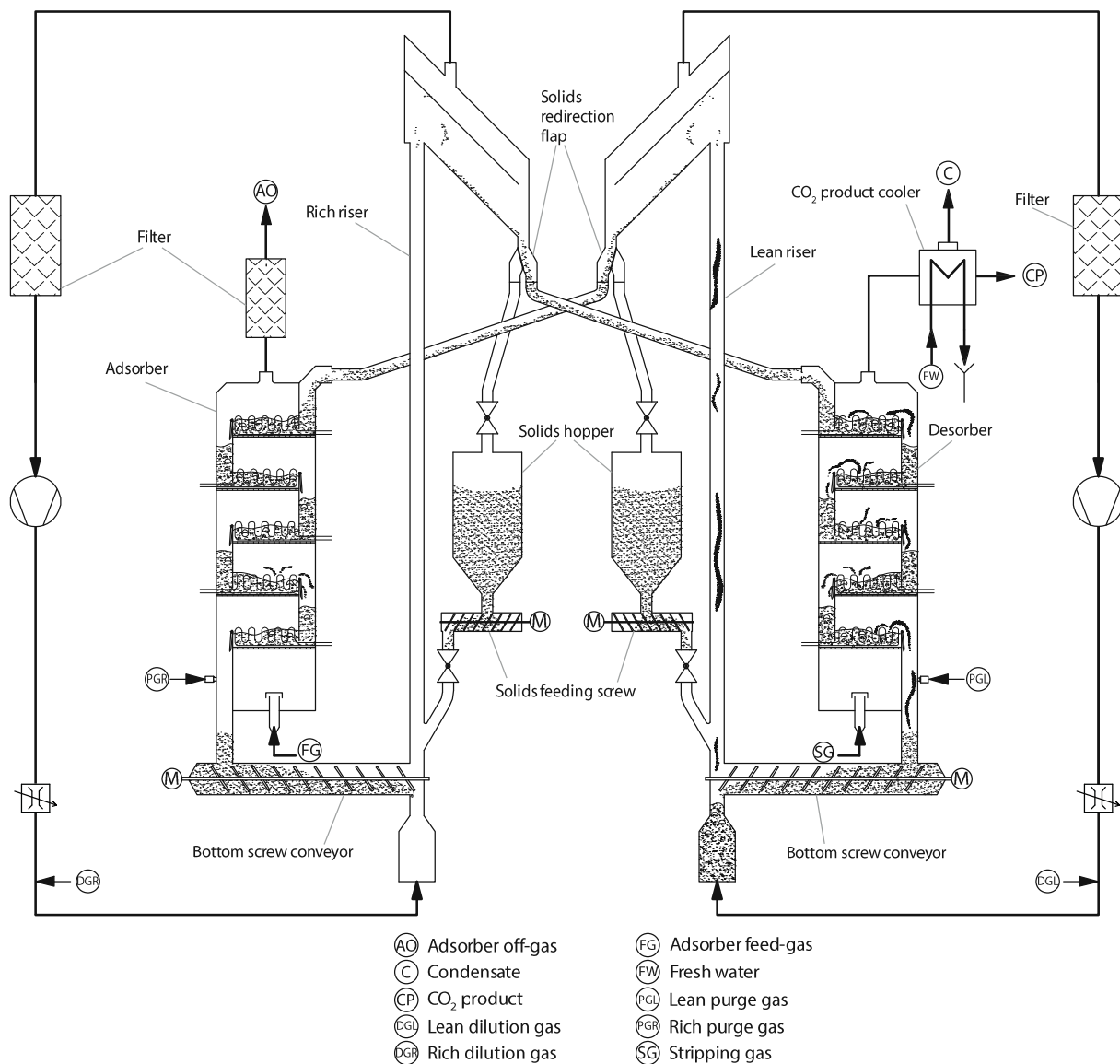


Figure 44: Schematic illustration of the TSA BSU during live-gas testing in Güssing (adapted from Schöny [95])

There was no major deviation between the methods described in Section 3.3 and the methods applied during this campaign. The solids circulation rate and the distribution of the solids inventory was automatically controlled via the drive frequency of the bottom screw conveyors. The bottom screw

conveyors were calibrated, so that the drive frequency of the screw conveyor below the desorber could be used to set the desired SCR (as shown in Schöny et al [146]). Furthermore, the adjacent bottom screw conveyor was used to control the distribution of the solids inventory between the columns. The control value used for this purpose was the desorber pressure drop.

The procedure carried out to determine the SCR was similar as described in Section 3.3.2. The solids redirection flap in the lean transport loop was adjusted to direct lean solids into the empty solids hopper. After an accumulation time of at least 30 seconds, the solids redirection flap was returned to its original position so that the lean sorbent can enter the adsorber. The solids hopper is subsequently emptied into a container, which is weighed. The mass of accumulated solids is then divided by the accumulation time to yield the SCR in  $\text{kg}\cdot\text{h}^{-1}$ . This procedure is repeated three times and the average SCR calculated and used for further calculations.

Additionally to the NDIR sensors used to determine the  $\text{CO}_2$  concentration in the adsorber feed gas and the adsorber off-gas, a multi-component gas analyzer was used to determine the concentration of  $\text{SO}_2$  as well as  $\text{NO}$  and  $\text{NO}_2$ . The utilized analyzer was a Rosemount NGA 2000. This multi-component gas analyzer measured  $\text{NO}$  using NDIR,  $\text{NO}_2$  based on the chemiluminescence principle, and  $\text{SO}_2$  using UV absorption. Each sensor was calibrated with  $\text{N}_2$  (i.e. 0 ppmNO, 0 ppm $\text{NO}_2$  and 0 ppm $\text{SO}_2$ ) and three different calibration gases. The calibration gases exhibited a concentration of 50 ppmNO, 50 ppm $\text{NO}_2$  and 100 ppm $\text{SO}_2$ . It should be noted that by installing a three-way valve upstream of the Rosemount NGA 2000, the source of the measuring gas was switchable, thus allowing continuous  $\text{SO}_2$  and  $\text{NO}_x$  measurement of either the adsorber feed gas or the adsorber off-gas.

It should be noted that the degradation rate of the sorbent was evaluated based on the reduction of the capture performance in the experimental runtime. Furthermore, the SCR was measured after each operating point and the extracted sorbent material returned to the TSA BSU after the SCR was determined.

#### 4.3.2 Operating conditions

The effect of  $\text{NO}$ ,  $\text{NO}_2$  and  $\text{SO}_2$  were investigated in the course of three different operating points, henceforth referred to as Test A, Test B and Test C. As can be seen in Table 13, the target operating temperature and gas feeding rates of both columns as well as the  $\text{CO}_2$  and  $\text{O}_2$  concentration of the adsorber feed gas were kept constant for all operating points.

Adsorber operating temperature	70-80	[°C]
Adsorber superficial gas velocity	0.3	[ $\text{m}\cdot\text{s}^{-1}$ ]
Adsorber feed gas $\text{O}_2$ concentration	10	[vol% $\text{O}_2$ ]
Adsorber feed gas $\text{CO}_2$ concentration	9	[vol% $\text{CO}_2$ ]
Steam flow to adsorber	0	[ $\text{kg}\cdot\text{h}^{-1}$ ]
Desorber operating temperature	120-125	[°C]
Desorber stripping steam flow-rate	8.5	[ $\text{kg}\cdot\text{h}^{-1}$ ]

**Table 13: Target operating conditions during the conducted degradation tests**

Test A was carried out to serve as a benchmark for all following operating points. Here, the treated gas was mixed from bottles and an identical  $\text{CO}_2$  and  $\text{O}_2$  concentration as measured in the flue-gas of the

gas engines was set. During this operating point, the SCR was adjusted to achieve a capture efficiency of 90%. This SCR served as a set value for all subsequent operating points. In Test B, flue gas from the gas engines, which had been pre-conditioned by the FBA located upstream of the adsorber, was treated by the TSA BSU. In the last test, Test C, the FBA was bypassed thus directing flue gas from the gas engines directly to the adsorber.

It should be noted that Test A and Test B are representative three-hour excerpts of a 24 hour-test. This was done, to allow a comparison to Test C, which features a considerably higher  $\text{NO}_x$  and  $\text{SO}_2$  concentration. Graphs showing the selected performance indicators throughout both 24-hour tests can be found in the Appendix (see Figure 67 and Figure 68).

### 4.3.3 Results & Discussion

As can be seen in Table 14, an SCR of  $23.5\text{kg}\cdot\text{h}^{-1}$  was necessary to achieve a capture efficiency of 90% during Test A; for the subsequent tests only a slight deviation from this SCR was determined. The adsorber operating temperatures deviated only slightly from the target operating temperature of 70-80 °C. In the desorber, it was possible to maintain the operating temperature window between 119 °C to 126°C for all operating points.

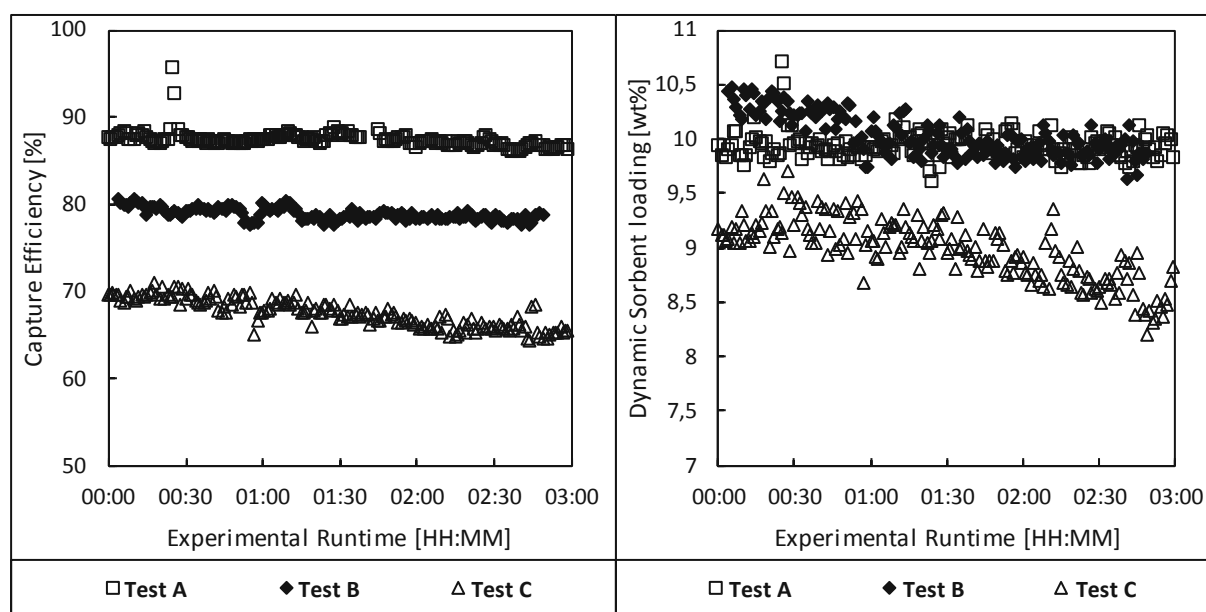
The greatest deviation from the target value is seen in the adsorber feed gas velocity. Here, a superficial gas velocity of  $0.3\text{ m}\cdot\text{s}^{-1}$  in the adsorber was targeted for all operating points. As can be seen, this is only achieved for the initial operating point, where the entirety of the adsorber feed gas was mixed from bottles. In the following operating points, the superficial gas velocity in the adsorber increases to  $0.33\text{ m}\cdot\text{s}^{-1}$  and  $0.36\text{ m}\cdot\text{s}^{-1}$ . This was due to frequent fluctuations in the load of the gas engine, which ultimately entailed a fluctuating flow rate of flue gas into the adsorber. Rather than constantly adjusting the flow rate via the needle valve located downstream of the flue gas rotameter, it was chosen to set the needle valve to the desired value at the beginning of each test and leave this setting unchanged for the rest of the test. These load fluctuations of the gas engine had a rather low impact on the time-averaged  $\text{O}_2$  and  $\text{CO}_2$  concentration of the produced flue gas.

Nevertheless, it can be seen that the concentration of  $\text{SO}_2$  and  $\text{NO}_x$  could be varied in a broad range. By preconditioning the flue gas in the course of Test B, the  $\text{NO}$  concentration of the adsorber feed gas could be reduced to 65 ppm, whilst  $\text{NO}_2$  and  $\text{SO}_2$  was almost removed completely, i.e. 5 ppm $\text{NO}_2$  and 1 ppm $\text{SO}_2$  in the adsorber feed gas respectively. It can be seen, that at the time of Test C the  $\text{NO}$  concentration was beyond the detection limit of the utilized analyzer (i.e. 180 ppm $\text{NO}$ ) whilst, the concentration of  $\text{NO}_2$  and  $\text{SO}_2$  in the flue gas were 140 ppm $\text{NO}_2$  and 35 ppm $\text{SO}_2$  respectively.

	Test A	Test B	Test C	
Solids circulation rate	23.5	23.4	23.7	[kg·h <sup>-1</sup> ]
Adsorber operating temperature	67.4-78.4	68.7-80.9	69.9-78.8	[°C]
Adsorber feed gas velocity	0.30	0.33	0.36	[m·s <sup>-1</sup> ]
Adsorber feed gas O <sub>2</sub> concentration	10.8	10.8	11.1	[vol%O <sub>2</sub> ]
Adsorber feed gas CO <sub>2</sub> concentration	9.0	9.1	9.2	[vol%CO <sub>2</sub> ]
Adsorber feed gas NO concentration	0	65	>180	[ppmv]
Adsorber feed gas NO <sub>2</sub> concentration	0	5	140	[ppmv]
Adsorber feed gas SO <sub>2</sub> concentration	0	1	35	[ppmv]
Steam flow to adsorber	0	0	0	[kg·h <sup>-1</sup> ]
Desorber operating temperature	119.2-123.5	121.4-123.6-	122.3-126.0	[°C]
Desorber stripping steam flow-rate	8.5	8.5	8.5	[kg·h <sup>-1</sup> ]

**Table 14: Operating conditions of the TSA BSU during the conducted degradation tests (values are averaged over the entire runtime)**

Figure 45 shows the capture efficiency and the dynamic sorbent loading in the course of all tests conducted in this campaign.



**Figure 45: Capture efficiency and dynamic sorbent loading during the conducted degradation tests**

Despite an absence of NO<sub>x</sub> and SO<sub>2</sub> in the adsorber feed gas, a minor decline of the capture efficiency is apparent in the course of Test A. Since the column temperature and SCR were kept in a narrow range during all tests, the root cause for the slight decline of the capture efficiency is due to loss of active amine sites on the sorbent. Amine loss can be caused by solids entrainment, thermal degradation/amine leaching (i.e. volatilization of low molecular-weight amines from the sorbent material) and oxidative degradation (i.e. oxidation and subsequent loss or deactivation of amines). It should be noted that urea formation can be excluded because the desorber is fluidized by steam, which

is known to prevent and even reverse urea formation (see Section 2.4.1). The average dynamic sorbent loading throughout Test A was calculated to 10 wt%, whereas the trend throughout the experimental runtime was similarly flat as the capture efficiency.

When regarding the capture efficiency of Test B, it can be seen that there is a difference of almost 6 % between the start of Test B and the end of Test A. The reason for this is that the data seen for Test A and Test B are excerpts taken from the end of 24-hour experiments as shown in the Appendix (see Figure 67 and Figure 68). This means that prior to the start of Test B, the sorbent material had already been exposed to a rather low concentration of  $\text{NO}_x$  and  $\text{SO}_2$  as well as potential thermal degradation for approx. 19 hours. However, it can be seen that the trend of the capture efficiency deteriorates at a slightly faster rate than during Test A i.e.  $-0.56 \text{ \%}\cdot\text{h}^{-1}$  during Test B compared to  $-0.46 \text{ \%}\cdot\text{h}^{-1}$  during Test A. Since the increase in the flue gas feeding rate is higher than the decrease in capture efficiency in Test B, the dynamic sorbent loading starts at a higher value at the beginning of Test B compared to Test A. It can be seen that the dynamic sorbent loading settles at an average of 10.7 wt%, which is similar to the dynamic sorbent loading achieved during Test A. It is important to note that the inlet and outlet concentration of  $\text{NO}_2$ ,  $\text{SO}_2$  and  $\text{NO}$  were measured multiple times in the course of Test B. It was found that  $\text{NO}_2$  and  $\text{SO}_2$  could no longer be detected at the outlet of the adsorber, whilst  $\text{NO}$  apparently passed through the adsorber. This is a strong indication that  $\text{NO}$  does not interact with the Sorbent A, and thus does not cause degradation. These measurements were repeated in the course of Test C, with similar results. Although the  $\text{SO}_2$  and  $\text{NO}_2$  levels were exceptionally high in the adsorber feed gas, Sorbent A could effectively remove these constituents from the flue gas whilst not interacting with  $\text{NO}$ . A similar result was seen in the course of fixed bed tests conducted by Rezaei and Jones [133]. Here an amine functionalized sorbent was exposed to 200 ppmNO for multiple cycles resulting in no noticeable change in the  $\text{CO}_2$  capacity, whilst  $\text{NO}_2$  and  $\text{SO}_2$  were irreversibly bound. In this campaign however it could not be ascertained whether  $\text{SO}_2$  and  $\text{NO}_2$  were bound to the sorbent irreversibly because the  $\text{CO}_2$  product was not analyzed for  $\text{NO}_2$  and  $\text{SO}_2$ . In the light of the severe deterioration of the  $\text{CO}_2$  capture performance during Test C, i.e. an average capture performance reduction of  $-1.7 \text{ \%}\cdot\text{h}^{-1}$ , irreversible degradation of the  $\text{CO}_2$  capacity of the sorbent can be assumed.

From the concentration of  $\text{NO}_2$  and  $\text{SO}_2$  during Test C, it can be estimated that a total of  $0.33 \text{ mol}_{\text{NO}_2}$  and  $0.08 \text{ mol}_{\text{SO}_2}$  had adsorbed onto Sorbent A during the experimental runtime. Rezaei and Jones [133] concluded from fixed bed experiments that  $\text{SO}_2$  and  $\text{NO}_2$  are irreversibly bound to amine functionalized sorbents. If the same assumption is made for the experimental campaign presented in this work, and assuming that these constituents react with the same stoichiometry with the amines as  $\text{CO}_2$ , this would lead to a reduction of the sorbent working capacity by 3.9 %, i.e. from 9.2 wt% to 8.8 wt% during the experimental runtime. This value is the same order of magnitude as the measured reduction of the dynamic sorbent loading within the experimental runtime of 6.7 %, i.e. from 9.2 wt% to 8.6 wt%.

#### 4.3.4 Conclusion

In the course of an experimental campaign, the  $\text{CO}_2$  capture performance of the TSA BSU was investigated at different concentrations of  $\text{NO}$ ,  $\text{NO}_2$  and  $\text{SO}_2$  of a flue gas.

In the course of two tests with 65 ppmNO and over 180 ppmNO present in the flue gas, the inlet and outlet concentrations of  $\text{NO}$  in the adsorber revealed that  $\text{NO}$  passed through the column. This

indicates that NO does not lead to degradation of Sorbent A and thus confirms observations made in a fixed bed setup by Rezaei and Jones [133].

It was shown that a concentration of 35 ppmSO<sub>2</sub> and 140 ppmNO<sub>2</sub> in the flue gas leads to severe sorbent degradation and thus to a reduction of the CO<sub>2</sub> capture performance of the BSU. When brought into contact with primary amines, SO<sub>2</sub> forms sulfites and sulfates [147]. For this reason, it is assumed that sulfites and sulfates will form and accumulate on the surface of the amine-functionalized sorbents upon prolonged exposure to SO<sub>2</sub>. The resulting conversion of amine groups entails a reduction in the sorbent CO<sub>2</sub> adsorption capacity. Since the detrimental reaction of amines with SO<sub>2</sub> is intrinsic to the alkaline nature of amines, strategies that aim at reclaiming the adsorptive properties of the sorbent can be recommended as subject for future research. During investigation performed by Hallenbeck et al. [135], 35 % of the CO<sub>2</sub> capacity of an amine functionalized sorbent poisoned by SO<sub>2</sub> could be regained after treatment with NaOH. From this result, it was reasoned that SO<sub>2</sub> degradation occurs by at least two mechanisms, one of which can be reversed by NaOH. Similar strategies may be a cheaper alternative to replacing degraded sorbent with fresh one and may even be cheaper than reducing the SO<sub>2</sub>-level of the treated flue gas to levels acceptable for the utilized sorbent.

Nitramines and nitrosamines are known to be toxic and potentially carcinogenic [148]. The formation of these compounds are amongst the high number of possible reaction-pathways for primary and secondary amines with NO<sub>2</sub>. Whilst primary amines only form a highly unstable nitrosamine, Fostås et al. [105] have shown that MEA, a primary amine can degrade to a secondary amine, which in turn can form stable nitrosamines. If stable and volatile nitramines or nitrosamines are formed in a TSA process, these compounds will eventually be emitted from the process and will need to be removed from the respective streams. Since these measures would increase the cost of CO<sub>2</sub> capture, it is recommended that future investigations analyze the off-gases of the columns and the CO<sub>2</sub> cooler condensate for nitramines and nitrosamines when NO<sub>2</sub>-containing flue gases are treated.

## 4.4 EMISSIONS FROM AMINE FUNCTIONALIZED SOLID SORBENT

In amine scrubbing units, amine loss over the absorber off-gas can be considerable due to e.g.  $\text{SO}_3$  [106] or dust [107] present in the flue-gas, amine volatility [149] or oxidative degradation of the solvent [98]. To conform to environmental guidelines, amine emissions in the  $\text{CO}_2$  depleted flue-gas must be minimal (e.g. daily average of maximum 6 ppmv total amines [101]). Typically, emissions are reduced by means of a water-wash section down-stream of the absorber [150], whereas the resulting effluent is returned to the process. However, considerable amine emissions in form of aerosols or  $\text{NH}_3$  emissions can persist despite a water wash section [103,108]. In MEA-based scrubbers such effects may make alternative emission reduction measures, such as Brownian demister units [108] or acid wash systems [103,104] necessary.

Emission reduction measures such as the ones mentioned above, not only increase investment cost but can also increase the operating cost of PCCC processes. This is because end-of-pipe emission reduction measures typically add a pressure drop to the flue gas path and thus lead to an increased power requirement of the flue-gas blower. It is therefore key for any PCCC system to identify emissions and assess whether auxiliary systems are required for the removal of critical components. For this reason, two 120-hour experiments were carried out in the TSA BSU, each with a different type of amine-functionalized sorbent. The sorbents that were subject of these investigations were Sorbent A and Sorbent B, whereas the corresponding experiments will be referred to as Experiment A and Experiment B. During these experiments, comprehensive sampling of various gas and liquid streams took place to determine the emissions of the BSU throughout the experimental runtime. Furthermore, tests were carried out by a project partner in a TGA to determine whether the  $\text{CO}_2$  adsorption capacity of the utilized sorbents decreases in the course of the experiments.

In the course of this campaign, the experimental setup corresponded to the description given in Section 3.1 whereas additional sampling nozzles were installed to allow for sample collection.

### 4.4.1 Experimental Setup

In the experimental campaign discussed in this section, numerous liquid and solid samples were collected to determine process emissions and particle attrition respectively. Liquid, gaseous and solids samples were taken via the five sampling valves shown in Figure 46.



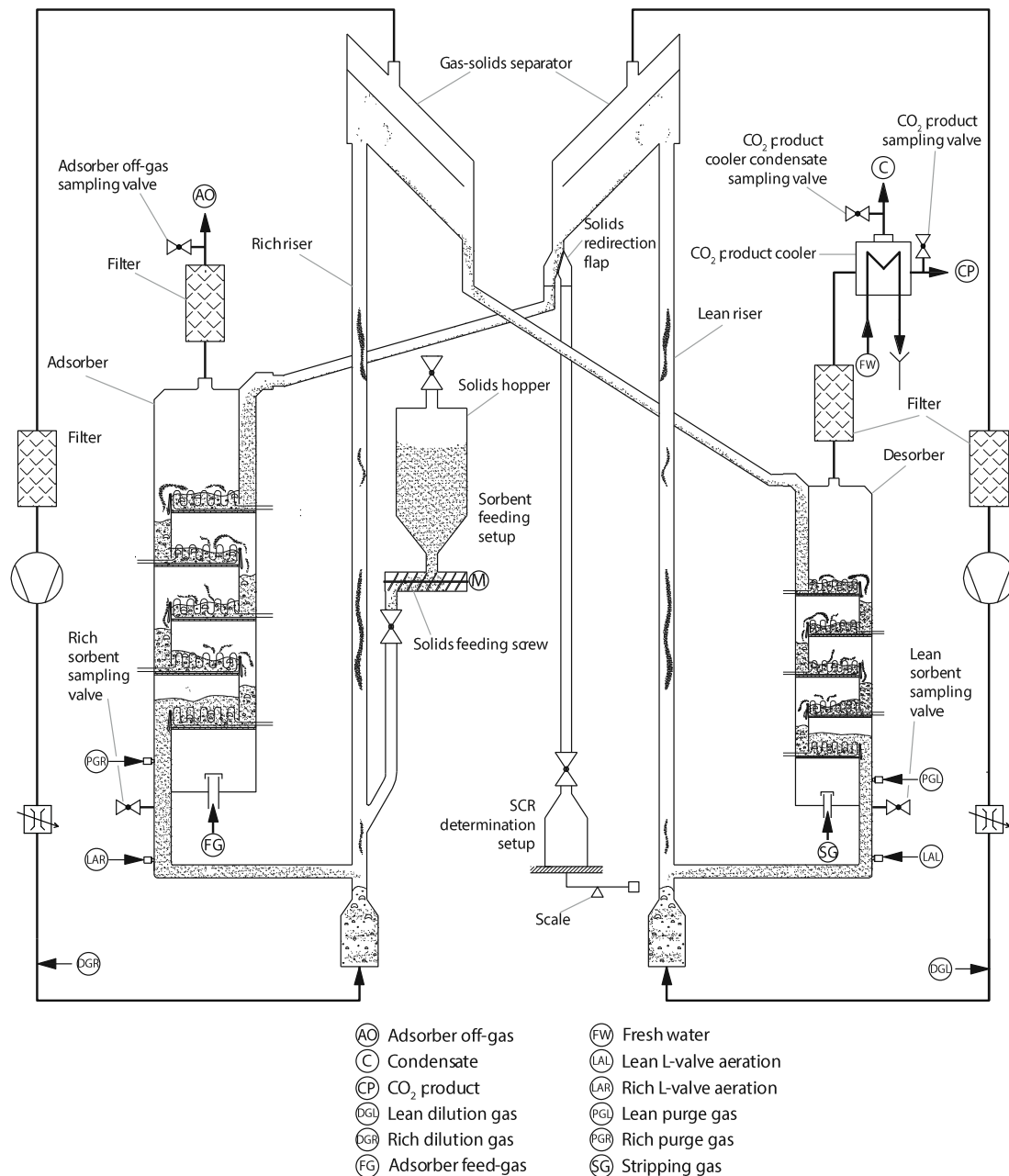


Figure 46: Schematic illustration of the TSA BSU during the emission tests

Gaseous emissions in the adsorber off-gas or CO<sub>2</sub> product were determined either by means of detector tubes measurements or by diverting a partial flow of these gases through an impinger setup, and subsequently carrying out chemical analyses on the contents of the impingers. The impinger setup consisted of a heated hose, a cascade of impingers, a gas-sampling pump and a gas meter. It should be noted that isokinetic sample extraction principles were not followed in this campaign, as neither mist nor dust was expected at the sample extraction locations. The impinger cascade was immersed in the basin of a cryostat cooled to approx. 4°C. The contents of three impingers was used for analyses. The first impinger was empty and used to sample condensate, whereas two subsequent impingers were filled with approx. 100 ml of ultra-pure water for the collection of water-soluble components from the sampled gas. The utilized gas-sampling pump featured a rotameter, a needle valve and a thermocouple

installed in the gas passage. The flow rate of gas was set  $1 \text{ l}\cdot\text{min}^{-1}$  whereas the sampling duration was approx. 1 hour. A diaphragm gas meter installed at the end of this setup determined the volume of sampled gas. Moreover, the condensate formed in the  $\text{CO}_2$  product cooler was sampled daily via the  $\text{CO}_2$  product cooler condensate sampling valve (shown in Figure 46). Measurements carried out with detector tubes were taken at the adsorber off-gas sampling valve and the  $\text{CO}_2$  product sampling valve. Valves installed in the moving bed sections below the columns (see rich and lean sorbent sampling valves in Figure 46) were used to extract samples of lean and rich sorbent. It should be noted that solids sampling was carried out according to the procedure described in Section 3.1.6, thus thus sorbent material within the dead volume between the sorbent sampling device (shown in Figure 34) and the moving bed was discarded. Furthermore, the  $10\text{-}\mu\text{m}$  canister-type dust filters installed in the off-gas lines of the columns as well as those within the riser loops were weighed before and after each experiment to determine the mass of elutriated fines.

#### 4.4.2 Analytical methods

Amine leaching or evaporation of active amine sites as well as degradation of amines and subsequent loss will result in nitrogenous emissions and to the emission of organic carbons. To quantify these emissions in the adsorber off-gas,  $\text{CO}_2$  product and  $\text{CO}_2$  product cooler condensate, the contents of the impingers as well as  $\text{CO}_2$  product cooler condensate samples were analyzed regarding their total organic carbon (TOC) and total nitrogen (TN) content. TOC measurements were carried out according to ASTM D7573 using a Shimadzu TOC-L<sub>CPH</sub>-type analyzer with a quantification limit of  $5 \text{ mg}\cdot\text{l}^{-1}$ . A Multitek N/S elemental boat-type analyzer was used to determine the TN content of samples in accordance with ASTM D5762. The quantification limit of this analyzer was  $1 \text{ mg}\cdot\text{l}^{-1}$ .

In addition, gas detector tubes supplied by Gastec Corporation were used to measure the concentration of various species in the off-gases of the adsorber and desorber during the experiments. Amine emissions were measured using detector tubes No. 180 and No. 180L. Although these detector tubes are designed to measure the concentration of primary amines, they can also be used to measure a range of other amines. Furthermore, the presence of some nitrogenous substances e.g. ammonia in the measuring gas lead to the increased readings of the amine concentration. For more information on the measuring interferences of detector tubes No. 180 and No. 180L, the reader is referred to the respective instruction manuals [151,152]. Detector tube No. 180, was used to measure the concentration of amines in the adsorber off-gas during Experiment A and had a measuring range of 5-100 ppm. Since lower emissions were expected for Experiment B, detector tubes with a higher sensitivity were used. These detector tubes (No. 180L) had a measuring range of 0.5-10 ppm. Detector tube measurements of amines were not carried out for the  $\text{CO}_2$  product as it was assumed that amines would be found in the condensate of the  $\text{CO}_2$  product cooler rather than in the  $\text{CO}_2$  product itself. This assumption was verified by occasional detector tube measurements conducted on the  $\text{CO}_2$  product during both 120-hour experiments. Since aldehyde-formation is associated with amine degradation, the concentration of formaldehyde and acetaldehyde was also monitored at the gas outlets of the TSA BSU. The concentration of formaldehyde was measured with detector tubes No. 92 and No. 92L, with a measuring range of 5-750 ppm and 1-20 ppm respectively. Furthermore, detector tubes No. 91M and No. 91L were used to measure the concentration of acetaldehyde in the concentration range of 8-6400 ppm and 0.1-40 ppm respectively.

Deactivation of amine functionalized sorbent materials can be a result of thermal and oxidative degradation, which in turn can bring about emissions. To evaluate the extent of these degradation mechanisms within the BSU during the 120-hour tests, a TGA study was conducted with both sorbent materials in absence of oxygen. By carrying out over 100 desorption/adsorption cycles with fresh samples of the utilized sorbents, the sorbent was exposed to thermal degradation alone, rather than oxidative degradation or amine loss through fragmentation. For these tests, a Mettler Toledo TGA/SDTA 851e-type TGA was used. Whilst Sorbent A could be investigated in TGA without pre-treatment, it was observed that Sorbent B yielded convoluted results in TGA tests if not dried in advance. This was because of water evaporation. For this reason, Sorbent B was dried for 4 hours at a temperature of 120°C in a N<sub>2</sub> atmosphere. The cyclic tests were initiated with a desorption step. Here, the sorbent was held at a temperature of 120°C for 1 hour in an N<sub>2</sub> atmosphere. The sample of Sorbent A was then cooled to 75°C, whereas Sorbent B was cooled to 50°C. Once this temperature was reached, N<sub>2</sub> was partially replaced by CO<sub>2</sub> to form a gas mixture containing 4 vol%CO<sub>2</sub>. These conditions were held for 1 hour. The next desorption step was initiated after CO<sub>2</sub> was replaced by N<sub>2</sub> and the sorbent was heated to 120°C.

The CO<sub>2</sub> adsorption capacity measured in the course of the cyclic test was compared to the CO<sub>2</sub> adsorption capacity of sorbent samples taken in the course of the 120-hour tests. The CO<sub>2</sub> adsorption capacity of sorbent samples was determined by subjecting the sample to a single desorption/adsorption cycle in the TGA. The duration and conditions during the adsorption and desorption cycle were identical to those during the cyclic tests.

#### **4.4.3 Operating conditions**

The flue-gas treated in the course of both 120-hour tests was generated synthetically from bottled gases (N<sub>2</sub> & CO<sub>2</sub>) and dry pressurized air. Its composition was chosen in a way to mimic the flue-gas of a natural gas combined cycle. Thus, the adsorber was fluidized by a gas containing a relatively low CO<sub>2</sub> concentration of 4 vol%CO<sub>2</sub> and an oxygen concentration of 9 vol%O<sub>2</sub>. Table 15 shows that the sorbent inventory of the BSU was 1.1 kg higher for Experiment A than for Experiment B. This was due to the difference in bulk density between the two sorbents. Nevertheless, the hydrodynamic properties of the two sorbents were similar enough to be able to operate both experiments at the same gas-feeding rates in the columns.

	Experiment A	Experiment B	
Flue-gas flow rate	16.8	16.8	[Nm <sup>3</sup> ·h <sup>-1</sup> ]
N <sub>2</sub> flow rate	8.9	8.9	[Nm <sup>3</sup> ·h <sup>-1</sup> ]
CO <sub>2</sub> flow rate	0.7	0.7	[Nm <sup>3</sup> ·h <sup>-1</sup> ]
PA flow rate	7.2	7.2	[Nm <sup>3</sup> ·h <sup>-1</sup> ]
Adsorber steam flow	0	0.6*	[kg·h <sup>-1</sup> ]
Flue-gas O <sub>2</sub> concentration	9	9	[vol%]
Flue-gas CO <sub>2</sub> concentration	4.2	4.2	[vol%]
Target adsorber operating temperature	70-75	45-50	[°C]
Stripping steam feeding rate	8.5	8.5	[kg·h <sup>-1</sup> ]
Target desorber operating temperature	120-125	100-105	[°C]
Sorbent inventory	6	4.9	[kg]

**Table 15: Bench scale unit feed-gas properties and sorbent inventories during two 120-hour experiments with different types of amine functionalized solid sorbents. \*Steam added to adsorber feed-gas during Experiment B to eliminate electrostatic charging.**

As can be seen in Table 15, the target operating temperatures of the adsorber and the desorber vary between the two 120-hour tests. These temperatures were chosen in accordance with the sorbent properties and manufacturer recommendations. For the PEI impregnated sorbents such as Sorbent A, Xu et al. [125] have found that a drastic reduction of the adsorption rate can be expected at temperatures below 75 °C since the adsorption step is kinetically controlled. The only feasible option for achieving high working capacities with these types of sorbents is thus to set the adsorber operating temperature as close to this threshold as possible, ergo a target adsorber operating temperature of 70-75 °C was chosen for Experiment A. In the TSA BSU, the target desorber operating temperature was strongly influenced by the amount of heat that could be transferred in the columns and the desired working capacity of the sorbent. It was found that a desorber operating temperature of 120 °C, was feasible regarding the heating and cooling demand in the columns, allowed high working capacities and allowed for high cyclic stability of the PEI impregnated sorbent [118].

For Sorbent B, manufacturer specifications stated a maximum operating temperature of 100 °C. However, to avoid condensation of stripping steam in the desorber, the maximum operating temperature of the desorber was chosen to 100-105 °C. Furthermore, a limitation concerning the adsorption rate, as observed with Sorbent A did not apply to Sorbent B. Therefore, the adsorber operating temperature was mainly governed by the amount of heat that can be extracted from the adsorber at a certain CO<sub>2</sub> capture rate than by the adsorption rate. It was found that an adsorber operating temperature between 45 °C and 50 °C allowed for acceptable working capacities and sufficient cooling and heating in the columns of the TSA BSU.

It is clear that the operating temperatures of the process can have an influence on the degradation rate of the utilized sorbents and thus process emissions. However, process emissions are not only a result of the utilized sorbent, but also a result of process conditions required to allow for efficient CO<sub>2</sub> capture. Although it may be possible to operate the TSA BSU with Sorbent A at Experiment B-conditions and vice versa, these operating conditions would not be representative for practical application, where efficient CO<sub>2</sub> capture at low-cost is the primary goal.

#### 4.4.4 Results & Discussion

Table 16 shows the SCR required to achieve the 90% capture goal, as well as the median operating temperature over all 5 stages for the entire experimental runtime. As can be seen, a lower SCR was necessary to achieve the 90% capture target with Sorbent A, compared to Sorbent B because of the higher amine loading of Sorbent A.

	Sorbent A	Sorbent B	
Median adsorber operating temperature	68.1	49.1	[°C]
Median desorber operating temperature	126.3	103.3	[°C]
Solids circulation rate	13.5	15.4	[kg·h <sup>-1</sup> ]

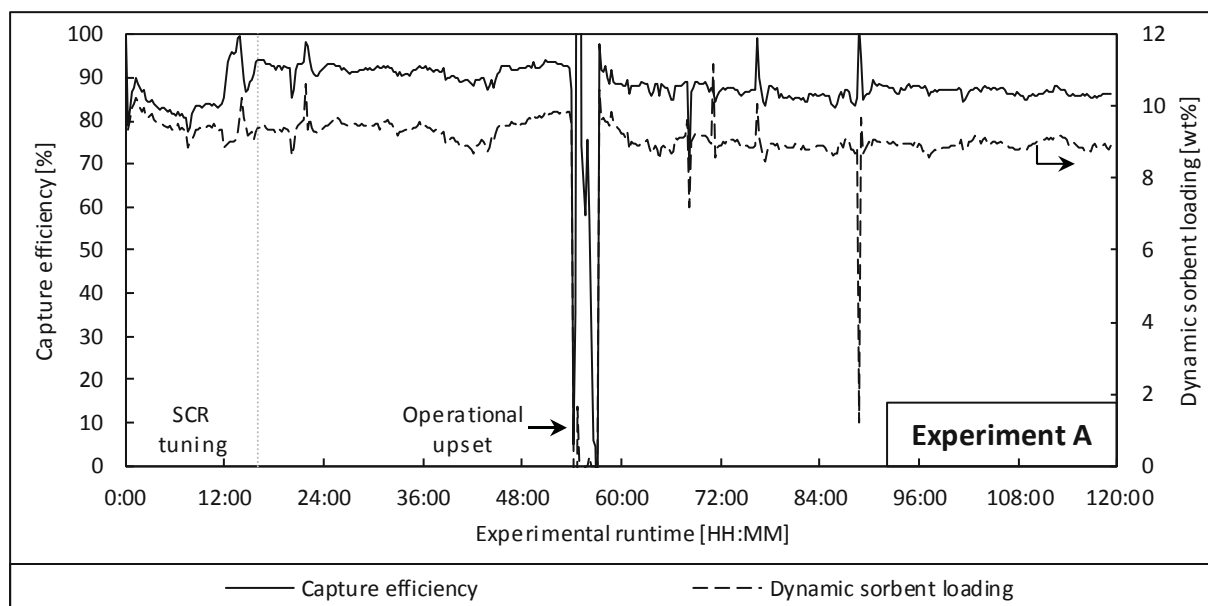
**Table 16: Median operating temperature range and solids circulation rate during two 120-hour experiments with Sorbent A and Sorbent B**

The temperatures of each fluidized bed stage in the columns together with the SCR in the course of both Experiment A and Experiment B are shown in the appendix of this work (see Figure 69 & Figure 70).

In the following, the CO<sub>2</sub> capture performance, results regarding gaseous and liquid emission and results from TGA tests will be presented.

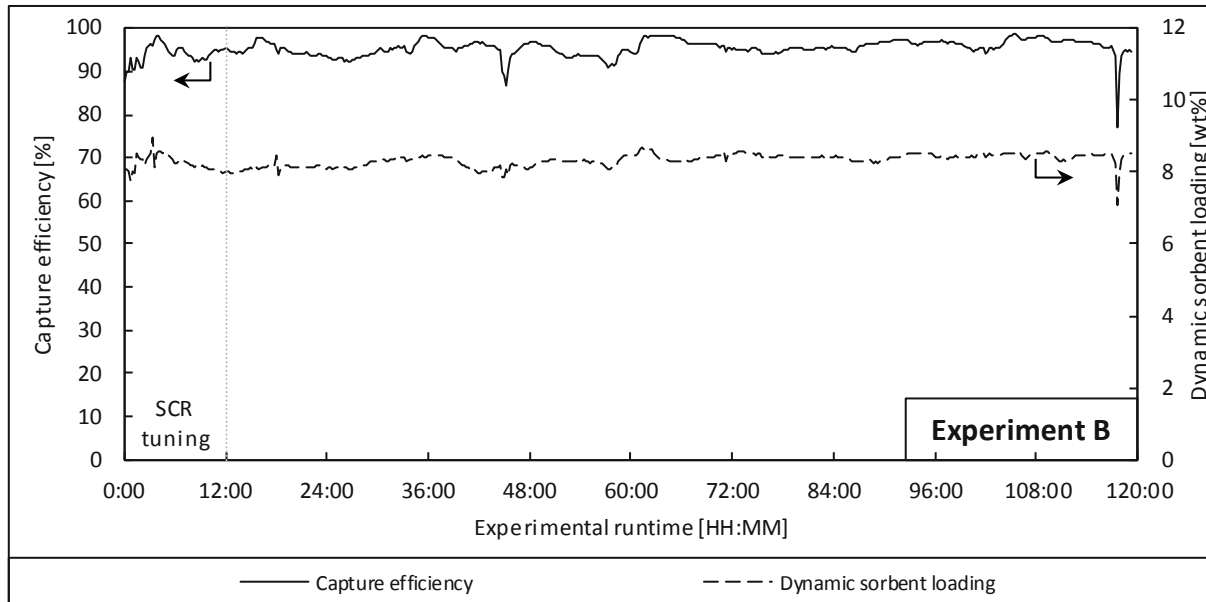
#### CO<sub>2</sub> capture performance

As mentioned, the SCR was varied in the initial hours of the experiments to reach a capture efficiency of over 90%. As can be seen in Figure 47, this was achieved after approx. 16 hours of Experiment A. At hour 54, an operational upset occurred due to condensation of steam near the solids outlet of the desorber, which ceased solids circulation. However, after brief maintenance work, operation continued. It can be seen that the capture efficiency continuously decreases from approx. 94% in the 16<sup>th</sup> hour to about 86% at 120 hours.



**Figure 47: Graphs showing the CO<sub>2</sub> capture performance in the course of the 120-hour experiment using Sorbent A.**

As shown in Figure 48, the CO<sub>2</sub> capture performance in the course of the experiment with Sorbent B was more stable compared to the former experiment. Here the SCR was varied until the 12<sup>th</sup> hour, where a capture efficiency of 95% could be achieved. After this point, a steady decline of the CO<sub>2</sub> capture performance, as seen during Experiment A cannot be determined, which indicates a lower amine degradation and loss rate.



**Figure 48: Graphs showing the CO<sub>2</sub> capture performance in the course of the 120-hour experiment using Sorbent B.**

### ***Gaseous emissions***

As can be seen in Table 17 and Table 18, the TOC content of a majority of impinger samples taken during both experiments was below the detection limit of the utilized analyzer. The exceptions were TOC and TN measurement of samples from CO<sub>2</sub> product-impingers taken during Experiment A. Here the TOC content ranged from 3.81 mg<sub>C</sub>·kg<sub>CO<sub>2</sub></sub><sup>-1</sup> up to 5.46 mg<sub>C</sub>·kg<sub>CO<sub>2</sub></sub><sup>-1</sup>. Similarly, the TN content of impinger samples was highest when CO<sub>2</sub> product was sampled during Experiment A and reached values up to 0.55 mg<sub>N</sub>·kg<sub>CO<sub>2</sub></sub><sup>-1</sup>. It should be noted that when interpreting the measured TN content as being attributed entirely to ammonia emissions, which is often measured in amine scrubbing processes, the resulting ammonia concentration would be below 0.66 mg<sub>NH<sub>3</sub></sub>·kg<sub>CO<sub>2</sub></sub><sup>-1</sup> (or 2.1 ppmv) for all measurements.

Time on Stream [HH:MM]	Experiment A			
	Adsorber Off-gas		CO <sub>2</sub> Product	
	TOC [mg <sub>C</sub> ·Nm <sup>-3</sup> ]	TN [mg <sub>N</sub> ·Nm <sup>-3</sup> ]	TOC [mg <sub>C</sub> ·kg <sub>CO<sub>2</sub></sub> <sup>-1</sup> ]	TN [mg <sub>N</sub> ·kg <sub>CO<sub>2</sub></sub> <sup>-1</sup> ]
11:24	<4.16	<0.83	4.33	<0.44
95:50	<5.02	<1	5.46	0.55
117:15	<4.57	<0.91	3.81	0.42

**Table 17: Results from total organic carbon and total nitrogen analysis of impinger samples taken during the 120-hour experiment using Sorbent A**

Time on Stream [HH:MM]	Experiment B			
	Adsorber Off-gas		CO <sub>2</sub> Product	
	TOC [mg <sub>C</sub> ·Nm <sup>-3</sup> ]	TN [mg <sub>N</sub> ·Nm <sup>-3</sup> ]	TOC [mg <sub>C</sub> ·kg <sub>CO<sub>2</sub></sub> <sup>-1</sup> ]	TN [mg <sub>N</sub> ·kg <sub>CO<sub>2</sub></sub> <sup>-1</sup> ]
14:07	<4.26	<0.85	<2.53	<0.51
63:47	<5.26	<1.05	<2.13	<0.42
109:37	<5.18	<1.04	<2.09	<0.42

**Table 18: Results from total organic carbon and total nitrogen analysis of impinger samples taken during the 120-hour experiment using Sorbent B**

The results of detector tube measurements, shown in Table 19 and Table 20, verify the emission behavior suggested by the results of the TOC and TN measurements. It is seen that the emissions from the adsorber are particularly low compared to the emission levels found in the CO<sub>2</sub> product regardless of the sorbent used in the experiment. During Experiment A, the adsorber off-gas only rarely exceeded the lower detection limit of the amines detector tubes, whereas the concentration of acetaldehyde and formaldehyde stays below 1 ppm and 0.2 ppm respectively. Concerning detector tube measurements of the CO<sub>2</sub> product, it was found that appreciable amounts of acetaldehyde and formaldehyde were detected during the Experiment with sorbent A. By comparing the TOC and detector tube measurements of the CO<sub>2</sub> product, it was determined that a large part of the TOC emissions in this stream consisted of formaldehyde. Nevertheless, the concentration of acetaldehyde and formaldehyde in the CO<sub>2</sub> product settle to levels below 5 ppm and 8 ppm after the first 24 hours of Experiment A. A different emission behavior was observed during Experiment B, where neither amines, acetaldehyde nor formaldehyde could be detected in the off-gases of the BSU during the entire experimental runtime.

Despite the presence of oxygen in the adsorber, results from gaseous emission measurements suggest that sorbent degradation is higher at hot conditions.

Time on Stream [HH:MM]	Experiment A				
	Amines [ppmv]	Acetaldehyde [ppmv]		Formaldehyde [ppmv]	
	Adsorber Off-gas	Adsorber Off-gas	CO <sub>2</sub> Product	Adsorber Off-gas	CO <sub>2</sub> Product
3:44	6	<1	20	<0.2	75
8:44	<5	<1	5	<0.2	12
24:01	<5	<1	3	<0.2	5
45:19	<5	<1	2	<0.2	5
65:08	7.5	<1	2	<0.2	5
69:41	<5	<1	2	<0.2	5
80:49	<5	<1	2	<0.2	5
94:19	<5	<1	2	<0.2	<8
106:29	<5	1	n.A.	<0.2	<5
116:44	<5	<1	<5	<0.2	5

**Table 19: Results from detector tube measurements in the adsorber off-gas and CO<sub>2</sub> product using detector tubes during the 120-hour experiment using Sorbent A**

Time on Stream [HH:MM]	Experiment B				
	Amines [ppmv]	Acetaldehyde [ppmv]		Formaldehyde [ppmv]	
	Adsorber Off-gas	Adsorber Off-gas	CO <sub>2</sub> Product	Adsorber Off-gas	CO <sub>2</sub> Product
13:34	<0.5	<1	<1	<0.1	<0.1
15:02	<0.5	<1	<1	<0.1	<0.1
38:04	<0.5	<1	<1	<0.1	<0.1
60:49	<0.5	<1	<1	<0.1	<0.1
85:57	<0.5	<1	<1	<0.1	<0.1

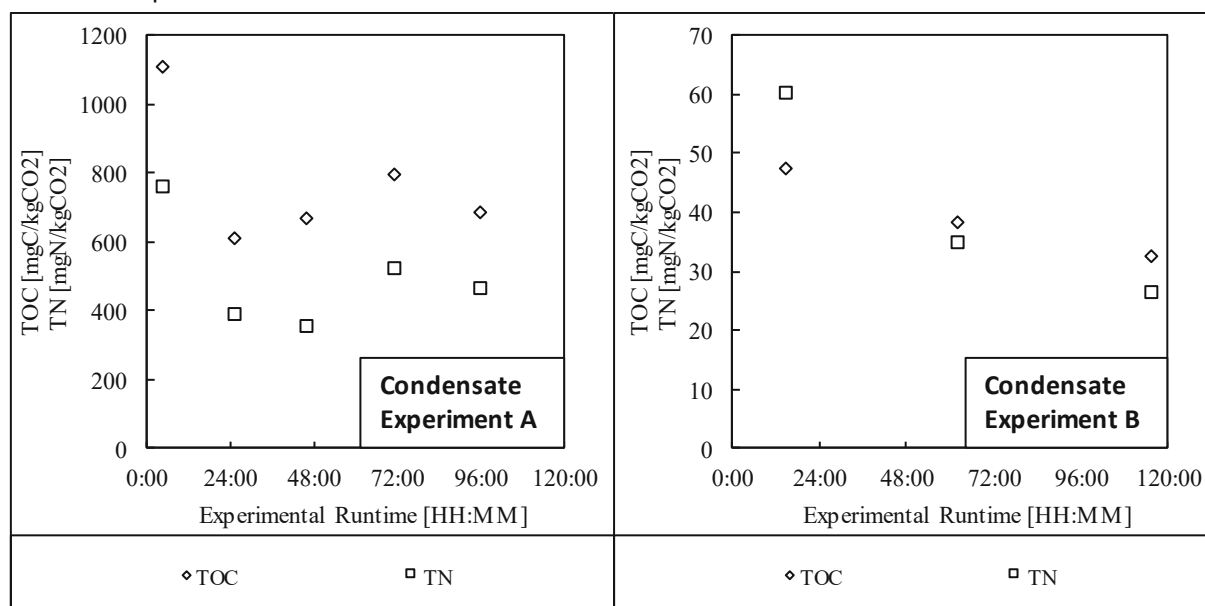
**Table 20: Results from detector tube measurements in the adsorber off-gas and CO<sub>2</sub> product using detector tubes during the 120-hour experiment using Sorbent B**

### CO<sub>2</sub> product condensate

The flow rate of stripping steam fed to the desorber was held constant at 8.5 kg·h<sup>-1</sup> in the course of both experiments. The desorber off-gas, which consisted of approx. 94 % steam, entered the CO<sub>2</sub> product cooler, where the dew point was measured at the gas outlet. Given the dew points of approx. 20°C and 10°C, it was estimated that 97.5 % and 98.7 % of the steam present in the desorber off-gas could be condensed during Experiment A and B respectively. From the results shown in Figure 49, it can be seen that the concentration of organic carbons and nitrogenous components in the CO<sub>2</sub> cooler condensate are at least ten times higher during Experiment A compared to Experiment B. It should be mentioned that Experiment A took place prior to Experiment B, thus the high TOC and TN levels measured in the CO<sub>2</sub> product cooler condensate during the initial 24 hours of Experiment B may be attributed to residue from Experiment A rather than a start-up effect during Experiment B.



By comparing the results given in Table 17 and Figure 49, it can be seen that during Experiment A, TOC and TN measurements of the CO<sub>2</sub> product condensate were two or even three orders of magnitude higher than the same measurements of impinger samples taken from the CO<sub>2</sub> product. Thus, most degradation products accumulate in the condensate rather than in the CO<sub>2</sub> product once the desorber off-gas is cooled. Since the TOC and TN measurements of impinger samples taken during Experiment B were below the detection limit of the analyzers, a quantitative comparison in this regard cannot be made for Experiment B.



**Figure 49: Results from total organic carbon and total nitrogen analysis of condensate samples from the CO<sub>2</sub> product cooler taken during the 120-hour experiment using Sorbent A (left) and Sorbent B (right). Please note the difference in y-axis scale.**

### Fines

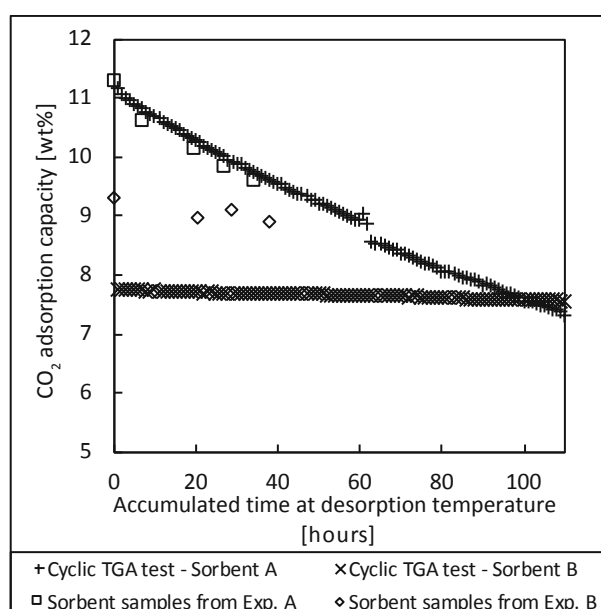
The physical stability of the utilized sorbents was evaluated by means of the weight gain of canister filters installed in the off-gas lines of the columns and the solids transport lines. For this reason, these filters were weighed before and after the experiment. As can be seen in Table 21, the average entrainment rate is considerably higher during Experiment A compared to Experiment B. To verify that the entrained particles were fines and generated by attrition, a PSD analysis was carried out on the contents of the canister filters used during Experiment A. As shown in Table 21 the diameter of a vast majority of entrained particles was smaller than 45.9 μm, therefore these particles can be considered fines. In the light of the significant difference in the average entrainment rate between the experiments, Sorbent A was deemed the physically less stable sorbent.

	Average entrainment rate [g/h]	$d_{10}$ [ $\mu\text{m}$ ]	$d_{50}$ [ $\mu\text{m}$ ]	$d_{90}$ [ $\mu\text{m}$ ]
<b>Experiment A</b>	3.31	5.2	14.1	45.9
<b>Experiment B</b>	<0.5	n.A.	n.A.	n.A.

**Table 21: Particle size distribution of solids samples and average solids entrainment rates throughout the 120-hour tests**

### TGA tests

Results from gaseous emission measurements together with results from TOC and TN measurements of the  $\text{CO}_2$  product condensate clearly show that sorbent degradation at hot conditions dominate total process emission. For this reason, the results from TGA investigations are given as the measured  $\text{CO}_2$  adsorption capacity as a function of the cumulated sorbent residence time at desorption conditions (as seen in Figure 50).



**Figure 50: The  $\text{CO}_2$  adsorption capacity of Sorbent A and Sorbent B in the course of cyclic TGA tests and the  $\text{CO}_2$  adsorption capacity of sorbent samples taken during the 120-hour tests as a function of the cumulative time at desorption conditions.**

The experimental campaign showed that there was a clear deterioration of the  $\text{CO}_2$  capture performance in the course of Experiment A. This behavior was reflected in the cyclic TGA tests by a significant reduction of the measured  $\text{CO}_2$  adsorption capacity of Sorbent A. The  $\text{CO}_2$  adsorption capacity loss rate of Sorbent A was quantified to an average of 3.48 wt% $\text{CO}_2$  per 100 hours at desorption conditions. This value is over twenty times higher than the loss seen during the cyclic tests performed with Sorbent B, with 0.16 wt% $\text{CO}_2$  per 100 hours at desorption conditions. It is worth noting that it only took 100 hours at desorption conditions for the  $\text{CO}_2$  adsorption capacity of Sorbent A to decrease to the same value as Sorbent B. This emphasizes the stability of Sorbent B, since the  $\text{CO}_2$  adsorption capacity of Sorbent A was initially 45% higher. The samples of Sorbent A taken during the 120-hour test, match the results from the cyclic tests. This shows that thermal degradation is the predominant degradation mechanism and can thus be regarded as a significant cause for a reduction of the  $\text{CO}_2$

adsorption capacity of Sorbent A during the 120-hour experiment. When comparing the CO<sub>2</sub> adsorption capacity of Sorbent B, a difference of approximately 1.5 wt%<sub>CO<sub>2</sub></sub> can be seen between the sorbent used during the cyclic test and samples taken from Experiment B. This is because the adsorption temperature during the cyclic test was 10°C higher (i.e. 50°C) than during the CO<sub>2</sub> capacity measurements of the sorbent samples (i.e. adsorption temperature of 40°C). Furthermore, during Experiment B the flue-gas contained moisture, which has shown to increase the CO<sub>2</sub> adsorption capacity of amine functionalized sorbents [113]. Regardless of the differences in CO<sub>2</sub> adsorption capacity, the average degradation rates of Sorbent B are significantly lower than those exhibited by Sorbent A. However, a considerable difference in the average degradation rate of Sorbent B was observed between the cyclic test (i.e. 0.18 wt%<sub>CO<sub>2</sub></sub> per 100 hours) and the sorbent samples (i.e. 0.96 wt%<sub>CO<sub>2</sub></sub> per 100 hours). This difference can only be explained by a degradation mechanism that was not evoked during the cyclic TGA test. Since the cyclic TGA tests were carried out in the absence of oxygen, oxidative degradation is an obvious cause for a stronger decrease of the CO<sub>2</sub> adsorption capacity during Experiment B. It should be mentioned that gaseous emissions, which are indicative for oxidative degradation, could not be detected in the adsorber off-gas.

### **Discussion**

The deterioration of the capture efficiency in the course of the 120-hour experiment with Sorbent A was an indication for a continuous loss of active amines. This was clearly reflected by the emissions found in the gas and liquid streams stemming from the CO<sub>2</sub> product cooler, as well as the high amount of elutriated fines. In the initial hours of the experiment, the amine loss rate was exceptionally high, whereas a significant change in the CO<sub>2</sub> capture performance was not determined in the same period. This was likely due to volatilization of low molecular-weight amines together with fragmentation and subsequent loss of amines from the outer layer of the sorbent. In the course of TGA tests, it could be shown that thermal degradation, i.e. breaking and subsequent evaporation of PEI branches in the high temperature environment of the desorber, played a predominantly role in the reduction of the CO<sub>2</sub> adsorption capacity of Sorbent A. Furthermore, the comparably high concentration of acetaldehyde and formaldehyde found in the CO<sub>2</sub> product as well as a high content of organic carbons found in the CO<sub>2</sub> product condensate, suggest an ingress of ambient air into the rich riser blower, which led to partial oxidation of degradation products in the desorber. Particularly low emissions were measured in the course of Experiment B. In the adsorber off-gas, the emission levels were comparable to those measured during Experiment A. The effluent and the CO<sub>2</sub> product however had emission levels that were significantly lower than those measured during Experiment A or even below the detection limit of the utilized analytical method. This is owed to the covalent bond between amine sites and the polymer support. Hence, volatilization of amines from the sorbent can be largely prevented. This was also validated by results gained during cyclic TGA tests. Although the emission levels of the CO<sub>2</sub> cooler condensate were at least an order of magnitude lower during Experiment B compared to Experiment A, this stream still represented the greatest source of emissions from the TSA BSU. It could be argued that due to the milder regeneration conditions in the desorber, lower emissions would be expected during Experiment B. However, the operating temperatures were chosen so that a comparable CO<sub>2</sub> capture efficiency can be achieved with both sorbents under the consideration of the individual sorbent properties. The author of this work believes that this approach best reflects the strategy of setting operating conditions in practical applications and enables the evaluation of process emissions based on the CO<sub>2</sub> capture performance. Furthermore, it is important to note that in the

course of the 120-hour experiments over 370 adsorption/desorption cycles were carried out with Sorbent B, compared to approx. 270 cycles with Sorbent A because of the lower circulation rate required to achieve 90% capture during the tested period.

#### 4.4.5 Comparison with emissions from the MEA scrubbing process

Recently, the emissions of an aqueous MEA scrubber were investigated at the CO<sub>2</sub> Technology Centre in Mongstad (TCM) [99,153]. Special emphasis was placed on the environmental emissions of the investigated MEA scrubber i.e. the off-gas of the absorber. The data gained during this campaign is particularly suited for a comparison to the results presented in this work. Unlike most emission investigations on MEA scrubbers reported in literature, the flue gas treated at TCM contained a particularly low concentration of SO<sub>2</sub> & NO<sub>x</sub>. (i.e. <1 ppm SO<sub>2</sub> & 3ppm NO<sub>x</sub>). This is relevant because these species evidently accelerate amine degradation. It should be noted that, although Rezaei and Jones [133] showed that SO<sub>2</sub> and NO<sub>2</sub> lead to a considerable reduction of the CO<sub>2</sub> adsorption capacity, the underlying mechanisms are not well understood. Therefore, it is unclear whether SO<sub>2</sub> and NO<sub>2</sub> will entail increased process emissions from a TSA process.

Nevertheless, the absorber at TCM was equipped with a two-stage water wash section designed to reduce amine loss from the process, thus considerably reducing environmental amine emissions. It was found that within the first week of the experiments, the NH<sub>3</sub> concentration in the absorber off-gas leveled off to approx. 20 ppmv, MEA emissions were quantified to approx. 1 ppmv and the concentration of acetaldehyde was approx. 0.25 ppmv.

The analyses carried out in the course of this work could not verify the presence of NH<sub>3</sub>. However, the total nitrogen content of the adsorber off-gas and the CO<sub>2</sub> product was measured. These analyses not only account for nitrogen contained in amines, but also for nitrogen in NH<sub>3</sub>. However, the total nitrogen content was below the detection limit of the analyzer for all measurements of the adsorber off-gas. For the sake of comparability, it will be assumed that the total nitrogen content of the adsorber off-gas is entirely attributed to NH<sub>3</sub>. According to this assumption, the highest potential NH<sub>3</sub> concentration of the adsorber off-gas throughout both experiments would be below 2.1 ppmv (i.e. lower than 1.05 mg<sub>N</sub>·Nm<sup>-3</sup>, the detection limit), hence significantly lower than the 20 ppmv observed in the MEA campaign at TCM.

MEA emissions during the TCM campaign of approx. 1 ppmv are compared to the primary amine concentration measured using detector tubes in this work. In Experiment A, the primary amine concentration was mostly below the detection limit of 5 ppmv, but spikes of 6-7.5 ppmv were measured. In Experiment B the concentration of primary amines was below the detection limit of 0.5 ppmv for all measurements.

The measurements of the acetaldehyde concentration showed a similar behavior as that of amines. Only one measurement, during Experiment A, was above the detection limit of 1 ppm, whereas all other measurements, including those conducted during Experiment B, were below the detection limit. Within the same runtime, the nitrogenous emissions from the adsorber of the TSA BSU seem to be lower than from the absorber of the MEA scrubber at TCM, regardless of the sorbent used. Whilst both sorbents showed lower emissions in terms of NH<sub>3</sub> and amines, a clear distinction must be made in terms of acetaldehyde emission. During Experiment A, a spike in the acetaldehyde concentration was measured, which was fourfold the value measured in the off-gas of the MEA scrubber. In the case of

Sorbent B, a clear comparison concerning acetaldehyde emissions cannot be made, since the detection limit of the utilized detector tubes was not exceeded.

#### 4.4.6 Conclusion

In the course of two 120-hour experiments in the TAS BSU, two different amine functionalized solid sorbents were tested. In the course of the experiments, gaseous emissions from the off-gases of the adsorber and the desorber, liquid emissions in the form of CO<sub>2</sub> product cooler condensate and solid emissions (as elutriated fines) were quantified.

Whilst gaseous emissions from the adsorber were similar and rather low during both experiments, significant differences were determined for all other emissions. The amine loss rate of Sorbent A was particularly high and entailed a steady decline of the CO<sub>2</sub> capture efficiency. Due to the formation of degradation products and volatilization of amines, the concentration of organic carbons and nitrogenous compounds was notably high in the CO<sub>2</sub> product as well as in the CO<sub>2</sub> product cooler condensate. Cyclic TGA tests showed that thermal degradation in the desorber was the dominant degradation mechanism for Sorbent A. However, it was also shown that attrition and subsequent elutriation of fines from the system contributed to the amine loss rate, and thus to the deterioration of the CO<sub>2</sub> capture performance seen in the course of Experiment A. Amine loss during Experiment B was limited due to the strong bond between amine sites and the polymer support together with the attrition resistance of Sorbent B. TOC and TN analyses as well as detector tube measurements for primary amines, acetaldehyde and formaldehyde from both the adsorber off-gas and the CO<sub>2</sub> product were consistently under the detection limit. Furthermore, samples of the CO<sub>2</sub> product cooler condensate showed to contain about one tenth of the organic carbon and nitrogenous compounds measured during Experiment A.

These results show clearly that sorbent materials with amines covalently bound to a support are superior in terms of sorbent stability and process emissions compared to sorbents prepared by a wet impregnation method. Low amine loss rates entail low sorbent make-up rate and a reduction in emission reduction measures. The usage of amine-grafted sorbents thus has the potential to reduce the CO<sub>2</sub> capture cost in practical application compared to using amine-impregnated sorbents.

A comparison of environmental emission between an aqueous MEA process and the results gained herein showed that the TSA process produced lower nitrogenous emissions, whereas this is not as clear comparison cannot be made concerning acetaldehyde emissions due to limitations in analytical techniques. This outcome underlines one of the key advantages of the TSA process using amine functionalized solid sorbents compared to aqueous amine scrubbing.

Notwithstanding the emission data acquired in this campaign, it is possible that species such as SO<sub>x</sub> or NO<sub>x</sub> present in industrial flue-gases or aging of the sorbent may result in increased degradation and emissions from a TSA process even when Sorbent B is used. It is thus recommended that future work investigate sorbent degradation and process emissions in the presence of SO<sub>x</sub> and NO<sub>x</sub> as well as the CO<sub>2</sub> capture performance and process emissions in the course of an even longer period.

Notwithstanding the emission data acquired in this campaign, the experimental runtime is rather short compared to commercial scale processes. Therefore, a prolonged emission test where real flue-gas is treated is recommended as subject for future research.

## 4.5 WATER TRANSPORT

The combustion of virtually all fuels leads to the formation of a flue gas that contains considerable amounts of steam. Although a cooler will be required upstream of the adsorber to cool the treated flue gas to adsorber operating temperature, a further reduction of the flue gas dew point represents an added cooling demand and potentially also higher CO<sub>2</sub> capture costs. To keep the cooling requirement of the flue gas low, the humidity of the treated gas will be near saturation when entering the adsorber. As shown by Figure 24 in Section 2.4.1, the water adsorption capacity of Sorbent B increases with relative humidity and can be many times higher than the adsorption capacity of CO<sub>2</sub>. Some researchers have proposed TSA systems in which CO<sub>2</sub> is used in the desorber as a fluidizing agent [44,114]. In such systems, the humidity within the desorber is virtually zero, thus water adsorption in the adsorber is limited by supply rather than the relative humidity of the treated gas, whilst high amounts of water would be stripped from the sorbent in the dry milieu of the desorber. Because the heat of water adsorption can be in the range of the heat of water condensation (e.g. 43 kJ·molH<sub>2</sub>O<sup>-1</sup> for Sorbent B [114]), this effect can considerably increase the adsorber cooling duty and desorber heat demand.

The low heat demand of the TSA process is an anticipated advantage over conventional MEA scrubbing. Since water adsorption can influence the process heat demand, it is key to gain an understanding of the interaction between the utilized sorbent material and water vapor throughout the TSA process.

In the present system, steam is used in the desorber as a stripping gas, and the relative humidity in the desorber can be controlled with the desorber operating temperature. Previous work, see Section 4.2, has indicated that water co-adsorption can take place in the desorber, hence the associated heat released during water adsorption can counter-balance the heat required for CO<sub>2</sub> desorption and the amount of heat that needs to be supplied via immersed bed heat exchangers. Conversely, net adsorption of water in the desorber and subsequent desorption of water in the adsorber can counter-balance the cooling requirement in the adsorber.

A series of experiments was carried out in the TSA BSU to assess water transport within the TSA process and determine how water adsorption can be influenced by selected operating conditions. In the course of these experiments, water-adsorption/-desorption was quantified in the adsorber and its impact on the desorber heat demand evaluated.

With the exception of a gas cooler installed in the lean riser gas line, the experimental setup used in the course of this campaign corresponded to the description given in Section 3.1, whereas the sorbent used throughout this campaign was Sorbent B.

### 4.5.1 Experimental setup

As can be seen in Figure 51 the setup of the TSA BSU largely matched the description given in Section 3.1. Since the conducted experiments involved the determination of water transported between the columns, a gas-liquid cooler was installed in the lean riser loop. This was done to dry the recycle gas in the lean riser loop to preclude steam condensation on potential cold-spots. The lean riser gas cooler was equipped with a condensate drain connection. A peristaltic pump connected to the condensate drain connection of the lean riser gas cooler continuously pumped the generated condensate into a container.

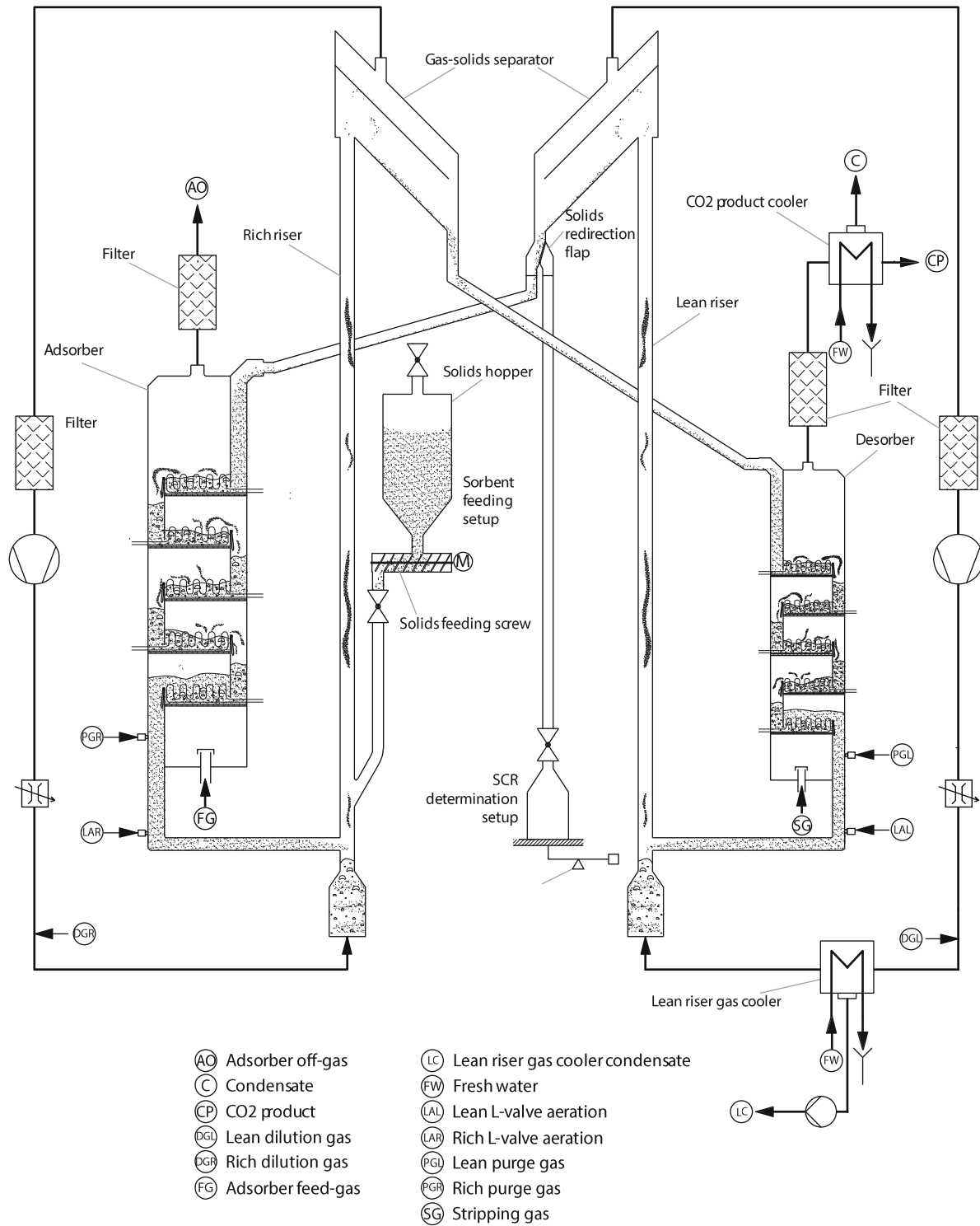


Figure 51: Schematic illustration of the TSA BSU during the water transport tests

#### 4.5.2 Methods

To assess water transport between the columns, the water mass balance of the system was established. This required the water content of the adsorber off-gas and adsorber feed gas as well as the mass flow rate of condensate generated in the lean riser gas cooler. To determine the water

content of the gas streams, a partial flow was diverted and passed through a setup, which essentially acts as a condensate trap. This setup consisted of a hose heated to 120 °C, four cooled impingers connected in series and a gas sampling pump with an integrated bellows meter for the determination of the dry gas sample amount. The impingers were cooled to a temperature of 4 °C, whereas the first three impingers were empty, and the fourth was filled with a defined amount of dry silica gel. The entire impinger setup was weighed before and after the gas sampling period and the mass gain was considered the mass of water within the gas sample. This mass was subsequently divided by the dry gas sample amount to yield the water content of the gas. A peristaltic pump connected to the lean riser cooler, continuously drained condensate into a container, which was weighed before and after the sampling period.

It should be noted that one operating point was carried out in which the desorber was fluidized by N<sub>2</sub>. Here the desorber off gas was sampled in addition to the adsorber feed gas, adsorber off gas and condensate formed in the lean riser gas cooler so that the water balance could be closed and the accuracy of the chosen method could be evaluated.

### Calculations

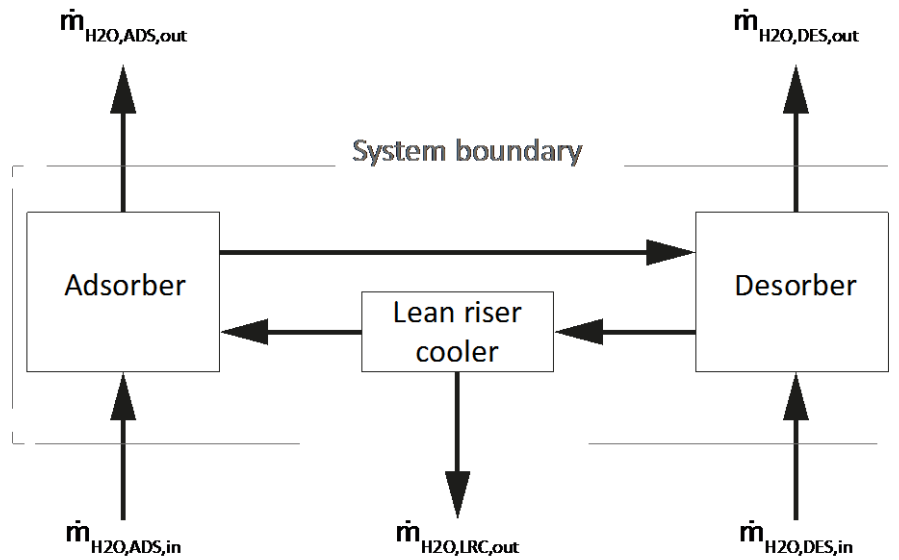
As shown in Eq. 41, the relative humidity ( $rH$ ) of the column feed gases was calculated using the absolute pressure ( $p_{Stage\ 1}$ ) and bed temperature ( $T_{Stage\ 1}$ ) in Stage 1 of the columns, together with the volume fraction of steam measured in the column feed gases ( $y_{H_2O,ADS,in}$ ).

$$rH = \frac{p_{H_2O,Stage\ 1}}{p_{H_2O,sat}(T_{Stage\ 1})} \cdot 100\% = \frac{p_{Stage\ 1} \cdot y_{H_2O,ADS,in}}{p_{H_2O,sat}(T_{Stage\ 1})} \cdot 100\% \quad \text{Eq. 41}$$

As can be seen, the measured pressure ( $p_{Stage\ 1}$ ) and bed temperature ( $T_{Stage\ 1}$ ) have a considerable impact on the calculated relative humidity. Due to the appreciable pressure drop of the sintered-filter-type gas distributor installed in the bottom-most fluidized bed stages, and because the temperature in the wind-box frequently deviated from the measured fluidized bed temperatures, pressure and temperature measurements from the bottom-most adsorber and desorber stage were used for calculation of the relative humidity of the column feed gases. Since the desorber column was only fluidized by either nitrogen or steam, the relative humidity of the desorber feed gas was either zero (i.e. when  $y_{H_2O,ADS,in} = 0$ ) or a function of the absolute pressure and the temperature (i.e. when  $y_{H_2O,ADS,in} = 1$ ) respectively.

A schematic illustration of the considered system boundary used for the water mass balance together with the sources and drains of water to and from the TSA BSU are shown in Figure 52.





**Figure 52: Schematic illustration showing the water balance created for the assessment of water transport**

As shown in Figure 52 and Eq. 42-Eq. 45, the mass flow of water to the adsorber ( $\dot{m}_{H_2O,ADS,in}$ ) via the treated flue gas, the mass flow of water in the adsorber off-gas ( $\dot{m}_{H_2O,ADS,out}$ ) and the mass flow of condensate formed in the lean riser gas cooler ( $\dot{m}_{H_2O,LRC,out}$ ) are required so that the amount of transported steam can be determined.

$$\Delta\dot{m}_{H_2O,ADS} + \Delta\dot{m}_{H_2O,DES} - \dot{m}_{H_2O,LRC,out} = 0 \rightarrow \Delta\dot{m}_{H_2O,DES} = \dot{m}_{H_2O,LRC,out} - \Delta\dot{m}_{H_2O,ADS} \quad \text{Eq. 42}$$

if  $\Delta\dot{m}_{H_2O,ADS}$  and  $\Delta\dot{m}_{H_2O,DES}$  are defined as follows:

$$\Delta\dot{m}_{H_2O,ADS} = \dot{m}_{H_2O,ADS,in} - \dot{m}_{H_2O,ADS,out} \quad \text{Eq. 43}$$

and

$$\Delta\dot{m}_{H_2O,DES} = \dot{m}_{H_2O,DES,in} - \dot{m}_{H_2O,DES,out} \quad \text{Eq. 44}$$

then:

$$\dot{m}_{H_2O,LRC,out} + \dot{m}_{H_2O,ADS,out} - \dot{m}_{H_2O,ADS,in} = \dot{m}_{H_2O,DES,in} - \dot{m}_{H_2O,DES,out} \quad \text{Eq. 45}$$

If  $\Delta\dot{m}_{H_2O,DES}$  assumes a negative value, water is effectively transported from the adsorber to the desorber. At constant temperature, this would not only result in a parasitic cooling duty in the adsorber, but also increase the heating duty in the desorber. In contrast, water transport from the desorber to the adsorber is indicated by a positive value of  $\Delta\dot{m}_{H_2O,DES}$ .

To evaluate the impact of water transport on the energy requirement of the desorber, the heat input in the desorber was calculated according to the equations given in Section 3.3.4.

To allow comparison of the sensible heat demand in the desorber with the additional heat requirement for water desorption, the heat of water adsorption or regeneration was assumed to be  $-43 \text{ kJ}\cdot\text{mol}_{H_2O}^{-1}$

(i.e.  $-2.389 \text{ MJ}\cdot\text{kg}_{\text{H}_2\text{O}}^{-1}$ ), as determined for Sorbent B by Veneman et al. [114]. As shown in Eq. 46,  $\Delta\dot{m}_{\text{H}_2\text{O},\text{DES}}$  (given in  $\text{g}\cdot\text{h}^{-1}$ ) was multiplied with the enthalpy of water evaporation to yield the estimated heat release in the desorber due to water adsorption. This value was divided by the captured amount of  $\text{CO}_2$  to yield the specific heat of water adsorption given in  $\text{MJ}\cdot\text{kg}_{\text{CO}_2}^{-1}$ .

$$q_{\text{DES},\text{H}_2\text{O}} = \frac{\frac{\Delta\dot{m}_{\text{H}_2\text{O},\text{DES}}}{1000 \cdot 3600} * -2.389 \frac{\text{MJ}}{\text{kg}_{\text{H}_2\text{O}}}}{\frac{\dot{m}_{\text{capt}}}{24 * 3600}} \quad \text{Eq. 46}$$

As shown by Eq. 47, Eq. 46 was modified to allow for the calculation of the specific heat of water adsorption released in the adsorber. Similarly to  $q_{\text{DES},\text{H}_2\text{O}}$ ,  $q_{\text{ADS},\text{H}_2\text{O}}$  is also given in  $\text{MJ}\cdot\text{kg}_{\text{CO}_2}^{-1}$ .

$$q_{\text{ADS},\text{H}_2\text{O}} = \frac{\frac{\Delta\dot{m}_{\text{H}_2\text{O},\text{ADS}}}{1000 * 3600} * -2.389 \frac{\text{MJ}}{\text{kg}_{\text{H}_2\text{O}}}}{\frac{\dot{m}_{\text{capt}}}{24 * 3600}} \quad \text{Eq. 47}$$

### 4.5.3 Operating conditions

As can be seen in Table 22, four different operating points were set in the course of the experimental campaign. Steam was used as a stripping gas in the desorber column in the initial three operating points, which will be referred to as Wet A, Wet B and Wet C. Here, the forward flow temperature of thermal oil was successively reduced from  $140^\circ\text{C}$  to  $105^\circ\text{C}$ , thereby causing a reduction of the desorber operating temperature. In carrying out this operating temperature reduction, the saturation pressure of steam is also reduced. Hence, due to the constant absolute pressure and constant feed gas composition (i.e. 100 vol% steam), the relative humidity in the desorber was successively increased from Wet A to Wet C. It should be mentioned that the SCR was held constant in the course of these operating points.

In the final operating point, referred to as “Dry”, the temperature of thermal oil was again increased to  $140^\circ\text{C}$  and the stripping gas in the desorber entirely replaced by  $\text{N}_2$ , thereby reducing the humidity of the feed gas to zero.

	Wet A	Wet B	Wet C	Dry	
Thermal oil temperature	140	120	105	140	$[\text{C}]$
Desorber stripping steam flow-rate	8.5	8.5	8.5	0	$[\text{kg}\cdot\text{h}^{-1}]$
Desorber nitrogen flow rate	0	0	0	7	$[\text{Nm}^3\cdot\text{h}^{-1}]$

**Table 22: Operating conditions of the desorber during the conducted water transport investigation**

It must be mentioned that the target operating conditions of the adsorber were maintained at the values given in Table 23. The flow of cooling water to the adsorber heat exchanger coils was manually adjusted to achieve the target operating temperature window of  $50^\circ\text{C}$ - $60^\circ\text{C}$  in all stages. Furthermore, the targeted flow-rate and composition of the adsorber feed gas was constant throughout the entire experimental campaign.

Adsorber operating temperature	50-60	[°C]
Adsorber feed gas flow rate	16.8	[Nm <sup>3</sup> ·h <sup>-1</sup> ]
Adsorber steam flow rate	1	[kg·h <sup>-1</sup> ]
Adsorber feed gas velocity (wet)	0.33	[m·s <sup>-1</sup> ]
Adsorber feed gas O <sub>2</sub> concentration (dry)	9	[vol%O <sub>2</sub> ]
Adsorber feed gas CO <sub>2</sub> concentration (dry)	4	[vol%CO <sub>2</sub> ]
Steam flow to adsorber	1	[kg·h <sup>-1</sup> ]

**Table 23: Target operating conditions of the adsorber during the conducted water transport investigation**

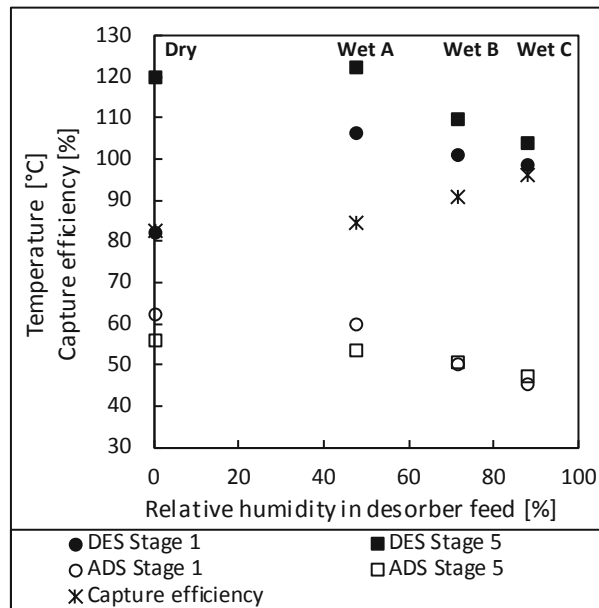
#### 4.5.4 Results & Discussion

As shown in Table 24, the relative humidity in the adsorber feed gas could be kept in a narrow range (i.e. 51.6 %-53.2 %) for all operating points with the exception of Wet C. Here, the unit operator overshot the required cooling duty, which led to a decrease of the column temperature. This entailed a slight increase of the relative humidity of the column feed gas (i.e. to 62.4 %). By decreasing the temperature of desorber stage 1 from 122.3 °C during Wet A to 103.8 °C in the course of Wet C, the relative humidity of the desorber feed gas was almost doubled (from 47.6%-87.7%). The SCR was constant for the initial three operating points and decreased for experiment Dry (i.e. 19.6 kg·h<sup>-1</sup> vs 17.9 kg·h<sup>-1</sup>). The polymer support makes Sorbent B especially prone to electrostatic charging, especially under dry conditions. Although the adsorber feed gas was humidified by a low flow of steam, the sorbent was dried to such a degree in the desorber that electrostatic charging occurred during experiment Dry. The solids started to show cohesive behavior, thus reducing solids throughput through the lean L-valve.

	Wet A	Wet B	Wet C	Dry	
Thermal oil temperature	142.8	122.5	107.5	142.8	[°C]
Relative humidity in adsorber feed gas	51.6	53.2	62.4	52.3	[%]
Adsorber stage 1 temperature	53.7	50.6	47.1	56.0	[°C]
Relative humidity in desorber feed gas	47.6	71.1	87.7	0.0	[%]
Desorber stage 1 temperature	122.3	109.9	103.8	119.9	[°C]
Solids circulation rate	19.6	19.6	19.6	17.9	[kg·h <sup>-1</sup> ]
Temperature swing*	60.5	55.0	54.2	44.4	[°C]

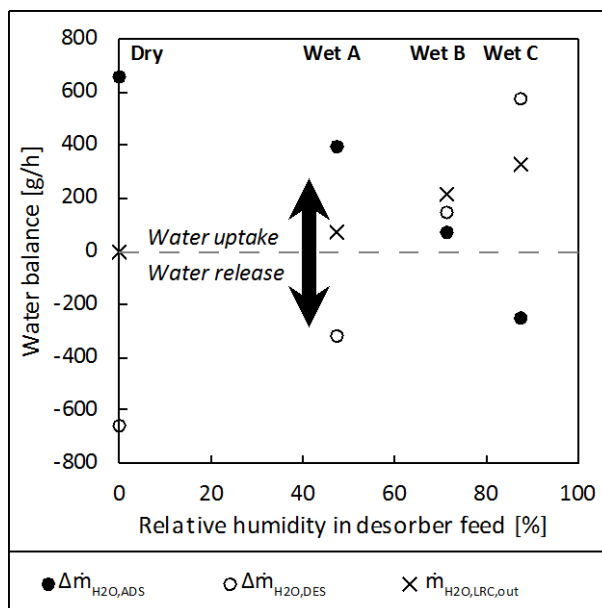
**Table 24: Table showing selected operating conditions of the TSA BSU during the conducted water transport investigation. \*Difference in the mean operating temperatures of the columns calculated according to Eq. 40.**

As can be seen in Figure 53, a slight increase in the capture efficiency was observed as the relative humidity in the desorber increased. Because the relative humidity of the adsorber feed gas stayed in a narrow range, this observation was attributed to a reduction of the average adsorber operating temperature rather than an increase in the sorbent's CO<sub>2</sub> adsorption capacity due to increased bicarbonate formation.



**Figure 53: Graph showing the temperatures of stage 1 and stage 5 in the adsorber and desorber together with the capture efficiency as a function of the relative humidity in the desorber feed gas.**

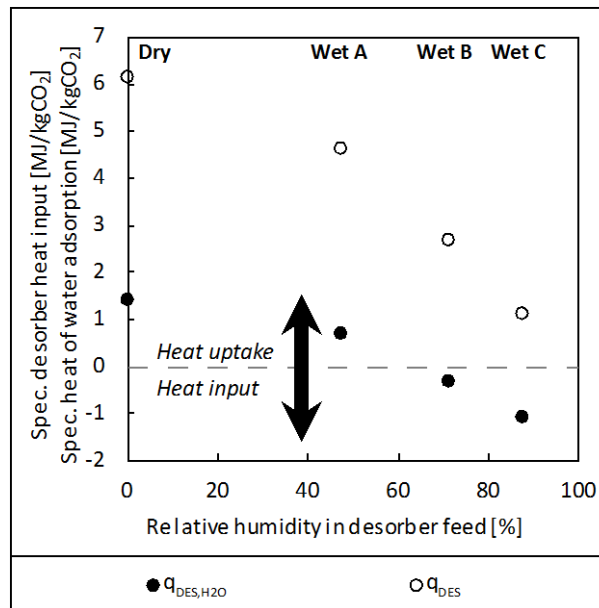
Figure 53 also shows the operating temperature window of the columns by means of the temperatures in Stage 1 and Stage 5. It can be seen that the axial temperature distribution in the desorber is over 35 °C during Dry. Furthermore, the decreased SCR compared to the Wet operating points, contributed to achieving the lowest CO<sub>2</sub> capture efficiency measured throughout this campaign. Nevertheless, when comparing Dry with Wet A, it can be seen that the use of steam as stripping gas in the desorber led to a considerable reduction of the axial temperature distribution in the desorber although the thermal oil temperatures were identical. A similar reduction of the axial temperature distribution can be seen in the adsorber, as the relative humidity in the desorber increases. This is because, water adsorption in the adsorber decreases as the relative humidity in the desorber increases, thus leading to a reduction of the cooling duty in the adsorber and a reduction of the heat demand in the desorber. This effect allows more efficient cooling and heating via the immersed bed heat exchangers and allows for achieving higher average operating temperatures in the desorber and lower average operating temperatures in the adsorber. Furthermore, minimal temperature distributions across the columns allow the sorbent to reside at the desired temperature for longer and thus come closer to equilibrium.



**Figure 54:** Graph showing the measured water uptake/release in the adsorber and collected amount of water from the lean riser gas cooler together with the calculated water uptake/release in the desorber according to the water balance as a function of the relative humidity in the desorber feed gas.

The measured water uptake/release in the adsorber, the collected amount of water from the LRC as well as the calculated uptake/release of water in the desorber are shown in Figure 54. It should be reiterated that the water balance is such, that water uptake/release in the desorber is inverse to the water uptake/release in the adsorber and offset by the collected amount of water in the LRC. If the LRC were not installed, water uptake in the adsorber would be equal to water release in the desorber and vice versa. As can be seen in Figure 54, this is only the case during Dry. Here the sorbent is dried in the desorber so that no water can be released in the lean riser loop and thus collected in the LRC. As the desorber off-gas consisted of only low amounts of water, compared to the “Wet” operating points, it was feasible to determine its water content. Therefore it was possible to close the water mass balance at this operating point and thus assess the method accuracy. An error of  $4.87 \text{ g}\cdot\text{h}^{-1}$  was measured from a total of  $1260 \text{ g}\cdot\text{h}^{-1}$  of water fed to the adsorber. This is equal to a measuring error of 0.39 %.

It can be seen that the net amount of adsorbed water decreases in the adsorber as the relative humidity in the desorber increases. In the desorber the opposite effect is seen, whereas, due to the LRC, water is adsorbed in both columns during Wet B (i.e. at a relative humidity of 71.1 % in the desorber feed gas). During Wet C, i.e. at a relative humidity of 87.7 % in the desorber feed gas, the behavior seen in Dry and Wet A are reversed and water is effectively transported from the desorber to the adsorber.

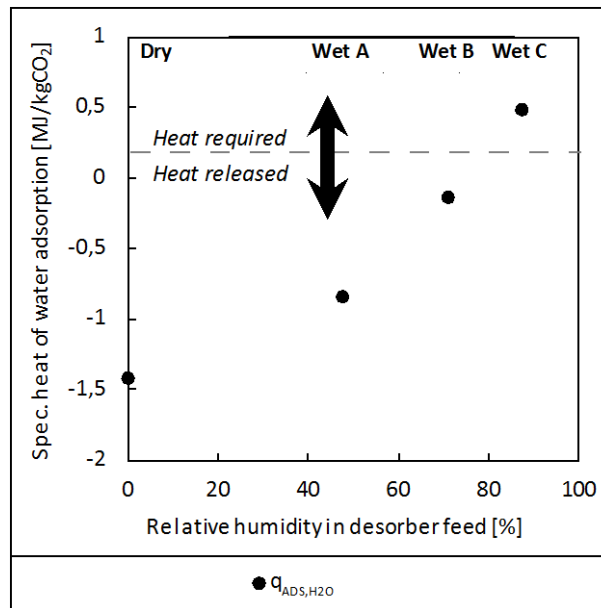


**Figure 55: Graph showing the measured heat input in the desorber together with the specific heat of water adsorption in the desorber as a function of the relative humidity in the desorber feed gas.**

As can be seen in Figure 55, the observed release and adsorption of water in the desorber has a distinct impact on the desorber heat input. As the relative humidity in the desorber feed gas increases, less water is released in the desorber, thereby leading to a reduction of the heat requirement for the steam desorption process. Heat, resulting from steam adsorption, is effectively released in the desorber at a relative humidity of 71.1 % in the desorber feed gas. However, the lowest heat input is measured at a relative humidity of 87.7 % in the desorber feed gas with approx.  $-1.12 \text{ MJ}\cdot\text{kgCO}_2^{-1}$ .

In the light of the results presented in Figure 55, the observed reduction of the axial temperature distribution in the desorber can be explained by a reduction of the desorber heat demand brought about by decreased steam desorption.

Nevertheless, a difference is seen between the spec. desorber heat input ( $q_{DES}$ ) and the specific heat of water adsorption ( $q_{DES,H2O}$ ). Since both these values are related to the capture amount of  $\text{CO}_2$  in each operating point, the influence of the latent heat is constant for all operating points. It can further be seen, that as the relative humidity in the desorber feed is increased,  $q_{DES}$  undergoes a stronger decrease than  $q_{DES,H2O}$ . This is assumed to be a result of a reduction in the sensible heat requirement in the desorber because the temperature swing decreases as the relative humidity in the desorber increases (i.e. from  $60.5 \text{ }^\circ\text{C}$  during Wet A to  $54.2 \text{ }^\circ\text{C}$  during Wet C).



**Figure 56: Graph showing the specific heat of water adsorption in the adsorber as a function of the relative humidity in the desorber feed gas.**

A calculation of the released and required heat for water adsorption was also carried out for the adsorber, as seen in Figure 56. A cooling effect of water desorption was only determined at a desorber feed gas humidity of 87.7 %. This partially counter-balances the sensible cooling demand and the cooling demand for CO<sub>2</sub> adsorption. As mentioned, the LRC decreases the water loading of the lean sorbent. Therefore, in the adsorber a cooling effect of water release can be expected at a lower relative humidity of the desorber feed gas, if the BSU is operated without a cooler installed in the lean riser loop.

#### 4.5.5 Conclusion

An investigation was carried out in the TSA BSU to evaluate the effect of water co-adsorption at various humidity levels of the desorber feed gas. The transported amount of water between the columns was quantified by sampling the feed- and off-gas of the adsorber as well as the condensate formed in a cooler installed in the lean transport line. Since the desorber was fluidized by steam the relative humidity could be varied by varying the desorber operating temperature. One operating point was carried out with N<sub>2</sub> as a regeneration agent in the desorber.

It could be shown that at a relative humidity of 62.4 % in the adsorber feed gas and a relative humidity of 87.7 % in the desorber feed gas, adsorption of steam in the adsorber can be prevented. In this operating point, water was effectively transported from the desorber to the adsorber, thus counter-balancing the heating and cooling requirement in the adsorber and desorber. In all other cases, water was adsorbed in the adsorber, thus adding to the cooling demand in the adsorber. In the desorber, water adsorption occurred during both a relative humidity of 87.7 % and 71.1 %. At these operating points, steam counter balanced the heating requirement in the desorber and measurably reduced the amount of heat that needed to be supplied via the immersed bed heat exchanger coils.

However, the heat for steam adsorption has been measured to be similarly high as the heat of steam evaporation, thus the reduction in the desorber heat demand is added to the heat requirement of the

steam generator. It should be assumed that steam transported from the desorber to the adsorber is not reclaimed from the adsorber off-gas and returned to the steam producing process. Therefore, steam that is allowed to adsorb in the desorber can be considered consumed. A trade-off between the consumption of low quality steam and the implementation of heat transfer surface area in the desorber and adsorber can add flexibility and thus be of great value in a techno-economical evaluation. Moreover, limitations that arise from the implementation of densely packed heat exchanger tube bundles in the FB columns, such as poor solids mixing, can be avoided if instead steam adsorption is allowed in the desorber. It should be also be mentioned steam adsorption or desorption in the desorber can affect the gas velocity profile in the desorber. This effect will be especially pronounced when the desorber is designed with a small cross-section, i.e. designed for low stripping steam flow rates. To be able to consider the effect of steam adsorption in the design of a TSA desorber, a model needs to be developed that quantifies both water and CO<sub>2</sub> adsorption/desorption at various operating conditions of the TSA system.



## 4.6 LEAN/RICH HEAT EXCHANGE

In the amine scrubbing process, the bulk of sensible heat can be recovered from the lean solvent in so-called lean/rich heat exchangers. To realize lean/rich heat exchange (LRHX), the lean solvent exiting the regenerator is passed through a liquid-liquid heat exchanger, which is used to preheat the rich solvent exiting the adsorber. LRHX has been implemented in amine scrubbing since the patenting of the process in 1930 [24], therefore extensive know-how on the design and operation of such heat exchangers has been gathered. The typical designs of the liquid/liquid heat exchangers used for LRHX have historically been tube and plate-type heat exchangers [154], whilst in recent years the plate-and-frame-type design has been increasingly implemented and has shown to offer high thermal efficiencies whilst allowing for easy maintenance [36,155]. In systems where heat is exchanged with a solid sorbent a fluid must act as an intermediate for heat exchange. However, this makes at least two heat exchangers necessary. One solids/liquid heat exchanger for recovering heat from the lean sorbent and one solids/liquid heat exchanger for preheating of the rich sorbent. By implementing counter-current heat exchange, the heat transfer efficiencies can be considerably increased thereby reducing the required size of the heat exchanger and its cost. A suitable design for liquid/solid heat exchangers, which implement this regime, are moving-bed heat exchangers. Here solids are transported downward by gravity and pipes or plates within the moving bed of solids are used to transport a heat transfer fluid in an upward direction. However, moving bed heat exchangers reportedly feature significantly lower HTC's than fluidized bed heat exchangers [44].

In this section, a possible heat exchanger configuration, consisting of two moving bed heat exchangers will be investigated and used to simulate LRHX in the TSA BSU. Furthermore, an additional fluidized bed heat exchanger installed upstream of the desorber will be used to reduce the heating requirement of the desorber. The newly installed subsystems are investigated in terms of their influence on the TSA process, whereas special attention is attributed to interferences with the operability of the TSA BSU and changes in the measured heat demand of the desorber. Furthermore, the achievable HTC's in the moving bed heat exchangers will be determined and compared to literature data.

As will be explained in Section 4.6.1, two different designs of the moving bed heat exchangers were implemented. In case of a significant difference of the achievable HTC's, this will allow to give a clearer design recommendation for moving bed heat exchangers at a larger scale. In this way, a foundation for further optimization and development of a suitable heat recovery system is laid. Furthermore, Section 4.6.1 will also elaborate on numerous changes that were made to the experimental setup of the TSA BSU compared to the experimental setup described in Section 3.1.

It should also be noted that Sorbent B was used throughout these investigations.

### 4.6.1 Experimental setup

As shown in Figure 57, two moving bed heat exchangers (MBHXs) were installed in the standpipe section between the solids outlets of the columns and the L-valves. It would be possible to mount the moving bed heat exchangers above the columns, between the gravitational gas-solids separators and the solids inlets of the columns, however this configuration would make an additional device for sorbent flow control necessary. Here, an L-valve would control the flow of sorbent as is the case in the TSA BSU, however to allow the formation of a moving bed in the MBHXs, an e.g. L-valve at each of the solid outlets of the MBHXs needs to be installed to control the solids level in the respective MBHX.

Both MBHX installed in the TSA BSU are counter current heat exchangers equipped with horizontal finned-tube bundles as shown in the technical drawings in the Appendix (see Figure 71 and Figure 72). Finned tubes were chosen rather than bare tubes to increase the installed heat transfer surface area and thus increase the overall heat transfer rate. The fin height is 9 mm, whereas the bare tube diameter is 30 mm. Although the tube pitch, as well as cross-section of both MBHXs are identical, the fin density and the height of the MBHXs vary. The heat exchanger tubes installed in the rich heat exchanger (RHX) have a fin density of 300 fins per meter of tube, whereas those in the LHX have a fin density of 200 fins per meter. To make a similar heat transfer surface area available in both MBHX, the lean heat exchanger (LHX) is 84 mm longer and thus incorporates two additional heat exchanger tube rows than the RHX. This design allowed a heat transfer surface area of 2.3 m<sup>2</sup> in the RHX and a heat transfer surface area of 2.2 m<sup>2</sup> in the LHX.

To reduce the sensible heat demand in the desorber to zero, the temperature of the sorbent at the inlet of the desorber must match the desorber operating temperature. However, carrying out the entire temperature swing in the RHX, may lead to undesirable operating conditions. This is because an increase of the sorbent temperature may be accompanied by a release of gas. High amounts upward travelling gas may interfere with downward flowing solids, whereas downward flowing gas may lead to loss of solids throughput control through the L-valve. To enable a further increase of the sorbent temperature at the inlet of the desorber, a fluidized bed heat exchanger, i.e. the pre-desorber seen in Figure 57, is installed downstream of the RHX, in the bottom section of the rich riser. The pre-desorber is heated by thermal oil and features a bundle of bare pipes with a total heat transfer surface area of 0.14 m<sup>2</sup>. As can be seen in Figure 57, gas can flow freely between the rich riser loop and the desorber. Because the fluidizing agent in the rich riser is recycled, any gas that is released by the sorbent will entail an equal amount of gas to flow from the rich riser loop into the desorber. Assuming a continuous supply of heat to the pre-desorber, the recycle gas will become a mixture of steam and CO<sub>2</sub>, i.e. the gases released by the sorbent. Since both these gases make up the desorber off-gas, gas flow from the rich transport line to the desorber is tolerable.

A notable difference between the BSU configuration in Section 3.1 and the configuration seen in Figure 57 is the fluidizing agent of the lean riser. Instead of being recycled, a partial flow of adsorber off-gas is diverted and used to fluidize the lean riser. In this way, the lean riser acts as a sixth adsorber stage in which the contacting regime is co-current.

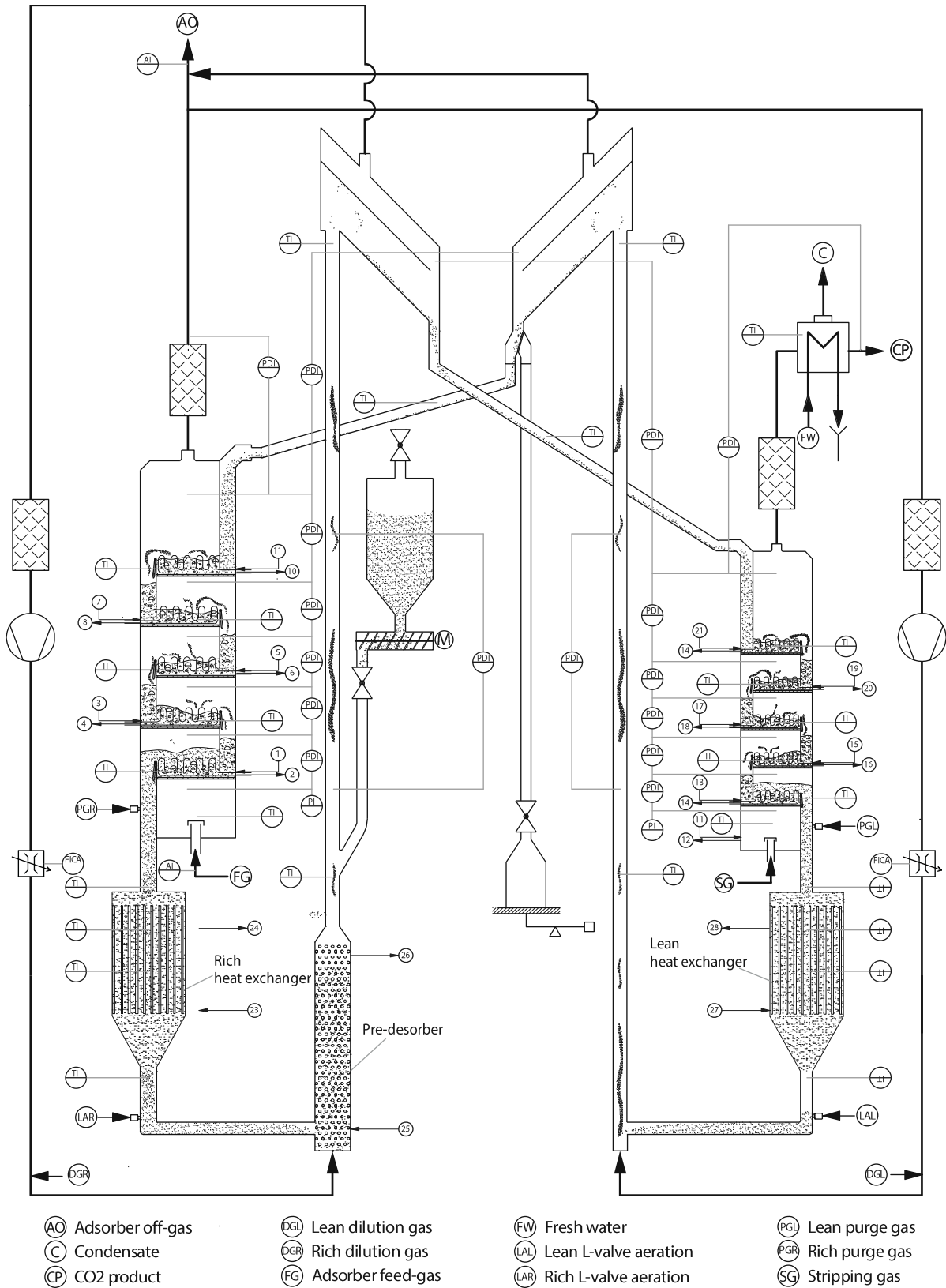


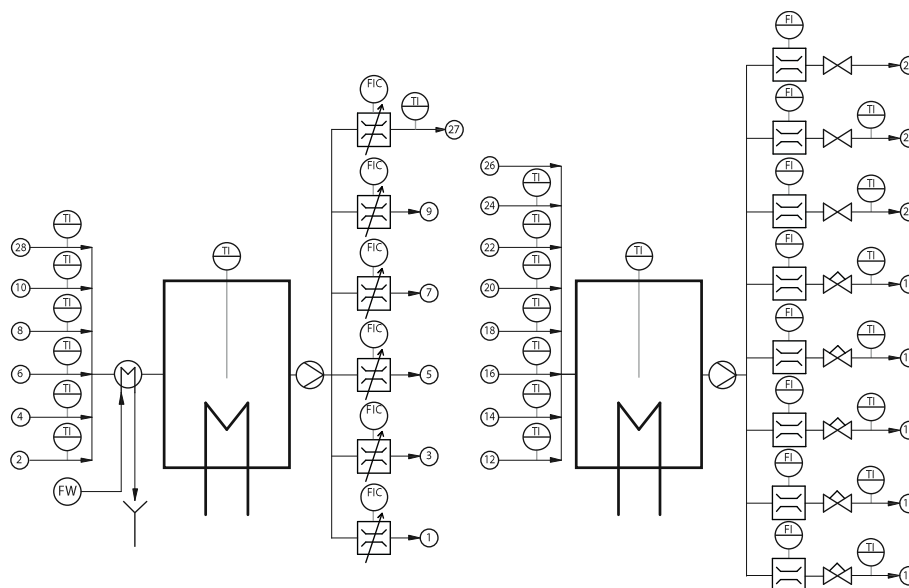
Figure 57: Schematic illustration of the instrumentation used in the TSA BSU during the lean/rich heat exchanger tests

### Instrumentation

For determining the achievable HTC in the MBHXs knowledge of the logarithmic mean temperature difference as well as the amount of transferred heat is required. As seen by the instrumentation of the TSA BSU in Figure 57, additional temperature sensors were installed in the MBHXs. The inlet and outlet temperatures of the sorbent was required for calculation of the logarithmic mean temperature difference. The temperature sensors used for this purpose were CANTrans PT-1000-type RTDs supplied by Jumo, with a measuring range of  $-50\text{ }^{\circ}\text{C}$  to  $150\text{ }^{\circ}\text{C}$  and an accuracy that complies with class B of the DIN EN 60751 standard. These temperature sensors were also used for monitoring of the intermediate temperatures of the sorbent at two locations within each MBHX.

Because the heat capacity of the heat transfer fluids was well known, the amount of transferred heat was determined using the forward and return temperatures of the heat transfer fluid together with its heat capacity and flow rate. The thermal oil flow rate to the RHX was measured by a calibrated turbine flow meter and the cooling water flow rate to the LHX measured by a DK800-type rotameter supplied by Krohne. The utilized rotameter is within the accuracy class 2.5 of the VDI/VDE 351 standard. Furthermore, the same PT-1000-type RTDs as mentioned above were used to measure the forward and return temperature of the cooling water and thermal oil in the LHX and RHX respectively. As shown in Figure 58, the thermal oil and cooling water network was extended to allow heating of the RHX and the pre-desorber with thermal oil and cooling of the LHX with cooling water. It should be noted that the transferred amount of heat was not determined in the pre-desorber because the forward and return temperature of thermal oil to this heat exchanger was not measured. It should be mentioned that the flow rate of the thermal oil pump is limited to approx.  $10\text{ kg}\cdot\text{min}^{-1}$ .

Additionally, the solids temperatures at the inlet of the columns was monitored using two PT-100-type RTDs that comply with the accuracy class 1/3 class B of the DIN EN 60751 standard.



**Figure 58: Schematic illustration of the cooling water tank, thermal oil tank and associated instrumentation during the lean/rich heat exchanger tests**

#### 4.6.2 Data analysis

In the course of the experiment, the cooling duty in the adsorber is calculated to evaluate the impact of the LHX on the cooling duty in the adsorber required to achieve the target operating temperature. It should be noted however, that the calculated values are inaccurate and can only be used to compare cooling duties between the individual phases of the experiment. This is because visual inspection of the fluidized beds through the borosilicate reactor walls of the adsorber was considered a higher priority than minimizing the heat losses through the reactor walls and thus allowing for accurate determination of the cooling duty in the adsorber stages. For this reason, the adsorber was not insulated and individual stages were not equipped with temperature sensors at the cooling water inlet (as seen in Figure 58). The forward flow temperature of coolant to all adsorber stages was assumed equal to the cooling water temperature at the inlet of the LHX. The adsorber cooling duty was calculated according to Eq. 48.

$$\dot{Q}_{ADS} = \sum_{Stage=1}^5 \dot{m}_{CW, Stage} \cdot c_{p, CW} \cdot (T_{CW, FF, LHX} - T_{CW, RF, Stage}) \quad \text{Eq. 48}$$

For the conducted experiment, the cooling duty of the LHX and the heat input of the RHX were continuously calculated. This was done via a heat balance over the cooling water (CW) and thermal oil (TO) in the LHX and RHX respectively:

$$\dot{Q}_{RHX} = \dot{m}_{TO} \cdot c_{p, TO} \cdot (T_{TO, FF} - T_{TO, RF}) \quad \text{Eq. 49}$$

$$\dot{Q}_{LHX} = \dot{m}_{CW} \cdot c_{p, CW} \cdot (T_{CW, FF} - T_{CW, RF}) \quad \text{Eq. 50}$$

By using the duties of the moving bed heat exchangers together with the heat transfer surface area and the logarithmic mean temperature difference, the HTC ( $h_{RHX}$  and  $h_{LHX}$ ) of the moving bed heat exchangers can be calculated as shown in Eq. 51 and Eq. 52.

$$h_{RHX} = \frac{|\dot{Q}_{RHX}|}{dT_{log, RHX} \cdot 2,2m^2} \quad \text{Eq. 51}$$

$$h_{LHX} = \frac{|\dot{Q}_{LHX}|}{dT_{log, LHX} \cdot 2,3m^2} \quad \text{Eq. 52}$$

The logarithmic mean temperature differences,  $dT_{log, RHX}$  and  $dT_{log, LHX}$  were calculated using the inlet and outlet temperatures of the heat transfer fluids and the inlet and outlet temperatures of the solids as shown in Eq. 53 and Eq. 54.

$$dT_{log, RHX} = \frac{(T_{TO, RF} - T_{s, RHX, in}) - (T_{TO, FF} - T_{s, RHX, out})}{\ln \frac{(T_{TO, RF} - T_{s, RHX, in})}{(T_{TO, FF} - T_{s, RHX, out})}} \quad \text{Eq. 53}$$

$$dT_{log, LHX} = \frac{(T_{s, LHX, in} - T_{CW, RF}) - (T_{s, LHX, out} - T_{CW, FF})}{\ln \frac{(T_{s, LHX, in} - T_{CW, RF})}{(T_{s, LHX, out} - T_{CW, FF})}} \quad \text{Eq. 54}$$

Since the heat input and the cooling duty in the heat exchangers is calculated via the heat balance on the heat transfer medium side of the heat exchangers, the introduced/extracted heat may not exclusively reflect the sensible heat required to heat the solids to a specific temperature. In the RHX, the introduced heat may also include the latent heat for steam or CO<sub>2</sub> desorption.

The indicators used to assess the simulated recovery of sensible heat in the LHX ( $HR_{LHX}$ ) and RHX ( $HR_{RHX}$ ) are shown in Eq. 55 and Eq. 56 respectively. The simulated heat recovery in each MBHX is given as a percentage of the quotient between the temperature approach of the sorbent in respect to the average operating temperature of the adjacent column ( $T_{DES} - T_{s,LHX,out}$  and  $T_{s,RHX,out} - T_{ADS}$ ) and the temperature swing ( $\Delta T_{ADS,DES}$ ). Unity of  $HR_{LHX}$  and  $HR_{RHX}$ , is thus reached when the solids outlet temperature of the LHX and RHX equals the operating temperature of the adjacent column respectively.

A similar indicator as  $HR_{LHX}$  and  $HR_{RHX}$  was chosen as a performance indicator for the pre-desorber. As can be seen in Eq. 57, the relative temperature approach in the pre-desorber ( $\Delta T_{PreDES}^*$ ) approaches unity if the sorbent can be heated to the average desorber operating temperature. At these conditions, the desorber heat demand is reduced to the latent heat requirement only, thus reducing the required heat transfer area in the desorber.

$$HR_{LHX} = \frac{T_{DES} - T_{s,LHX,out}}{\Delta T_{ADS,DES}} \cdot 100\% \quad \text{Eq. 55}$$

$$HR_{RHX} = \frac{T_{s,RHX,out} - T_{ADS}}{\Delta T_{ADS,DES}} \cdot 100\% \quad \text{Eq. 56}$$

$$\Delta T_{PreDES}^* = \frac{T_{s,PreDES,out} - T_{s,RHX,out}}{\Delta T_{ADS,DES}} \cdot 100\% \quad \text{Eq. 57}$$

### 4.6.3 Operating Conditions

Target operating temperature ranges were defined for the adsorber and the desorber, as shown in Table 25. The temperature of cooling water and thermal oil were kept constant and the column temperatures were maintained by manually adjusting the flow rate of cooling water and thermal oil to the individual adsorber and desorber stages. The resulting cooling duty and heating demand in the columns was calculated to evaluate the impact of the newly installed subsystems (RHX, LHX and pre-desorber) on the TSA BSU. As can be seen in Table 25, a fixed flow of adsorber off-gas was diverted to fluidize the lean riser. It should also be noted that the installed MBHX increased the sorbent inventory of the TSA BSU to 15.5 kg, whereas 4.2 kg can be attributed to the RHX and 5.2 kg to the LHX.

Adsorber operating temperature	45-50	[°C]
Adsorber feed gas velocity	0.32	[m·s <sup>-1</sup> ]
Adsorber feed gas O <sub>2</sub> concentration	9	[vol%O <sub>2</sub> ]
Adsorber feed gas CO <sub>2</sub> concentration	3.5	[vol%CO <sub>2</sub> ]
Cooling water temperature	35	[°C]
Steam flow to adsorber	0.5	[kg·h <sup>-1</sup> ]
Desorber operating temperature	100-105	[°C]
Desorber stripping steam flow-rate	8.5	[kg·h <sup>-1</sup> ]
Lean purge gas flow rate	0.032	[Nm <sup>3</sup> ·h <sup>-1</sup> ]
Thermal oil temperature	108	[°C]
Solids circulation rate	14.2	[kg·h <sup>-1</sup> ]
Lean riser gas flow rate	13	[m <sup>3</sup> ·h <sup>-1</sup> ]
Sorbent inventory	15.5	[kg]

**Table 25: Target operating conditions during the conducted test with lean/rich heat exchange**

The test was composed of three phases. In each phase, a different subsystem was activated and the impact on the TSA BSU evaluated. In Phase 1, the LHX was activated and a solids temperature of 50 °C at the outlet, i.e. a simulated  $HR_{LHX}$  approaching unity, was targeted. As can be seen in Table 25, the lean purge gas flow rate was set to a rather low value of 0.032 Nm<sup>3</sup>·h<sup>-1</sup> of N<sub>2</sub> to inhibit a slip of steam and subsequent condensation in the cooled LHX.

As mentioned, the focus of this experiment was on the installed MBHX. For this reason in the second phase, a thermal oil flow rate budget of 1.5 kg·min<sup>-1</sup> was assigned for heating the pre-desorber. This was done instead of targeting a specific temperature in the rich riser to make a thermal oil flow rate reserve available for the RHX.

In Phase 3, the RHX was activated and a solids temperature at the RHX outlet of 90 °C was targeted, i.e. a  $HR_{RHX}$  of slightly over 70 %. This target temperature was chosen in accordance with available CO<sub>2</sub> adsorption data of Sorbent B. The CO<sub>2</sub> equilibrium loading should be more or less identical for a CO<sub>2</sub> concentration of 3.5 vol%CO<sub>2</sub> at a temperature of 50°C and a CO<sub>2</sub> concentration of 100 vol%CO<sub>2</sub> at a temperature of 90°C. Therefore, 90°C was considered the temperature at which the release of CO<sub>2</sub> from the sorbent is expected to be rather low in the RHX.

#### 4.6.4 Results & Discussion

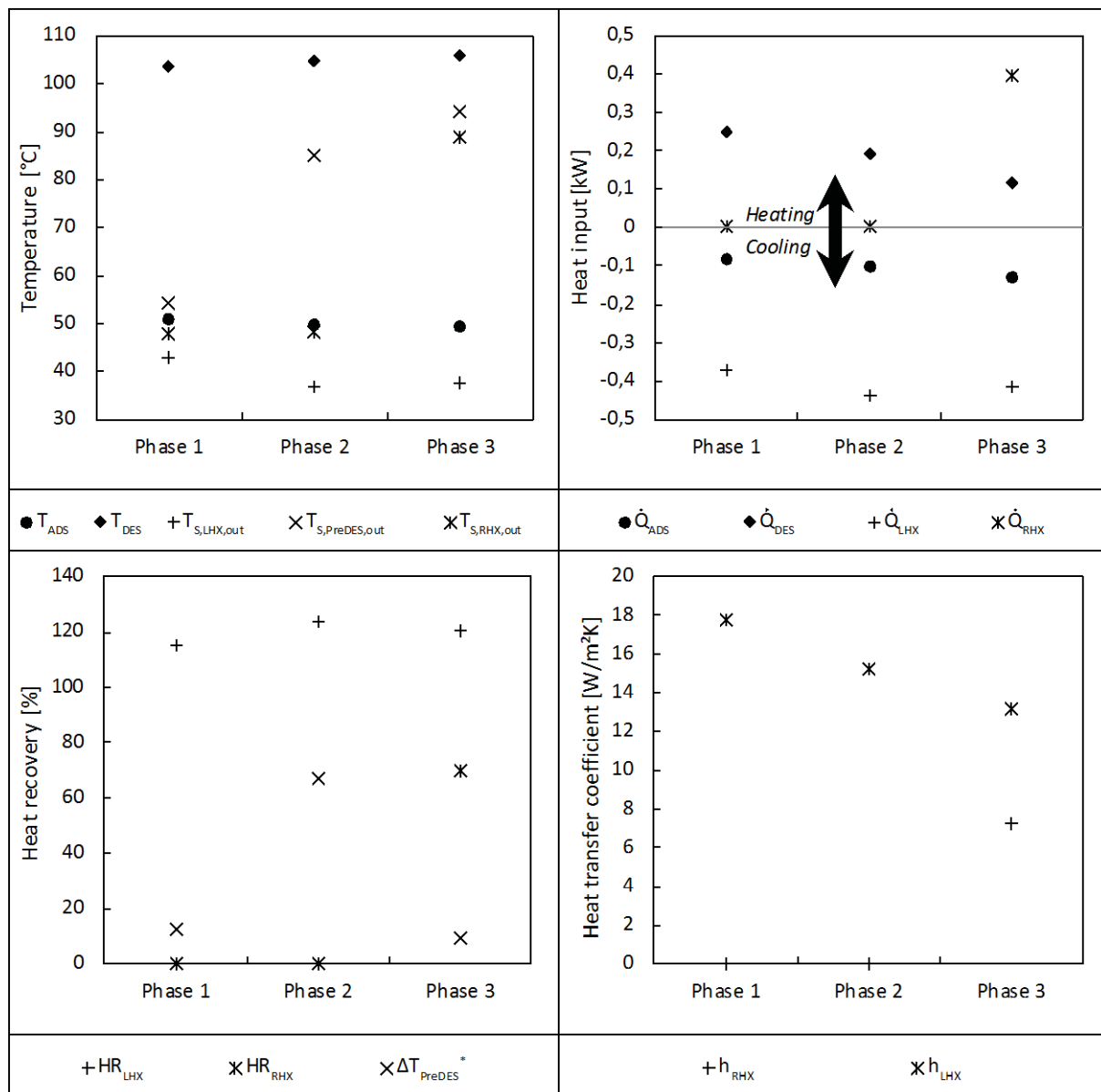
By adequately adjusting the flow rate of thermal oil and cooling water, only a slight increase and decrease of the average operating temperatures of the desorber and adsorber were recorded respectively. Throughout the test, the adsorber cooling duty decreased from approx. 130 W (without considering heat losses to the environment) to approx. 80 W, which led to a decrease of the average column temperatures from 50.8 °C to 49.2 °C. In Figure 59, it can be seen that the lean solids exiting the LHX could be cooled to temperatures below the average adsorber operating temperature throughout the entire experiment. This indicates that the entire sensible cooling demand of the process was met by the LHX, thereby simulating a  $HR_{LHX}$  of over 100 %. Therefore, only the latent heat for CO<sub>2</sub> adsorption needed to be extracted from the adsorber, whereas in the light of the results given in Section 4.5, it is likely that this was partially counter-balanced by the heat demand for H<sub>2</sub>O

desorption. Condensation in the LHX was not observed in the entire experimental runtime, hence the low flow rate of  $N_2$  (i.e.  $0.032 \text{ Nm}^3 \cdot \text{h}^{-1}$ ) introduced as a lean purge gas, can be considered sufficient to prevent excessive slip of steam from the desorber to the LHX at the prevailing operating conditions. It should be noted that the lean riser is fluidized by adsorber off-gas, which contains oxygen. Therefore, the LHX is not only a device required for heat recovery, but is also a safeguard for oxidative degradation of the sorbent in the lean riser. This is because the LHX reduces the temperature of the sorbent to a level (i.e.  $50 \text{ }^\circ\text{C}$ ), at which oxidative degradation has shown to no longer effect the  $\text{CO}_2$  adsorption capacity of the sorbent [43].

In Phase 2, the solids temperature at the outlet of the pre-desorber, i.e. the temperature at the bottom of the rich riser, could be raised to  $84.9 \text{ }^\circ\text{C}$ . Thereby realizing a relative temperature approach in the pre-desorber of 64 %. As seen, this could reduce the desorber heat input by 22 % i.e. from 246 W to 192 W, whereas a slight increase of the average desorber temperature, from  $103.5 \text{ }^\circ\text{C}$  to  $104.5 \text{ }^\circ\text{C}$  was observed. Preheating the sorbent can reduce the measured desorber heat input by an increase of the sorbent temperature, a reduction in the  $\text{CO}_2$  loading and a reduction of the water loading. An increase of the sorbent temperature obviously decreases the sensible heat demand in the desorber, whilst a reduction of the  $\text{CO}_2$  loading reduces the latent heat demand in the desorber. However, a reduction of the  $\text{H}_2\text{O}$  loading can intensify  $\text{H}_2\text{O}$  adsorption in the desorber, which can counter-balance both the heat demand for  $\text{CO}_2$  desorption and the sensible heat demand at the cost of steam transportation to the adsorber and an increased heat demand of the pre-desorber. Nevertheless, the experimental setup did not allow for determining a potential reduction of the  $\text{H}_2\text{O}$  or  $\text{CO}_2$  loading of the sorbent at the sorbent inlet of the desorber.

By activating the RHX in Phase 3, the sorbent temperature could be increased to  $88.7 \text{ }^\circ\text{C}$  at the outlet of the RHX, whereas a temperature of  $93.9 \text{ }^\circ\text{C}$  was achieved at the outlet of the pre-desorber. These temperatures represent a  $HR_{RHX}$  of 70 % and a  $\Delta T_{PreDES}^*$  of 9 %, which means that the bulk sensible heat was supplied in the RHX (i.e. 88 %). It is noteworthy, that compared to Phase 2 the heat input in the desorber dropped by 39 % (from 192 W to 118 W) in Phase 3. This disproportionate decrease in the desorber heating demand indicates that considerable amounts of latent heat was supplied by the heat exchangers, which in turn causes the release of  $\text{CO}_2$  or  $\text{H}_2\text{O}$ . The pressure gradient between the rich riser and the adsorber controls the flow direction of the released gas. If the pressure gradient is directed upward, high amounts of released gas can hinder the downward flow of sorbent. Conversely, a higher pressure in the adsorber than in the rich riser will direct released gas downward. In this case, the released gas can entail a reduction of the required L-valve aeration flow rate to maintain a constant SCR. Between Phase 2 and Phase 3, the L-valve aeration did not undergo a decrease, therefore it can be assumed that gas released by the sorbent in the RHX during Phase 3 travelled upwards. However, at the prevailing operating conditions, the released gas did not interfere with solids transport from the adsorber. A slight flow of gas from the RHX towards the adsorber can have advantages. This is because an upward flow of gas can purge the interstitial volume of the moving bed in the standpipe and thus prevent a slip of flue gas to the desorber. A slip of flue gas from the adsorber into the desorber via the rich riser loop can entail the contamination of the  $\text{CO}_2$  product with “non-condensable” gases present in the flue gas (i.e.  $N_2$  and  $O_2$ ). Preventing gas slip is of particular importance, when the capture  $\text{CO}_2$  is compression and liquefied as non-condensable present in the  $\text{CO}_2$  can increase compression work [156].



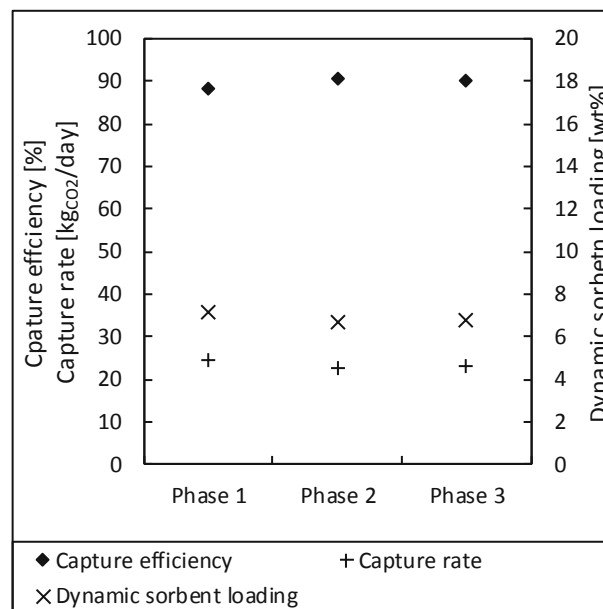


**Figure 59: Selected temperatures throughout the TSA BSU (top left), the amount of extracted and supplied heat in the columns and MBHXs (top right), the achieved LRHX in the MBHXs and pre-desorber (bottom left) and heat transfer coefficient of the moving bed heat exchangers (bottom right) during the conducted test with simulated lean/rich heat exchange.**

The HTC was continuously calculated in the MBHXs. In Figure 59, it can be seen that the HTCs,  $h_{RHX}$  and  $h_{LHX}$ , were in the range of  $13 \text{ W}\cdot\text{m}^{-2}\cdot\text{K}^{-1}$  up to  $18 \text{ W}\cdot\text{m}^{-2}\cdot\text{K}^{-1}$  in the LHX whilst in the RHX a value of only  $7 \text{ W}\cdot\text{m}^{-2}\cdot\text{K}^{-1}$  was measured.

Wall-to-moving bed heat transfer depends mainly on the solids diameter, particle conductivity and the solids residence times (i.e. the solids velocity) [157–159]. Obuskovic et al. [160,161] conducted measurements of the HTC between a moving bed of solids and a single finned tube-type heating cartridge at varying solids velocities. The bed materials used in these investigations were sand, polyethylene and copper, whereas the mean diameter of bulk particles ranged from  $110 \mu\text{m}$  up to  $1.6 \text{ mm}$ . Obuskovic et al. [160,161] developed a mathematical model which could replicate 85 % of the measured values with a deviation of  $\pm 20 \%$ . The derived empirical correlation for the HTC between a

moving bed of solids and a finned tube can be seen in the Appendix of this work (see Section 8.9). According to the proposed correlation, the expected HTC for the RHX and the LHX used in the course of this work are  $23.0 \text{ W}\cdot\text{m}^{-2}\cdot\text{K}^{-1}$  and  $22.6 \text{ W}\cdot\text{m}^{-2}\cdot\text{K}^{-1}$  respectively. Although the HTC in the LHX could be predicted with reasonable accuracy (i.e. a deviation of approx. 25 %), the predicted HTC in the RHX deviated considerably from the values measured in the course of Phase 3 of the test. This deviation may partially be attributed to the absorption of latent heat by the rich sorbent moving through the RHX, which led to the release of adsorbed gas. It should be noted that the HTC was calculated using the introduced heat via the thermal and the logarithmic mean temperature difference, which takes the inlet and outlet temperatures of both the sorbent and the thermal oil into account. Therefore, a temperature change of thermal oil that does not entail a temperature change of the sorbent will lead to reduction of the calculated HTC. Since the amount and composition of the released gas is unknown, the true HTC of the RHX cannot be determined. Therefore, the performance of the different MBHX designs in terms of the achievable HTC cannot be evaluated and a clear design recommendation regarding the fin density on the tube cannot be given.

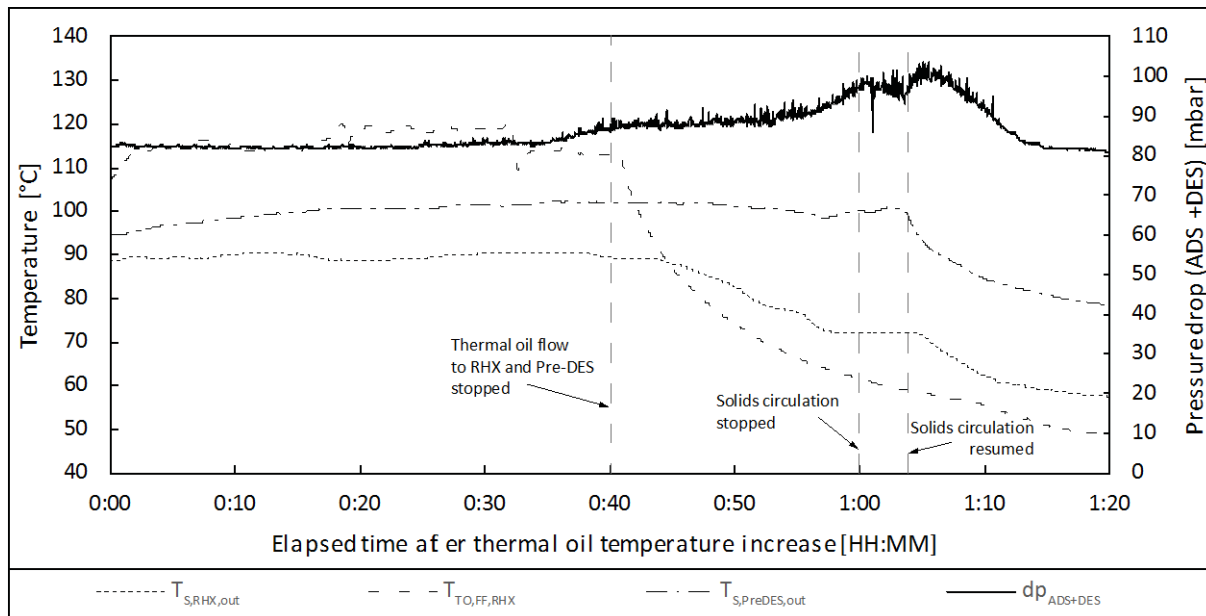


**Figure 60: Graph showing the CO<sub>2</sub> capture performance during the conducted test with simulated lean/rich heat exchange.**

Since the operating conditions of the TSA BSU, such as stripping steam flow rate, adsorber operating temperature, SCR and desorber operating temperature were virtually constant in the course of the test, a rather small impact of simulated LRHX on the CO<sub>2</sub> capture performance is seen in Figure 60. As shown in the graph, the CO<sub>2</sub> capture efficiency stayed between 88.2 % and 90.7 % during the entire experiment. The slight reduction of the dynamic sorbent loading (i.e. from 7.2 wt% to 6.7 wt%) and the capture rate (i.e. from  $24.4 \text{ kgCO}_2\cdot\text{day}^{-1}$  to  $22.8 \text{ kgCO}_2\cdot\text{day}^{-1}$ ) are a result of fluctuations of the adsorber feed gas CO<sub>2</sub> concentration (between 3.17 vol%CO<sub>2</sub> and 3.49 vol%CO<sub>2</sub>) in the course of the test.

### Additional testing

After the test, it was chosen to increase the thermal oil temperature from 108 °C to 119 °C, in an effort to increase the sorbent temperature at the outlet of the pre-desorber. During this test, the thermal oil flow rate to the desorber stages and the RHX were reduced to maintain the same temperatures as in Phase 3 of the test, i.e. 105.8 °C and 88.7 °C respectively. Simultaneously, the flow rate of thermal oil to the pre-desorber was maximized. It should be noted that apart from these changes, the operating conditions of the TSA BSU were left unchanged.



**Figure 61: Graph showing selected temperatures and the sum of column pressure drops as a function of the elapsed time after a temperature increase of thermal oil after the conducted test with simulated lean/rich heat exchange.**

Figure 61, shows selected temperatures and the sum of pressure drops over both the adsorber and desorber column, for one hour and twenty minutes after the thermal oil temperature was increased. It can be seen that within the initial 35 minutes, a temperature of 102.2 °C could be achieved at the outlet of the pre-desorber i.e. a relative temperature approach in the pre-desorber ( $\Delta T_{PreDES}^*$ ) of 22.2 %. However, it can also be seen that the sum of column pressure drops (shown in Figure 61 as  $dp_{ADS+DES}$ ) undergoes a slight increase between 00:35 and 00:40. This figure has shown to be a reliable indicator for the sorbent inventory of the BSU, and the observed change of 6 % within the rather short timeframe could not be explained. To avoid a potential operational upset, it was chosen to abort this additional test. Therefore, the thermal oil flow to the RHX and the pre-desorber was stopped and the thermal oil temperature reduced to 108 °C, i.e. the value set during Phase 3 of the test. The MBHXs hold 60 % of the entire solids inventory, therefore the formation of a cavity in one of the MBHXs can drastically influence the measured inventory in the columns. It was hypothesized that the higher tube wall temperatures in the RHX led to the release of high amounts of gas from sorbent material near the heat exchanger tube walls. The released gas flows upwards and interferes with the downward flow of solids. In a narrow region of the RHX, this may have led to the formation of solids bridges and to a cavity within the RHX. It should be mentioned that solids bridging is more likely to

occur at the small scale of the BSU, because the small cross-sections of the standpipe and sorbent inlet of the RHX increase the influence of wall-friction on particle movement.

Nevertheless, the transparent tubing at the solids inlet and solids outlet of both MBHXs was visually inspected at approx. 00:40. At the inlet of the RHX, a stagnant bed of solids was observed, whilst a moving bed was observed at the inlet of LHX. Simultaneously, a moving bed was observed at the outlets of both MBHXs.

Although the thermal oil temperature decreases drastically, an observed increase of the column inventory made it necessary to halt solids circulation. In this time, BSU operators introduced vibrations to the RHX. As can be seen in Figure 61, this resulted in a reduction of the column inventory. Solids circulation was resumed and by introducing vibrations, the RHX could be refilled with solids thereby restoring the original column inventory during the cool-down phase. It should be noted that this behavior confirms the hypothesized formation of a cavity in the RHX.

#### 4.6.5 Conclusion

Heat integration within a process can contribute to a reduction of the overall process heat demand. In the investigated TSA process, heat integration can be realized by lean/rich heat exchange i.e. by pre-heating rich solids using heat recovered from the lean sorbent material exiting the desorber. One moving bed heat exchanger was installed below each of the columns, and lean/rich heat exchange was simulated by heating and cooling the rich and lean moving bed heat exchangers with thermal oil and cooling water respectively. An additional fluidized bed heat exchanger was installed upstream of the desorber, i.e. the pre-desorber, to further increase the sorbent temperature to desorber operating temperatures.

The results of the first test with the newly installed heat exchangers showed that a simulated heat recovery rate of 70 % could be achieved in the RHX. In the pre-desorber the sorbent temperature could be increased from 88.7 °C at the outlet of the RHX to 93.9 °C, which significantly reduced the desorber heat input by over 50 % compared to operation without these heat exchangers in operation. In the LHX the sorbent could be cooled below the average operating temperature of the adsorber during all operating points. This not only shows that a heat recovery rate of over 100 % could be simulated in the LHX, but also that the utilized purge gas in the standpipe between desorber and LHX worked as intended and could prevent condensation of steam in the LHX. Furthermore, the low sorbent temperatures achieved at the outlet of the LHX show that the LHX fulfills its purpose as a safeguard to protect the sorbent material from oxidative degradation in the lean riser.

Nevertheless, the measured HTC of the MBHXs, i.e.  $13 \text{ W}\cdot\text{m}^{-2}\cdot\text{K}^{-1}$  up to  $18 \text{ W}\cdot\text{m}^{-2}\cdot\text{K}^{-1}$  in the LHX and  $7 \text{ W}\cdot\text{m}^{-2}\cdot\text{K}^{-1}$  in the RHX were rather low. Especially in the RHX, the HTC showed considerable deviation to predictions made by a heat transfer model developed by Obuskovic et al. [160]. The low measured values were attributed to the endothermal release of adsorbed  $\text{CO}_2$  and water from the sorbent in the RHX.

In an effort to increase the temperature of the rich sorbent entering the desorber and thus reduce the sensible heat demand in the desorber to zero, an additional test was carried out in which the thermal oil temperature was increased from 108 °C to 119 °C. This change entailed operational issues, which were indicative for the release of high amounts of gas from the sorbent in the RHX. It was assumed that the flow direction of the released gas was upwards towards the adsorber. This effect can be regarded as advantageous since it can reduce the slip of flue gas into the  $\text{CO}_2$  product via the rich riser.

However, based on at the small scale of the BSU and the associated wall-effects, it is likely that a solids bridge was formed near the inlet of the RHX, which was followed by the formation of a cavity and an inventory transfer from the RHX to the columns. At a larger scale, a higher pipe diameter of the standpipe should significantly reduce the influence of wall friction on the moving bed. Therefore, issues associated with solids bridging should not occur at the inlet of the RHX. However, at a larger scale measures should be put in place to prevent the fluidization of the solids in the standpipe between the RHX to the adsorber. A possibility could be to install a bypass line equipped with a valve in the RHX, so that released gas can be diverted towards the rich riser.

## 5. CONCLUSIONS AND RECOMMENDATIONS FOR NEXT SCALE

Experiments at bench scale have been a valuable tool in the development of the TSA process for CO<sub>2</sub> capture using amine-functionalized sorbents. In 2018, a TSA pilot unit based on the interconnected multi-stage fluidized bed design with a CO<sub>2</sub> capture capacity of 1 ton<sub>CO<sub>2</sub></sub>·day<sup>-1</sup> was constructed and put into operation [162]. Results gained in the course of the experimental campaigns presented herein have de-risked various aspects of the process and have served as valuable input in the design of the TSA pilot unit.

Based on the obtained results from the experimental campaigns presented in this work, a number of recommendations were made for the TSA pilot unit design that are also valid for the implementation of TSA in multi-stage fluidized bed systems using amine-functionalized sorbents at an even larger scale.

- **Bubble breaking:** The adsorber footprint will have a considerable impact on the construction cost of TSA units. To allow for treating the maximum amount of flue gas at the lowest possible footprint, the superficial gas velocity in the adsorber must be increased. The effects of increasing adsorber feed gas velocities was investigated in Section 4.1. At superficial gas velocities above 0.68 m·s<sup>-1</sup>, insufficient gas-solids contact entailed a reduction in the achievable CO<sub>2</sub> capture performance. Visual observations indicate that this was brought about by bubble coalescence and subsequent slip of gas through the bubble phase of the fluidized bed, especially in the downcomer section. It is therefore recommended that bubble breaking internals be implemented in the adsorber to minimize gas slip even at high flue gas feeding rates. The adsorber of the TSA pilot unit features heat exchanger tubes bundles immersed in each fluidized bed stage (see Figure 62). These tube bundles not only allow for efficient heat transfer but also have a bubble breaking effect.
- **Adsorber downcomer design:** With the internal downcomer design implemented in the TSA BSU, a low flow of gas is required to promote solids transport from the downcomer into the fluidized bed stage below. This gas flow is supplied via the gas distributor, which is shared with the fluidized bed section. Because the column gas feeding rate has a strong influence on the bed state in the downcomer, the formation and coalescence of bubbles in the internal downcomer can contribute to gas slip at high column feed gas velocities. An alternative design of the downcomers that decouples the bed state in the downcomer from the gas feeding rate of the column, not only increases the flexibility of the TSA system but also reduces the risk of gas slip through the downcomer at high superficial gas velocities in the column. This can be achieved by implementing external downcomers equipped with L-valves, where solids throughput is controlled by the aeration rate of the L-valve. Since flexibility, both in terms of the column feed gas flow rate and the achievement of high column feed gas velocities, is more relevant in the adsorber than in the desorber, the implementation of external downcomers is recommended in the design of the adsorber column. In the adsorber of the TSA pilot unit, external downcomers have been implemented in the adsorber as solids transport devices, whereas L-valves manage the transport of solids from the downcomer into the next-lower stage (see Figure 62).

- **Immersed bed heat exchanger tube bundles:** At multiple occasions throughout the presented experimental campaigns (i.e. in Section 4.1 and in Section 4.2), process performance was limited by the amount of heat that could be extracted or supplied in the columns. This is largely due to the limited space available at bench scale rather than an intrinsic issue with the process. To allow an increased ratio of heat transfer surface to bed volume compared to the BSU and provide internals for bubble breaking, heat exchanger bundles immersed in the fluidized beds of the adsorber and desorber are recommended. Both columns of the TSA pilot unit feature these types of heat transfer surfaces in all fluidized bed stages (see Figure 62). In the desorber, this increased the heat transfer surface area immersed in the fluidized bed stages of the desorber from  $42.6 \text{ m}^2 \cdot \text{m}^{-3}$  in the BSU to  $64.5 \text{ m}^2 \cdot \text{m}^{-3}$  in the TSA pilot unit.
- **SO<sub>2</sub> and NO<sub>x</sub> in the treated flue gas:** Nitrogen oxides and sulphur dioxide are components commonly found in flue gases; therefore, an understanding of the interaction between these gases and the sorbent materials used in TSA is important for further upscaling. In an experimental campaign, described in Section 4.3, a flue gas consisting of considerable amounts of nitrogen monoxide (NO), nitrogen dioxide (NO<sub>2</sub>) and sulphur dioxide (SO<sub>2</sub>) was treated in the BSU. By evaluating the development of the CO<sub>2</sub> capture performance in the course of three experiments, the effect of these trace components could be investigated. It was found that NO does not interact with Sorbent A, whereas NO<sub>2</sub> and SO<sub>2</sub> result in a reduction of the CO<sub>2</sub> capture performance. Therefore the presence of SO<sub>2</sub> and NO<sub>2</sub> in the adsorber feed gas should be avoided when using Sorbent A as these species lead to considerable degradation and will thus make high sorbent make-up rates necessary.
- **Recommended sorbent material:** Section 4.4, was dedicated to a comparison between a PEI impregnated silica-type sorbent, i.e. Sorbent A, and a polymer-based sorbent with primary amine covalently bound to the sorbent surface, i.e. Sorbent B. In the course of two 120-hour experiments, the two sorbent materials were not only evaluated in terms of the achievable process performance, but also regarding the sorbent degradation rate and process emissions. The higher amine content of Sorbent A allowed operation at a lower SCR. However, high amine loss rates resulted in a considerable decrease of the CO<sub>2</sub> capture performance. Sorbent B showed to be highly tolerant to attrition, cause lower emissions in the CO<sub>2</sub> product and the CO<sub>2</sub> product cooler condensate, and was more resistant towards thermal and oxidative degradation. These factors not only reduce the requirements for potential emission reduction measures, but also reduce the required sorbent make-up rate. These are factors that can have a strong impact on the construction cost and the operational cost of TSA, therefore Sorbent B can be recommended as a sorbent material for TSA systems that are operated at similar conditions as the TSA BSU. From the results gained in the course of this campaign, it was chosen to operate the TSA pilot unit with Sorbent B.
- **Water co-adsorption:** Water is a major component of typical flue-gases and can be adsorbed by Sorbent B. Water adsorption in the adsorber can impose a parasitic cooling and heating demand on the adsorber and desorber respectively; therefore, this operating mode must be avoided. In Section 4.5, it was established that the direction of water transport between the columns can be influenced via the relative humidity of the column feed gases. Furthermore, a significant decrease of the desorber heat input was measured when allowing steam adsorption in the desorber. These findings result in two different scenarios that affect both the design and the operating conditions of a TSA system at a larger scale. If results from a techno-economical evaluation show that significant amounts of steam can be consumed to reduce construction

costs associated with installing heat transfer surfaces in the desorber and adsorber, then the desorber is to be operated in a way that a higher relative humidity is achieved in the desorber than in the adsorber. If steam consumption is to be avoided, the provided heat transfer surface area in the desorber needs to be high, and the desorber operated in way that the relative humidity in the desorber feed is equal or slightly higher than the relative humidity of the adsorber feed gas. A flue gas cooler was installed upstream of the adsorber of the TSA pilot unit to gain control over the relative humidity of the adsorber feed gas, whereas the relative humidity in the desorber can be controlled via the temperature, similar to the TSA BSU. Water transport is a subject of the piloting campaign and gained findings will be considered in a techno-economic evaluation that will be carried out.

- **Lean/rich heat exchange:** Lean/rich heat exchange is a heat integration measure by which sensible heat from the lean sorbent exiting the desorber is transferred to the rich sorbent exiting the adsorber. In the course of an experimental campaign presented in Section 4.6, two moving bed heat exchangers were integrated in the TSA BSU to simulate lean/rich heat exchange. A lean/rich heat exchange of 70 % on the heated side and over 100 % on the cooled side could be simulated. However, if the heat transfer fluid used to heat the rich moving bed heat exchanger exceeds a certain value, the release of adsorbed gas from the sorbent can lead to the obstruction of solids flow from the adsorber. To allow the released gas to escape towards the rich riser, instead of disturbing sorbent flow, a bypass line equipped with a control valve is recommended to connect the top section of the rich moving bed heat exchanger with the rich riser. This recommendation was implemented in the design of the TSA unit at pilot scale (see Figure 62).
- **Moving bed heat exchange:** Counter-current heat exchange between a bed of solids and a heat transfer fluid can be realized using moving bed heat exchangers. During an experimental campaign in the TSA BSU, two moving bed heat exchangers were installed to investigate lean/rich heat exchange. However, during the initial test, shown in Section 4.6, heat transfer coefficients in the range of  $7\text{-}18\text{ W}\cdot\text{m}^{-2}\cdot\text{K}^{-1}$  were achieved. At greater scale, these low values will make the implementation of a large heat exchanger design necessary and thus increase construction cost. However, the heat transfer coefficient in moving bed heat exchangers is highly dependent on the solids residence time at the heat transfer surface and can therefore be severely increased by an increase of the solids velocity through the heat exchanger. For this reason, it is recommended that the design of the moving bed heat exchangers allows for a high solids velocity. This will enable higher heat transfer coefficients and thus a compact design of the moving heat exchanger. In the design of the moving bed heat exchangers used in the pilot unit, this recommendation was considered and the solids velocity increased by an order of magnitude compared to values achieved in the BSU.



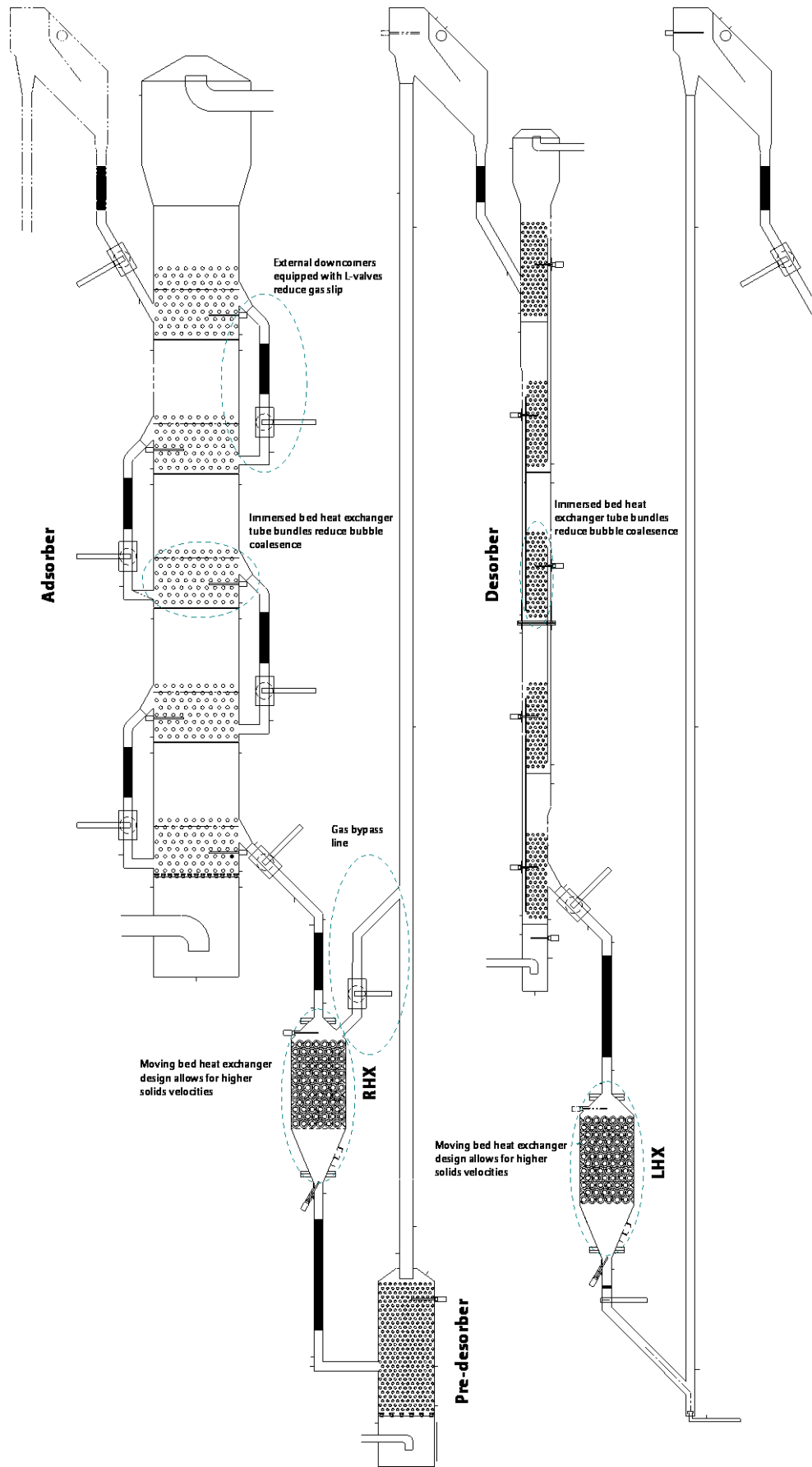


Figure 62: Schematic illustration of the TSA pilot unit design. Realized design recommendations made within this work are highlighted in green dashed circles.

## 6. OUTLOOK AND PROPOSALS FOR FUTURE RESEARCH

This work has shown that TSA using amine-functionalized sorbents has the potential to be a competitive CO<sub>2</sub> capture technology. Especially, the low environmental emissions of the TSA process compared to conventional MEA scrubbing is a factor, which can contribute considerably to a cost reduction of CO<sub>2</sub> capture. With each scale, the design of the TSA process will be optimized further and intrinsic limitations of the process will become more apparent. With the larger dimensions of the constructed pilot unit, many features that could not be implemented in the TSA BSU due its small dimensions could be realized. The implementation of heat exchanger tube bundles, which was not feasible at bench scale, reduce both heat transfer and mass transfer limitations observed in the TSA BSU. Since heat exchanger tube bundles act as bubble breakers in the fluidized beds of the adsorber, gas bypassing through the bubble phase of the fluidized bed stages will be reduced at high superficial gas velocities. The implementation of heat exchanger tube bundles in the desorber enable a significantly higher heat transfer surface area to bed volume ratio in the desorber of the pilot unit. Furthermore, at a larger scale issues concerning solids bridging, as observed in the RHX of the TSA BSU, are less likely due to the larger pipe diameters, thus reducing the impact of wall-friction on solids flow. Long-term continuous operation of the pilot unit will allow an in-depth investigation of process emissions, sorbent degradation, the process energy demand and will thus allow a more detailed techno-economic evaluation of the process. However, the experimental campaigns carried out in this work have revealed that further experimental work is required that is beyond the scope of experimental investigations that can be carried out in the TSA pilot unit. Considering this, the author proposes the following subjects for future research:

- **SO<sub>2</sub> and NO<sub>x</sub> influence on Sorbent B and amine reclamation:** In the course of Section 4.3, it was shown that Sorbent A degrades significantly when contacted with SO<sub>2</sub> and NO<sub>2</sub>, whereas NO did not have a noticeable degrading effect. However, due to the higher stability and lower thermal and oxidative degradation of Sorbent B, it was chosen to carry out further upscaling of the TSA process with Sorbent B. A study is proposed that investigates the influence of SO<sub>2</sub>, NO<sub>2</sub> and NO on the CO<sub>2</sub> adsorption capacity of Sorbent B. It must be determined if a concentration threshold of SO<sub>2</sub> and NO<sub>x</sub> exists, under which sorbent degradation does not occur or occurs at a particularly slow rate. In cases where SO<sub>2</sub> and NO<sub>x</sub> interact with the sorbent, it must be evaluated whether this is accompanied by amine loss, i.e. the formation of emissions. A special focus must be laid on nitrosamine and nitramine formation. This is because Fostås et al. [105] has shown that primary amines can degrade to secondary amines, therefore it is possible that nitrosamines can be formed in reaction with NO<sub>2</sub>. If it is determined that NO<sub>x</sub> or SO<sub>2</sub> does not lead to amine loss, but rather to the deactivation of the amine sites on the sorbent surface and thus to a reduced CO<sub>2</sub> adsorption capacity, strategies for reactivating i.e. reclaiming the amine must be explored. In amine scrubbing, so-called amine reclamation is applied, to recover amines from a degraded amine solution. It has been shown that by adding NaOH to an amine functionalized sorbent poisoned by SO<sub>2</sub>, the CO<sub>2</sub> adsorption capacity can be partially regained [135]. Therefore, a proof of concept for amine reclamation from a degraded amine functionalized sorbent has already been delivered. Since this process reduces the make-up rate of fresh sorbent to the TSA process, its implementation will reduce OPEX.

- **Moving bed heat exchanger optimizations:** In Section 4.6 an experimental campaign was carried out which investigated lean/rich heat exchange in the TSA BSU. It was found that moving bed heat exchangers are a suitable means for achieving high lean/rich heat exchange values since counter-current heat exchange between a heat transfer fluid and solids can be realized. However, low heat transfer coefficients were measured, which implicates a large heat exchanger design. For the TSA pilot unit, a significant increase of the solids velocity was recommended, which will also increase the heat transfer coefficient. However, the general design was kept similar i.e. a finned tube heat exchanger bundle with a triangular pitch as a heat transfer surface. Since lean/rich heat exchange will play an important role in the proposed TSA process, it is worth exploring alternative designs. The focus here must not only lie in achieving high solids velocities but also in guaranteeing a uniform solids velocity across the entire heat exchanger cross-section. This will be challenging as the cross-section of the moving bed heat exchanger grows at a larger scale. Therefore, a viable solution for scalability of the heat exchanger design must also be found.
- **CO<sub>2</sub> product purity:** Flue gas slip from the adsorber to the desorber can potentially contaminate the CO<sub>2</sub> product within the proposed TSA system. Since CO<sub>2</sub> is typically transported in its liquid form, the concentration of impurities needs to be minimal to minimize the risk of corrosion (e.g. pipeline corrosion) and minimize the power demand for CO<sub>2</sub> liquefaction. In the TSA system investigate herein, the standpipe between the adsorber and the L-valve are used to seal the adsorber from the desorber. A purge gas can be introduced to induce a local high-pressure point within the standpipe and thus influence the pressure profile in a way that gas slip from the adsorber to the desorber can be prevented. However, the purge gas flows can flow in both directions (i.e. towards the adsorber and towards the desorber), thus only a gas containing CO<sub>2</sub>, steam or a mixture of these gases are to be used since these species are also tolerated in the desorber off gas. Since these gas constituents can be adsorbed by amine-functionalized sorbents, only the portion of the purge gas that is not adsorbed is available to increase pressure. It is worth experimentally investigating the sealing effect of a purge gases at different purge gas compositions, purge gas flow rates, sorbent loadings at the adsorber outlet, solids circulation rates and solids temperatures so that a high CO<sub>2</sub> product purity can be maintained at various operating conditions.

## 7. NOTATION

### List of symbols

Symbol	Description	Unit
$A$	Area or surface area or cross-section	[m <sup>2</sup> ]
$Ar$	Archimedes number	[-]
$b(T)$	adsorption constant	[-]
$c_p$	Heat capacity at constant pressure	[J·kg <sup>-1</sup> ·K <sup>-1</sup> ]
$c_{mf}$	Heat capacity of the bed at minimum fluidization conditions	[J·kg <sup>-1</sup> ·K <sup>-1</sup> ]
$C_W$	Drag coefficient	[-]
$dp$	Pressure drop	[mbar]
$dp_{ADS+DES}$	sum of column pressure drops	[mbar]
$d_{col}$	Column diameter	[m]
$d_b$	Bubble diameter	[m]
$d_p$	Sieve diameter	[m]
$d_s$	surface diameter	[m]
$d_{sv}$	Sauter mean diameter	[m]
$dSl$	Dynamic sorbent loading	[wt%]
$dSl_{max}$	Theoretical maximum dynamic sorbent loading	[wt%]
$dT_{log}$	logarithmic mean temperature difference	[K]
$d_t$	Tube diameter	[m]
$d_v$	volume diameter	[m]
$E_1$	heat of adsorption of the first layer	[J·mol <sup>-1</sup> ]
$E_n$	heat of adsorption of the n <sup>th</sup> layer	[J·mol <sup>-1</sup> ]
$F$	Flow rate	[Nm <sup>3</sup> ·h <sup>-1</sup> ]
$g$	Gravitational constant	[m·s <sup>-2</sup> ]
$G_s$	Solids flux	[kg·m <sup>-2</sup> ·s <sup>-1</sup> ]
$h$	Heat transfer coefficient	[W·m <sup>-2</sup> ·K <sup>-1</sup> ]
$k_e$	effective thermal conductivity	[W·m <sup>-1</sup> ·K <sup>-1</sup> ]
$H$	Height	[m]
$HR$	Heat recovery	[%]
$\Delta H$	Enthalpy	[kJ·mol <sup>-1</sup> ]
$k$	Rate constant	[-]
$K$	Pre-exponential factor	[-]
$L$	Characteristic length	[m]
$\dot{m}$	Mass flow rate	[kg·h <sup>-1</sup> ]
$\dot{m}_{capt}$	CO <sub>2</sub> capture rate	[kg <sub>CO2</sub> ·day <sup>-1</sup> ]
$n_b$	Bubble frequency	[Hz]
$p_A$	Partial pressure of the adsorptive	[Pa]
$p_{H2O}$	Partial pressure of water	[Pa]
$p_{op}$	Operating pressure	[Pa]
$R$	Universal gas constant	[J·K <sup>-1</sup> ·mol <sup>-1</sup> ]
$Re$	Reynolds number	[-]
$rH$	Relative humidity	[%]
$R_n$	radius of curvature at the nose of a bubble	[m]
$SCR$	Solids circulation rate	[kg·h <sup>-1</sup> ]
$q$	sorbent loading or	[mol·kg <sup>-1</sup> ]

(continued)

Symbol	Description	Unit
$q_m$	Sorbent loading required to attain monolayer completion	[mol·kg <sup>-1</sup> ]
$\Delta q$	Working capacity	[mol·kg <sup>-1</sup> ]
$\Delta q_\infty$	Ideal working capacity	[mol·kg <sup>-1</sup> ]
$\dot{Q}$	Rate of heat flow	[W]
$\dot{Q}_{DES}$	Desorber heat input	[kW]
$q_{DES}$	Specific desorber heat input	[MJ·kg <sub>CO<sub>2</sub></sub> <sup>-1</sup> ]
$\dot{Q}_{Loss}$	Heat losses from the desorber column	[kW]
$R_c$	Contact resistance	[m <sup>2</sup> ·K·W <sup>-1</sup> ]
$t$	time	[s]
$T$	Temperature	[K]
$\Delta T$	Temperature difference	[K]
$\Delta T_{DES-ADS}$	Temperature swing	[°C]
$U$	Superficial (gas) velocity	[m·s <sup>-1</sup> ]
$V$	Volume	[m <sup>3</sup> ]
$v_m$	Volume of gas required to form a mono-molecular layer	[l]
$y$	Volume fraction	[-]

### List of greek symbols

Symbol	Description	Unit
$\varepsilon$	Bed voidage	[-]
$\Phi$	Sphericity	[-]
$\mu$	Dynamic viscosity	[kg·m <sup>-1</sup> ·s <sup>-1</sup> ]
$\rho$	Density	[kg·m <sup>-3</sup> ]
$\tau$	Residence time	[s]
$\delta$	Volumetric fraction	[-]
$\eta_{capt}$	CO <sub>2</sub> capture efficiency	[%]

### Abbreviations

Symbol	Description
AO	Adsorber off-gas
BET	Brunauer, Emmett and Teller
BDU	Brownian Demister Unit
BSU	Bench scale unit
C	Condensate
CCS	Carbon capture and sequestration
CFC-12	Dichlorodifluoromethane
CHP	Combined heat and power
CP	CO <sub>2</sub> product
DEA	Dimethanolamine
ERF	Effective radiative forcing
FB	Fluidized bed
FBA	Fixed bed adsorber
FCC	Fluid catalytic cracking
FG	Flue gas
FW	Fresh water

(continued)

<b>Symbol</b>	<b>Description</b>
GHG	Greenhouse gas
HTC	Heat transfer coefficient
IGCC	integrated gasification combined cycle
LAL	Lean L-valve aeration
LAR	Rich L-valve aeration
LHX	Lean heat exchanger
LRC	Lean riser cooler
LRHX	Lean/rich heat exchange or lean/rich heat exchanger
MBHX	Moving bed heat exchanger
MEA	Monoethanolamine
MFC	Mass flow controller
NDELA	N-nitrosodiethanolamine
NGCC	Natural gas combine cycle
PCCC	Post-combustion CO <sub>2</sub> capture
PCS	Process control system
PA	Pressurized air
PEI	Polyethyleneimine
PGL	Lean purge gas
PGR	Rich purge gas
RF	Radiative forcing
RHX	Rich heat exchanger
SCR	Solids circulation rate
SG	Stripping gas
TCM	CO <sub>2</sub> Technology Centre in Mongstad
TGA	Thermogravimetric analyzer/ Thermogravimetric analysis
TOC	Total organic carbon
TN	Total nitrogen
TSA	Temperature swing adsorption
WMGHG	Well-mixed greenhouse gas

### **Subscripts**

<b>Symbol</b>	<b>Description</b>
ADS	Adsorption/(in the) Adsorber
Air	Air
b	Bulk
br	Bubble rise
col	column
DC	Downcomer
DES	Desorption/(in the) Desorber
distr	Distributor
DGL	Dilution gas lean
f	fluid
FB	Fluidized bed
FF	Forward flow
g	Gas

(continued)

<b>Symbol</b>	<b>Description</b>
gas	Gas
gc	Gas convective
in	At the inlet
log	logarithmic
LRC	Lean riser condensate
max	maximal
mb	Minimum bubble
mf	Minimum fluidization
op	operating
opt	optimal
out	At the outlet
p	particle
pc	Particle convective
PGL	Purge gas lean
pt	Packet
pt,i	Packet at a specific point in time
r	radiative
RF	Return flow
s	solids
sat	saturation
sens	Sensible
spec	Specific
Stage	Stage
t	terminal
TO	Thermal oil
vessel	vessel
Weir	Weir
w	Wall region

## REFERENCES

- [1] J. Lean, D. Rind, Climate forcing by changing solar radiation, *J. Clim.* 11 (1998) 3069–3094. doi:10.1175/1520-0442(1998)011<3069:CFBCSR>2.0.CO;2.
- [2] J. Haigh, Grantham Institute for Climate Change, Briefing paper No. 5 - Solar influences on Climate, 2011.
- [3] NASA Goddard Institute for Space Studies, GISTEMP Team, 2018: GISS Surface Temperature Analysis (GISTEMP), (2018). [https://data.giss.nasa.gov/gistemp/faq/abs\\_temp.html](https://data.giss.nasa.gov/gistemp/faq/abs_temp.html).
- [4] G. Myhre, D. Shindell, F.-M. Bréon, W. Collins, J. Fuglestad, J. Huang, D. Koch, J.-F. Lamarque, D. Lee, B. Mendoza, T. Nakajima, A. Robock, G. Stephens, T. Takemura, H. Zhang, Anthropogenic and Natural Radiative Forcing, *Clim. Chang.* 2013 Phys. Sci. Basis. Contrib. Work. Gr. I to Fifth Assess. Rep. Intergov. Panel Clim. Chang. (2013) 659–740. doi:10.1017/CBO9781107415324.018.
- [5] V. Ramaswamy, O. Boucher, J. Haigh, D. Hauglustaine, J. Haywood, G. Mayhre, T. Nakajima, G.Y. Shi, S. Solomon, Radiative Forcing of Climate Change, in: *IPCC Third Assess. Rep. Clim. Chang.*, 2001.
- [6] Earth System Research Laboratory: Global Monitoring Division, Trends in atmospheric Carbon Dioxide, (2018). <https://www.esrl.noaa.gov/gmd/ccgg/trends/full.html>.
- [7] IPCC, Climate Change 2014: Synthesis Report, 2014. doi:10.1017/CBO9781107415324.
- [8] R.J. Petit, D. Raynaud, I. Basile, J. Chappellaz, C. Ritz, M. Delmotte, M. Legrand, C. Lorius, L. Pe, Climate and atmospheric history of the past 420,000 years from the Vostok ice core, Antarctica, *Nature*. 399 (1999) 429–413. doi:10.1038/20859.
- [9] O. Hoegh-Guldberg, D. Jacob, M. Taylor, M. Bindi, S. Brown, I. Camilloni, A. Diedhiou, R. Djalante, K. Ebi, F. Engelbrecht, J. Guiot, Y. Hijioka, S. Mehrotra, A. Payne, S.I. Seneviratne, A. Thomas, R. Warren, G. Zhou, Impacts of 1.5°C of Global Warming on Natural and Human Systems, in: V. Masson-Delmotte, P. Zhai, H.O. Pörtner, D. Roberts, J. Skea, P.R. Shukla, A. Pirani, W. Moufouma-Okia, C. Péan, R. Pidcock, S. Connors, J.B.R. Matthews, Y. Chen, X. Zhou, M.I. Gomis, E. Lonnoy, T. Maycock, M. Tignor, T. Waterfield (Eds.), *IPCC Glob. Warm. 1.5°C*, 2018.
- [10] M.R. Allen, O.P. Dube, W. Solecki, F. Aragón-Durand, W. Cramer, S. Humphreys, M. Kainuma, J. Kala, N. Mahowald, Y. Mulugetta, R. Perez, M. Wairiu, K. Zickfeld, Framing and Context, in: V. Masson-Delmotte, P. Zhai, H.O. Pörtner, D. Roberts, J. Skea, P.R. Shukla, A. Pirani, W. Moufouma-Okia, C. Péan, R. Pidcock, S. Connors, J.B.R. Matthews, Y. Chen, X. Zhou, M.I. Gomis, E. Lonnoy, T. Maycock, M. Tignor, T. Waterfield (Eds.), *IPCC Glob. Warm. 1.5°C*, 2018.
- [11] IPCC, Summary for Policymakers, in: P. Zhai, H.O. Pörtner, D. Roberts, J. Skea, P.R. Shukla, A. Pirani, W. Moufouma-Okia, C. Péan, R. Pidcock, S. Connors, J.B.R. Matthews, Y. Chen, X. Zhou, M.I. Gomis, E. Lonnoy, T. Maycock, M. Tignor, T. Waterfield (Eds.), *IPCC Glob. Warm. 1.5°C*, World Meteorological Organization, Geneva, Switzerland, 2018.
- [12] J. Rogelj, D. Shindell, K. Jiang, S. Fifita, P. Forster, V. Ginzburg, C. Handa, H. Khesghi, S. Kobayashi, E. Kriegler, L. Mundaca, R. Sférian, M. V. Vilariño, Mitigation Pathways Compatible with 1.5°C in the Context of Sustainable Development, in: V. Masson-Delmotte, P. Zhai, H.O. Pörtner, D. Roberts, J. Skea, P.R. Shukla, A. Pirani, W. Moufouma-Okia, C. Péan, R. Pidcock, S. Connors, J.B.R. Matthews, Y. Chen, X. Zhou, M.I. Gomis, E. Lonnoy, T. Maycock, M. Tignor, T. Waterfield (Eds.), *IPCC Glob. Warm. 1.5°C*, 2018.
- [13] C. Le Quéré, R.M. Andrew, P. Friedlingstein, S. Sitch, J. Hauck, J. Pongratz, P.A. Pickers, J.I. Korsbakken, G.P. Peters, J.G. Canadell, A. Arneeth, V.K. Arora, L. Barbero, A. Bastos, L. Bopp, F. Chevallier, L.P. Chini, P. Ciais, S.C. Doney, T. Gkritzalis, D.S. Goll, I. Harris, V. Haverd, F.M. Hoffman, M. Hoppema, R.A. Houghton, G. Hurtt, T. Ilyina, A.K. Jain, T. Johannessen, C.D. Jones, E. Kato, R.F. Keeling, K.K. Goldewijk, P. Landschützer, N. Lefèvre, S. Lienert, Z. Liu, D. Lombardozzi, N. Metzl, D.R. Munro, J.E.M.S. Nabel, S.-I. Nakaoka, C. Neill, A. Olsen, T. Ono, P. Patra, A. Peregón, W. Peters, P. Peylin, B. Pfeil, D. Pierrot, B. Poulter, G. Rehder, L. Resplandy, E. Robertson, M. Rocher, C. Rödenbeck, U. Schuster, J. Schwinger, R. Sférian, I. Skjelvan, T.



- Steinhoff, A. Sutton, P.P. Tans, H. Tian, B. Tilbrook, F.N. Tubiello, I.T. van der Laan-Luijkx, G.R. van der Werf, N. Viovy, A.P. Walker, A.J. Wiltshire, R. Wright, S. Zaehle, B. Zheng, *Global Carbon Budget 2018*, *Earth Syst. Sci. Data*. 10 (2018) 2141–2194. doi:10.5194/essd-10-2141-2018.
- [14] International Energy Agency, *World Energy Outlook 2018*, IEA Publications, 2018.
- [15] International Energy Agency, *Energy Technology Perspectives 2017*, 2017.
- [16] H. de Coninck, A. Revi, M. Babiker, P. Bertoldi, M. Buckeridge, A. Cartwright, W. Dong, J. Ford, S. Fuss, J. Hourcade, D. Ley, R. Mechler, P. Newman, A. Revokatova, S. Schultz, L. Steg, T. Sugiyama, *Strengthening and Implementing the Global Response*, in: V. Masson-Delmotte, P. Zhai, H.O. Pörtner, D. Roberts, J. Skea, P.R. Shukla, A. Pirani, W. Moufouma-Okia, C. Péan, R. Pidcock, S. Connors, J.B.R. Matthews, Y. Chen, X. Zhou, M.I. Gomis, E. Lonnoy, T. Maycock, M. Tignor, T. Waterfield (Eds.), *IPCC Glob. Warm. 1.5°C*, 2018.
- [17] M.R. Allen, H. de Coninck, O.P. Dube, O. Hoegh-Guldberg, D. Jacob, K. Jiang, A. Revi, J. Rogelj, J. Roy, D. Shindell, W. Solecki, M. Taylor, P. Tschakert, H. Waisman, S.A. Halim, P. Antwi-Agyei, F. Aragón-Durand, M. Babiker, P. Bertoldi, M. Bindi, S. Brown, M. Buckeridge, I. Camilloni, A. Cartwright, W. Cramer, P. Dasgupta, A. Diedhiou, R. Djalante, W. Dong, K.L. Ebi, F. Engelbrecht, S. Fifita, J. Ford, P. Forster, S. Fuss, V. Ginzburg, J. Guiot, C. Handa, B. Hayward, Y. Hijioka, J.-C. Hourcade, S. Humphreys, M. Kainuma, J. Kala, M. Kanninen, H. Kheshgi, S. Kobayashi, E. Kriegler, D. Ley, D. Liverman, N. Mahowald, R. Mechler, S. Mehrotra, Y. Mulugetta, L. Mundaca, P. Newman, C. Okereke, A. Payne, R. Perez, P.F. Pinho, A. Revokatova, K. Riahi, S. Schultz, R. Sférian, S.I. Seneviratne, L. Steg, A.G.S. Rodriguez, T. Sugiyama, A. Thomas, M.V. Vilariño, M. Wairiu, R. Warren, K. Zickfeld, G. Zhou, *Technical Summary*, in: V. Masson-Delmotte, P. Zhai, H.O. Pörtner, D. Roberts, J. Skea, P.R. Shukla, A. Pirani, W. Moufouma-Okia, C. Péan, R. Pidcock, S. Connors, J.B.R. Matthews, Y. Chen, X. Zhou, M.I. Gomis, E. Lonnoy, T. Maycock, M. Tignor, T. Waterfield (Eds.), *IPCC Glob. Warm. 1.5°C*, 2018.
- [18] J.D. Figueroa, T. Fout, S. Plasynski, H. Mcllvried, R.D. Srivastava, *Advances in CO<sub>2</sub> capture technology-The U.S. Department of Energy's Carbon Sequestration Program*, *Int. J. Greenh. Gas Control*. 2 (2008) 9–20. doi:10.1016/S1750-5836(07)00094-1.
- [19] IPCC, *IPCC Special Report on Carbon Dioxide Capture and Storage*, Cambridge University Press, 2005. doi:10.1002/anie.201000431.
- [20] A.E. Creamer, B. Gao, *Overview of CO<sub>2</sub> Capture Technology*, in: *Carbon Dioxide Capture An Eff. W. to Combat Glob. Warm.*, 2015: pp. 17–25. doi:10.1007/978-3-319-17010-7.
- [21] G. Puxty, M. Maeder, *The fundamentals of post- combustion capture*, in: *Absorption-Based Post-Combustion Capture of Carbon Dioxide*, Feron, P.H, 2016: pp. 13–34.
- [22] P. Kolbitsch, J. Bolh??r-Nordenkampf, T. Pr??ll, H. Hofbauer, *Operating experience with chemical looping combustion in a 120 kW dual circulating fluidized bed (DCFB) unit*, *Int. J. Greenh. Gas Control*. 4 (2010) 180–185. doi:10.1016/j.ijggc.2009.09.014.
- [23] E.S. Rubin, J.E. Davison, H.J. Herzog, *The cost of CO<sub>2</sub> capture and storage*, *Int. J. Greenh. Gas Control*. 40 (2015) 378–400. doi:https://doi.org/10.1016/j.ijggc.2015.05.018.
- [24] R. R. Bottoms (Girdler Corp.), "Separating acid gases," (1930) U.S. Patent 1783901.
- [25] K. Stéphenne, *Start-up of world's first commercial post-combustion coal fired ccs project: Contribution of shell cansolv to saskpower boundary dam iccs project*, *Energy Procedia*. 63 (2014) 6106–6110. doi:10.1016/j.egypro.2014.11.642.
- [26] H.C. Mantripragada, H. Zhai, E.S. Rubin, *Boundary Dam or Petra Nova – Which is a better model for CCS energy supply?*, *Int. J. Greenh. Gas Control*. 82 (2019) 59–68. doi:10.1016/j.ijggc.2019.01.004.
- [27] P. Khakharia, H.M. Kvamsdal, E.F. da Silva, T.J.H. Vlugt, E. Goetheer, *Field study of a Brownian Demister Unit to reduce aerosol based emission from a Post Combustion CO<sub>2</sub> Capture plant*, *Int. J. Greenh. Gas Control*. 28 (2014) 57–64. doi:10.1016/j.ijggc.2014.06.022.
- [28] Y. Le Moullec, T. Neveux, *Process modifications for CO<sub>2</sub> capture*, in: P.H.. Feron (Ed.), *Absorption-Based Post-Combustion Capture of Carbon Dioxide*, 2016: pp. 305–340.
- [29] H. Lepaumier, D. Picq, P. Carrette, *New Amines for CO<sub>2</sub> Capture. II. Oxidative Degradation Mechanisms*, *Ind. Eng. Chem. Res.* 48 (2009) 9068–9075. doi:10.1021/ie9004749.

- [30] Y. Lin, T. Rochelle, Optimization of Advanced Flash Stripper for CO<sub>2</sub> Capture using Piperazine, *Energy Procedia*. 63 (2014) 1504–1513. doi:10.1016/j.egypro.2014.11.160.
- [31] K.S. Fisher, C. Beitler, C. Rueter, K. Searcy, Integrating MEA regeneration with CO<sub>2</sub> compression and peaking to reduce CO<sub>2</sub> capture costs, (2005).
- [32] M.R.M. Abu-Zahra, A.S. El Nasr, A. Al Hajaj, E.L.V. Goetheer, Techno-economics of liquid absorbent-based post-combustion CO<sub>2</sub> processes, in: P.H.M. Feron (Ed.), *Absorption-Based Post-Combustion Capture of Carbon Dioxide*, 2016: pp. 685–710.
- [33] D. Singh, E. Croiset, P.L. Douglas, M.A. Douglas, Techno-economic study of CO<sub>2</sub> capture from an existing coal-fired power plant: MEA scrubbing vs. O<sub>2</sub>/CO<sub>2</sub> recycle combustion, *Energy Convers. Manag.* 44 (2003) 3073–3091. doi:10.1016/S0196-8904(03)00040-2.
- [34] M. Gruenewald, A. Radnjanski, Gas-liquid contactors in liquid absorbent-based PCC, in: P.H.M. Feron (Ed.), *Absorption-Based Post-Combustion Capture of Carbon Dioxide*, Elsevier B.V., 2016: pp. 342–364.
- [35] R. Veneman, T. Hilbers, D.W.F. Brillman, S.R.A. Kersten, CO<sub>2</sub> capture in a continuous gas-solid trickle flow reactor, *Chem. Eng. J.* 289 (2016) 191–202. doi:10.1016/j.cej.2015.12.066.
- [36] S. Jan, M.D.E. Rijke, CO<sub>2</sub> removal by Amine Absorption and Condensed Rotational Separation : Energy Consumption & Equipment Sizing, Technical University Eindhoven, 2012.
- [37] R.P. Lively, R.R. Chance, W.J. Koros, Enabling low-cost CO<sub>2</sub> capture via heat integration, *Ind. Eng. Chem. Res.* 49 (2010) 7550–7562. doi:10.1021/ie100806g.
- [38] A.J. Reynolds, T.V. Verheyen, E. Meuleman, Degradation of amine-based solvents, in: P.H.M. Feron (Ed.), *Absorption-Based Post-Combustion Capture of Carbon Dioxide*, 2016: pp. 399–423.
- [39] G.T. Rochelle, Conventional amine scrubbing for CO<sub>2</sub> capture, in: P.H.M. Feron (Ed.), *Absorption-Based Post-Combustion Capture of Carbon Dioxide*, 2016: pp. 35–68.
- [40] X. Xu, C. Song, B.G. Miller, A.W. Scaroni, Adsorption separation of carbon dioxide from flue gas of natural gas-fired boiler by a novel nanoporous “molecular basket” adsorbent, *Fuel Process. Technol.* 86 (2005) 1457–1472. doi:10.1016/j.fuproc.2005.01.002.
- [41] R.S. Franchi, P.J.E. Harlick, A. Sayari, Applications of pore-expanded mesoporous silica. 2. Development of a high-capacity, water-tolerant adsorbent for CO<sub>2</sub>, *Ind. Eng. Chem. Res.* 44 (2005) 8007–8013. doi:10.1021/ie0504194.
- [42] W. Zhang, H. Liu, C. Sun, T.C. Drage, C.E. Snape, Performance of polyethyleneimine-silica adsorbent for post-combustion CO<sub>2</sub> capture in a bubbling fluidized bed, *Chem. Eng. J.* 251 (2014) 293–303. doi:10.1016/j.cej.2014.04.063.
- [43] Q. Yu, J.D.L.P. Delgado, R. Veneman, D.W.F. Brillman, Stability of a Benzyl Amine Based CO<sub>2</sub> Capture Adsorbent in View of Regeneration Strategies, *Ind. Eng. Chem. Res.* 56 (2017) 3259–3269. doi:10.1021/acs.iecr.6b04645.
- [44] H. Krutka, S. Sjostrom, T. Starns, M. Dillon, R. Silverman, Post-combustion CO<sub>2</sub> capture using solid sorbents: 1 MWe pilot evaluation, *Energy Procedia*. 37 (2013) 73–88. doi:10.1016/j.egypro.2013.05.087.
- [45] A.H. Berger, A.S. Bhowan, Comparing physisorption and chemisorption solid sorbents for use separating CO<sub>2</sub> from flue gas using temperature swing adsorption, *Energy Procedia*. 4 (2011) 562–567. doi:10.1016/j.egypro.2011.01.089.
- [46] IUPAC, *Compendium of Chemical Terminology (the “Gold Book”)*, 2nd ed., Blackwell Scientific Publications, Oxford, 1997. doi:https://doi.org/10.1351/goldbook.
- [47] D. Bathen, M. Breitbach, *Adsorptionstechnik*, Springer Berlin Heidelberg, Berlin, Heidelberg, 2001. doi:10.1007/978-3-642-18235-8.
- [48] A. Dąbrowski, Adsorption — from theory to practice, *Adv. Colloid Interface Sci.* 93 (2001) 135–224. doi:10.1016/S0001-8686(00)00082-8.
- [49] C.W. Scheele, *Chemische Abhandlung von der Luft und dem Feuer*, (1777) §96.
- [50] F. Rouquerol, J. Rouquerol, K.S.W. Sing, P. Llewellyn, G. Maurin, *Adsorption by Powders and Porous Solids*, 2nd ed., Elsevier B.V., 2014.
- [51] T. Lowitz, Anzeige einiger neuen Handgriffe, die wesentliche Weinsteinssäure vollkommen rein,

- weiß und schön krystallisirt zu verfertigen, *Chem. Ann.* (1786).
- [52] T. von Saussure, Beobachtungen über die Absorption der Gasarten durch verschiedene Körper, *Ann. Phys.* 47 (1814) 113–183. doi:10.1002/andp.18140470602.
- [53] P. Chappuis, Ueber die Absorption der Kohlensäure durch Holzkohle und deren Abhängigkeit von Druck und Temperatur, *Ann. Phys.* 248 (1881) 161–180. doi:10.1002/andp.18812480202.
- [54] H. Kayser, Ueber die Verdichtung von Gasen an Oberflächen in ihrer Abhängigkeit von Druck und Temperatur - erster Theil, *Ann. Phys.* 248 (1881) 526–537. doi:10.1002/andp.18812480404.
- [55] H. Kayser, Ueber die Verdichtung von Gasen an Oberflächen in ihrer Abhängigkeit von Druck und Temperatur - zweiter Theil, *Ann. Phys.* 250 (1881) 450–468. doi:10.1002/andp.18812501105.
- [56] H. Freundlich, Über die Adsorption in Lösungen, *Zeitschrift Für Phys. Chemie.* 57 (1907) 385–470.
- [57] M. Polanyi, Ueber die Adsorption vom Standpunkt des dritten Wärmesatzes, *Verhandlungen Der Dtsch. Phys. Gesellschaft.* 16 (1914) 1012–1016.
- [58] I. Langmuir, The constitution and fundamental properties of solids and liquids. Part I. Solids, *J. Am. Chem. Soc.* 38 (1916) 2221–2295. doi:10.1021/ja02268a002.
- [59] I. Langmuir, The constitution and fundamental properties of solids and liquids. II. Liquids, *J. Am. Chem. Soc.* 39 (1917) 1848–1906. doi:10.1021/ja02254a006.
- [60] I. Langmuir, The adsorption of gases on plane surfaces of glass, mica and platinum, *J. Am. Chem. Soc.* 40 (1918) 1361–1403. doi:10.1021/ja02242a004.
- [61] P.H. Emmett, S. Brunauer, The Use of Low Temperature van der Waals Adsorption Isotherms in Determining the Surface Area of Iron Synthetic Ammonia Catalysts, *J. Am. Chem. Soc.* 59 (1937) 1553–1564. doi:10.1021/ja01287a041.
- [62] S. Brunauer, P.H. Emmett, E. Teller, Adsorption of Gases in Multimolecular Layers, *J. Am. Chem. Soc.* 60 (1938) 309–319. doi:10.1021/ja01269a023.
- [63] D.M. Ruthven, *Principles of adsorption and adsorption processes*, John Wiley & Sons, Inc., 1984.
- [64] J. Rouquerol, D. Avnir, C.W. Fairbridge, D.H. Everett, J.H. Haynes, N. Pernicone, J.D.F. Ramsay, K.S.W. Sing, K.K. Unger, Recommendations for the characterization of porous solids, *Pure Appl. Chem.* 66 (1994) 1739–1758. doi:10.1351/pac199466081739.
- [65] X. Xu, C. Song, R. Wincek, J.M. Andresen, B.G. Miller, A.W. Scaroni, Separation of CO<sub>2</sub> from Power Plant Flue Gas Using a Novel CO<sub>2</sub> “Molecular Basket” Adsorbent, *ACS Div. Fuel Chem. Prepr.* 48 (2003) 162–163. doi:10.1016/j.jrp.2007.09.007.
- [66] W.-J. Son, J.-S. Choi, W.-S. Ahn, Adsorptive removal of carbon dioxide using polyethyleneimine-loaded mesoporous silica materials, *Microporous Mesoporous Mater.* 113 (2008) 31–40. doi:10.1016/j.micromeso.2007.10.049.
- [67] D. Saha, S. Deng, Adsorption equilibrium and kinetics of CO<sub>2</sub>, CH<sub>4</sub>, N<sub>2</sub>O, and NH<sub>3</sub> on ordered mesoporous carbon, *J. Colloid Interface Sci.* 345 (2010) 402–409. doi:10.1016/j.jcis.2010.01.076.
- [68] K.W. Kolasinski, *Surface Science: Foundations of Catalysis and Nanoscience*, 3rd ed., John Wiley & Sons, Ltd, 2012.
- [69] A.W. Adamson, A.P. Gast, *Physical Chemistry of Surfaces*, John Wiley & Sons, Inc., 1997.
- [70] W.J. Thomas, B. Crittenden, *Adsorption Technology and Design*, Elsevier Science & Technology Books, 1998.
- [71] G.E. Keller, Gas-Adsorption Processes: State of the Art, in: T.E. Whyte, C.M. Yon, E. Wagner (Eds.), *Ind. Gas Sep.*, 1983: pp. 145–169.
- [72] R.T. Yang, *Gas Separation by Adsorption Processes*, 1987.
- [73] D. Kunii, O. Levenspiel, *Fluidization Engineering*, 2nd ed., Butterworth-Heinemann, 1991.
- [74] American Chemical Society, *National Historic Chemical Landmarks: The Fluid Bed Reactor*, (n.d.).  
<https://www.acs.org/content/acs/en/education/whatischemistry/landmarks/fluidbedreactor.html> (accessed January 23, 2019).

- [75] D. Wang, L.S. Fan, Particle characterization and behavior relevant to fluidized bed combustion and gasification systems, in: F. Scala (Ed.), *Fluid. Bed Technol. near-Zero Emiss. Combust. Gasif.*, Woodhead Publishing Ltd., 2013. doi:10.1533/9780857098801.1.42.
- [76] H. Hofbauer, *Wirbelschichttechnik: Unterlagen zur Vorlesung SS2012*, 6th ed., 2012.
- [77] E. Zehetner, *Cold Flow Model Study on a Sorbent Based Multistage Fluidized Bed System for Continuous CO<sub>2</sub> Capture*, TU Wien, 2017.
- [78] S. Ergun, Fluid flow through packed columns, *Chem. Eng. Prog.* 48 (1952) 89–94.
- [79] C.Y. Wen, Y.H. Yu, A generalized method for predicting the minimum fluidization velocity, *A.I.Ch.E.* 12 (1966). doi:https://doi.org/10.1002/aic.690120343.
- [80] D. Geldart, Types of Gas Fluidization, *Powder Technol.* 7 (1973) 285–292.
- [81] R.M. Davies, G.I. Taylor, The mechanics of large bubbles rising through extended liquids and through liquids in tubes, *Proc. R. Soc. A.* 200 (1950). doi:https://doi.org/10.1098/rspa.1950.0023.
- [82] R. Clift, J.R. Grace, Continuous bubbling and slugging, in: J.F. Davidson, D. Harrison, R. Clift (Eds.), *Fluidization*, Second Edi, Academic Press, London, 1985: pp. 73–128.
- [83] G.B. Wallis, *One-dimensional two-phase flow*, McGraw-Hill, 1969.
- [84] J.F. Davidson, D. Harrison, *Fluidized Particles*, Cambridge University Press, 1963.
- [85] J.S. Dennis, Properties of stationary (bubbling) fluidised beds relevant to combustion and gasification systems, in: F. Scala (Ed.), *Fluid. Bed Technol. near-Zero Emiss. Combust. Gasification2*, Woodhead Publishing Ltd., 2013. doi:10.1533/9780857098801.1.77.
- [86] J.R. Grace, C.J. Lim, Properties of circulating fluidized beds (CFB) relevant to combustion and gasification systems, in: F. Scala (Ed.), *Fluid. Bed Technol. near-Zero Emiss. Combust. Gasif.*, Woodhead Publishing Ltd., 2013: pp. 147–176. doi:10.1533/9780857098801.1.147.
- [87] J.R. Grace, A.S. Issangya, D. Bai, J. Zhu, Situating the high-density circulating fluidized bed, *A.I.Ch.E.* 45 (1999) 2108–2116.
- [88] J.R. Grace, Contacting modes and behaviour classification of gas-solid and other two-phase suspensions, *Can. J. of Chem. Eng.* 64 (1986) 353–363. doi:10.1002/cjce.5450640301.
- [89] M. Stollhof, S. Penthor, K. Mayer, H. Hofbauer, Estimation of the Solid Circulation Rate in Circulating Fluidized Bed Systems, *Powder Technol.* 336 (2018) 1–11. doi:https://doi.org/10.1016/j.powtec.2018.05.033.
- [90] J.F. Richardson, W.N. Zaki, Sedimentation and Fluidisation: Part I, *Chem. Eng. Res. Des.* 75 (1997) 82–100. doi:https://doi.org/10.1016/S0263-8762(97)80006-8.
- [91] W.-C. Yang, *Handbook of fluidization and fluid-particle systems*, 2003.
- [92] F. Di Natale, R. Nigro, F. Scala, Heat and mass transfer in fluidized bed combustion and gasification systems, in: F. Scala (Ed.), *Fluid. Bed Technol. near-Zero Emiss. Combust. Gasif.*, Woodhead Publishing Ltd., 2013: pp. 177–253. doi:10.1533/9780857098801.1.177.
- [93] H.S. Mickley, D.F. Fairbanks, Mechanism of Heat Transfer to Fluidized Beds, *A.I.Ch.E.* 1 (1955) 374–384. doi:10.1002/aic.690010317.
- [94] A. Baskakov, The mechanism of heat transfer between a fluidized bed and a surface, *Int. Chem. Eng.* 4 (1964) 320.
- [95] G. Schöny, *Post Combustion CO<sub>2</sub> Capture based on Temperature Swing Adsorption – from Process Evaluation to Continuous Bench Scale Operation*, (2015).
- [96] O. Molerus, Heat transfer in gas fluidized beds Part 2. Dependence of heat transfer on gas velocity, *Powder Technol.* 70 (1992) 15–20. doi:10.1016/0032-5910(92)85049-2.
- [97] S. Chi, G.T. Rochelle, Oxidative Degradation of Monoethanolamine, *Ind. Eng. Chem. Res.* 41 (2002) 4178–4186. doi:10.1021/ie010697c.
- [98] S.J. Vevelstad, I. Eide-Haugmo, E.F. Da Silva, H.F. Svendsen, Degradation of MEA; A theoretical study, *Energy Procedia.* 4 (2011) 1608–1615. doi:10.1016/j.egypro.2011.02.031.
- [99] A.K. Morken, S. Pedersen, E.R. Kleppe, A. Wisthaler, K. Vernstad, Ø. Ullestad, N.E. Flø, L. Faramarzi, E.S. Hamborg, Degradation and Emission Results of Amine Plant Operations from MEA Testing at the CO<sub>2</sub> Technology Centre Mongstad, *Energy Procedia.* 114 (2017) 1245–1262. doi:10.1016/j.egypro.2017.03.1379.

- [100] S.B. Fredriksen, K.J. Jens, Oxidative degradation of aqueous amine solutions of MEA, AMP, MDEA, Pz: A review, *Energy Procedia*. 37 (2013) 1770–1777. doi:10.1016/j.egypro.2013.06.053.
- [101] A.K. Morken, B. Nenseter, S. Pedersen, M. Chhaganlal, J.K. Feste, R.B. Tyborgnes, Ø. Ullestad, H. Ulvatn, L. Zhu, T. Mikoviny, A. Wisthaler, T. Cents, O.M. Bade, J. Knudsen, G. de Koeijer, O. Falk-Pedersen, E.S. Hamborg, Emission Results of Amine Plant Operations from MEA Testing at the CO<sub>2</sub> Technology Centre Mongstad, *Energy Procedia*. 63 (2014) 6023–6038. doi:10.1016/j.egypro.2014.11.636.
- [102] C. Gouedard, D. Picq, F. Launay, P.L. Carrette, Amine degradation in CO<sub>2</sub> capture. I. A review, *Int. J. Greenh. Gas Control*. 10 (2012) 244–270. doi:10.1016/j.ijggc.2012.06.015.
- [103] J.N. Knudsen, O.M. Bade, M. Anheden, R. Bjorklund, O. Gorset, S. Woodhouse, Novel concept for emission control in post combustion capture, *Energy Procedia*. 37 (2013) 1804–1813. doi:10.1016/j.egypro.2013.06.058.
- [104] P. Khakharia, A. Huizinga, C. Jurado Lopez, C. Sanchez Sanchez, F. de Miguel Mercader, T.J.H. Vlugt, E. Goetheer, Acid Wash Scrubbing as a Countermeasure for Ammonia Emissions from a Postcombustion CO<sub>2</sub> Capture Plant, *Ind. Eng. Chem. Res.* 53 (2014) 13195–13204. doi:10.1021/ie502045c.
- [105] B. Fostås, A. Gangstad, B. Nenseter, S. Pedersen, M. Sjøvoll, A.L. Sørensen, Effects of NO<sub>x</sub> in the flue gas degradation of MEA, *Energy Procedia*. 4 (2011) 1566–1573. doi:10.1016/j.egypro.2011.02.026.
- [106] T. Kamijo, Y. Kajiyu, T. Endo, H. Nagayasu, H. Tanaka, T. Hirata, T. Yonekawa, T. Tsujiuchi, SO<sub>3</sub> impact on amine emission and emission reduction technology, *Energy Procedia*. 37 (2013) 1793–1796. doi:10.1016/j.egypro.2013.06.056.
- [107] P. Moser, S. Schmidt, K. Stahl, G. Vorberg, G.A. Lozano, T. Stoffregen, F. Rösler, Demonstrating emission reduction - Results from the post-combustion capture pilot plant at Niederaussem, *Energy Procedia*. 63 (2014) 902–910. doi:10.1016/j.egypro.2014.11.100.
- [108] E.F. da Silva, H. Kolderup, E. Goetheer, K.W. Hjarbo, A. Huizinga, P. Khakharia, I. Tuinman, T. Mejdell, K. Zahlsen, K. Vernstad, A. Hyldbakk, T. Holten, H.M. Kvamsdal, P. van Os, A. Einbu, Emission studies from a CO<sub>2</sub> capture pilot plant, *Energy Procedia*. 37 (2013) 778–783. doi:10.1016/j.egypro.2013.05.167.
- [109] A. Samanta, A. Zhao, G.K.H. Shimizu, P. Sarkar, R. Gupta, Post-combustion CO<sub>2</sub> capture using solid sorbents: A review, *Ind. Eng. Chem. Res.* 51 (2012) 1438–1463. doi:10.1021/ie200686q.
- [110] J. Wang, L. Huang, R. Yang, Z. Zhang, J. Wu, Y. Gao, Q. Wang, D. O'Hare, Z. Zhong, Recent advances in solid sorbents for CO<sub>2</sub> capture and new development trends, *Energy Environ. Sci.* 7 (2014) 3478–3518. doi:10.1039/C4EE01647E.
- [111] S. Choi, J.H. Drese, C.W. Jones, Adsorbent Materials for Carbon Dioxide Capture from Large Anthropogenic Point Sources, *ChemSusChem*. 2 (2009) 796–854. doi:10.1002/cssc.200900036.
- [112] P.J.E. Harlick, A. Sayari, Applications of Pore-Expanded Mesoporous Silica . 5 . Triamine G1. Harlick, P. J. E. & Sayari, A. Applications of Pore-Expanded Mesoporous Silica . 5 . Triamine Grafted Material with Exceptional CO<sub>2</sub> Dynamic and Equilibrium Adsorption Performanc, (2007) 446–458.
- [113] X. Xu, C. Song, B.G. Miller, A.W. Scaroni, Influence of Moisture on CO<sub>2</sub> Separation from Gas Mixture by a Nanoporous Adsorbent Based on Polyethylenimine-Modified Molecular Sieve MCM-41, *Ind. Eng. Chem. Res.* 44 (2005) 8113–8119. doi:10.1021/ie050382n.
- [114] R. Veneman, N. Frigka, W. Zhao, Z. Li, S. Kersten, W. Brillman, Adsorption of H<sub>2</sub>O and CO<sub>2</sub> on supported amine sorbents, *Int. J. Greenh. Gas Control*. 41 (2015) 268–275. doi:10.1016/j.ijggc.2015.07.014.
- [115] R. Serna-Guerrero, E. Da'na, A. Sayari, New Insights into the Interactions of CO<sub>2</sub> with Amine-Functionalized Silica, *Ind. Eng. Chem. Res.* 47 (2008) 9406–9412. doi:10.1021/ie801186g.
- [116] N.K. Sandhu, D. Pudasainee, P. Sarkar, R. Gupta, Steam Regeneration of Polyethylenimine-Impregnated Silica Sorbent for Postcombustion CO<sub>2</sub> Capture: A Multicyclic Study, *Ind. Eng. Chem. Res.* 55 (2016) 2210–2220. doi:10.1021/acs.iecr.5b04741.
- [117] A. Heydari-Gorji, A. Sayari, Thermal, oxidative, and CO<sub>2</sub>-induced degradation of supported

- polyethylenimine adsorbents, *Ind. Eng. Chem. Res.* 51 (2012) 6887–6894. doi:10.1021/ie3003446.
- [118] T.C. Drage, K.M. Smith, A. Arenillas, C.E. Snape, Developing strategies for the regeneration of polyethylenimine based CO<sub>2</sub> adsorbents, *Energy Procedia*. 1 (2009) 875–880. doi:10.1016/j.egypro.2009.01.116.
- [119] K. Li, J. Jiang, F. Yan, S. Tian, X. Chen, The influence of polyethyleneimine type and molecular weight on the CO<sub>2</sub> capture performance of PEI-nano silica adsorbents, *Appl. Energy*. 136 (2014) 750–755. doi:10.1016/j.apenergy.2014.09.057.
- [120] A. Goeppert, S. Meth, G.K. Surya Prakash, G.A. Olah, Nanostructured silica as a support for regenerable high-capacity organoamine-based CO<sub>2</sub> sorbents, *Energy Environ. Sci.* 3 (2010) 1949–1960. doi:10.1039/c0ee00136h.
- [121] A. Heydari-Gorji, Y. Belmabkhout, A. Sayari, Polyethylenimine-Impregnated Mesoporous Silica: Effect of Amine Loading and Surface Alkyl Chains on CO<sub>2</sub> Adsorption, *Langmuir*. 27 (2011) 12411–12416. doi:dx.doi.org/10.1021/la202972t.
- [122] G. Qi, Y. Wang, L. Estevez, X. Duan, N. Anako, A.-H.A. Park, W. Li, W. Jones, E.P. Giannelis, High efficiency nanocomposite sorbents for CO<sub>2</sub> capture based on amine-functionalized mesoporous capsules, *Energy Environ. Sci.* 4 (2011) 444–452. doi:10.1039/c0ee00213e.
- [123] W. Zhao, Z. Zhang, Z. Li, N. Cai, Investigation of thermal stability and continuous CO<sub>2</sub> capture from flue gases with supported amine sorbent, *Ind. Eng. Chem. Res.* 52 (2013) 2084–2093. doi:10.1021/ie303254m.
- [124] X. Xu, C. Song, J.M. Andresen, B.G. Miller, A.W. Scaroni, Adsorption separation of CO<sub>2</sub> from simulated flue gas mixtures by novel CO<sub>2</sub> “molecular basket” adsorbents, *Int. J. Environ. Technol. Manag.* 4 (2004) 32–52. doi:10.1504/ijetm.2004.004630.
- [125] X. Xu, C. Song, J.M. Andresen, B.G. Miller, A.W. Scaroni, Novel polyethylenimine-modified mesoporous molecular sieve of MCM-41 type as high-capacity adsorbent for CO<sub>2</sub> capture, *Energy and Fuels*. 16 (2002) 1463–1469. doi:10.1021/ef020058u.
- [126] W.R. Alesi, J.R. Kitchin, Evaluation of a primary amine-functionalized ion-exchange resin for CO<sub>2</sub> capture, *Ind. Eng. Chem. Res.* 51 (2012) 6907–6915. doi:10.1021/ie300452c.
- [127] M. Parvazinia, S. Garcia, M. Maroto-Valer, CO<sub>2</sub> capture by ion exchange resins as amine functionalised adsorbents, *Chem. Eng. J.* 331 (2018) 335–342. doi:10.1016/j.cej.2017.08.087.
- [128] A.P. Tirio, R. Wagner, Process and apparatus for carbon dioxide and carbonyl sulfide capture via ion exchange resin, US 9,028,590 B2, 2015. <https://patentimages.storage.googleapis.com/51/c3/17/046950575d1af6/US9028590.pdf>.
- [129] LANXESS Deutschland GmbH, Product information Lewatit VP OC 1065, (2017). <http://lpt.lanxess.com/en/products-lpt/product-key-word-search/lewatitr-vp-oc-1065/> (accessed February 3, 2019).
- [130] E. Sonnleitner, G. Schöny, H. Hofbauer, Assessment of zeolite 13X and Lewatit® VP OC 1065 for application in a continuous temperature swing adsorption process for biogas upgrading, *Biomass Convers. Biorefinery*. 8 (2018) 379–395. doi:10.1007/s13399-017-0293-3.
- [131] R. Veneman, W. Zhao, Z. Li, N. Cai, D.W.F. Brillman, Adsorption of CO<sub>2</sub> and H<sub>2</sub>O on supported amine sorbents, *Energy Procedia*. 63 (2014) 2336–2345. doi:10.1016/j.egypro.2014.11.254.
- [132] A. Sayari, Y. Belmabkhout, Stabilization of amine-containing CO<sub>2</sub> adsorbents: Dramatic effect of water vapor, *J. Am. Chem. Soc.* 132 (2010) 6312–6314. doi:10.1021/ja1013773.
- [133] F. Rezaei, C.W. Jones, Stability of Supported Amine Adsorbents to SO<sub>2</sub> and NO<sub>x</sub> in Postcombustion CO<sub>2</sub> capture. 2. Multicomponent Adsorption, *Ind. Eng. Chem. Res.* 53 (2014) 12103–12110. doi:10.1021/ie502024z.
- [134] T.O. Nelson, A. Kataria, P. Mobley, M. Soukri, J. Tanthana, RTI’s Solid Sorbent-Based CO<sub>2</sub> Capture Process: Technical and Economic Lessons Learned for Application in Coal-fired, NGCC, and Cement Plants, *Energy Procedia*. 114 (2017) 2506–2524. doi:10.1016/j.egypro.2017.03.1409.
- [135] A.P. Hallenbeck, J.R. Kitchin, Effects of O<sub>2</sub> and SO<sub>2</sub> on the Capture Capacity of a Primary-Amine Based Polymeric CO<sub>2</sub> Sorbent, *Ind. Eng. Chem. Res.* 52 (2013) 10788–10794.

- doi:10.1021/ie400582a.
- [136] R. Veneman, Z.S. Li, J.A. Hogendoorn, S.R.A. Kersten, D.W.F. Brillman, Continuous CO<sub>2</sub> capture in a circulating fluidized bed using supported amine sorbents, *Chem. Eng. J.* 207–208 (2012) 18–26. doi:10.1016/j.cej.2012.06.100.
- [137] W. Zhao, Z. Zhang, Z. Li, N. Cai, Continuous CO<sub>2</sub> capture in dual fluidized beds using silica supported amine, *Energy Procedia.* 37 (2013) 89–98. doi:10.1016/j.egypro.2013.05.088.
- [138] R.W. Breault, J.L. Spenik, L.J. Shadle, J.S. Hoffman, M.L. Gray, R. Panday, R.C. Stehle, Carbon capture test unit design and development using amine-based solid sorbent, *Chem. Eng. Res. Des.* 112 (2016) 251–262. doi:10.1016/j.cherd.2016.06.020.
- [139] T.O. Nelson, L.J.I. Coleman, A. Kataria, M. Lail, M. Soukri, D.V. Quang, M.R.M.A. Zahra, Advanced solid sorbent-based CO<sub>2</sub> capture process, *Energy Procedia.* 63 (2014) 2216–2229. doi:10.1016/j.egypro.2014.11.241.
- [140] D.C. Guío-Pérez, T. Pröll, J. Wassermann, H. Hofbauer, Design of an Inductance Measurement System for Determination of Particle Residence Time in a Dual Circulating Fluidized Bed Cold Flow Model, *Ind. Eng. Chem. Res.* 52 (2013) 10732–10740. doi:http://dx.doi.org/10.1021/ie400211h.
- [141] T. Pröll, G. Schöny, G. Sprachmann, H. Hofbauer, Introduction and evaluation of a double loop staged fluidized bed system for post-combustion CO<sub>2</sub> capture using solid sorbents in a continuous temperature swing adsorption process, *Chem. Eng. Sci.* 141 (2016) 166–174. doi:10.1016/j.ces.2015.11.005.
- [142] F. Dietrich, G. Schöny, J. Fuchs, H. Hofbauer, Experimental study of the adsorber performance in a multi-stage fluidized bed system for continuous CO<sub>2</sub> capture by means of temperature swing adsorption, *Fuel Process. Technol.* 173 (2018) 103–111. doi:10.1016/j.fuproc.2018.01.013.
- [143] E. Zehetner, G. Schöny, J. Fuchs, T. Pröll, H. Hofbauer, Fluid-dynamic study on a multi-stage fluidized bed column for continuous CO<sub>2</sub> capture via temperature swing adsorption, *Powder Technol.* 316 (2017) 528–534. doi:https://doi.org/10.1016/j.powtec.2016.11.065.
- [144] Y. Jin, F. Wei, Y. Wang, Effect of Internal Tubes and Baffles, in: *Handb. Fluid. Fluid-Particle Syst.*, 2003: pp. 180–208.
- [145] Güssing Energy Technologies, Kurzbeschreibung und Darstellung der wichtigsten Parameter der FICFB- Wirbelschichtvergasung und der nachgeschalteten Einheiten zur Synthesegasnutzung, Present. Symp. “Optimierte KWK-Systeme” 21.05.2008. (2008). [http://www.get.ac.at/Downloads.html?file=tl\\_files/Download/Praesentationen/20080521\\_Symposium/DP0536\\_B106a\\_Anlage\\_BKG.pdf](http://www.get.ac.at/Downloads.html?file=tl_files/Download/Praesentationen/20080521_Symposium/DP0536_B106a_Anlage_BKG.pdf) (accessed February 24, 2019).
- [146] G. Schöny, F. Dietrich, J. Fuchs, T. Pröll, H. Hofbauer, A multi-stage fluidized bed system for continuous CO<sub>2</sub> capture by means of temperature swing adsorption – First results from bench scale experiments, *Powder Technol.* 316 (2017) 519–527. doi:10.1016/j.powtec.2016.11.066.
- [147] S. Zhou, S. Wang, C. Sun, C. Chen, SO<sub>2</sub> effect on degradation of MEA and some other amines, *Energy Procedia.* 37 (2013) 896–904. doi:10.1016/j.egypro.2013.05.184.
- [148] H.E. Buist, S. Devito, R.A. Goldbohm, R.H. Stierum, J. Venhorst, E.D. Kroese, Hazard assessment of nitrosamine and nitramine by-products of amine-based CCS: Alternative approaches, *Regul. Toxicol. Pharmacol.* 71 (2015) 601–623.
- [149] N. MacDowell, N. Florin, A. Buchard, J. Hallett, A. Galindo, G. Jackson, C.S. Adjiman, C.K. Williams, N. Shah, P. Fennell, An overview of CO<sub>2</sub> capture technologies, *Energy Environ. Sci.* 3 (2010) 1645. doi:10.1039/c004106h.
- [150] M. Wang, A. Lawal, P. Stephenson, J. Sidders, C. Ramshaw, Post-combustion CO<sub>2</sub> capture with chemical absorption: A state-of-the-art review, *Chem. Eng. Res. Des.* 89 (2011) 1609–1624. doi:10.1016/j.cherd.2010.11.005.
- [151] Gastec Corporation, Instruction manual amines detector tube No. 180, (n.d.). <https://www.gastec.co.jp/files/user/asset/pdf/en/instructionmanual/en/180.pdf> (accessed September 6, 2018).
- [152] Gastec Corporation, Instruction manual amines detector tube No. 180L, (n.d.).

- <https://www.gastec.co.jp/files/user/asset/pdf/en/instructionmanual/en/180L.pdf> (accessed September 6, 2018).
- [153] E. Gjernes, S. Pedersen, T. Cents, G. Watson, B.F. Fostås, M.I. Shah, G. Lombardo, C. Desvignes, N.E. Flø, A.K. Morken, T. De Cazenove, L. Faramarzi, E.S. Hamborg, Results from 30 wt% MEA Performance Testing at the CO<sub>2</sub> Technology Centre Mongstad, *Energy Procedia*. 114 (2017) 1146–1157. doi:10.1016/j.egypro.2017.03.1276.
- [154] D.H. Mackenzie, F.C. Prambil, C.A. Daniels, J.A. Bullin, Design & Operation of Selective Sweetening Plant using MDEA, (1987). <https://www.bre.com/PDF/Design-and-Operation-of-a-Selective-Sweetening-Plant-Using-MDEA.pdf>.
- [155] Y.-J. Lin, G.T. Rochelle, Heat Transfer Enhancement and Optimization of Lean/Rich Solvent Cross Exchanger for Amine Scrubbing, *Energy Procedia*. 114 (2017) 1890–1903. doi:10.1016/j.egypro.2017.03.1320.
- [156] E. De Visser, C. Hendriks, M. Barrio, M.J. Mølnvik, G. De Koeijer, S. Liljemark, Y. Le, Dynamis CO<sub>2</sub> quality recommendations, *Int. J. Greenh. Gas Control*. 2 (2008) 478–484. doi:10.1016/j.ijggc.2008.04.006.
- [157] M. Colakyan, Moving bed heat transfer and fluidized elutriation, Oregon State University, 1984.
- [158] W.N. Sullivan, R.H. Sabersky, Heat transfer to flowing granular media, *Int. J. Heat Mass Transf.* 18 (1975) 97–107. doi:[https://doi.org/10.1016/0017-9310\(75\)90012-5](https://doi.org/10.1016/0017-9310(75)90012-5).
- [159] J. Niegsch, D. Kiineke, P. Weinspach, Heat transfer and flow of bulk solids in a moving bed, *Chem. Eng. Process. Process Intensif.* 33 (1994) 73–89. doi:[https://doi.org/10.1016/0255-2701\(94\)85006-2](https://doi.org/10.1016/0255-2701(94)85006-2).
- [160] N. Obuskovic, M. Colakyan, J.G. Knudsen, Heat Transfer Between Moving Beds of Solids and a Transverse Finned Tube, *Heat Transf. Eng.* 12 (1991) 46–52. doi:10.1080/01457639108939751.
- [161] N. Obuskovic, Heat transfer between moving beds of solids and a transverse finned tube, Oregon State University, 1985.
- [162] G. Schöny, J. Fuchs, M. Infantino, J. van de Graaf, H. Hofbauer, Pilot scale demonstration of solid sorbent CO<sub>2</sub> capture technology at a biomass power station, in: 14th Int. Conf. Greenh. Gas Control Technol., 2018.



## 8. APPENDIX

### 8.1 GAS DISTRIBUTOR PRESSURE DROP AS A FUNCTION OF THE SUPERFICIAL GAS VELOCITY IN THE COLUMNS

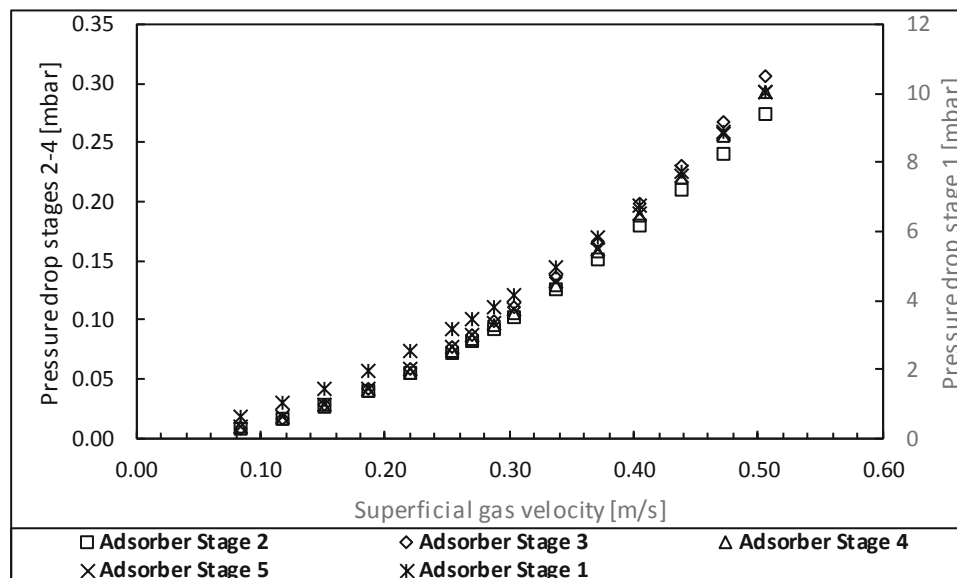


Figure 63: Graph showing the measured bed pressure drop of the each fluidized bed stage of the adsorber with closed downcomer flaps as a function of the superficial gas velocity

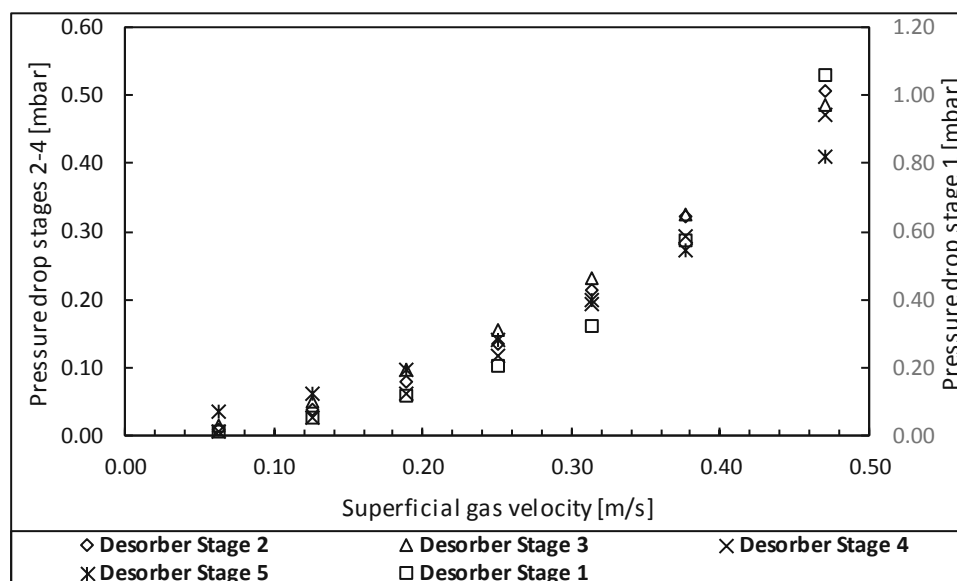


Figure 64: Graph showing the measured bed pressure drop of the each fluidized bed stage of the desorber with closed downcomer flaps as a function of the superficial gas velocity

## 8.2 CALCULATION OF THE MEASURING ERROR OF RTDs ACCORDING TO DIN EN 60751

- Class A:  $dT = \pm (0.15 \text{ °C} + 0,002 \cdot T)$
- Class B:  $dT = \pm (0.30 \text{ °C} + 0,005 \cdot T)$
- 1/3 Class B:  $dT = \pm (1/3 \cdot (0,30 \text{ °C} + 0,005 \cdot T))$
- 1/10 class B:  $dT = \pm (1/10 \cdot (0,30 \text{ °C} + 0,005 \cdot T))$

## 8.3 CALCULATION OF THE MEASURING ERROR OF VARIABLE AREA FLOW METERS ACCORDING TO VDI/VDE 351

- $dV = (0.75 \cdot M + 0.25 \cdot E) \cdot \frac{K}{100}$

whereas “M” is the measured value, “E” is the full scale value and “K” the accuracy class

## 8.4 LEGEND OF SYMBOLS USED IN P&IDs


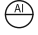









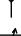


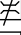

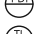


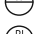
















 AC	Adsorber off-gas	 AI	Analysis indicator, PCS-integrated		Grate
 C	Condensate	 FI	Flow indicator, PCS-integrated		Vent to ambient
 CP	CO2 product	 FIA	Flow indicator controller with alarm function, local		Spring, safe position open
 DGL	Dilution gas (lean)	 FIC	Flow indicator controller, local		Battery limit
 DGR	Dilution gas (rich)	 FIC	Flow indicator controller, PCS-integrated		Flow meter with needle valve
 FG	Adsorber feed-gas	 PDI	Differential pressure indicator, PCS-integrated		Flow meter
 FW	Fresh water	 TI	Temperature indicator, PCS-integrated		Blower
 LAL	L-valve aeration (lean)	 PI	Pressure indicator, PCS-integrated		Pump
 LAR	L-valve aeration (rich)				Heat Exchanger
 PGR	Purge gas (rich)				Heater
 PGL	Purge gas (lean)				Control valve
 SG	Stripping gas				Globe valve
					Three-way valve
					Safety valve
					Pressure reduction valve
					Electric motor

Figure 65: Legend of symbols used in Figure 35, Figure 37 and Figure 36.

## 8.5 DESORBER HEAT LOSS AS A FUNCTION OF THE FORWARD FLOW TEMPERATURE OF THERMAL OIL

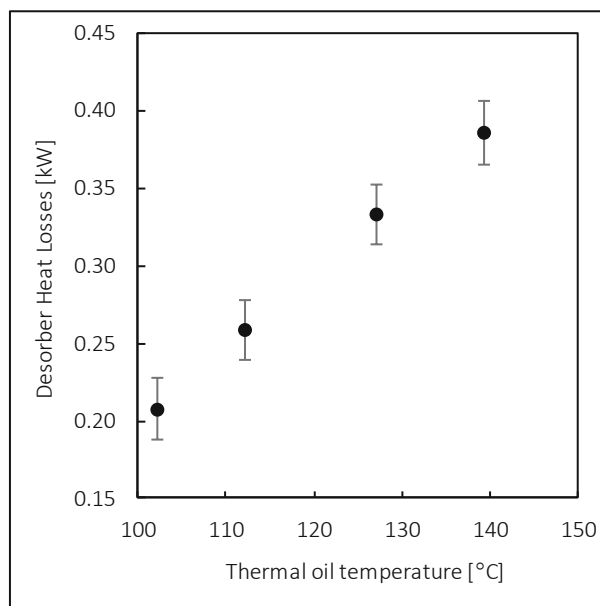


Figure 66: Desorber heat loss as a function of the forward flow temperature of thermal oil

## 8.6 PERFORMANCE INDICATORS IN THE COURSE OF 24-HOUR DEGRADATION TESTS

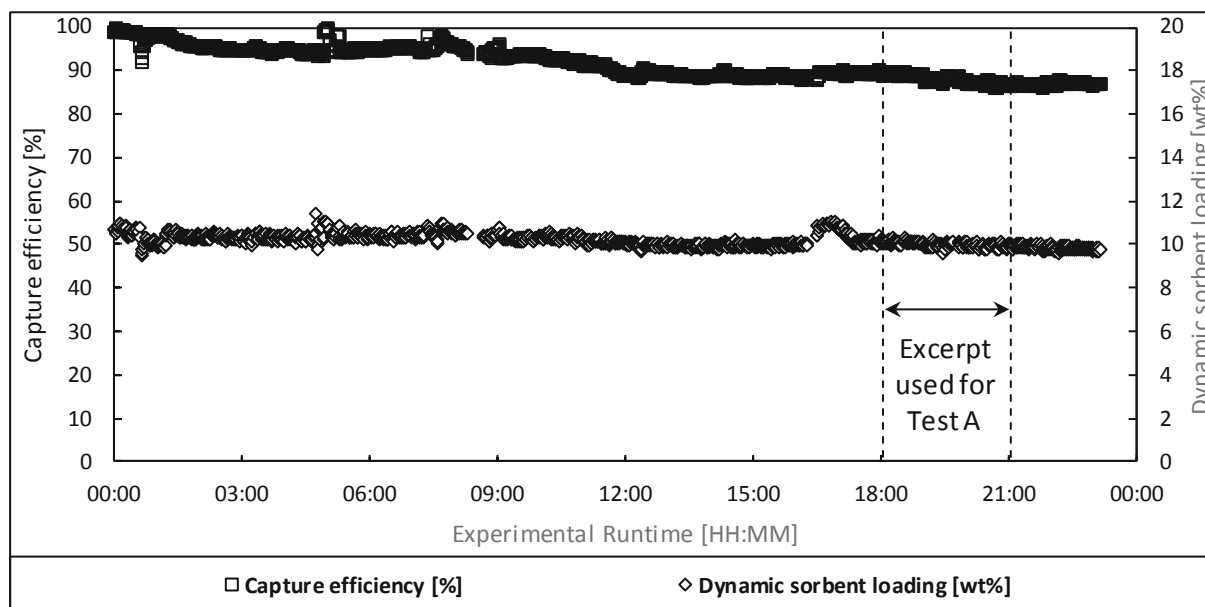


Figure 67: Graph showing the capture efficiency and dynamic sorbent loading in the course of a 24-hour degradation experiment with Sorbent A whilst treating flue gas mixed from bottles in the TSA BSU.

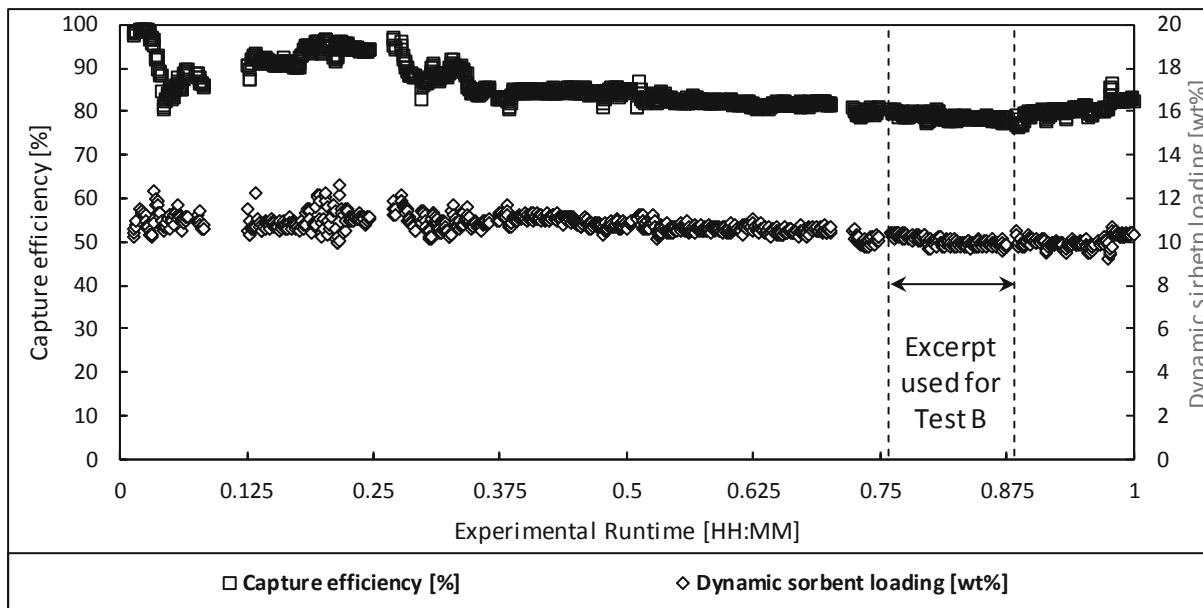


Figure 68: Graph showing the capture efficiency and dynamic sorbent loading in the course of a 24-hour degradation experiment with Sorbent A whilst treating pre-conditioned flue gas from a gas engine in the TSA BSU.

### 8.7 SUPPLEMENTARY INFORMATION TO 120-HOUR EXPERIMENTS

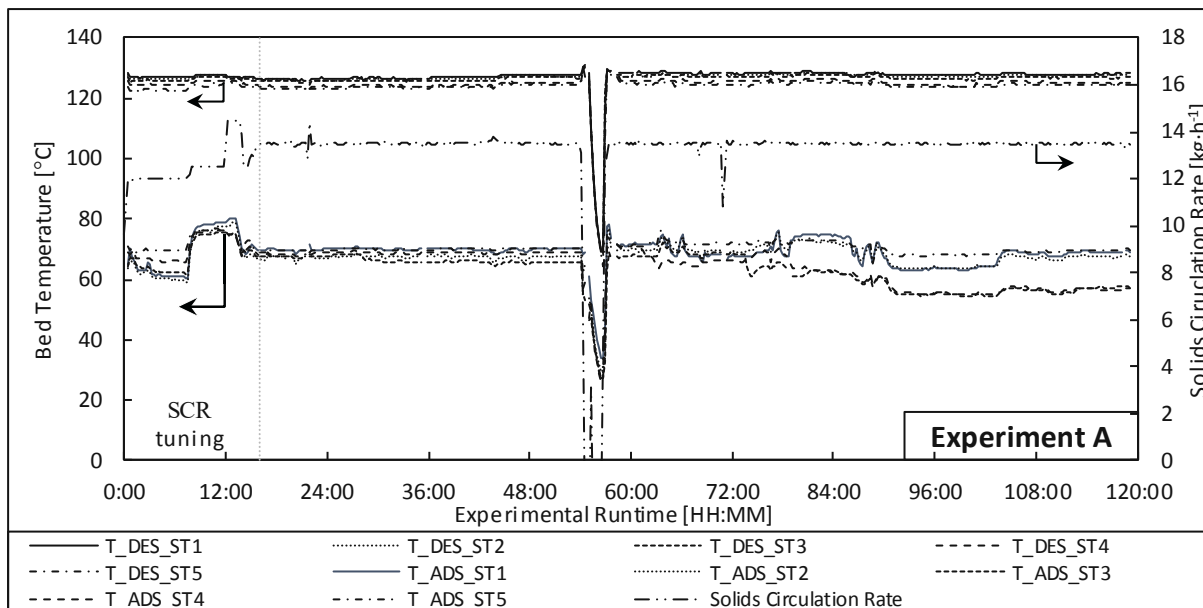
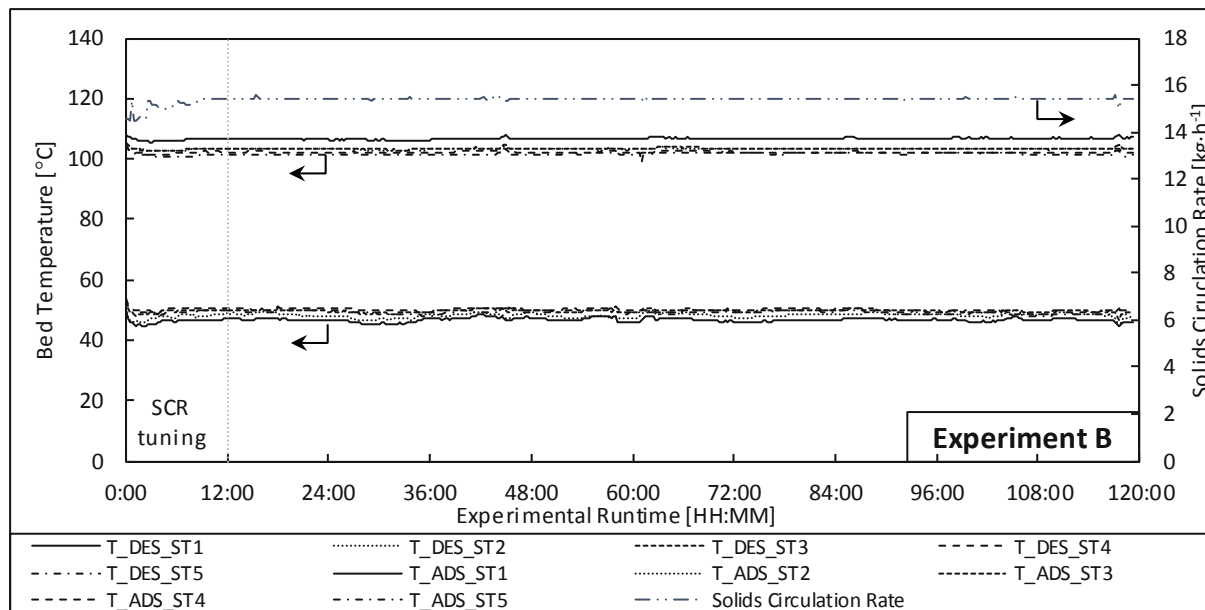


Figure 69: Graphs showing column stage temperatures and the solids circulation rate in the course of the 120-hour experiment using Sorbent A.



**Figure 70: Graphs showing column stage temperatures and the solids circulation rate in the course of the 120-hour experiment using Sorbent B.**

### 8.8 MOVING-BED HEAT EXCHANGER DESIGN

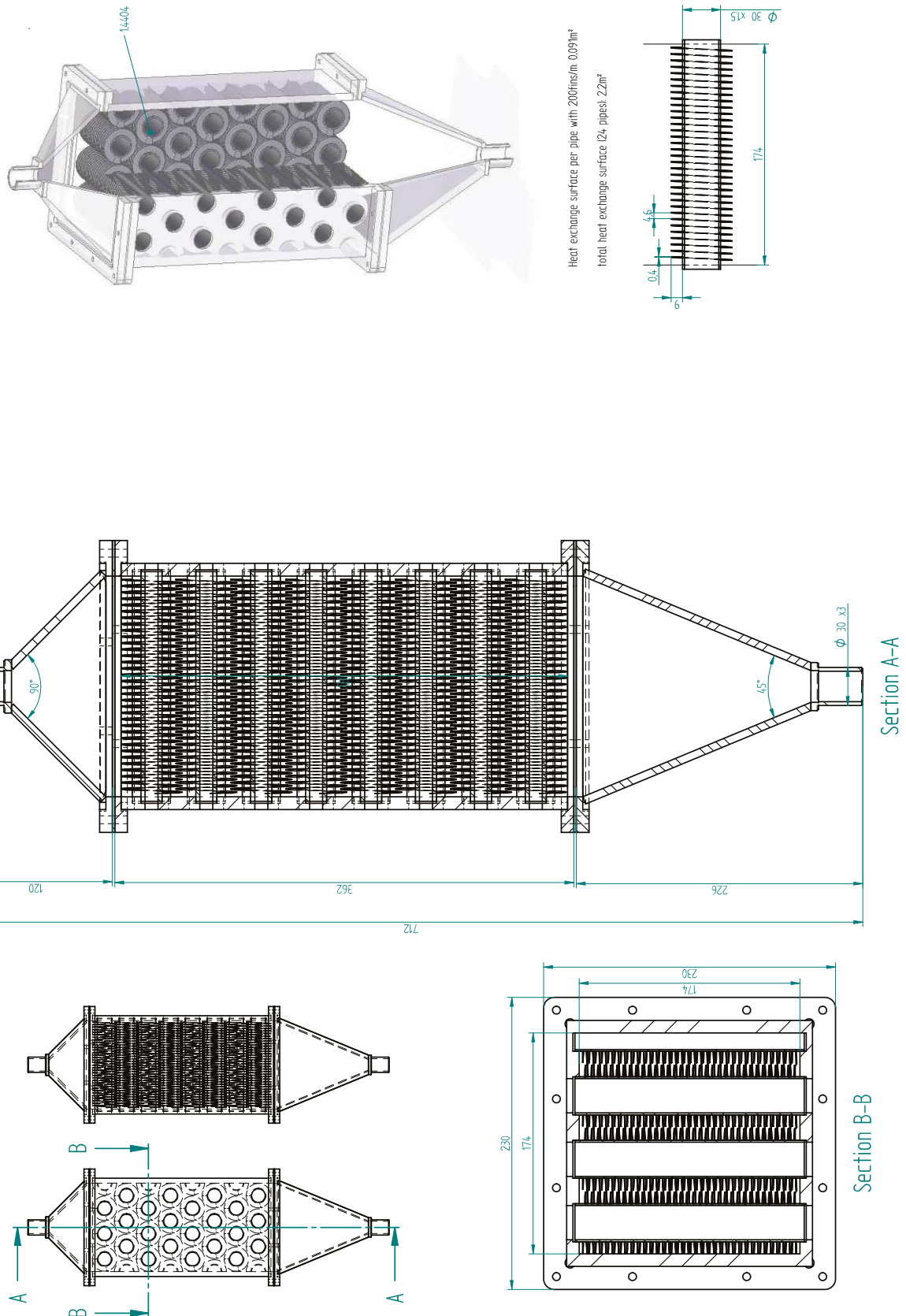


Figure 71: Technical drawing showing the design of the moving bed heat exchanger with heat exchanger pipes with 200 fins per meter (i.e. HEX-200)

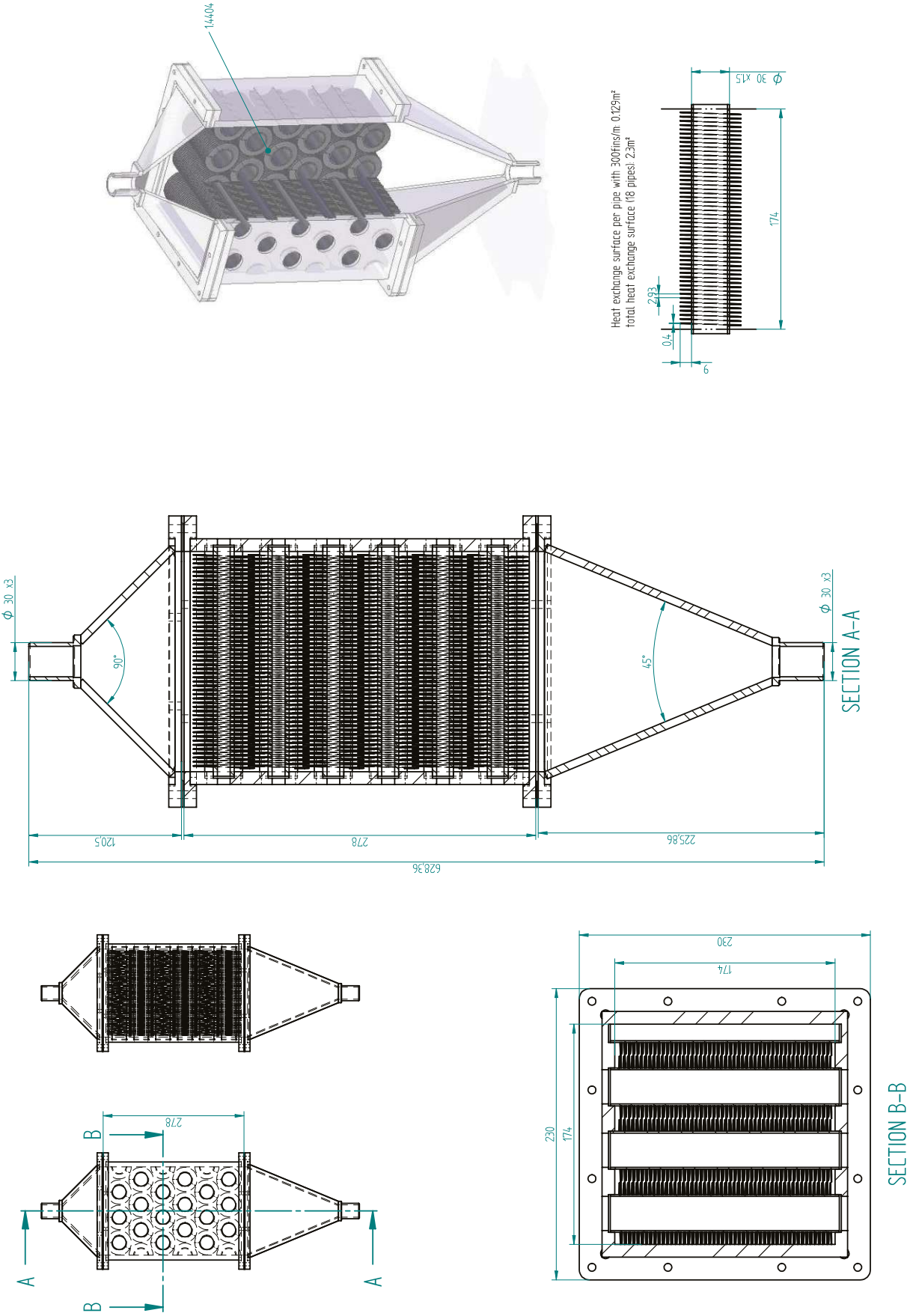


Figure 72: Technical drawing showing the design of the moving bed heat exchanger with heat exchanger pipes with 300 fins per meter (i.e. HEX-300)

## 8.9 HEAT TRANSFER COEFFICIENT BETWEEN A MOVING BED OF SOLIDS AND A FINNED TUBE

Empirically derived correlation of the heat transfer coefficient between a moving bed of solids and a finned tube as determined by Obuskovic [161]:

$$h = \frac{1}{R_c + 0.5 \cdot \sqrt{\frac{\pi \cdot t}{k_e \cdot \rho_b \cdot c_{p,s}}}} \quad \text{Eq. 58}$$

$$R_c = \frac{6.7 \cdot 10^{-5} \cdot d_p^2}{k_g} \quad \text{Eq. 59}$$